

Dynamic Simulation and Control of Optical Systems

Von der Fakultät Konstruktions-, Produktions- und
Fahrzeugtechnik der Universität Stuttgart
zur Erlangung der Würde eines Doktor-Ingenieurs (Dr.-Ing.)
genehmigte Abhandlung

von

Johannes Störkle

geboren in Waldshut-Tiengen

Hauptberichter: Prof. Dr.-Ing. Prof. E.h. Peter Eberhard

Mitberichter: Prof. Dr.-Ing. Herbert Gross

Tag der mündlichen Prüfung: 27. September 2018

Institut für Technische und Numerische Mechanik
der Universität Stuttgart

2018

Preface

Why does one study optical systems at an institute for mechanics? Well, there are outstanding physicists who design optics with unbelievably precise surfaces and they are always finding clever ways to go beyond physical limits. On the other hand, there are brilliant mechanical engineers who develop and design suitable geometries for the assembly and placement of the optical components. However, when operating a high-precision optical system, it often becomes clear that the environment is not as static as assumed because of mechanical vibration and associated optical disturbances. Therefore, the combined dynamic-optical behavior must be simulated, analyzed and optimized in advance, which requires multidisciplinary knowledge and practical methods.

Accordingly in 2010, Prof. Peter Eberhard of the Institute of Engineering and Computational Mechanics (ITM), and Prof. Wolfgang Osten of the Institute of Applied Optics (ITO), initiated two multidisciplinary research projects about the simulation of dynamically disturbed optical systems [Wengert16, Gilbergs18]. During my study at the University of Stuttgart, I enthusiastically wrote my student thesis [Störkle11] in this field of research. I luckily was given the opportunity to continue the doctoral research project of my predecessor, Nicolai Wengert, who did an excellent job.

For me, the last five years were very defining and enriching, not only because of the professional discourse with my great ITM colleagues and other research scientists, but also due to the close supervision of Prof. Peter Eberhard. He runs the Institute in a perfect way which enabled me to strike a good balance between educational teaching, industrial projects, and scientific research. In particular, I'd like to thank Dr. Pascal Ziegler, Prof. Michael Hanss and Jun.-Prof. Jörg Fehr for the great advises and the humorous coffee breaks. Furthermore, many thanks to my students who contributed to the research topic: Henrik Ebel, Felix Schlotterbeck, Simon Schäfer, Xinyi Zheng, Diana Teske, Felix Trautwein, Shaojian Liang, Florian Bechler, Anna Mack, Aruna Dissanayaka and finally, Luzia Hahn, who will continue this project. Additionally, I would like to thank my co-examiner Prof. Herbert Gross for his valuable feedback and his kindness.

Am Ende möchte ich mich natürlich auch noch ganz herzlich bei meiner lebenswerten Susan, meinen großartigen Eltern, meinen zwei Lieblingsbrüdern, meinen drei wunderbaren Schwestern, deren Familien und sämtlichen Freunden für die Unterstützung bedanken.

Stuttgart, im September 2018

Johannes Störkle

*“I’m starting with the man in the mirror
I’m asking him to change his ways
And no message could have been any clearer
If you want to make the world a better place
Take a look at yourself, and then make a change”*

- Michael Jackson

Contents

Kurzfassung	XI
Abstract	XIII
1 Introduction	1
1.1 Concept of Adaptive Optics	6
1.2 Dynamical-optical Applications	7
1.3 Contents and Goal of the Thesis	8
2 Mechanical Fundamentals	11
2.1 Multibody Systems	11
2.2 Finite Element Systems	13
2.3 Model Order Reduction	13
2.4 Elastic Multibody Systems	17
2.5 Control Theory	18
3 Optical Fundamentals	23
3.1 Geometrical Optics	23
3.2 Ray Tracing Theory	26
3.2.1 Ray Description	26
3.2.2 Surface Descriptions	27
3.2.3 Intersection of a Ray and a Surface	30
3.2.4 Refraction and Reflection in 3D	32
3.3 Properties of Optical Systems	33
3.3.1 Paraxial Image Formation	34
3.3.2 Entrance and Exit Pupils	36

3.3.3	Optical Aberrations	37
3.3.4	Zernike Polynomials	39
3.3.5	Resolution	43
3.4	Wave Optics	44
3.4.1	Wave-Particle Duality	44
3.4.2	Interference, Irradiance and Coherence	48
3.4.3	Fourier Optics	50
3.4.4	Exposure Simulation	54
4	Dynamical-optical Simulations	57
4.1	Simulation Strategies	57
4.2	Implementations for the Integrated Modeling	60
4.2.1	Kinematics of Optical Surfaces	60
4.2.2	Approximation of Optical Surfaces	63
4.2.3	Non-sequential Ray Tracing for Segmented Mirrors	67
4.2.4	Wavefront Analysis	68
4.3	Mechanical Simulations	72
4.3.1	Frequency Domain	74
4.3.2	Time Domain	77
4.4	Linear Dynamical-optical Analysis	81
4.4.1	Kinematic-optical Sensitivities	81
4.4.2	Mechanical-optical Transfer Function	83
4.5	Further Investigations	86
4.5.1	Influence of the MOR on optical Simulation	87
4.5.2	Influence of the Dynamical-optical Simulation Method	89
4.6	Adaptive Optics for a Segmented Telescope	92
4.6.1	Kinematic-optical Model Under Disturbance	92
4.6.2	Control Strategy for M2	95
4.6.3	Simulation of the AO-Control	96

5	Experimental Realization of a Dynamical-optical Control	101
5.1	Conception and Modeling	101
5.1.1	Previous Test Setup	102
5.1.2	Active Control Extension	104
5.2	Arrangement of the Hardware Systems	107
5.2.1	Lens Actuator System	109
5.2.2	Force Sensor System	112
5.2.3	Position Sensor System	115
5.2.4	Control Unit System	118
5.2.5	Vision Sensor System	120
5.3	Development of the Control Strategy	123
5.3.1	Controller Design	123
5.3.2	Simulation and Tuning	125
5.4	Experimental Investigation	127
5.4.1	Deployment on Hardware	128
5.4.2	Measurement Results	129
5.4.3	Variation of Model Parameters	132
6	Conclusion and Outlook	135
	Appendix	139
A.1	Derivation of the GRIN Ray Equation	139
A.2	OM-Sim	141
	Bibliography	143
	Abbreviation, Symbols and Notations	155

Kurzfassung

Die Arbeit behandelt die simulationsbasierte Untersuchung und Regelung von optischen Systemen, die mechanisch beeinflusst werden. Der Schwerpunkt liegt auf der dynamisch-optischen Modellierung von schwingungsempfindlichen Spiegelsystemen. Diese kommen beispielsweise in großen Astronomie-Teleskopen oder in hochpräzisen Lithographie-Objektiven zum Einsatz.

Solche auflösungsoptimierten Spiegelsysteme haben die Besonderheit, dass deren optische Oberflächen meist durch hochdimensionale Polynome definiert werden. Darüber hinaus weisen die Spiegelsysteme üblicherweise eine Obstruktion auf, insbesondere wenn aufgrund einer konzentrischen Spiegelanordnung das Zentrum des Primärspiegels vom Sekundärspiegel verdeckt wird. Für die quantitative Untersuchung dieser Systeme betrachtet man optische Wellenfrontfehler, die durch kreis- oder ringförmige Zernike-Polynome beschrieben werden. Im Gegensatz dazu wird das Auflösungsvermögen eines Systems qualitativ anhand der Strahlungsverteilung auf dem Bildschirm bewertet, da im resultierenden Bild zusätzliche wellenoptische Effekte, wie Beugung und Interferenz, enthalten sind.

Bei Teleskopen bestehen die großflächigen Primärspiegel meist konstruktionsbedingt aus vielen einzelnen hexagonalen Spiegelsegmenten, die mit präziser Sensorik und Aktorik positioniert werden. Außerdem werden optische Aberrationen aufgrund von atmosphärischen Störungen üblicherweise mittels sogenannter Adaptiver Optiken kompensiert. In der Praxis kann man diese Bildfehler meist innerhalb von wenigen Sekunden erfassen und durch aktiv-verformbare Spiegel ausregeln.

Zur Verbesserung der Leistungsfähigkeit dieser optischen Systeme, sollten jedoch auch dynamische Störungen in der Mechanik, also kleine Bewegungen und Verformungen der optischen Oberflächen, berücksichtigt werden. Hier sind umweltbedingte Schwingungsanregungen, die z.B. aufgrund von seismischen Aktivitäten oder Windströmungen entstehen, von konstruktionsbedingten Störungen zu unterscheiden. Letztere werden von den enthaltenen Instrumenten- und Positioniersystemen verursacht, die mit der dynamischen Gesamtstruktur verkoppelt sind. Für die Untersuchung dieser Fälle werden in der vorliegenden Arbeit multidisziplinäre Simulationen entwickelt. Anhand derer wird das dynamisch-optische Systemverhalten mittels modellordnungsreduzierten, flexiblen Mehrkörpersystemen abgebildet. Anschließend wird das mechanisch-optische System mit bei geringem Rechenaufwand dynamisch analysiert. Die Schwierigkeit ist dabei, die oben genannten Besonderheiten und Phänomene mit guter Näherung zu berücksichtigen. Insbesondere werden, dank der Fourier-optischen Analyse im Zeitbereich, auch Belichtungsprozesse simuliert.

Um Aberrationen aufgrund von hochfrequenten, mechanischen Schwingungen aktiv zu kompensieren, werden des Weiteren modellbasierte Regelungsstrategien entworfen. Dies wird neben Simulationsbeispielen auch durch ein Laborexperiment veranschaulicht. Let-

zteres wird mit einem preiswerten Versuchsaufbau für einen Studenten-Praktikumsversuch realisiert. Dabei kommen Arduino-Mikrocontroller, Positions- und Kraftsensoren sowie Hochgeschwindigkeitskameras zum Einsatz.

Abstract

This thesis deals with the simulation-based investigation and control of optical systems that are mechanically influenced. Here, the focus is on the dynamic-optical modeling of vibration-sensitive mirror systems, which are utilized, e.g., in large astronomy telescopes or high-precision lithography optics.

Such resolution-optimized mirror systems have a peculiarity in that their optical surfaces are often defined with high-dimensional polynomials. Also, the mirror systems usually have an obstruction, e.g., due to a concentric mirror arrangement. Thus, the center of the primary mirror is obscured by the secondary mirror. For the quantitative investigation of these systems, optical wavefront errors are considered, which are described by circular or annular Zernike polynomials. In contrast, the resolution of a system is qualitatively evaluated by the resulting image, as it also includes wave-optical effects, such as diffraction and interference.

The large-area primary mirrors of telescopes typically consist of many individual hexagonal mirror segments, which are positioned with precise sensors and actuators. Furthermore, an adaptive optical unit usually compensates for the optical aberrations due to atmospheric disturbances. In practice, these aberrations are detected, and corrected, within a few seconds using deformable mirrors.

However, to further improve the performance of these optical systems, dynamical disturbances in the mechanics, i.e., small movements and deformations of the optical surfaces, must also be taken into account. These vibration excitations are categorized as environmental. For instance, they arise due to seismic activity or wind currents. On the other hand, they are design-related, since the included instruments and positioning systems dynamically influence the overall system. For the investigation of these cases, multidisciplinary simulation methods are developed and presented. Based on this, the dynamical-optical system behavior is modeled using model-order-reduced, flexible multibody systems. Hence, the dynamical analysis of the mechanical-optical system can be performed at low computation costs. However, the difficulty is, to consider the above particularities of the mirror systems and the related physical phenomena with a good approximation. Thanks to the optical analysis in the time domain and using Fourier-optical concepts, one can also simulate exposure processes.

In order to actively compensate for aberrations due to high-frequency mechanical vibrations, model-based control strategies are also designed. They are not only demonstrated by means of simulation examples, but also illustrated through a laboratory experiment. The latter is realized with a low-cost test setup for student training using Arduino microcontrollers, position and force sensors, as well as high-speed cameras.

Chapter 1

Introduction

Just recently in 2015, we celebrated the *International Year of Light and Light-based Technologies*, as proclaimed by the UNESCO. The scientists, engineers, and experts from all over the world recognized the importance of raising global awareness about how light-based technologies promote sustainable development and provide solutions to global challenges and interests [IYL15]. The usage of light within technical applications is an imperative cross-cutting discipline of science in the 21st century and plays a vital role in our daily lives. Currently, in the field of optics, there are mainly two cutting-edge technologies, which are introduced in the following.

Optical Lithography

Since disruptive technologies such as wearable devices, autonomous vehicles, smart sensors, big data and artificial intelligence start to change the world, semiconductor technologies and lithography processes become more important. The current optical lithography is based on a wavelength of 193 nm, and the related illumination and projection optics consist of high-precision crystal lenses. Thereby, the light shines through a patterned surface called a photomask. That process casts the pattern onto the silicon wafer, where it is fixed by a photosensitive chemical and then etched onto the wafer [IEEE18]. The related optical exposure depends on the desired irradiance and can take up to a few seconds.

Today's state-of-the-art process further uses resolution enhancement technologies, as multi-patterning or optical proximity correction [Bisschop16], to reach feature sizes of about 50 nm. During the multi-patterning, e.g., three or four different photomasks are utilized to produce a single pattern on a chip, but this process is quite complex and expensive. Hence, the further improvement of these processes and machines is limited. But how can we manufacture next-generation computer chips with a higher density of transistors to meet Moore's law [Moore65]?

In literature, one can find the Abbe resolution criterion [GrossSingerTotzeck07]. According

to that, the maximal feature size is limited by the critical distance

$$\text{CD}_{\text{Abbe}} = k_{\text{CD}} \frac{\lambda}{\text{NA}}, \quad (1.1)$$

whereby the process factor k_{CD} cannot be smaller than 0.25. So in order to resolve smaller feature size, either the numerical aperture NA has to be increased, or the wavelength λ has to be reduced. Due to construction and reflection issues, the NA can hardly be greater than 0.95 within vacuum, and 1.35 within an immersion [SchootEtAl17]. Hence, the use of extreme ultraviolet (EUV) light with a wavelength of about 13.5 nm is the principal technology [IEEE18].

However, the glass of a lens would absorb the EUV photons immediately, so the illumination optics and the telecentric projection optics have to be designed through levitated mirrors instead. Herein lies another challenge, as the mirrors must be polished and mounted with extreme precision. To put this into perspective, if one of the mirrors were to be blown up to the size of Germany, the biggest bump would need to be less than one-tenth of a millimeter high. These mirrors are coated with around one hundred thin layers to promote their reflectivity; some layers are as thin as 3 nm. Additionally, as even air absorbs EUV light, the whole exposure system, including the wafer, must be integrated into a large vacuum chamber [ElectroOptics18]. Since the radiant power of the EUV light is quite weak, it could take up to a few minutes for the exposure [KunkemöllerEtAl15]. The schematic setup of a corresponding machine is illustrated in Figure 1.1.

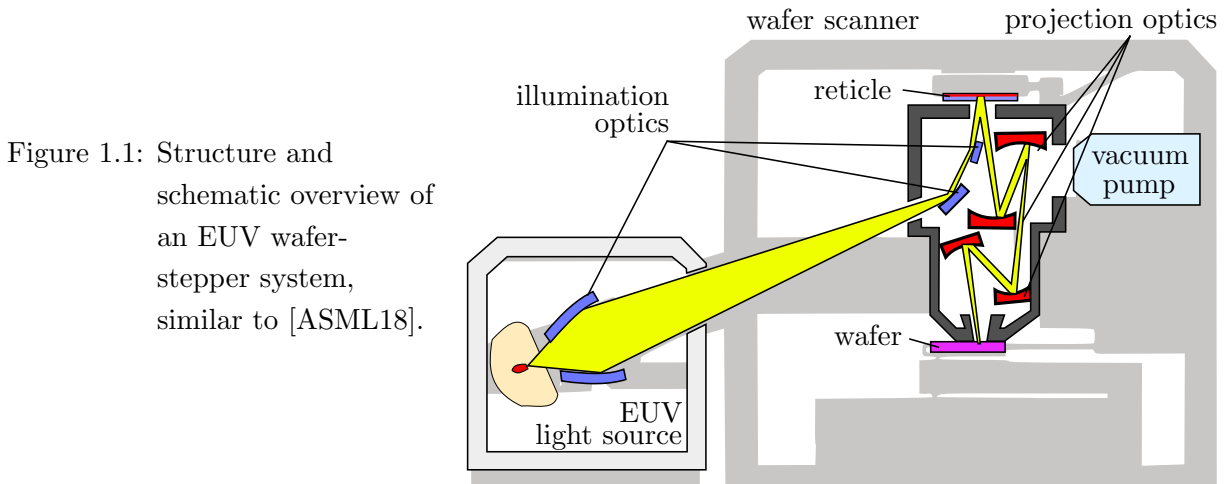


Figure 1.1: Structure and schematic overview of an EUV wafer-stepper system, similar to [ASML18].

Figure 1.2(a) illustrates a future EUV optics, which is developed by Zeiss and ASML. The current generation is called Starlith 3400 and consists of 10 mirrors [Zeiss18].

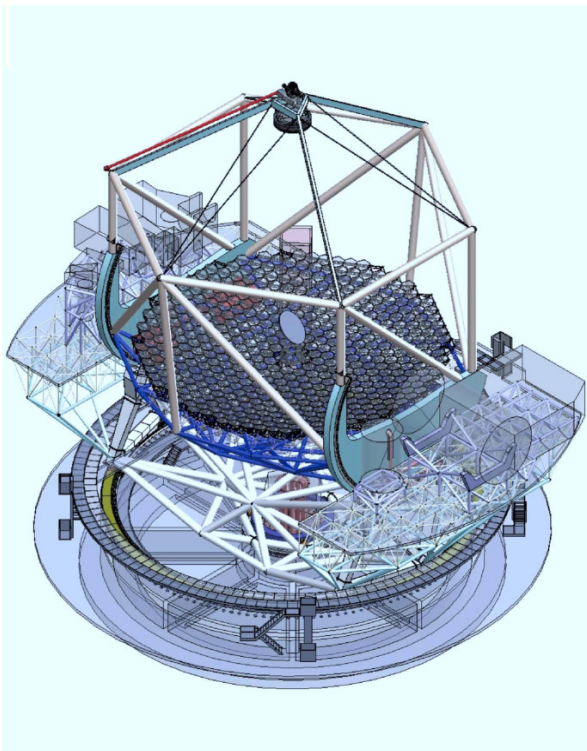
However, as Moore's law has driven features to ever-smaller dimensions, new physical effects that could be effectively ignored in the past are now affecting the process. For instance, that the lithographic optics are very sensitive with respect to mechanical disturbances. During the exposure time, even small displacements, deformations, and vibrations can be sufficient to produce unacceptably aberrated images on the wafer. Sources of these incidents can



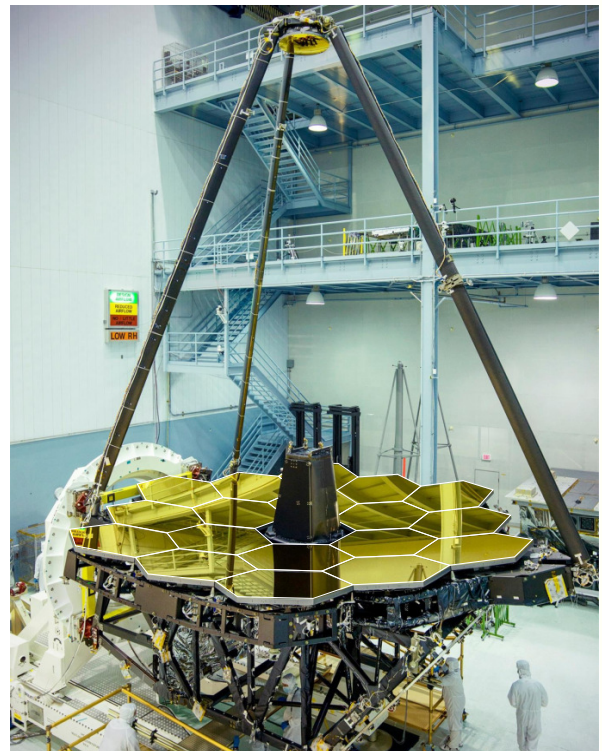
(a) optics for EUV lithography [ASML18]



(b) single mirror FIRST [Herschel18]



(c) segmented TMT [UsudaEtAl14]



(d) segmented JWST [JWST18]

Figure 1.2: Applications for high-precision mirror optics.

be minimal excitations at the optical components, e.g., from the noise of coolers, seismic ground excitations or influences of the wafer motion system. In order to reduce such effects and to improve the overall mechanical-optical robustness, strategies like vibration isolation [Butler11], structural optimization [WengertEberhard13] or active vibration compensation [Seifried14] can be considered. Therefore, multidisciplinary simulation models have to be developed. They can be used to analyze, predict and improve such a dynamical-optical behavior.

Further typical examples, where small mechanical disturbances affect a high-precision optical system, can be found in the field of astronomical telescopes.

Astronomical Telescopes

Astronomy has been an important driver for the development of advanced technology, such as the most sensitive detectors of light, radio waves, high-precision sensors, and actuators, as well as the fastest computers [IYL15]. The need to study the fascinating space requires sophisticated electronics and extreme-precision adaptive optics (AO) as well as cutting-edge engineering. Modern space-based and ground-based mirror telescopes are among the most advanced machines ever built and are outstanding educational devices for introducing the latest complex technology.

For instance, large ground-based telescope as the Extremely Large Telescope (ELT) or the Thirty Meter Telescope (TMT) according to Figure 1.2(c) are considered worldwide as one of the highest priorities in ground-based astronomy. Due to its large size, the related primary mirrors typically consist of many individual hexagonal mirror segments, which are positioned with precise sensors and actuators. The telescopes will vastly advance astrophysical knowledge, allowing detailed studies of subjects including planets around other stars, the first objects in the Universe, super-massive black holes, and the nature and distribution of the dark matter and dark energy which dominate the Universe [ESO18].

In Figure 1.2(b) the space-based Herschel telescope [Herschel18] is shown. It was active from 2009 to 2013 and was the largest infrared single mirror space telescope ever launched. With a diameter of 3.5 m, its primary mirror was four times bigger than any previous infrared space telescope, and almost one and a half times larger than the Hubble Space Telescope.

The James Webb Space Telescope (JWST), which is currently one of the most famous telescopes, is depicted in Figure 1.2(d). Its primary mirror is composed of 18 hexagonal mirror segments that combine to create a mirror with a diameter of 6.5 m. An overview of the JWST is presented in [Clampin11], and the launch to space is planned for 2020 [JWST18].

Usually, a basic mirror telescope consists of a primary mirror (M1) and a secondary mirror (M2) [AndersenEnmark11]. For instance, two different designs are sketched in

Figure 1.3(a) and (b). The first one presents the unobscured Gregorian model. The circular aperture stop (AS) determines the regarded field of light rays. These rays can be considered as parallel since the observed object is at a very far distance. Next, the M1 projects the incidental light rays to the M2, which finally focuses the circular optical field at the image plane. In contrast, the other design of Cassegrain has a centered obstruction, since the secondary mirror is in the way of the incidental light rays. This circumstance leads to an annular optical field, which is again focused on the image plane. Most of the built telescopes are based on the Cassegrain design. But why are these telescopes usually so large?

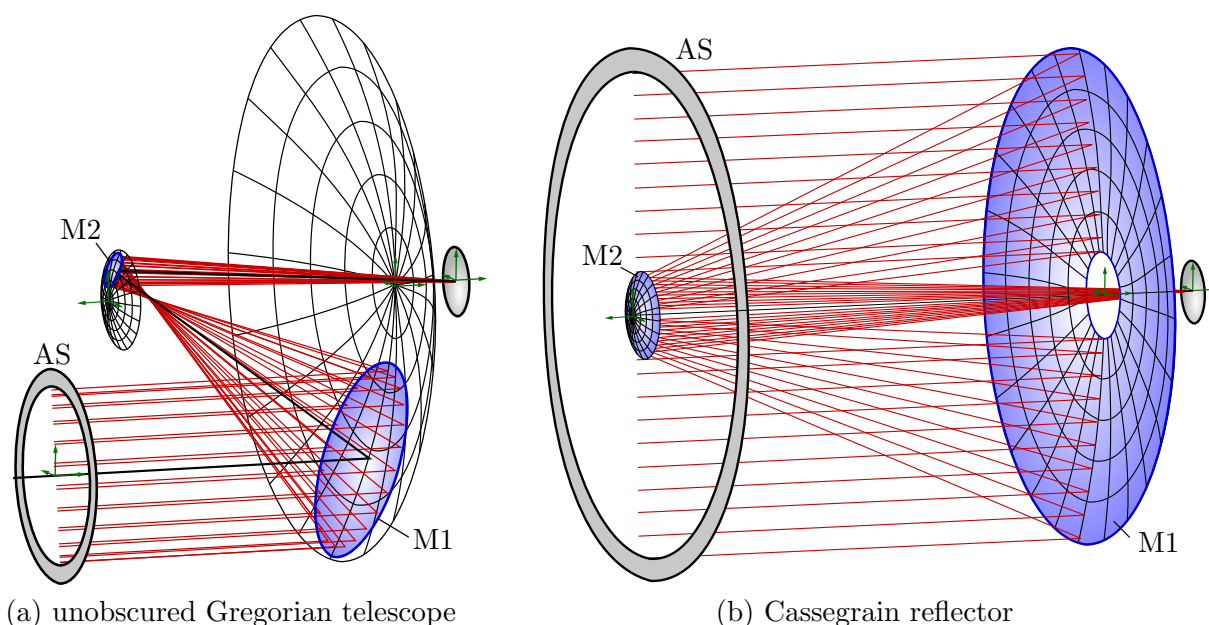


Figure 1.3: Basic examples for the design of optical mirror systems.

The size of a telescope is essential for two reasons: one is the amount of light it can collect, and the other is the level of detail it can see. As a 39 m telescope, the ELT will gather 15 times more light than the largest optical telescopes operating today. It will also provide images 15 times sharper than those from the Hubble Space Telescope. The ELT performance is thus orders of magnitude better than that of the currently existing facilities. Such a telescope may, eventually, revolutionize our perception of the universe, much as Galileo's telescope did, 400 years ago [ESO18].

Anyhow, for the system and control engineers, the concept of adaptive optics (AO) is exciting since it combines intentional mirror deformations with optical accuracy. Hence, it is explained in the following.

1.1 Concept of Adaptive Optics

According to the concept of AO, a deformable mirror is used to compensate the optical aberrations due to atmospheric disturbances. The atmospheric disturbances are usually in the low-frequency range, and it is sufficient to use sample times of a couple of seconds. Thereby, the related optical aberrations are typically detected with a Shack-Hartmann Wavefront Sensor (SHWFS) [Ebel14]. The task of the AO unit is to control the deformation of an elastic mirror such that the current aberration is compensated. This ensures an undisturbed space observation or perfect image exposure as sketched in Figure 1.4(a).

However, the lightweight structures of a telescope mirror are also sensitive with respect to deformations and dynamical disturbances. During the astronomical observation, e.g., dynamic wind loads, the AO unit or other motion systems can unintentionally excite the whole construction including mounted mirrors. The mechanical disturbances can cause vibrations of the optical elements in the high-frequency range, as indicated in Figure 1.4(b). In order to compensate also for the mechanical vibrations, they can be detected in real-time, e.g., using Laser Doppler vibrometers (LDV), multiple position sensors and strain gauges. Based on this, the reconstruction of the mechanical mirror behavior can be performed, see also [Tyson15, BöhmEtAl14]. This approach is depicted in Figure 1.4(c). In the presence of delays, feed-forward controls can be used, as proposed in [RuppelEtAl13, BöhmEtAl16].

Apparently, dynamical-optical analyses are required for such developments. In the following, some applications are presented, where integrated models are used, or dynamical analyses are performed at optical systems.

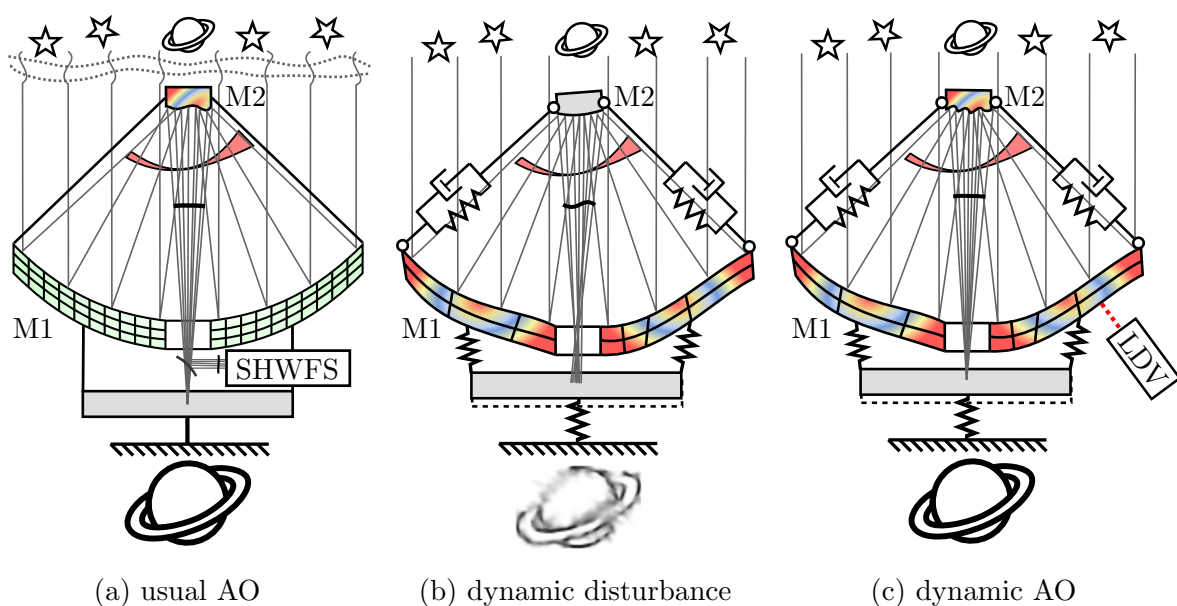


Figure 1.4: Different concepts of AO.

1.2 Dynamical-optical Applications

Many optical instruments are sensitive for mechanical vibrations and dynamic disturbances since they have to meet strong requirements in sometimes rough environments. The examples clarify the need for multidisciplinary concepts and approaches.

Notably, for the integrated modeling of telescopes, there are many contributions in literature. The dissertation of [Wengert16] has to be mentioned, since it explicitly presents the coupling of mechanical and optical lens simulations in a way, quite similar to the current work. The textbook of [AndersenEnmark11] and the dissertation of [Müller05] are very advisable, as they state an excellent overview about the mechanical and optical modeling of large ground-based telescopes. In particular, there are already model order reduction (MOR) methods proposed and applied, as well as Fourier-optical simulation methods. The consideration of astronomical instruments, interferometers, and radiometric devices is appropriately explained for mechanical engineers. Furthermore, the textbook of [Lemaitre09] focus on the elasticity theories and the different types of finite elements. Besides, it states the AO methods, the history and the application of optical designs for the astronomy. The concepts of AO in astronomy, e.g., using natural guide stars or laser beacons are deepened in the collected handbook of [Roddier04]. General procedure for mechanical engineers during the integrated modeling using the software packages Nastran, SigFit, CodeV, Zemax, and OSLO are exemplified in [DoyleGenbergMichels12, GenbergMichels17, ScolaEtAl14, PütschStollenwerkLoosen17]. These remarkable contributions analyze the so-called Structural-Thermal-Optical-Performance (STOP). Another highly recommended Ph.D. thesis is written by [Laslandes12], which presents developments and control concepts of space-active optics for future large observatories. Thereby, correcting deformable mirrors are utilized for space-based applications.

Since the field of engineering applications in astronomy is quite large, there are entirely a lot of related articles and proceedings published. For the ground-based ELT, TMT and LSST projects, many dynamic analyses using simulations are performed. For instance, some modeling frameworks and simulation toolkits, e.g., Zemax, Octopus, and CodeV, are proposed in [SedghiEtAl11, AngeliEtAl16]. The MOR is thereby also a particular issue [YuRobertsSharf04]. Through the integrated models, it is possible to investigate the vibration budget of the optical components [SedghiMüllerJakob16, MacMartinThompson15]. Further improvements concerning active damping [SedghiEtAl16], the extension to dynamic disturbance models due to wind [MacMynowskiEtAl10] and the simulation of the AO [ZamkotsianDohlenFerrari00, BasdenEtAl14, BoyerEtAl14, AngeliEtAl14] are published. Besides, it is possible to analyze the dynamic-optical performance of single segments [WitvoetEtAl15, NijenhuisHamelinckBraam12], and to perform aero-thermal simulations [VogiatzisThompson16].

On the other hand, there are also many space-based applications as the JWST, which are

dynamically studied. For instance, integrated models are thereby used for the investigation of operational segment alignments [HowardEtAl08] or for the secondary mirror figure compensation using primary mirror segment motions [HowardFeinberg09]. Another topic is the reaction wheel mechanical noise, which is one of the most significant sources of disturbance forcing on space-based observatories [LiuMaghamiBlaurock08, LeEtAl14].

1.3 Contents and Goal of the Thesis

Most of the mentioned contributions have a lot in common with this work. For instance, it is quite typical to describe the mechanical behavior of mirror optics using the finite element method. The usage of Zernike polynomials for the approximation of deformation and the introduction of kinematic-optical sensitivities are also quite typical.

However, there are also some new approaches, e.g., the utilization of elastic multibody simulation and model order reduction techniques in combination with concepts from optical simulations [StörkleEberhard17a]. Thereby, the mechanical behavior of mirror systems is described by a combination of rigid body motions and small deformations. This procedure allows extensive analyses of complex systems or single components in the time domain at low computational costs. In order to investigate the overall dynamical-optical system behavior, multi-disciplinary simulation strategies and software tools with convenient interfaces are proposed and developed, see also [Wengert16, StörkleEberhard16]. On the one hand, existing software tools for a finite-element simulation are employed and on the other hand, a model order reduction program called MatMorembs and an elastic multibody simulation program named Neweul-M² are used. Within this research project, the optical simulation program OM-Sim with an interface to elastic multibody simulations is refined and developed further, see also Secion A.2. As a consequence, the derived and introduced methods, simulation features, and the analyses according to this work are implemented in OM-Sim. The general procedure for dynamical-optical simulations using domain-specific software packages is shown in Figure 1.5. It sketches the various steps during the modeling and simulation process.

Another highlight of this work is the use of annular Zernike polynomials for the consideration of a centered obstruction within an optical system. Besides, the wave-optical effects and the imaging during exposure can be simulated according to Fourier-optical methods. The segmentation of mirrors can be taken into account [EberhardStörkleMack18]. The resulting analyses enable to study optical system error budget allocations including mounting tolerances, alignment errors, optical surface distortions, image stability, and wavefront errors.

This thesis is mainly structured in three parts:

- At first, the Chapters 2 and 3 present the fundamentals and modeling techniques

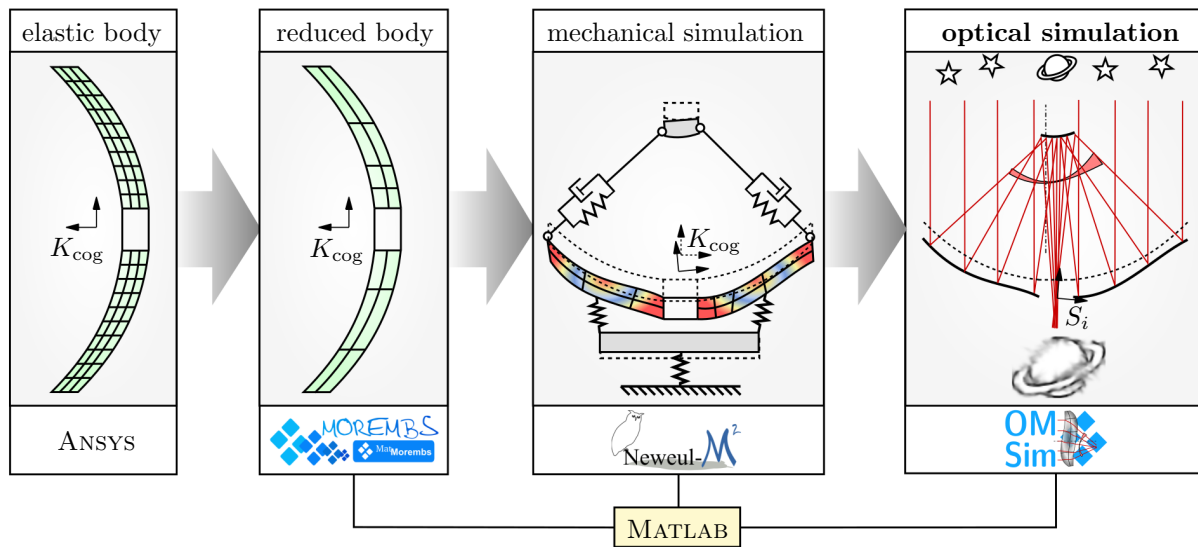


Figure 1.5: Basic procedure for describing dynamical-optical simulations.

of mechanical and optical systems. In particular, the optical theories are provided more detailed, since the properties of optical systems, the occurring phenomena and the concepts of optical modeling are significant.

- Second, Chapter 4 introduces the simulation workflow, the particular implementations for the interface data, the methods for the multidisciplinary analysis and the development of an AO controller. The corresponding examples clarify the execution of the proposed approaches.
- As the third and last part, an experiment for the optical compensation for mechanical vibrations is exemplified in Chapter 5. This low-cost test setup is based on Arduino microcontrollers, position and force sensors, as well as high-speed cameras.

Chapter 2

Mechanical Fundamentals

Mechanical models of coupled bodies are usually based on the method of rigid multibody systems (MBS) or elastic multibody systems (EMBS) with the floating frame of reference approach [SchwertassekWallrapp99]. The latter can consider elasticities of single bodies, e. g. by means of the finite element method (FEM). In contrast to a detailed and large global model, a reduced and modular EMBS can lead to the low computational effort. Furthermore, the system can be analyzed and assembled step by step, and it is possible to include only the relevant dynamical behavior due to the usage of appropriate model order reduction (MOR) methods. For some applications, e.g., in the field of adaptive optics, it is also necessary to observe or control system states, to improve or reduce the dynamical behavior. This section gives a brief introduction to the related theories and equations.

2.1 Multibody Systems

Often, the dynamics of a mechanical system can be described by ordinary differential equations. They can be derived applying the principles of mechanics. In consideration of a holonomic rigid MBS, the motion behavior, which could be nonlinear, can be described by n_{dof} generalized coordinates $\mathbf{q}_{\text{nl}}(t)$. Thereby, n_{dof} is the number of degrees of freedom (DOF). For j rigid bodies coupled in a tree structure, the *Newton-Euler equations* [SchiehlenEberhard14] in Cartesian coordinates can be formulated as

$$\underbrace{\begin{bmatrix} m_1 \mathbf{I} & & & & & \\ \mathbf{0} & \dots & & & & \\ \mathbf{0} & \mathbf{0} & m_j \mathbf{I} & & & \\ \mathbf{0} & \mathbf{0} & \mathbf{0} & \mathbf{I}_1 & & \\ \mathbf{0} & \mathbf{0} & \mathbf{0} & \mathbf{0} & \dots & \\ \mathbf{0} & \mathbf{0} & \mathbf{0} & \mathbf{0} & \mathbf{0} & \mathbf{I}_j \end{bmatrix}}_{\bar{\mathbf{M}}} \text{sym.} \cdot \underbrace{\begin{bmatrix} \mathbf{J}_{\text{T1}} \\ \dots \\ \mathbf{J}_{\text{Tj}} \\ \mathbf{J}_{\text{R1}} \\ \dots \\ \mathbf{J}_{\text{Rj}} \end{bmatrix}}_{\bar{\mathbf{J}}} \cdot \ddot{\mathbf{q}}_{\text{nl}} + \underbrace{\begin{bmatrix} m_1 \bar{\mathbf{a}}_1 \\ \dots \\ m_j \bar{\mathbf{a}}_j \\ \mathbf{I}_1 \bar{\boldsymbol{\alpha}}_1 + \tilde{\boldsymbol{\omega}}_1 \mathbf{I}_1 \boldsymbol{\omega}_1 \\ \dots \\ \mathbf{I}_j \bar{\boldsymbol{\alpha}}_j + \tilde{\boldsymbol{\omega}}_j \mathbf{I}_j \boldsymbol{\omega}_j \end{bmatrix}}_{\bar{\mathbf{q}}^c} = \underbrace{\begin{bmatrix} \mathbf{f}_1^a \\ \dots \\ \mathbf{f}_j^a \\ \mathbf{l}_1^a \\ \dots \\ \mathbf{l}_j^a \end{bmatrix}}_{\bar{\mathbf{q}}^a} + \underbrace{\begin{bmatrix} \mathbf{F}_1^r \\ \dots \\ \mathbf{F}_j^r \\ \mathbf{L}_1^r \\ \dots \\ \mathbf{L}_j^r \end{bmatrix}}_{\bar{\mathbf{Q}}} \cdot \mathbf{g} \quad (2.1)$$

with the masses m_j , the translational and rotational Jacobian matrices \mathbf{J}_{Tj} and \mathbf{J}_{Rj} , the local accelerations $\bar{\mathbf{a}}_j$, the local angular acceleration $\bar{\boldsymbol{\alpha}}_j$, and the angular velocity $\boldsymbol{\omega}_j$. The inertia tensors \mathbf{I}_j , the applied forces \mathbf{f}_j^a and moments \mathbf{l}_j^a , and the related distribution matrices \mathbf{F}_j^r and \mathbf{L}_j^r of the generalized reaction forces and moments \mathbf{g} , have to be represented with respect to the initial reference frame. The two latter matrices can be collected in the global distribution matrix $\bar{\mathbf{Q}}$. Furthermore, $\bar{\mathbf{M}}$ and $\bar{\mathbf{J}}$ are denoted as the global mass distribution matrix, and the global Jacobian matrix, $\bar{\mathbf{q}}^c$ summarizes the Coriolis and gyroscopic forces, and the vector $\bar{\mathbf{q}}^a$ represents the applied forces and moments. Because of the generalized orthogonality between the motions and the constraints, the virtual work of the reaction forces $\bar{\mathbf{J}}^\top \cdot \bar{\mathbf{Q}} = \mathbf{0}$ vanishes according to the *d'Alembert's principle* [SchiehlenEberhard14]. Thus, the Equations (2.1) can be simplified by a left pre-multiplication with the transposed global Jacobian matrix $\bar{\mathbf{J}}^\top$. As a result, the *equations of motion* of an ordinary MBS, which are usually nonlinear, are

$$\mathbf{M}_{\text{nl}}(\mathbf{q}_{\text{nl}}, t) \cdot \ddot{\mathbf{q}}_{\text{nl}} + \mathbf{k}(\dot{\mathbf{q}}_{\text{nl}}, \mathbf{q}_{\text{nl}}, t) = \mathbf{q}^a(\dot{\mathbf{q}}_{\text{nl}}, \mathbf{q}_{\text{nl}}, \mathbf{u}, t), \quad (2.2)$$

where $\mathbf{M}_{\text{nl}} \in \mathbb{R}^{n_{\text{dof}} \times n_{\text{dof}}}$ is the symmetric inertia matrix, $\mathbf{k}^c \in \mathbb{R}^{n_{\text{dof}}}$ is a vector of generalized gyroscopic forces including the Coriolis and centrifugal forces as well as the gyroscopic torques. The vector $\mathbf{q}^a \in \mathbb{R}^{n_{\text{dof}}}$ represents the generalized applied forces. Furthermore, Equation (2.2) can be rearranged and transformed into the nonlinear state-space representation

$$\underbrace{\begin{bmatrix} \dot{\mathbf{q}}_{\text{nl}} \\ \ddot{\mathbf{q}}_{\text{nl}} \end{bmatrix}}_{\dot{\mathbf{x}}_{\text{nl}}} = \underbrace{\begin{bmatrix} \dot{\mathbf{q}}_{\text{nl}} \\ \mathbf{M}_{\text{nl}}^{-1} \cdot (\mathbf{q}^a - \mathbf{k}^c) \end{bmatrix}}_{\mathbf{f}(\mathbf{x}_{\text{nl}}, \mathbf{u}, t)}, \quad (2.3)$$

where \mathbf{x}_{nl} is called the state vector and \mathbf{u} the input vector. If appropriate, Equation (2.2) can be linearized to

$$\mathbf{M}(t) \cdot \ddot{\mathbf{q}} + \mathbf{P}(t) \cdot \dot{\mathbf{q}} + \mathbf{Q}(t) \cdot \mathbf{q} = \bar{\mathbf{B}}(t) \cdot \mathbf{u}, \quad (2.4)$$

where \mathbf{M} is the symmetric, positive definite inertia matrix. The matrices \mathbf{P} and \mathbf{Q} characterize the velocity-dependent and position-dependent forces. If these matrices are time-invariant, they can be separated into their symmetric and skew symmetric parts

$$\mathbf{D} = \frac{1}{2}(\mathbf{P} + \mathbf{P}^\top), \quad \mathbf{G} = \frac{1}{2}(\mathbf{P} - \mathbf{P}^\top), \quad \mathbf{K} = \frac{1}{2}(\mathbf{Q} + \mathbf{Q}^\top), \quad \mathbf{N} = \frac{1}{2}(\mathbf{Q} - \mathbf{Q}^\top). \quad (2.5)$$

In particular, the positive semi-definite matrices have a physical meaning since \mathbf{D} characterizes the damping forces, \mathbf{G} the gyroscopic forces, \mathbf{K} the conservative stiffness forces, and \mathbf{N} the non-conservative forces [SchiehlenEberhard14]. The mechanical input matrix $\bar{\mathbf{B}}$ in combination with the input vector \mathbf{u} represents the external excitations.

Since for many applications, the elasticity of bodies has to be taken into account, the method of EMBS in combination with the FEM can be used, which are introduced in the following.

2.2 Finite Element Systems

The first step of creating an EMBS simulation is usually, to mechanically describe the sensitive optical components separately as elastic bodies. For that, a finite element (FE) program is utilized for the definition and meshing of the geometry. Alternatively, a computer-aided design (CAD) geometry can be imported and meshed. In order to arrange an elastic body later in an EMBS using a Buckens system, a reference frame K_{cog} should be defined in the center of mass and inertia. At first it is recommended, to define the body in a convenient reference frame, afterwards calculating its center of gravity and finally shifting the body to that position. After performing a modal analysis, the linear equations of motion of the linear FE model are accessible in binary files. For an elastic body with the vector of node displacements $\mathbf{q}_e(t)$, the mass matrix \mathbf{M}_e , damping matrix \mathbf{D}_e , and stiffness matrix \mathbf{K}_e , the equations of motion [Bathe96] have the form

$$\mathbf{M}_e \cdot \ddot{\mathbf{q}}_e(t) + \mathbf{D}_e \cdot \dot{\mathbf{q}}_e(t) + \mathbf{K}_e \cdot \mathbf{q}_e(t) = \mathbf{h}_e(t). \quad (2.6)$$

In case of an unconstrained body without any excitation, the vector $\mathbf{h}_e(t)$ vanishes, which otherwise describes the forces acting on the body. In order to represent viscous damping effects, Rayleigh damping can be used to determine the damping matrix as $\mathbf{D}_e = \alpha_R \mathbf{M}_e + \beta_R \mathbf{K}_e$ with the weighting factors α_R and β_R . Depending on the spatial resolution of the mesh, the number of elements and nodes can be enormous. Therefore, it is beneficial to apply MOR methods, which approximate the dynamical behavior with a much smaller number of DOF.

2.3 Model Order Reduction

The principle of MOR is based on the projection of the elastic coordinates \mathbf{q}_e onto a subspace \mathcal{V} , where the projection matrix is denoted by \mathbf{V} and the relationship can be formulated as $\mathcal{V} = \text{span}(\mathbf{V})$ [NowakowskiEtAl12]. This projection matrix is also called reduction basis and it describes the relationship between the elastic coordinates $\mathbf{q}_e(t)$, which are equal to the node displacements, and the reduced coordinates $\bar{\mathbf{q}}_e(t)$ with

$$\mathbf{q}_e \approx \mathbf{V} \cdot \bar{\mathbf{q}}_e. \quad (2.7)$$

The force excitation according to Equation (2.6) can be formulated as $\mathbf{h}_e(t) = \mathbf{B}_e \cdot \mathbf{u}(t)$, with the input vector $\mathbf{u}(t)$ and the input matrix \mathbf{B}_e . In case of an orthogonal projection of the equations of motion [Lehner07], the reduced model is

$$\underbrace{\mathbf{V}^\top \cdot \mathbf{M}_e \cdot \mathbf{V}}_{\bar{\mathbf{M}}_e} \cdot \ddot{\bar{\mathbf{q}}}_e(t) + \underbrace{\mathbf{V}^\top \cdot \mathbf{D}_e \cdot \mathbf{V}}_{\bar{\mathbf{D}}_e} \cdot \dot{\bar{\mathbf{q}}}_e(t) + \underbrace{\mathbf{V}^\top \cdot \mathbf{K}_e \cdot \mathbf{V}}_{\bar{\mathbf{K}}_e} \cdot \bar{\mathbf{q}}_e(t) = \underbrace{\mathbf{V}^\top \cdot \mathbf{B}_e}_{\bar{\mathbf{B}}_e} \cdot \mathbf{u}(t) \quad (2.8)$$

with the reduced mass matrix $\bar{\mathbf{M}}_e$, reduced damping matrix $\bar{\mathbf{D}}_e$, reduced stiffness matrix $\bar{\mathbf{K}}_e$, and reduced input matrix $\bar{\mathbf{B}}_e$. The process of applying a linear MOR on an elastic body,

which can also be a part of a system of substructures, is known as component mode synthesis (CMS) [HolzwarthEberhard14]. Most of these MOR methods can be classified into the two main groups of truncation-based and interpolation-based methods. The latter includes the methods based on *Krylov* subspaces. Examples for truncation-based methods are the *Modal Truncation* or the *Balanced Truncation* method based on Gramian matrices. The *Craig-Bampton* MOR method is both, truncation-based and interpolation-based. Table 2.1 gives an overview of MOR methods commonly used for CMS of substructures.

The best-known MOR method is the *Modal Truncation*. Thereby, the characteristics of the unconstrained free-floating body have to be analyzed in terms of its eigenfrequencies ω_i and eigenvectors \mathbf{v}_i , defined by the generalized eigenvalue problem (EVP)

$$(\mathbf{K}_e - \omega_i^2 \mathbf{M}_e) \cdot \mathbf{v}_i = \mathbf{0}. \quad (2.9)$$

Since the matrices are symmetric, the number of the linear independent eigenvectors is usually equal to the number of DOF [Hetzler08]. Besides, the eigenvectors are real and also called mode, eigenmodes, normal modes, vibration modes or mode shapes. In case of a modal transformation, all of them are used for the transformation matrix \mathbf{V} according to Equation (2.8). In order to achieve a reduction, the modes are usually reordered with respect to rising frequencies and afterwards, only the n_i lowest modes are kept as a reduction basis for the subspace \mathcal{V} , which results in $\mathbf{V} = [\mathbf{v}_1 \quad \mathbf{v}_2 \quad \dots \quad \mathbf{v}_{n_i}]$.

Unfortunately, for coupled substructure components in the EMBS, the straight-forward *Modal Truncation* using the free interface normal modes delivers unsatisfactory results [Dietz99]. However, the fixed interface normal modes can also be used as a projection basis according to the *Guyan's Static Condensation* [Guyan65]. By analogy, they can be calculated by solving the EVP (2.9) with retained interface coordinates. The application of this method is clarified in Example 1.

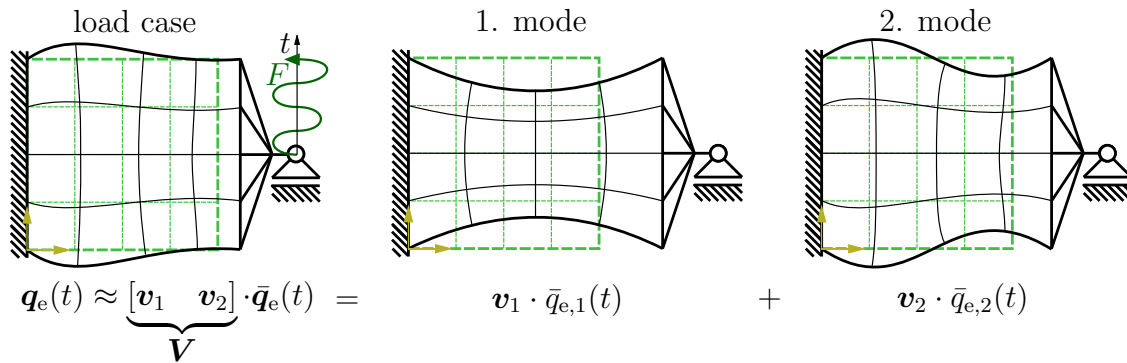
An improved set of shape functions, which contains so-called correction modes, can be obtained with the various methods from the field of CMS [HolzwarthEberhard14]. In this work, the *Craig-Bampton* MOR, *Balanced Truncation* MOR and *Krylov* subspaces method will be applied and investigated. The latter is based on moment-matching points, also called shifts [Panzer14] or expansion points, at definable frequencies. Furthermore, the order of moment-matching at each expansion point can be chosen. This order specifies the number of moments, which have to be matched at one point. For instance, if an expansion point of first order is chosen, not only the value of the transfer function will be matched, but also the slope of the transfer function at that point. Roughly speaking, the system responses for predefined interfaces are approximated at these frequency shifts combining transfer functions of second-order systems (PT2), which are determined using projection techniques based on *Krylov* subspaces [Lehner07]. The method of *Balanced Truncation* keeps the most relevant system states according to the Gramian matrices of controllability and observability. Both are affected by choice of the inputs and outputs and

Table 2.1: Overview of MOR methods commonly used for CMS of substructures, according to [Craig00], [VoormeerenValkRixen11], [Dietz99] and [Fehr11].

Method	Reduction basis	Comment
Hou and Goldmann, Modal Truncation	<ul style="list-style-type: none"> • free interface normal modes 	modes from EVP can be experimentally validated, poor accuracy
Guyan's Static Condensation	<ul style="list-style-type: none"> • fixed interface normal modes 	internal modes from EVP, medium accuracy
Craig-Bampton, Hurty, Bamford	<ul style="list-style-type: none"> • fixed interface normal modes • static interface constraint modes 	constraint modes result from unit displacements at the interfaces, accurate for low frequencies
Rubin and MacNeal, Bamford	<ul style="list-style-type: none"> • free interface normal modes • attachment modes 	attachment modes result from unit forces at the interfaces, force is transferred to displacement to enable assembly, reduced matrices are not block diagonal and less sparse, accurate for low frequencies
Martinez, Variant of Rubin, Dual Craig-Bampton	<ul style="list-style-type: none"> • rigid body modes • free interface normal modes • residual flexibility attachment modes 	if the interface is altered only the residual flexibility modes has to be recomputed, satisfies the interface equilibrium exactly, accurate for low frequencies
Inertia Relief Approach	<ul style="list-style-type: none"> • free interface normal modes • inertia-relief attachment modes 	applies self-equilibrated forces at all interface coordinates, accurate for low frequencies
Hintz, Mixed-Boundary Craig-Bampton	<ul style="list-style-type: none"> • set of free or fixed interface normal modes • set of constraint or attachment modes 	reduction basis dependent on the properties of neighboring component, accurate for components with different stiffness and at low frequencies
Krylov, Arnoldi, Lanczos, Laguerre, IRKA	<ul style="list-style-type: none"> • frequency response modes 	interpolation method based on subspaces, approximates the frequency response of the full system at specified frequencies, accurate for a wide frequency range
Balanced Truncation, Gramian, Hankel, POD, Frequency Weighted Gramian	<ul style="list-style-type: none"> • calculated by means of the controllability and observability Gramian matrices and their Hankel singular values 	keep the states that contribute considerably to the system's input-output behavior, extendable to a frequency weighted approach, reductions of very huge to relatively small model orders are possible, accurate

Example 1: Superposition according to *Guyan's Static Condensation*

Within this example, the dynamical behavior of a planar plate, which is pulled and clinched, is approximated by the use of *Guyan's Static Condensation*. Thereby it is assumed, that the deformation at any point of the body can be represented with the superposition of the two fixed interface normal modes \mathbf{v}_1 and \mathbf{v}_2 . The magnitudes of the mode fractions are described by the reduced coordinates $\bar{\mathbf{q}}_e(t)$, which are like time-dependended amplitudes of the modes. This imagination is sketched in the following.



can also be weighted for a specific frequency range. Thereby, the corresponding Hankel singular values are considered, which are related to specific energies. The well-known *Craig-Bampton* method [Craig00] combines fixed-interface normal modes with the input and output related static interface constraint modes.

With the application of a MOR method, the original system is projected to a decreased system of equations. In order to compare both systems by means of their eigenfrequencies and eigenvectors, the further modal analysis and modal transformation of the reduced order model can be performed. These eigenfrequencies and their related eigenvectors are sometimes also called pseudo-eigenfrequencies [Fransen12] and pseudo-eigenvectors [DickensStroeve00] since they usually have no physical meaning.

In order to assess the different MOR methods in the frequency domain, the Frobenius norm of the matrix of the system transfer functions can be calculated. With respect to the full and the reduced model, the transfer matrix is denoted by $\mathbf{H}_{\text{mech}}(s)$ and $\bar{\mathbf{H}}_{\text{mech}}(s)$, where s represents the complex frequency variable. In particular, the relative error defined as

$$\varepsilon_{\text{mor}}(s) = \frac{\|\mathbf{H}_{\text{mech}}(s) - \bar{\mathbf{H}}_{\text{mech}}(s)\|_F}{\|\mathbf{H}_{\text{mech}}(s)\|_F} \quad (2.10)$$

can be evaluated [Fehr11] for a more detailed comparison of the methods.

2.4 Elastic Multibody Systems

The reduced elastic body can be connected with other elements in a global EMBS using the floating frame of reference approach. Thereby, the motion of an arbitrary point of a body is separated into a rigid body motion $\mathbf{q}_r(t)$ of the reference frame and a superposed linear elastic deformation $\bar{\mathbf{q}}_e(t)$ with respect to the body reference frame. For a single elastic body in an EMBS, the equations of motion [SchwertassekWallrapp99] read

$$\left[\begin{array}{cc|c} m\mathbf{I} & m\tilde{\mathbf{c}}^\top(\bar{\mathbf{q}}_e) & \mathbf{C}_t^\top \\ m\tilde{\mathbf{c}}(\bar{\mathbf{q}}_e) & \mathbf{I}_e(\bar{\mathbf{q}}_e) & \mathbf{C}_r^\top(\bar{\mathbf{q}}_e) \\ \hline \mathbf{C}_t & \mathbf{C}_r(\bar{\mathbf{q}}_e) & \bar{\mathbf{M}}_e \end{array} \right] \cdot \left[\begin{array}{c} \mathbf{a}_r \\ \boldsymbol{\alpha}_r \\ \ddot{\bar{\mathbf{q}}}_e \end{array} \right] + \left[\begin{array}{c} \mathbf{0} \\ \mathbf{0} \\ \bar{\mathbf{D}}_e \cdot \dot{\bar{\mathbf{q}}}_e + \bar{\mathbf{K}}_e \cdot \bar{\mathbf{q}}_e \end{array} \right] + \mathbf{h}^\omega = \mathbf{f}^a + \mathbf{f}^r, \quad (2.11)$$

whereby the introduced reduced equations of motion (2.8) describing the deformation of the elastic body are embedded. The translational and rotational rigid body acceleration $\ddot{\mathbf{q}}_r = [\mathbf{a}_r \quad \boldsymbol{\alpha}_r]^\top$ are multiplied with the mass and inertia terms including the total body mass m , the current center of mass position $\tilde{\mathbf{c}}$ and the inertia tensor \mathbf{I}_e . Furthermore, the translational and rotational coupling matrices are denoted by \mathbf{C}_t and \mathbf{C}_r . In particular, the vector of the generalized centrifugal and Coriolis forces \mathbf{h}^ω vanishes for systems with only translational motions. Finally, the vectors of applied and reaction forces and torques are denoted by \mathbf{f}^a and \mathbf{f}^r .

After performing a numerical integration of the EMBS in the time domain, the mechanical results should be prepared in a post-processing step for the intended optical simulation. The deformed optical surfaces are described by FE nodes, which have to be extracted. Figures 2.1(a) and (b) clarify the relationships for a single mirror, modeled in an EMBS using a Buckens floating frame of reference K_{cog} . Thereby, the mechanical result is given by means of the rigid body motion $\mathbf{q}_r(t)$, the initial node positions $\mathbf{p}_{k,\text{node}}$ and the deformation $\mathbf{V} \cdot \bar{\mathbf{q}}_e(t)$. For the optical model, a surface reference frame S_i can be introduced at the position $\mathbf{p}_{\text{mech2opt}}$, as further explained in Section 4.2.1 and 4.2.2.

It should also be noted, that the best practice is, to use the unit 'millimeter' for the entire optical model, which is suitable to the most optic programs. Besides, the modes can be normalized to ensure a meaningful optical assessment. As usual, the modes used for the MOR are normalized with respect to the masses, which leads to different orders of magnitude and can influence a later optical sensitivity analysis negatively. Therefore, it is proposed, to normalize every mode \mathbf{v}_i by means of its root mean square (RMS) of the absolute nodal displacements. Obviously, in 3D each node has the three translational mode components $v_{k,x}$, $v_{k,y}$ and $v_{k,z}$, which yields $\mathbf{v} \in \mathbb{R}^{n_k \times 3}$. The number of nodes is denoted by n_k . In consequence, the absolute displacement at a k^{th} node can be read $v_{k,\text{sum}} = \sqrt{v_{k,x}^2 + v_{k,y}^2 + v_{k,z}^2}$. For the consideration of a single mode, all nodal displacements can be collected in a vector named \mathbf{v}_{sum} . As a result, the calculation of a normalized mode

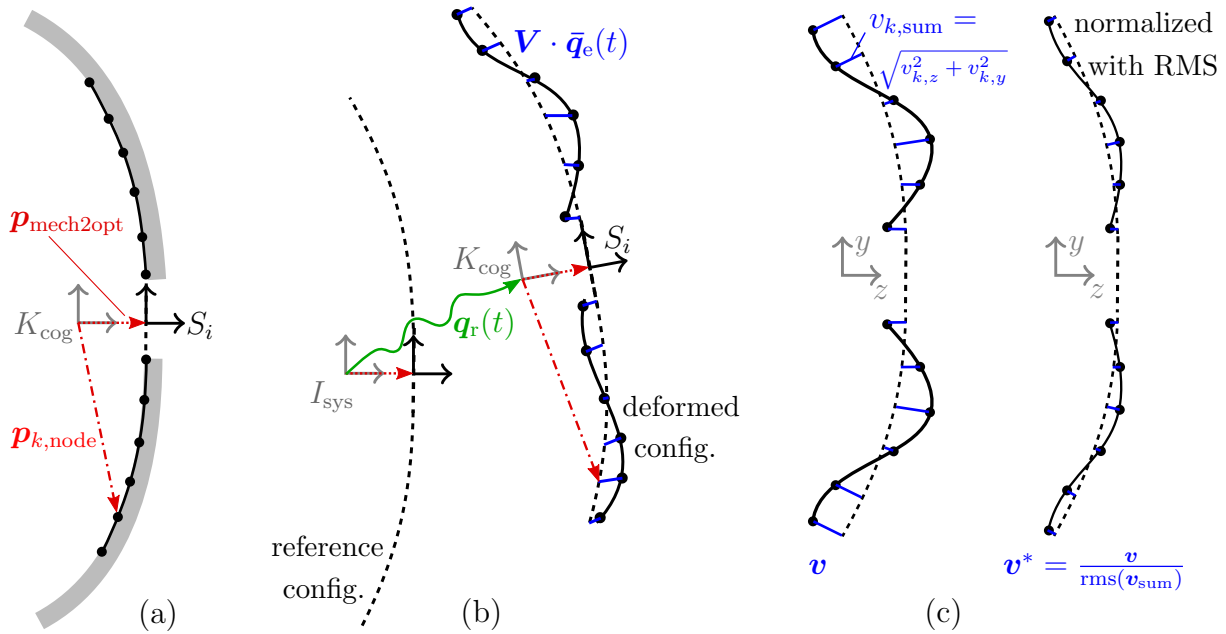


Figure 2.1: Description of an optical surface defined by FE nodes in (a), kinematic relationship for the usage of a Buckens system in (b) and normalization of a mode shape with its RMS in (c).

leads to

$$\mathbf{v}^* = \frac{\mathbf{v}}{\text{rms}(\mathbf{v}_{sum})} = \frac{\mathbf{v}}{\sqrt{\frac{1}{n_k} \sum_{k=1}^{n_k} v_{k,sum}^2}} = \frac{\mathbf{v} \sqrt{n_k}}{\sqrt{\sum_{k=1}^{n_k} v_{k,x}^2 + v_{k,y}^2 + v_{k,z}^2}} = \frac{\mathbf{v} \sqrt{n_k}}{\|\mathbf{v}\|_F}, \quad (2.12)$$

whereby in the last formulation the Frobenius norm can be conveniently used. According to Figure 2.1(c), this is sketched for a mode shape in 2D.

In the case of small motions, the Equations (2.11) are linear and result in the structure of Equation (2.4). Hence, linear control theory can be applied, e.g., in order to derive a model-based feedback control or a state observer.

2.5 Control Theory

The introduced linear equations of motion (2.4) can also be rearranged and transformed to a linear state-space representation

$$\underbrace{\begin{bmatrix} \dot{\mathbf{q}} \\ \ddot{\mathbf{q}} \end{bmatrix}}_{\dot{\mathbf{x}}} = \underbrace{\begin{bmatrix} \mathbf{0} & \mathbf{I} \\ -\mathbf{M}^{-1} \cdot \mathbf{Q} & -\mathbf{M}^{-1} \cdot \mathbf{P} \end{bmatrix}}_{\mathbf{A}} \cdot \underbrace{\begin{bmatrix} \mathbf{q} \\ \dot{\mathbf{q}} \end{bmatrix}}_{\mathbf{x}} + \underbrace{\begin{bmatrix} \mathbf{0} \\ \mathbf{M}^{-1} \cdot \mathbf{B} \end{bmatrix}}_{\mathbf{B}} \cdot \mathbf{u}, \quad (2.13)$$

where the states are represented by the vector $\mathbf{x} \in \mathbb{R}^n$. According to [Lunze08], the linear state-space representation of a system with multiple inputs and multiple outputs (MIMO)

generally results in

$$\begin{aligned}\dot{\mathbf{x}}(t) &= \mathbf{A} \cdot \mathbf{x}(t) + \mathbf{B} \cdot \mathbf{u}(t), \\ \mathbf{y}(t) &= \mathbf{C} \cdot \mathbf{x}(t) + \mathbf{D} \cdot \mathbf{u}(t),\end{aligned}\tag{2.14}$$

where \mathbf{A} is called the system matrix, \mathbf{B} is named input matrix, \mathbf{C} is denoted as the output matrix, and \mathbf{D} is the feedthrough matrix. The vector of measurable output states of the linear system is named \mathbf{y} . In order to consider the system in the frequency domain, the matrix of transfer functions can be calculated from the state-space model by

$$\mathbf{H}(s) = \mathbf{C}^\top \cdot (s\mathbf{I} - \mathbf{A})^{-1} \cdot \mathbf{B} + \mathbf{D}.\tag{2.15}$$

In many application like AO systems or for the active damping of mechanical vibrations, the dynamical system models are used to control or observe system states. Figure 2.2 indicates and summarizes the similarities of the design of state feedback controllers and state observers, based on the pole placement method or the optimal solution, see also [Lunze10] and [GrewalAndrews11]. For the observation of states, a static Kalman filter according to [Kalman60] is commonly used in practice. It is also called Kalman-Bucy filter (KF) or linear-quadratic estimator (LQE) and is explained in more detail in the following.

The KF is an observer, which optimally estimates unknown states by means of noisy measurements and an approximated dynamical system model. On the one hand, the errors of the measurements are described as the observation noise $\mathbf{v}(t)$, and on the other hand, the approximation errors of the model are represented by the process noise $\mathbf{w}(t)$. For the derivation of the method, it is assumed, that white Gaussian noise can represent both types. Hence, for the covariance and expectation value of the stochastic noises, they can be considered at two arbitrary time instants t_1 and t_2 . According to [Föllinger92] it yields

$$\text{cov}\{\mathbf{w}(t_1), \mathbf{w}(t_2)\} = E\{\mathbf{w}(t_1) \cdot \mathbf{w}^\top(t_2)\} = \mathbf{Q} \delta(t_1 - t_2),\tag{2.16}$$

$$\text{cov}\{\mathbf{v}(t_1), \mathbf{v}(t_2)\} = E\{\mathbf{v}(t_1) \cdot \mathbf{v}^\top(t_2)\} = \mathbf{R} \delta(t_1 - t_2)\tag{2.17}$$

with the Dirac δ -function. The matrices \mathbf{Q} and \mathbf{R} represent the constant power spectral density matrices of the process noise $\mathbf{w}(t)$ and the observation noise $\mathbf{v}(t)$, i.e., they characterize the inaccuracies of the model states and the measurements. Since the inaccuracies are commonly not known, they are chosen and adjusted as weighted matrices for the regarded application [Föllinger92]. The linear state-space model according to the equations (2.14) can be extended with process and measurement disturbances and results in

$$\begin{aligned}\dot{\mathbf{x}}(t) &= \mathbf{A} \cdot \mathbf{x}(t) + \mathbf{B} \cdot \mathbf{u}(t) + \mathbf{G} \cdot \mathbf{w}(t), \\ \mathbf{y}(t) &= \mathbf{C} \cdot \mathbf{x}(t) + \mathbf{v}(t)\end{aligned}\tag{2.18}$$

with the noise input matrix \mathbf{G} , see also [LewisXiePopa08]. In order to solve the estimation problem optimally, an estimator whose output $\hat{\mathbf{x}}(t)$ converges to the actual state $\mathbf{x}(t)$ has

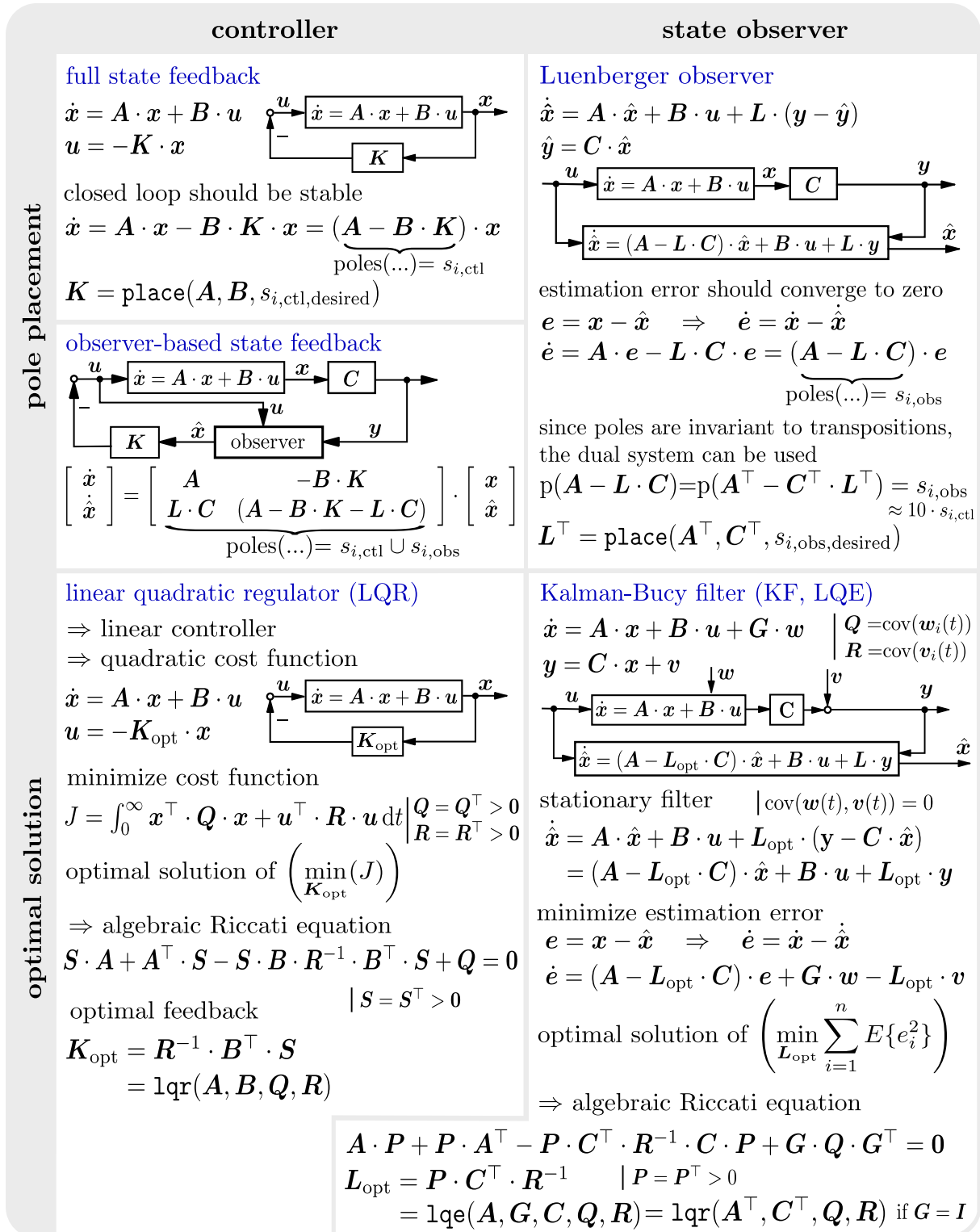


Figure 2.2: Overview of the design of state feedback controllers and state observers, based on the pole placement method or the optimal solution. The similarities are obvious since the `place` and `lqr` algorithms can be used for both, the controller and the observer design.

to be designed. Therefore, the observer dynamics is formulated as

$$\dot{\hat{\mathbf{x}}}(t) = \mathbf{A} \cdot \hat{\mathbf{x}}(t) + \mathbf{B} \cdot \mathbf{u}(t) + \mathbf{L}_{\text{opt}} \cdot (\mathbf{y}(t) - \hat{\mathbf{y}}(t)) \quad (2.19)$$

with the constant observer gain matrix \mathbf{L}_{opt} . This matrix affects the error-correcting portion and has to be calculated. The estimated output can be substituted with $\hat{\mathbf{y}} = \mathbf{C} \cdot \hat{\mathbf{x}}$ and the estimation errors result with $\mathbf{e} = \mathbf{x} - \hat{\mathbf{x}}$. Furthermore, the dynamics of the error can be formulated by means of the Equations (2.18) and (2.19) with

$$\dot{\mathbf{e}} = \dot{\mathbf{x}} - \dot{\hat{\mathbf{x}}} = (\mathbf{A} - \mathbf{L}_{\text{opt}} \cdot \mathbf{C}) \cdot \mathbf{e} + \mathbf{G} \cdot \mathbf{w} - \mathbf{L}_{\text{opt}} \cdot \mathbf{v}. \quad (2.20)$$

Since the estimation errors should converge as fast as possible, the optimal solution can be determined by minimizing the expectation values

$$\min_{\mathbf{L}_{\text{opt}}} \sum_{i=1}^n E\{e_i^2\} \quad (2.21)$$

as described in [Lunze10]. As a result, it yields

$$\mathbf{L}_{\text{opt}} = \mathbf{P} \cdot \mathbf{C}^{\top} \cdot \mathbf{R}^{-1}, \quad (2.22)$$

whereby the symmetrical matrix \mathbf{P} is the positive-semidefinite solution matrix of the Riccati equation

$$\mathbf{A} \cdot \mathbf{P} + \mathbf{P} \cdot \mathbf{A}^{\top} - \mathbf{P} \cdot \mathbf{C}^{\top} \cdot \mathbf{R}^{-1} \cdot \mathbf{C} \cdot \mathbf{P} + \mathbf{G} \cdot \mathbf{Q} \cdot \mathbf{G}^{\top} = \mathbf{0}. \quad (2.23)$$

The filter yields the exact conditional probability estimate in the special case that the errors are normally distributed and zero-mean. Mostly, these conditions cannot be evidenced, but the assumption of Gaussian noise and the resultant KF usually leads to a reasonable performance [Föllinger92].

According to Figure 2.2, the calculation of a linear-quadratic regulator (LQR) is quite similar. It also leads to a minimizing problem with respect to the chosen matrices \mathbf{Q} and \mathbf{R} , which weight the states \mathbf{x} in relation to the inputs \mathbf{u} . Again, this could be solved through the Riccati equation, but this time, the optimal feedback gain results. Roughly speaking, the LQR approach selects closed-loop poles that provide the optimal balance between the tracking errors and the control effort [Preumont06].

Since the introduced equations and formulations up to now only represent the mechanical system behavior, the fundamentals of the required optics are discussed in the following.

Chapter 3

Optical Fundamentals

In order to describe the optical behavior of a system, the physical principles and interactions have to be considered and understood. This chapter introduces the basics of geometrical optics, the strategy of ray tracing, the theory of imaging by means of optical systems, and the identification of optical aberrations. Furthermore, the wave character of light is taken into account, and various phenomena are discussed. The transition from the Huygens-Fresnel principle of wavelets to the Fourier optics is clarified, whereby related equations are mentioned. The wave-optical consideration is necessary since optical systems should be investigated both, quantitatively with the ray tracing, and qualitatively using image simulations and exposure simulations.

3.1 Geometrical Optics

The most basic approach, which describes the propagation of light, is the consideration in terms of rays [Hamilton28]. In geometrical optics, the ray is an abstraction useful for approximating the light paths within different media. The optical density of a medium is quantified by the refractive index, which is defined as

$$n = \frac{c_0}{c_M} = \sqrt{\varepsilon_r \mu_r}, \quad (3.1)$$

where c_0 is the speed of light in vacuum and c_M is the phase velocity of light in the medium. Furthermore, ε_r is the material's relative permittivity, and μ_r is its relative permeability.

According to the Fermat's principle, light always travels on the fastest way between two points [Gross05]. Therefore, in a homogeneous medium the needed time for a geometrical length s is $t_{\text{opt}} = s/c_M$ and has to be minimal. It is proportional to the optical path length (OPL), which is defined as

$$s_{\text{opl}} = n s. \quad (3.2)$$

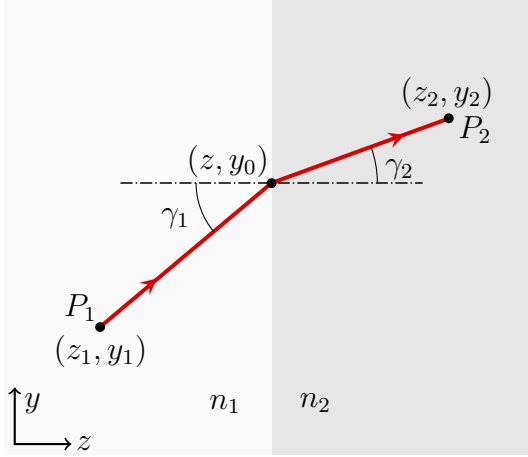


Figure 3.1: The refraction of light, at two different homogenous media.

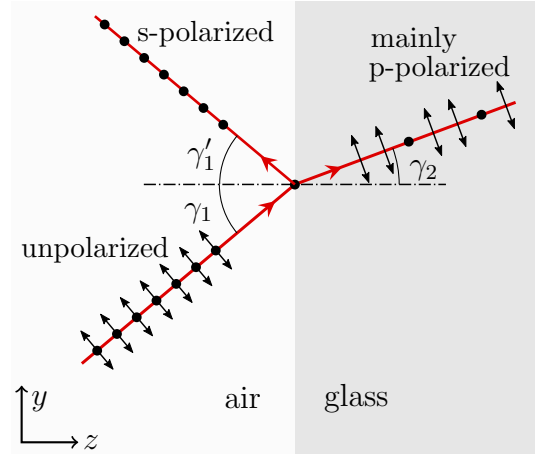


Figure 3.2: The reflection and refraction of unpolarized light, from air to glass.

A light ray traveling in a plane area from point P_1 to point P_2 within two different media is shown in Figure 3.1. For the sum of the OPL, it results

$$s_{\text{opl, sum}} = n_1 \sqrt{(z - z_1)^2 + (y_1 - y_0)^2} + n_2 \sqrt{(z_2 - z)^2 + (y_0 - y_2)^2}. \quad (3.3)$$

The minimum of the OPL can be obtained from

$$\frac{d}{dz} s_{\text{opl, sum}} = n_1 \frac{z - z_1}{\sqrt{(z - z_1)^2 + (y_1 - y_0)^2}} - n_2 \frac{z_2 - z}{\sqrt{(z_2 - z)^2 + (y_0 - y_2)^2}} = 0. \quad (3.4)$$

This directly leads to Snell's law

$$n_1 \sin(\gamma_1) = n_2 \sin(\gamma_2), \quad (3.5)$$

where the angles of incidence and refraction are denoted by γ_1 and γ_2 . The material-dependent indices of refraction are represented with n_1 and n_2 . Excursion 1 explains further phenomena, which occur during the refraction.

Anyway, Fermat's principle can be used again to derive the reflection law, which simply yields

$$\gamma_1 = \gamma'_1. \quad (3.6)$$

An inhomogeneous refraction index within a medium influences the path of a light ray [BornWolf99]. On the one hand, this can be undesired, e.g., if a density change causes it due to gas currents or thermo-mechanical stresses. On the other hand, it can be intentionally used, e.g., like in graded-index fibers, where the index of refraction in the core decreases continuously between the center and the cladding.

Within a graded index medium, the change of refraction results in a bending of the ray, which depends on the gradient-index (GRIN). In Figure 3.3 the GRIN-refraction and path

Excursion 1: Polarization, Fresnel equations, and Brewster's angle

Depending on the magnitude of the refractive indices, the incidence angle and the light's polarization, the rays are not only transmitted into the material, but a fraction of the light will also be reflected. For instance, unpolarized light in the air which meets glass with an incidence angle of 45° reflects about 10% of its energy according to the Fresnel equations [Gross05]. In particular, when this light is incident at the so-called Brewster angle, the light that is reflected from the surface is perfectly s-polarized, as indicated in Figure 3.2. In other words, the electric field only oscillates perpendicular to the plane of incidence. At the same time, the transmitted fraction is mainly p-polarized, i.e., the electric field only oscillates parallel to the plane of incidence. As shown on the right-hand side, unpolarized light oscillates in all directions perpendicular to the traveling axis. In order to produce linear polarized light in the direction of travel, e.g., a quartz or wire-grid polarizer can be used.

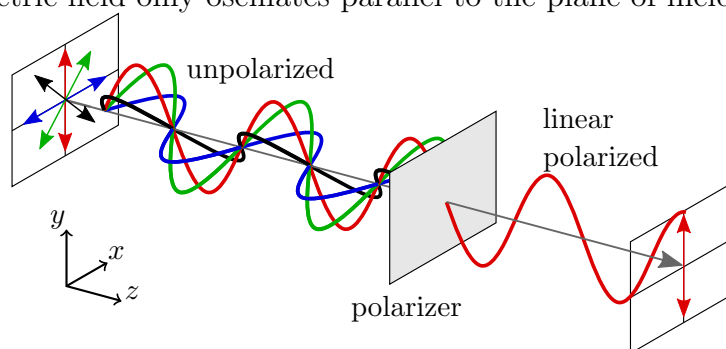
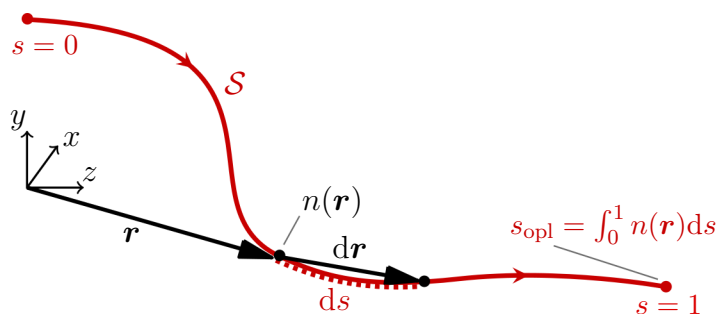


Figure 3.3: Refraction of a ray in a graded index medium.



of a light ray are sketched. Since the refraction index n is changing with respect to the position \mathbf{r} , the OPL according to Equation (3.2) has to be differentially formulated as

$$ds_{\text{opt}} = n(\mathbf{r}) ds. \quad (3.7)$$

After the integration along the path \mathcal{S} , the actual OPL leads to

$$s_{\text{opt}} = \int_{\mathcal{S}} n(\mathbf{r}) ds. \quad (3.8)$$

Moreover, the spatial path of the ray can generally be calculated by solving the *GRIN Ray Equation*

$$\frac{d}{ds} \left(n \frac{d\mathbf{r}}{ds} \right) = \frac{\partial n}{\partial \mathbf{r}}, \quad (3.9)$$

which is derived and discussed in Section A.1. Next, the method of ray tracing is presented, which allows the computation of light paths.

3.2 Ray Tracing Theory

This section gives a short introduction to the basic ray tracing formalisms [Gross05], which allow the computation of a ray path within an usual optical system. It is based on the linear algebra and the geometrical optics according to Section 3.1. Thereby, wave-optical effects are neglected, and it is focused on light rays in the three-dimensional space. Furthermore, it can be distinguished between non-sequential and sequential ray tracing, whereby the latter is considered here and processes a ray step by step, from one surface to another.

3.2.1 Ray Description

Mathematically, a light ray is a straight line described by a position vector $\mathbf{r} = [r_x \ r_y \ r_z]^\top$ of a part on the ray and a normalized direction vector. Using the Cardan angles α_C and β_C for the rotation around the x - and y -axis, a ray direction can be described with the unit vector

$$\mathbf{d} = \begin{bmatrix} \sin(\beta_C) \\ -\sin(\alpha_C) \cos(\beta_C) \\ \cos(\alpha_C) \cos(\beta_C) \end{bmatrix}. \quad (3.10)$$

In optical systems with homogeneous media, the ray changes the direction only at the surfaces. If a single ray is considered, which is emitted by a light source on the object plane, it propagates through the optical system until the image plane. Thereby, the ray is either reflected at mirror surfaces or refracted at lens surfaces. Thus, the quantities of interest are the intersection points and the corresponding ray directions. In sequential ray tracing used herein, the order of the surfaces passed by a ray is predetermined.

For the ray tracing algorithm, a ray intersection point ${}^{i-1}\mathbf{r}_{i-1}$ and a related ray direction ${}^{i-1}\mathbf{d}_{i-1}$ at an optical surface with the index $i - 1$ are considered in the corresponding reference frame S_{i-1} . Furthermore, the relative position ${}^{i-1}\mathbf{s}_i$ and relative orientation \mathbf{R}_i of the next surface reference frame S_i are given. Since it is important to treat each surface i separately with respect to the bounded frame S_i , the ray intersection point and the ray direction must be transformed from S_{i-1} to S_i with

$${}^i\mathbf{r}_{i-1} = \mathbf{R}_i^\top \cdot ({}^{i-1}\mathbf{r}_{i-1} - {}^{i-1}\mathbf{s}_i) \quad \text{and} \quad {}^i\mathbf{d}_{i-1} = \mathbf{R}_i^\top \cdot {}^{i-1}\mathbf{d}_{i-1}. \quad (3.11)$$

In order to simplify the notation, the ahead superscript is dropped and both quantities are always regarded with respect to the surface reference frame S_i .

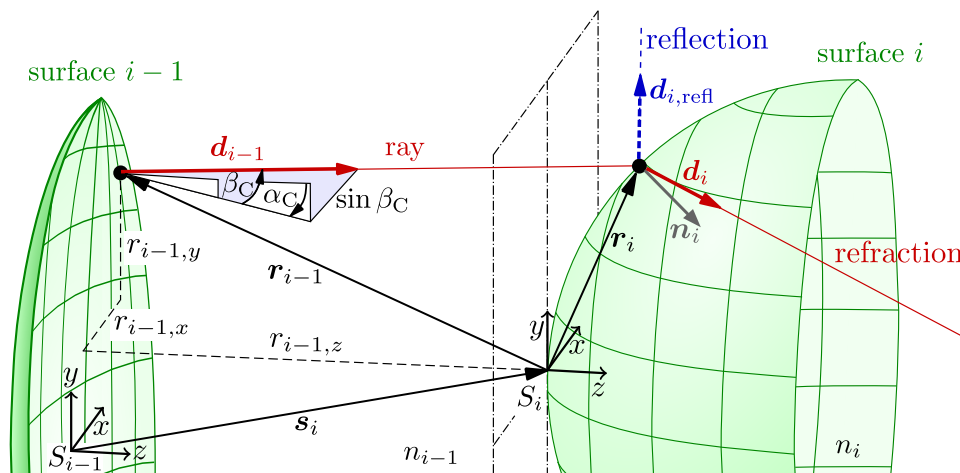


Figure 3.4: Ray description, sign convention and intersection calculation.

Next, the two surfaces and the single ray are shown in Figure 3.4. The ray can be described with

$$\mathbf{r} = \mathbf{r}_{i-1} + a \mathbf{d}_{i-1}, \quad (3.12)$$

whereby a specifies the scalar distance of an arbitrary point on the ray until to the position \mathbf{r}_{i-1} . Besides, the intersection \mathbf{r}_i of the ray and the current surface i can be regarded. If the distance a_i between the two intersection points is given, it follows the relationship

$$\mathbf{r}_i = \mathbf{r}_{i-1} + a_i \mathbf{d}_{i-1}. \quad (3.13)$$

Furthermore, the new ray direction \mathbf{d}_i due to a refraction is also indicated in Figure 3.4. It is based on the previous and current refractive indices n_{i-1} and n_i , as well as the normal unit vector \mathbf{n}_i at the surface intersection. In the case of a reflection, it is denoted with $\mathbf{d}_{i,\text{refl}}$. Before the computation of the intersection is introduced, the common surface types are defined.

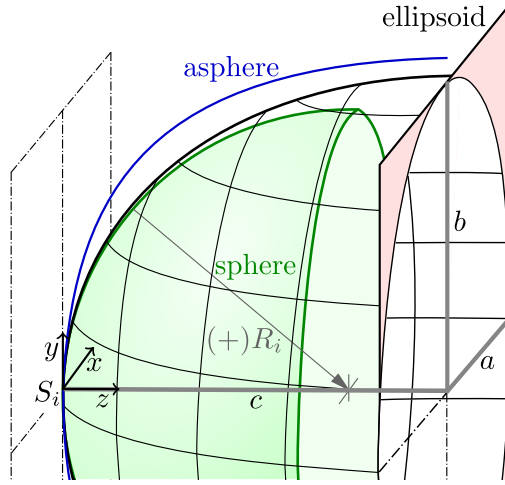
3.2.2 Surface Descriptions

For the ray tracing, the optical surfaces must be described continuously. Hence, this section introduces the surface types commonly used in the field of optics. In Figure 3.5 the different types are illustrated and compared. The radius of curvature R_i is positive if the related center is located on the side of the positive z -direction.

Sphere and Ellipsoid

In many applications, the lenses or mirrors are spherical or elliptical, because their production is quite low-priced and straightforward. Since a sphere is only one particular

Figure 3.5: Visualization of an ellipsoidal surface, a spherical surface and an aspherical surface.



case of an ellipsoid, the latter will only be considered here.

An ellipsoid, whose vertex point in the direction of z is in the origin, can be described by

$$\frac{x^2}{a^2} + \frac{y^2}{b^2} + \frac{(z - c)^2}{c^2} = 1, \quad (3.14)$$

where a , b and c are called the semi-principal axes. For $c = \frac{R_i}{1+\kappa}$ and $a = b = \frac{R_i}{\sqrt{1+\kappa}}$ it yields

$$(1 + \kappa)x^2 + (1 + \kappa)y^2 + ((1 + \kappa)z - R_i)^2 = R_i^2, \quad (3.15)$$

whereby κ describes the conic constant and R_i denotes a radius of curvature, which is virtual in the elliptical case. This can also be interpreted as a zero-isoplane at the potential V , which is also called implicit surface representation

$$V(x, y, z) = -\frac{1}{R_i}x^2 - \frac{1}{R_i}y^2 - \frac{1 + \kappa}{R_i}z^2 + 2z = 0. \quad (3.16)$$

Thereby, the gradient is equal to the direction $\tilde{\mathbf{n}}_i$ of the unit vector, which is orthogonal to the surface. At the position \mathbf{r}_i it yields the direction

$$\tilde{\mathbf{n}}_i = \text{grad}(V(\mathbf{r}_i)) = -\frac{1}{R_i} \begin{bmatrix} r_{i,x} \\ r_{i,y} \\ (1 + \kappa)r_{i,z} \end{bmatrix} + \begin{bmatrix} 0 \\ 0 \\ 1 \end{bmatrix} = \begin{bmatrix} -\frac{r_{i,x}}{R_i - r_{i,z}(1 + \kappa)} \\ -\frac{r_{i,y}}{R_i - r_{i,z}(1 + \kappa)} \\ 1 \end{bmatrix}. \quad (3.17)$$

The normal unit vector results in $\mathbf{n}_i = \frac{\tilde{\mathbf{n}}_i}{|\tilde{\mathbf{n}}_i|}$. The Equation (3.15) can be rewritten in the radial coordinate $\rho = \sqrt{x^2 + y^2}$ and it follows

$$z(\rho) = \frac{1}{1 + \kappa} \left(R_i - \sqrt{R_i^2 - (1 + \kappa)\rho^2} \right) = \frac{\rho^2}{R_i + \sqrt{R_i^2 - (1 + \kappa)\rho^2}}, \quad (3.18)$$

whereby a binominal expansion is used for the last arrangement.

The conic constant κ and the polynomial coefficients C_m for the different surface types can be represented by the parameter collection **asphere**, which is shown in Table 3.1. Besides, Zernike polynomials are also often used for aspherical surface descriptions as explained in Section 4.2.2.

In the following, the quantity $z_{\text{ref}}(x, y)$ is introduced, which generally represents a continuous surface description, regardless of whether the surface type is spherical, elliptical or aspherical.

3.2.3 Intersection of a Ray and a Surface

The main task of the ray tracing is to calculate the intersection of the rays with the surfaces. Therefore, the incoming ray according to Equation (3.12) is described with respect to the current surface reference frame S_i . For many surface descriptions, the intersection can be computed analytically [Gross05]. The exceptional ones have to be obtained numerically with iterative approximation procedures.

Elliptical Surface Intersection

Inserting the ray of Equation (3.13) into the ellipsoid from Equation (3.15), it follows

$$(1 + \kappa)(r_{i-1,x} + a_i d_{i-1,x})^2 + (1 + \kappa)(r_{i-1,y} + a_i d_{i-1,y})^2 + ((1 + \kappa)(r_{i-1,z} + a_i d_{i-1,z}) - R_i)^2 = R_i^2. \quad (3.24)$$

After some rearrangements, it results

$$\begin{aligned} & a_i^2(1 + \kappa)(d_{i-1,x}^2 + d_{i-1,y}^2 + (1 + \kappa)d_{i-1,z}^2) + \\ & 2a_i(1 + \kappa)(r_{i-1,x}d_{i-1,x} + r_{i-1,y}d_{i-1,y} + (1 + \kappa)r_{i-1,z}d_{i-1,z} - R_id_{i-1,z}) + \\ & (1 + \kappa)(r_{i-1,x}^2 + r_{i-1,y}^2 + (1 + \kappa)r_{i-1,z}^2 - 2(1 + \kappa)r_{i-1,z}R_i) = 0, \end{aligned} \quad (3.25)$$

and the condition $|\mathbf{d}_{i-1}|^2 = 1$ can be further is used. Multiplying the equation with $-\frac{1}{R_i(1+\kappa)}$ leads to

$$Ha_i^2 + 2Fa_i - G = 0 \quad (3.26)$$

with the intermediate parameters

$$\begin{aligned} H &= -\frac{1}{R_i}(1 + \kappa d_{i-1,z}^2), \quad F = d_{i-1,z} - \frac{\mathbf{r}_{i-1} \cdot \mathbf{d}_{i-1} + \kappa r_{i-1,z} d_{i-1,z}}{R_i}, \text{ and} \\ G &= \frac{|\mathbf{r}_{i-1}| + \kappa r_{i-1,z}^2}{R_i} - 2r_{i-1,z}. \end{aligned} \quad (3.27)$$

The solution of the quadratic equation is known as

$$a_i = \sqrt{\frac{F^2}{H} - \frac{G}{H} - \frac{F}{H}} = \frac{G}{F + \sqrt{F^2 + HG}}, \quad (3.28)$$

whereby the binomial theorem is used for the last rearrangement.

Aspherical Surface Intersection

The intersection of a ray according to Equation (3.13) and an aspherical surface $z_{AS}(x, y)$ cannot be solved analytically, but first can be formulated as the implicit problem $z_{AS}(x, y) - r_{i,z}(a_i) \stackrel{!}{=} 0$. Then, an iterative root-finding algorithm, e.g., the fixed-point iteration or the Newton-Raphson method [BurdenFaires04] can be applied. Thereby, the result can be approximately determined with a predefined error Δ . The fixed-point iteration is a fast and straightforward method, but it does not converge robustly for all cases. For instance, if the slope of a ray with respect to the optical axis is > 1 and the surface is only described by aspherical parameters, i.e. $R_i = 0$, than it is divergent. This circumstance often occurs for free-form mirror systems.

Anyhow, a scheme according to [Gross05] which is based on the Newton-Raphson-method has proven to be a very stable algorithm. It is briefly introduced in Algorithm 1 and the relationships are schematically illustrated in Figure 3.6. In particular, the spherical part is used for the first approximation, and the gradient is evaluated at several positions to obtain the normal vector and the related tangential plane.

Algorithm 1 Newton-Raphson-method for the ray tracing with an aspherical surface.

1. Neglect the aspherical terms and calculate the intersection with the spherical or elliptical part of the surface $\mathbf{r}_s = [x_s \quad y_s \quad z_s]^\top$.
2. Obtain the intersection of the ray at the x-y-plane

$$\mathbf{r}_0 = [x_0 \quad y_0 \quad z_0]^\top = \left[x_s - \frac{d_{i-1,x}}{d_{i-1,z}} z_s \quad y_s - \frac{d_{i-1,y}}{d_{i-1,z}} z_s \quad 0 \right]^\top.$$
3. Evaluate the aspherical function value $z_{AS1} := z_{AS}(x_s, y_s)$ and the normal direction $\mathbf{n}_1 := \mathbf{n}(x_s, y_s, z_{AS1})$ at the position $\bar{\mathbf{r}}_1 = [x_s \quad y_s \quad z_{AS1}]^\top$ in order to get the tangential plane $\mathbf{n}_1 \cdot (\mathbf{x} - \bar{\mathbf{r}}_1) = 0$.

repeat

4. Calculate the intersection of the tangential plane and the ray

$$\mathbf{n}_1 \cdot (\mathbf{r}_{i-1} + a_i \mathbf{d}_{i-1} - \bar{\mathbf{r}}_1) = 0 \Rightarrow a_i = \frac{\mathbf{n}_1 \cdot (\bar{\mathbf{r}}_1 - \mathbf{r}_{i-1})}{\mathbf{n}_1 \cdot \mathbf{d}_{i-1}}.$$

Thus, the new approximation of the intersection $\mathbf{r}' = [x' \quad y' \quad z']^\top$ results in

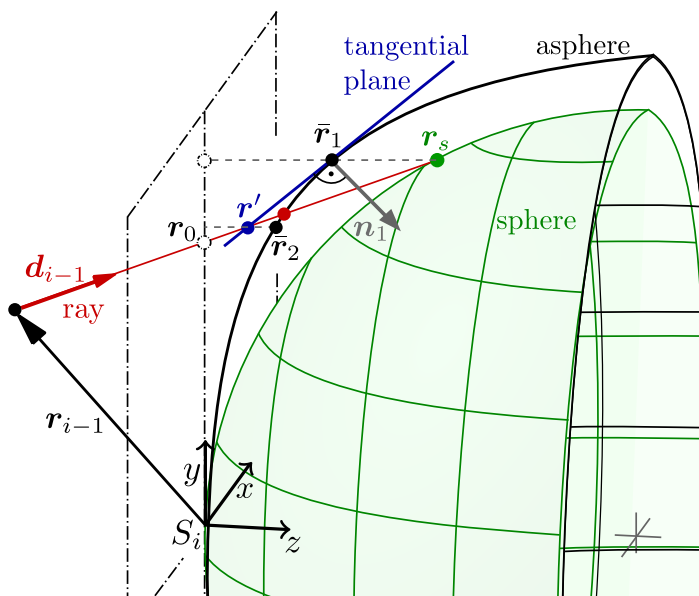
$$z' = a_i d_{i-1,z}, \quad y' = y_0 + \frac{d_{i-1,y}}{d_{i-1,z}} z' \quad \text{and} \quad x' = x_0 + \frac{d_{i-1,x}}{d_{i-1,z}} z'.$$

5. Evaluate the aspherical function value at the new position $z_{AS2} := z_{AS}(x', y')$ and the related normal direction $\mathbf{n}_2 := \mathbf{n}(x', y', z_{AS2})$ at position $\bar{\mathbf{r}}_2 = [x' \quad y' \quad z_{AS2}]^\top$.

until $|z_{AS2} - z_{AS1}| < \Delta$

Now, the ray-surface intersection is known, as well as the related normal unit vector and

Figure 3.6: Iterative calculation of ray and asphere intersection points according to Newton-Raphson's method.



the direction of the incident ray. The final task is to apply either the refraction law or the reflection law depending on the case of interest.

3.2.4 Refraction and Reflection in 3D

For the three-dimensional ray tracing, it is necessary to extend the planar refraction and reflection according to Section 3.1. The generalized relations are sketched in the Figures 3.7 and 3.8. Since the ray directions are unit vectors, they can also be described by means of the vectors \mathbf{n}_i and \mathbf{m}_i , whereby the latter is a vector orthogonal to \mathbf{n} and in the plane of the incident ray. With the angle of incidence γ_{i-1} and the angle of refraction γ_i the relationships result in

$$\mathbf{d}_{i-1} = \mathbf{m} \sin(\gamma_{i-1}) + \mathbf{n} \cos(\gamma_{i-1}) \quad \text{and} \quad \mathbf{d}_i = \mathbf{m} \sin(\gamma_i) + \mathbf{n} \cos(\gamma_i). \quad (3.29)$$

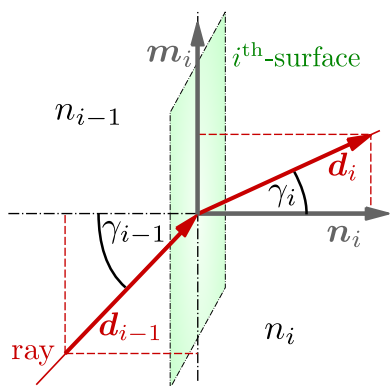


Figure 3.7: Refraction of a ray at a surface in the three-dimensional space.

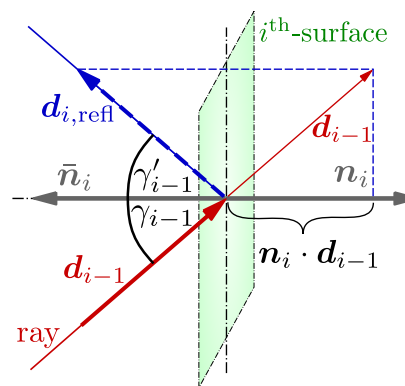


Figure 3.8: Reflection of a ray at a surface in the three-dimensional space.

The vector \mathbf{m} can be eliminated combining the two equations. With the Snell's law according to Equation (3.5), this leads to

$$\mathbf{d}_i = \frac{n_{i-1}}{n_i}(\mathbf{d}_{i-1} - \mathbf{n}_i \cos(\gamma_{i-1})) + \mathbf{n}_i \cos(\gamma_i). \quad (3.30)$$

Since the dot product is defined as $\mathbf{d}_{i-1} \cdot \mathbf{n}_i = |\mathbf{d}_{i-1}| |\mathbf{n}_i| \cos(\gamma_{i-1})$ and the regarded vectors have the absolute value of one, it can be read as $\cos(\gamma_{i-1}) = \mathbf{d}_{i-1} \cdot \mathbf{n}_i$. In order to obtain the term $\cos(\gamma_i)$ in dependence of the given quantities, the generalized unit circle formula $\sin^2(\alpha) + \cos^2(\alpha) = 1$ can be used. In combination with Equation (3.5) it yields

$$\cos(\gamma_i) = \sqrt{1 - \sin^2(\gamma_i)} = \sqrt{1 - \frac{n_{i-1}}{n_i} \sin^2(\gamma_{i-1})} = \sqrt{1 - \frac{n_{i-1}}{n_i} (1 - \cos^2(\gamma_{i-1}))}. \quad (3.31)$$

Finally, the terms can be insert in Equation (3.30), which results in

$$\begin{aligned} \mathbf{d}_i &= \frac{n_{i-1}}{n_i}(\mathbf{d}_{i-1} - (\mathbf{n}_i \cdot \mathbf{d}_{i-1})\mathbf{n}_i) + \mathbf{n}_i \sqrt{1 - \frac{n_{i-1}}{n_i} (1 - (\mathbf{d}_{i-1} \cdot \mathbf{n}_i)^2)} \\ &= \frac{1}{n_i}(n_{i-1} \mathbf{d}_{i-1} + J \mathbf{n}_i) \end{aligned} \quad (3.32)$$

with the intermediate parameters $J = \sqrt{n_{i-1}^2 - n_i^2 + I^2} - I$ and $I = n_i \mathbf{n}_i \cdot \mathbf{d}_{i-1}$. The reflection law can also be formulated vectorially. As illustrated in Figure 3.8, a reflected ray has the direction

$$\mathbf{d}_{i,\text{refl}} = \mathbf{d}_{i-1} - 2(\mathbf{n}_i \cdot \mathbf{d}_{i-1}) \mathbf{n}_i, \quad (3.33)$$

whereby \mathbf{d}_{i-1} is again the ray direction before the refraction and \mathbf{n}_i is the unit vector, which is orthogonal to the considered surface.

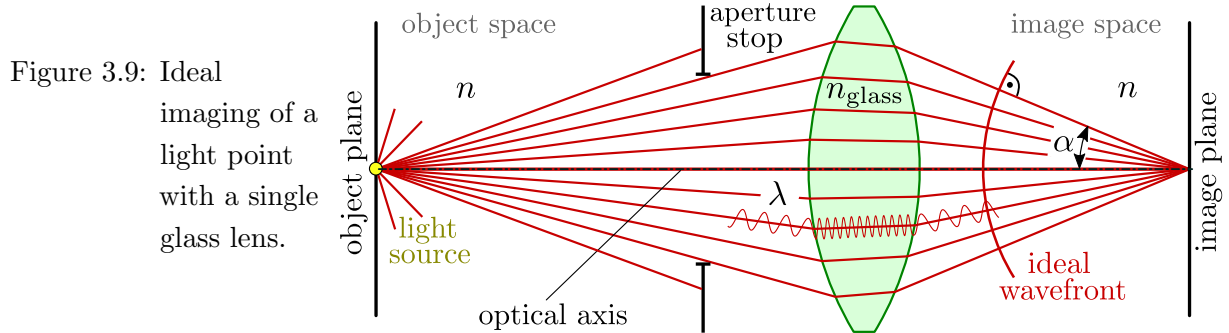
Next, the introduced ray tracing can be used for the analysis of the optical system properties, which is discussed in the following.

3.3 Properties of Optical Systems

In order to classify an optical system, the overall properties and purpose of the optical elements have to be considered and discussed. A basic optical system consist of an object plane, an aperture stop (AS), an image plane and optical elements, e.g., lenses or mirrors. Figure 3.9 shows ideal imaging, whereby a centered lens maps a light point located on the optical axis onto one point of the image plane. The OPL is also indicated by means of the sine-shaped curve. The light source emits rays in all directions within the object space, and the AS limits them to a determined range, which corresponds to the light intensity of the image. Thus, the so-called aperture angle α represents an important property of an optical system. In combination with the refraction index n within the image space, the numerical aperture is defined as

$$\text{NA} = n \sin \alpha. \quad (3.34)$$

Since a point light source produces spherical waves, their wavefronts are perpendicular to the rays. If the wavefronts are still spherical after passing an optical system and their sphere centers are located on the image plane, the imaging is ideal.



However, for the further understanding of the optical design, the image formation, the optical pupils, the optical aberrations, the polynomials for the related decomposition and the concepts of resolution are explained.

3.3.1 Paraxial Image Formation

In geometrical optics, the paraxial approximation is a small-angle approximation. It is valid for the rays, which lie close to the optical axis [Gross05]. For instance, it can be used for the estimation of the image formation at a thin lens using the related focal length f and the distance d of the *finite object-space*, as shown in Figure 3.10. Since thereby the quantities are represented with respect to the converging lens indicated by an arrow, it yields $f' = -f$. The focal length represents the intersection of a refracted ray with the optical axis, after this ray reached the lens axially parallel. Hence, the image distance d' can be calculated by the imaging equation

$$\frac{1}{d'} = \frac{1}{f'} + \frac{1}{d}. \quad (3.35)$$

The magnification of the imaging system is defined as the ratio of the image height y' and the object height y . It can be formulated according to the intercept theorem with

$$M = \frac{y'}{y} = \frac{d'}{d}. \quad (3.36)$$

For the analysis of the image formation, it is common to consider specific ray bundles, corresponding to the field points. They represent the emitted light of the object points and they have corresponding rays, that cross the optical axis at the system AS. Such a center ray is named chief ray (CR). If the AS is located at the focal length of the image space, the type of imaging is called *telecentric object-space* and the arriving CRs are parallel to

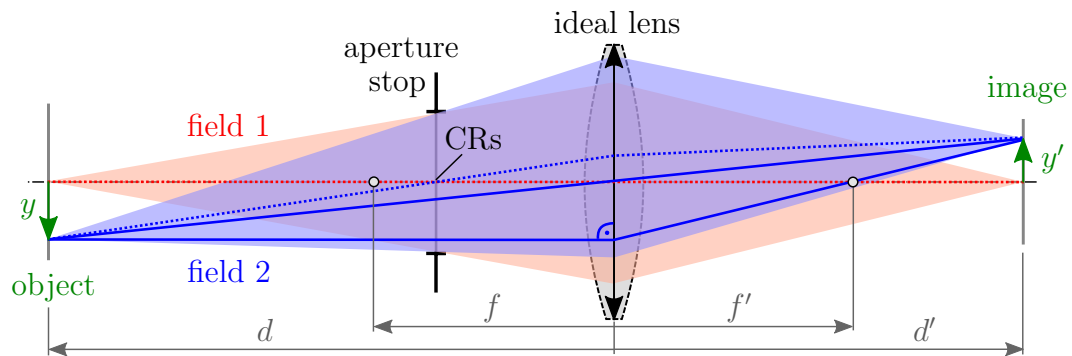


Figure 3.10: Explanation of the finite object-space imaging with a single lens.

the optical axis, as illustrated in Figure 3.11. In particular, optical systems with both, a telecentric object- and image-space, are used for machine vision and for the lithography, since they allow the lens to be focused to different distances without changing the size of the image.

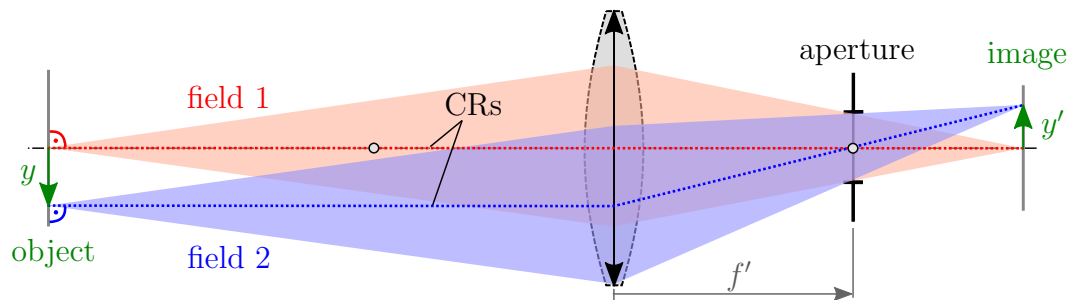


Figure 3.11: Explanation of the telecentric object-space imaging.

The third type is known as *infinity object-space* and is depicted in Figure 3.12. Thereby it is assumed, that the object is very far away, i.e. $d \gg d'$, and all rays of one field have the same inclination angle. For instance, this approach is used for the design of telescopes or binoculars. The next section introduces the concept of optical pupils, which is elementary for the design and analysis of optical systems.

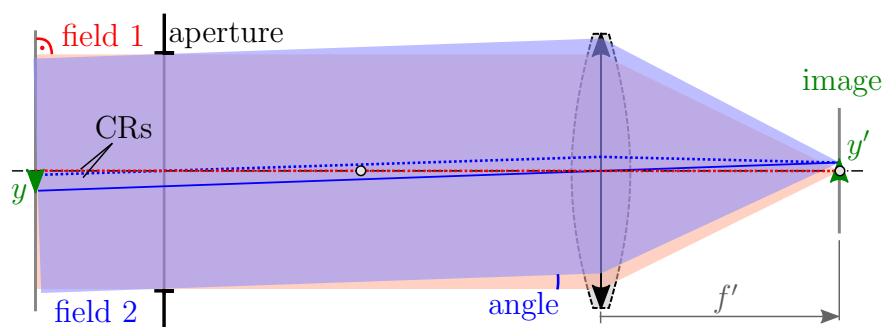


Figure 3.12: Explanation of the infinity object-space imaging.

3.3.2 Entrance and Exit Pupils

Obviously, the position and diameter of the aperture significantly influences the image formation. In order to characterize this influence, the so-called entrance pupil (EnP) and exit pupil (ExP) can be regarded, as explained in [Mahajan13]. If one considers the AS as an object, which is projected through the optics of the image-space, the resulting image determines the ExP diameter and position. The latter is specified with respect to the image plane and is positive in the z -direction.

In analogy, the image of the AS, which is projected through the optics of the object-space, defines the EnP. It is specified with respect to the object plane and is also positive in the z -direction. Figure 3.13 illustrates the graphical construction of this pupils at an ideal optical system with a finite object-space. Thereby, two different fields are regarded, which are bounded by the marginal rays. Hence, the EnP can be used during the building of the ray bundles for the ray tracing. The position of the ExP is also a quite significant quantity since there the optical wave aberrations are usually analyzed.

If the AS is located at a different position, the EnP and the ExP are changed. Figure 3.14 shows an optical imaging system consisting of two ideal lenses, whereby various cases of AS positions are demonstrated. The EnP is identical to the AS if the latter is located in front of the first optical element, as depicted for the upper two systems. Thereby, the intermediate image from the object-space projection is indicated with the point P . For the lower optical systems, the AS is located between the two lenses and within a focal

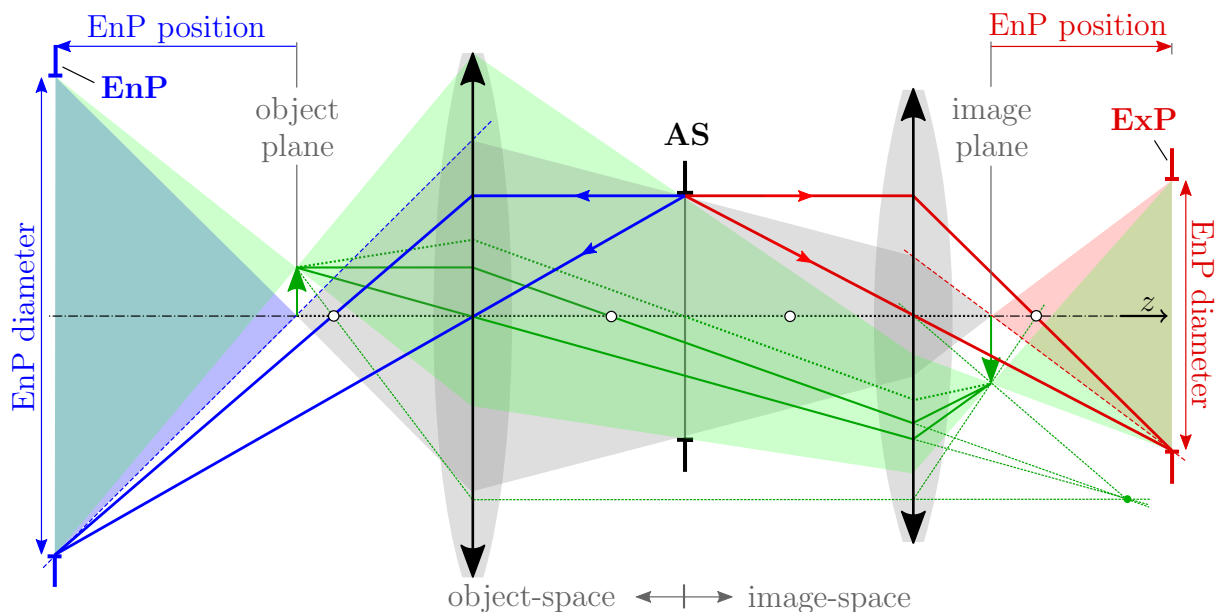


Figure 3.13: Construction of the EnP and the ExP by means of the AS, the focal length of the object-space and the focal length of the image space. In this example, the EnP position is < 0 and the ExP position is > 0 .

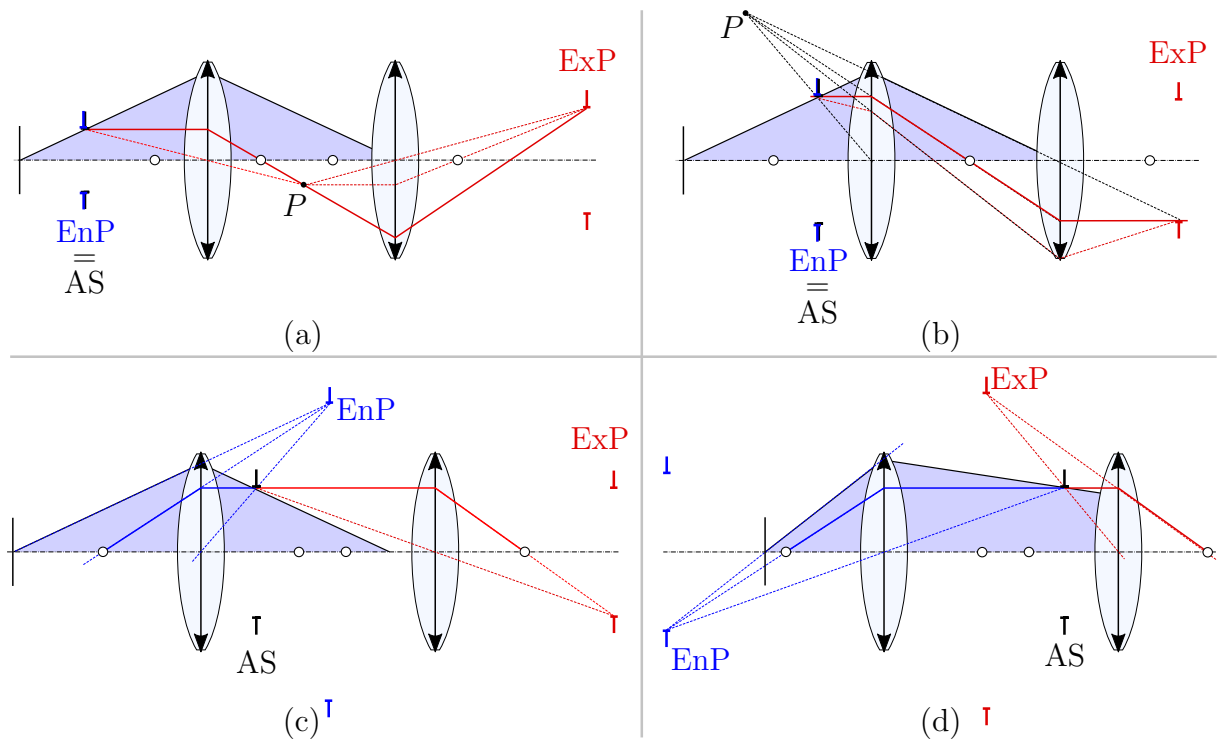


Figure 3.14: Different positions of the AS and the corresponding EnP and ExP.

length. Thus, either the EnP or the ExP results from the virtual image of the AS.

For the investigation of the performance of optical systems, the aberration theory can be utilized, which is explained in the following.

3.3.3 Optical Aberrations

According to optical methods, the accuracy of an optical system can be quantitatively assessed by means of optical aberrations. Next, the presence of a point-source object according to Figure 3.15 is considered. If the wavefront leaving the ExP differs significantly from the ideal spherical shape, then the optical system has an imaging error. In most cases, it is distinguished between the wavefront aberration (WFA) and the related line of sight (LOS) error. In particular, the latter represents the displacement of the image center of irradiance with respect to the object center of intensity, whereas the WFA generally characterizes the blurring and image quality [GrossSingerTotzeck05].

For the calculation of the WFA ΔW , the CR is traced until it hits the image plane, and at the corresponding position and orientation, a new reference frame C_{cr} is introduced. Moreover, the rays are traced until to a reference sphere located at the ExP, which characterizes an ideal wavefront W_{ideal} . The next step is, to subtract the OPL of the CR from the OPLs of the other rays, which determine the real wavefront W_{real} . This results in

$$\Delta W = W_{real} - W_{ideal}. \quad (3.37)$$

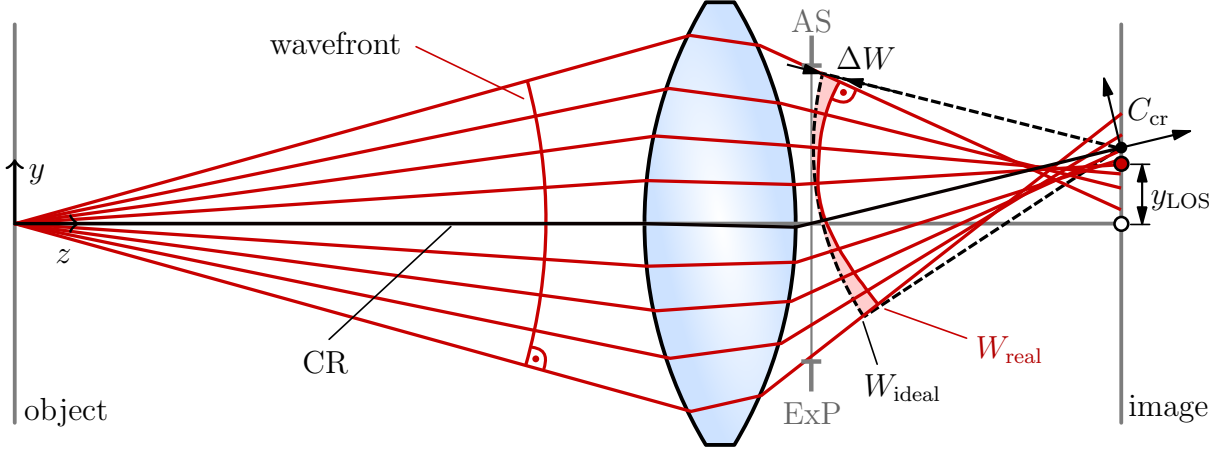


Figure 3.15: Explanation of the WFA ΔW and the LOS y_{LOS} .

Since the CR is not defined for *annular pupils*, a sphere with a suitable radius and center point is firstly fitted to the WFA in the ExP. Afterwards, the line which connects the pupil center and sphere center point defines the reference frame C_{cr} on the image plane by the related intersection point and orientation. Finally, the WFA with respect to C_{cr} can be expanded in Zernike polynomials [Zernike34] and the related coefficients directly describe the different kinds of optical aberrations like defocus, astigmatism, coma, trefoil or spherical aberration, as presented in the next section. The coefficients can be collected in the vector

$$\mathbf{a}_{\text{wfa}} = [\dots c_j \dots]^\top, \quad (3.38)$$

which represents the WFA. Since the second and third Zernike coefficient characterize a tilt, they can be used in combination with the CR deviation $[x_{\text{cr}} \ y_{\text{cr}}]^\top$ for calculating the LOS [Wengert16]. With the numerical aperture NA and the wavelength λ , it follows

$$\mathbf{a}_{\text{los}} = \begin{bmatrix} x_{\text{los}} \\ y_{\text{los}} \end{bmatrix} = \begin{bmatrix} x_{\text{cr}} - 2c_2\lambda/\text{NA} \\ y_{\text{cr}} - 2c_3\lambda/\text{NA} \end{bmatrix}. \quad (3.39)$$

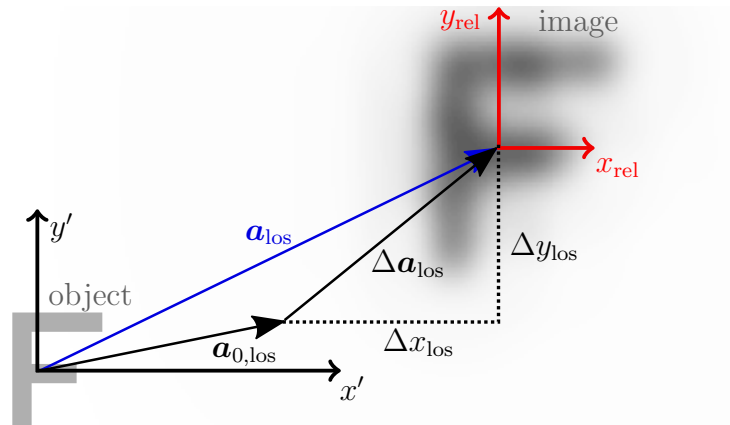
The orthogonal condition (3.48) of the standard Zernike polynomials simplifies the calculation of the RMS value of the remaining Zernike standard coefficients,

$$\Delta W_{\text{rms}} = \sqrt{\sum_{j=4}^{n_j} c_j^2}. \quad (3.40)$$

Usually, the optical aberrations are further split into a constant part \mathbf{a}_0 , which is present in the *reference configuration*, and a time dependent part $\Delta\mathbf{a}(t)$. This yields

$$\mathbf{a}(t) = \begin{bmatrix} \mathbf{a}_{\text{los}}(t) \\ \mathbf{a}_{\text{wfa}}(t) \end{bmatrix} = \underbrace{\begin{bmatrix} \mathbf{a}_{0,\text{los}} \\ \mathbf{a}_{0,\text{wfa}} \end{bmatrix}}_{\mathbf{a}_0} + \underbrace{\begin{bmatrix} \Delta\mathbf{a}_{\text{los}}(t) \\ \Delta\mathbf{a}_{\text{wfa}}(t) \end{bmatrix}}_{\Delta\mathbf{a}(t)}. \quad (3.41)$$

Figure 3.16: Relative image coordinates, with respect to the LOS and the absolute image coordinates x' and y' . The object and the magnified image are also indicated.



For example, the relations of the LOS within a certain configuration are sketched in Figure 3.16, whereby the relative image coordinates

$$x_{\text{rel}} = x' - x_{\text{los}} \quad \text{and} \quad y_{\text{rel}} = y' - y_{\text{los}} \quad (3.42)$$

are introduced. The mentioned Zernike polynomials are not only used for the representation of optical aberrations, but also for the approximation of surface deformations, as explained in Section 4.2.2. Since they are quite common in the field of optics, they are introduced in the following for both, circular and annular shapes.

3.3.4 Zernike Polynomials

According to the single indexing scheme of [Noll76, Mahajan81], the standard Zernike polynomials are considered with the radial normalized coordinate and the angle coordinate

$$\rho = \frac{1}{R_z} \sqrt{x^2 + y^2} \in [0, 1] \quad \text{and} \quad \theta = \arctan\left(\frac{y}{x}\right) \in [0, 2\pi] \quad (3.43)$$

on the unit circle. The semi-diameter R_z of the regarded area serves thereby as normalization factor. The Zernike circular polynomials are defined as

$$Z_j(\rho, \theta) = \begin{cases} \sqrt{2(n+1)} R_n^m \cos(m\theta) & \text{if } m \neq 0 \text{ and } j \text{ even,} \\ \sqrt{2(n+1)} R_n^m \sin(m\theta) & \text{if } m \neq 0 \text{ and } j \text{ odd,} \\ \sqrt{n+1} R_n^m & \text{if } m = 0 \end{cases} \quad (3.44)$$

with the radial term

$$R_n^m = \sum_{k=0}^{(n-m)/2} \frac{(-1)^k (n-k)!}{k! ((n+m)/2 - k)! ((n-m)/2 - k)!} \rho^{n-2k}. \quad (3.45)$$

The radial degree n can be calculated in dependence of j with

$$n = \text{floor}\left(\frac{\sqrt{8j-7}-1}{2}\right). \quad (3.46)$$

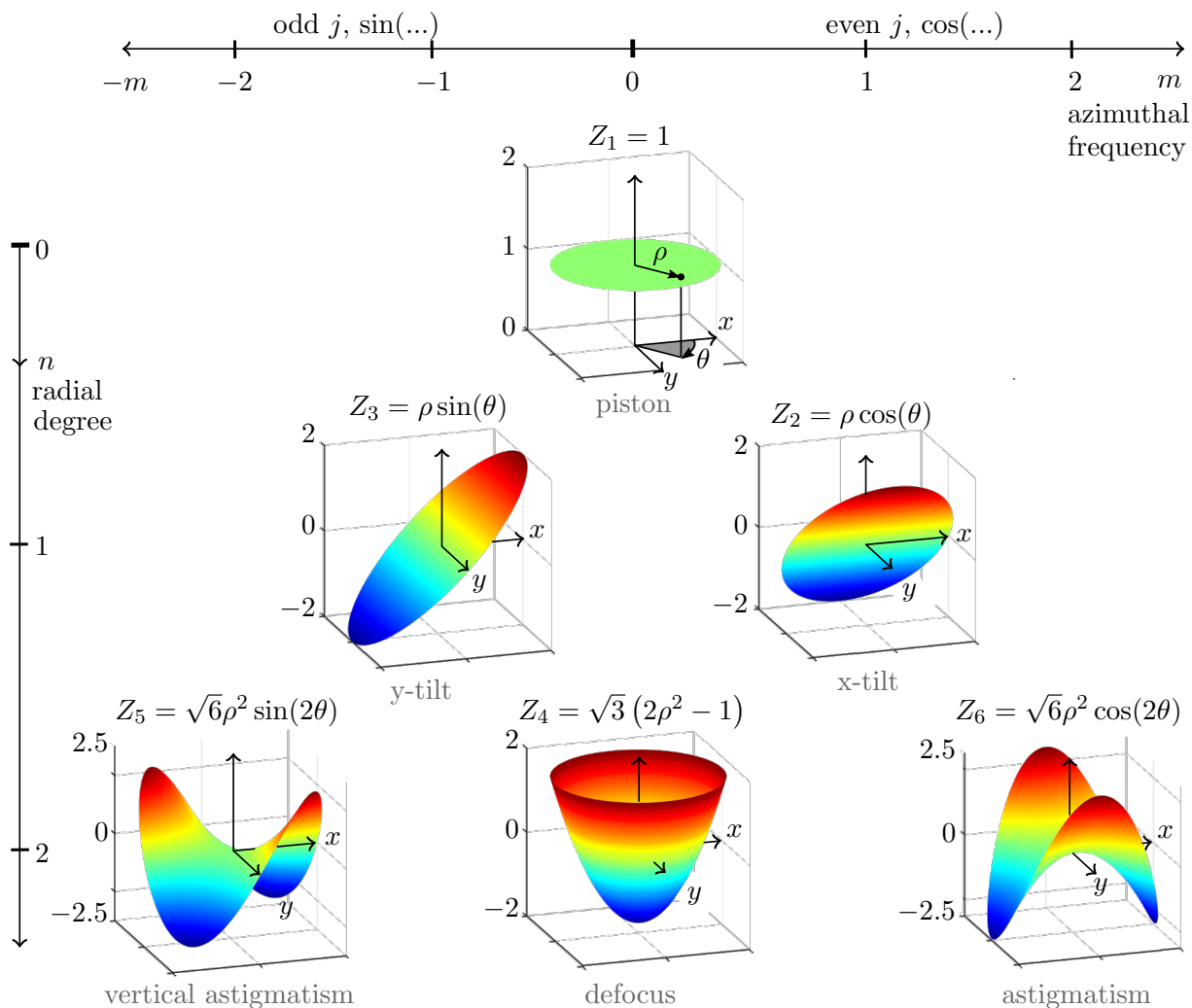


Figure 3.17: Zernike polynomials according to Noll's scheme, which also classify optical aberrations.

Afterwards, the azimuthal frequency m can be obtained with

$$m = \begin{cases} 2 \text{ floor} \left(\frac{2j - n(n+1)}{4} \right) & \text{if } n \text{ even,} \\ 2 \text{ ceil} \left(\frac{2j - n(n+1)}{4} \right) - 1 & \text{if } n \text{ odd.} \end{cases} \quad (3.47)$$

In particular, the polynomial basis of Zernike fulfill the orthogonality condition in the range of the unit circle

$$\int_0^1 \int_0^{2\pi} Z_j(\rho, \theta) Z_k(\rho, \theta) d\theta d\rho = \begin{cases} \text{const} & \text{if } k = j, \\ 0 & \text{otherwise.} \end{cases} \quad (3.48)$$

The first six Zernike polynomials are depicted in Figure 3.17 and the relationships of j , m and n , are indicated. For each polynomial, the kind of optical aberration is also

stated. Thus, an arbitrary WFA can be approximated and decomposed by means of these polynomial basis functions, and the resulting coefficients directly allow a classification of the optical aberrations. However, if the regarded area of the WFA is not circular but annular, the polynomial basis functions must also be annular, otherwise the physical interpretation of the resulting coefficients is not possible.

Zernike Annular Polynomials

In contrast to circular polynomials, the Zernike annular polynomials are orthogonal over an annulus. They were introduced by [Tatian74, Mahajan81], and in the following, the corresponding recursive description is presented.

The calculation of the Zernike annular polynomials can be performed by applying the Gram-Schmidt orthogonalization process. Since they are defined over an annulus onto the unit circle, the aperture ratio ε is introduced. For a set of polar coordinates ρ and θ according to Equation (3.43), the ratio is defined in the range $0 \leq \varepsilon < 1$ with

$$\varepsilon = \frac{R_{z,\text{inner}}}{R_z}, \quad (3.49)$$

whereby $R_{z,\text{inner}}$ is determined by the inner semi-diameter of the regarded annulus. The recursive calculation of the Zernike annular polynomials $\mathcal{Z}_j(\theta, \rho, \varepsilon)$ according to the single indexing convention of Noll is presented in [DaiMahajan07], and the structure is equal to Equation (3.44). However, for the Zernike annular polynomial, the radial term R_n^m of the circular formulation has to be replaced with the annular radial part \mathcal{R}_n^m . Furthermore, the radius results in the range $\varepsilon \leq \rho \leq 1$. The orthogonality condition is given by

$$\int_{\varepsilon}^1 \mathcal{R}_n^m(\rho, \varepsilon) \mathcal{R}_{n'}^m(\rho, \varepsilon) \rho \, d\rho = \frac{1 - \varepsilon^2}{2(n+1)} \delta_{nn'}, \quad (3.50)$$

whereas $\delta_{nn'}$ is the Kronecker delta defined as

$$\delta_{nn'} = \begin{cases} 1 & \text{for } n = n' \\ 0 & \text{for } n \neq n'. \end{cases}$$

The radial annular polynomials are obtained by applying the Gram-Schmidt orthogonalization process [Gramlich13] to the corresponding radial circle polynomials. This yields to

$$\mathcal{R}_n^m(\rho, \varepsilon) = \mathcal{N}_n^m \left[R_n^m(\rho) - \sum_{k=1}^{\frac{n-|m|}{2}} \mathcal{R}_{n-2k}^m(\rho, \varepsilon) \frac{2(n-2k+1)}{1-\varepsilon^2} \int_{\varepsilon}^1 R_n^m(\rho) \mathcal{R}_{n-2k}^m(\rho, \varepsilon) \rho \, d\rho \right] \quad (3.51)$$

with the normalization factor \mathcal{N}_n^m . Since the orthogonality condition must be satisfied,

one can derive the normalization factor by substituting (3.51) into (3.50), which results in

$$\mathcal{N}_n^m = \sqrt{\frac{\frac{1-\varepsilon^2}{2(n+1)}}{\int_{\varepsilon}^1 \left[R_n^m(\rho) - \sum_{k=1}^{\frac{n-|m|}{2}} \mathcal{R}_{n-2k}^m(\rho, \varepsilon) \frac{2(n-2k+1)}{1-\varepsilon^2} \int_{\varepsilon}^1 R_n^m(\rho) \mathcal{R}_{n-2k}^m(\rho, \varepsilon) \rho d\rho \right]^2 \rho d\rho}}. \quad (3.52)$$

The last two equations contain the recursive expression $\mathcal{R}_{n-2k}^m(\rho, \varepsilon)$. Thus, every radial annular polynomial at a given azimuthal frequency m and a radial order n depends on the radial annular polynomials with the same azimuthal frequency m and a radial order $n - 2$. The recursive calculation of Zernike polynomials can be performed, e.g., in Matlab by recursive function calls. Nevertheless, the calculations of radial annular polynomials with the same azimuthal frequency but different radial orders lead to identical sub-function calls, by which lower radial annular polynomials are computed several times. Besides, the normalization factor \mathcal{N}_n^m always has to be computed and requires numerical integration. Due to these facts, the explicit method for computing recursive polynomials based on the Gram-Schmidt orthogonalization process should be used, see also [Schäfer15].

The first 10 Zernike annular polynomial shapes are illustrated in Figure 3.18. Again, the annular

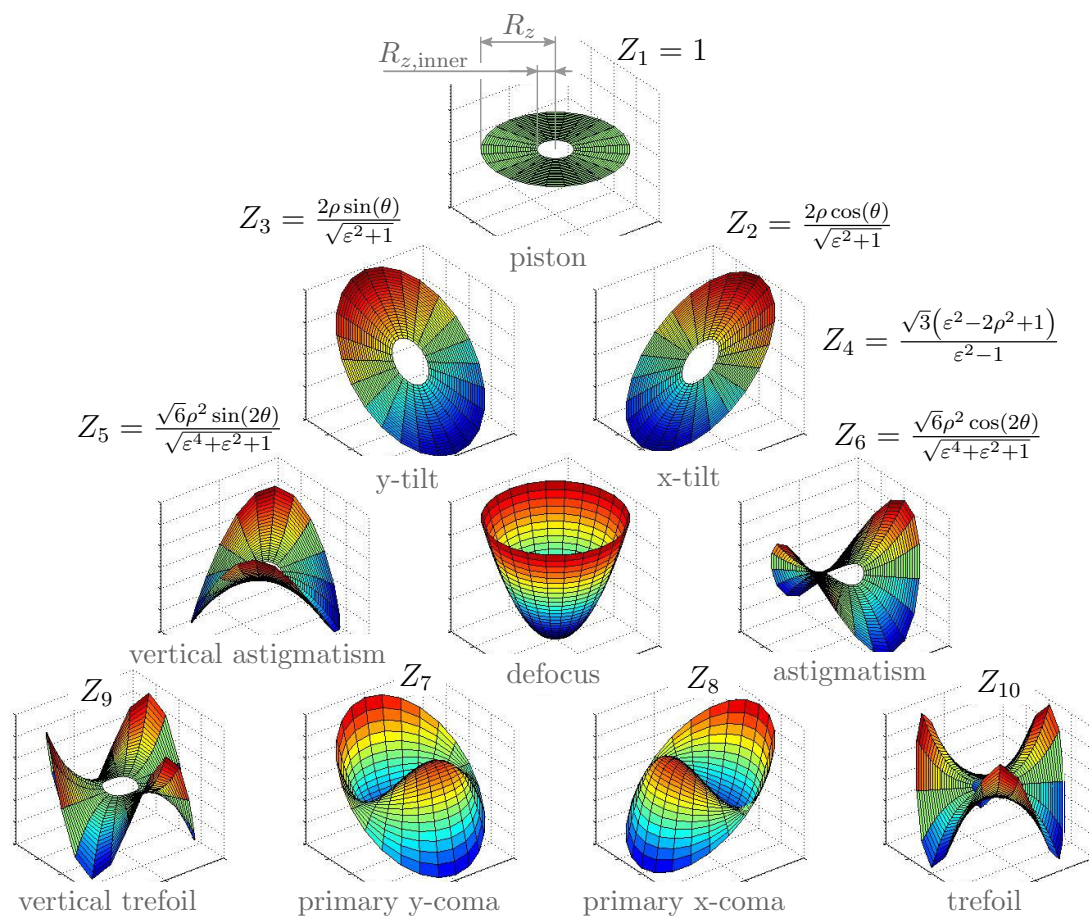


Figure 3.18: Zernike annular polynomial shapes according to Noll's scheme.

coefficients directly correspond to the common types of optical aberrations, which allows a physical interpretation of the simulated wavefront results.

In particular, one can find a relationship between the circular coefficients $\mathbf{c}_c = [\dots c_j \dots]^\top$ and the annular coefficients $\mathbf{c}_a = [\dots c_{a,j} \dots]^\top$. This can be formulated as the sub transformation matrix $\mathbf{M}_{|m|(2)n}^m$ [Schäfer15].

Thus, the computation of the equivalent circular coefficients on the basis of the annular coefficients can be performed with

$$\mathbf{c}_c = (\mathbf{M}_{|m|(2)n}^m)^\top \cdot \mathbf{c}_a, \quad (3.53)$$

whereby the physical validity of the equivalent circular coefficients vanishes.

In summary, it can be stated that the Zernike circular polynomials are used for the wavefront approximation of systems with a circular ExP, whereas annular polynomials are applied for the characterization of annular WFA. However, one can also use them for the description of deformed surfaces, which is explained in Section 4.2.2. Thereby, it is necessary to compute the derivatives of the Zernike polynomials for the ray tracing. An efficient implementation is proposed correspondingly in [Wengert16].

3.3.5 Resolution

For high performance optical systems the WFA is quite small and thus, the resolution and image quality on the screen is further limited by the phenomena of diffraction. In order to ascertain, whether an imaging system is *diffraction-limited*, the peak-to-peak value according to the Rayleigh criterion

$$\Delta W_{\text{pv}} \leq \frac{\lambda}{4} \quad (3.54)$$

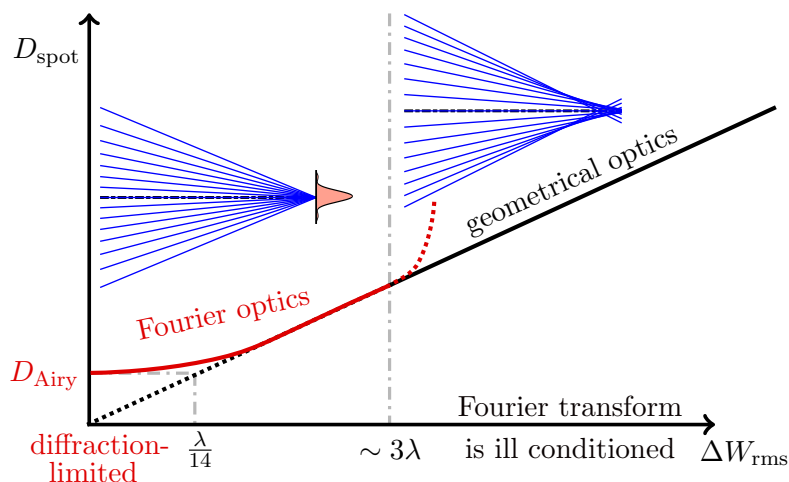
is often used. As an alternative, the Marechal criterion

$$\Delta W_{\text{rms}} \leq \frac{\lambda}{14} \quad (3.55)$$

can be consulted [GrossSingerTotzeck07]. If one considers the spot diameter D_{spot} of a ray field at the screen according to Figure 3.19, the limitations of the geometrical optics also became evident. For high-aberrated systems, the ray-optical approach delivers a blurred spot, which is close to the reality. However, in the case of very small aberrations, the spot seems to be perfectly focused in one point, but the distribution of the irradiance on the screen is rather similar to an Airy disk based on Fourier optics. Further details are discussed in Section 3.4.3.

So obviously, the previous ray-optical description of light is often not sufficient, since it cannot consider phenomena such as interference, diffraction, or polarization. Hence, further concepts of optical models are necessary, which are described in the following.

Figure 3.19: Spot calculation with the ray-optical and wave-optical approximation of light, similar to [Gross05].



3.4 Wave Optics

For many optical applications such as low-priced lenses for cameras, eyeglasses or binoculars, it is usually sufficient to design the systems only by means of ray optical methods. However, if the system should meet high requirements with respect to the accuracy and resolution, such as for lithographic lens and mirror systems, optical metrology, ground-based or space-based telescopes, the wave nature of light must be taken into account additionally. This section first introduces the usual descriptions of light in the field of electrodynamics and further explains some optical phenomena, properties, and expressions. At the end, the fundamentals of Fourier optics and a related method for the exposure simulation are briefly presented.

3.4.1 Wave-Particle Duality

According to the theoretical physics, light can generally be described by two different approaches, the classical electrodynamics and the quantum electrodynamics [Schmidt10], which are summarized in Figure 3.20. Within the quantum approach on the right-hand side, photons are elementary particles with no mass and no charge, and the light consists of one or more photons [PedrottiPedrotti93]. Thereby, photons and electrons move from point to point, and electrons emit and absorb photons which have the energy $\Delta E = hf$. Hence, the energy of a photon is equal to the product of the Planck's constant h and its frequency f . The quantum theory tells the probabilities of these motions and events in various situations, e.g., the probability amplitude for the emission or absorption of a photon can be estimated. For instance, this description can be used to represent the photoelectric effect, the Compton scattering, or the Planck-Einstein relation.

In contrast, the classical treatment describes light using co-oscillating electric and magnetic wave fields, which are continuous functions of space and time. Since light is thereby considered to propagate by means of waves, this description can predict phenomena such

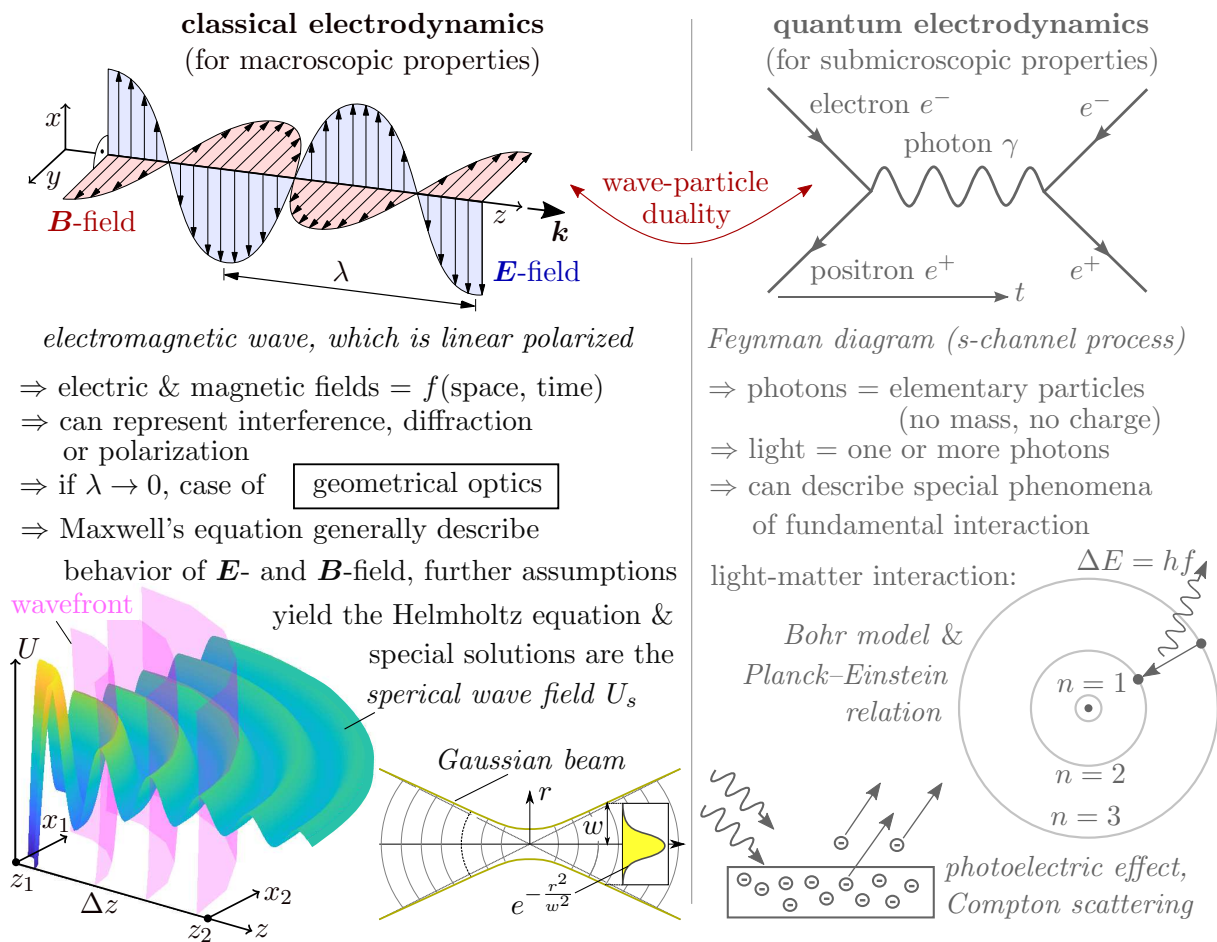


Figure 3.20: Physical description of light.

as interference and diffraction, which are not explained by the geometrical optics. Only if the wavelength λ of an electromagnetic wave is very small compared to the objects such as slits, grids or masks, the waves travel in straight lines with no bending around the edges of objects [SalehTeich91]. The same is true for optical systems, which are not diffraction-limited, as explained in Section 3.3.3. For the general field relations, *Maxwell's equations* are used to describe how electrically charged particles and objects influence the electric and magnetic fields.

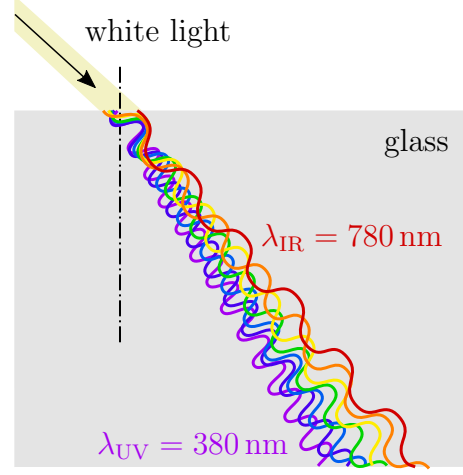
For the case of optical wave propagation through an isotropic, homogeneous, nondispersive, dielectric media, see also Excursion 2, the Maxwell equations can be simplified and combined to the *Helmholtz equation* [Schmidt10]. It can be solved for many applications, for example, one can find the spherical wave field

$$U_s(\mathbf{r}, t) = \frac{1}{|\mathbf{r}|} \hat{U}_s e^{i(\omega t - \mathbf{k} \cdot \mathbf{r})} = \frac{1}{|\mathbf{r}|} \hat{U}_s (\cos(\omega t - \mathbf{k} \cdot \mathbf{r}) + i \sin(\omega t - \mathbf{k} \cdot \mathbf{r})) \quad (3.56)$$

or the Gaussian beam as solutions. They satisfy the equation for special conditions and are sketched on the lower left-hand side in Figure 3.20. The quantity $U_s \in \mathbb{C}$ stands for any of the x , y or z -directed components of the electric field \mathbf{E} or the magnetic field \mathbf{B} .

Excursion 2: Dispersion, Homogeneity and Isotropy.

The so-called dispersion denotes the phenomenon in which the phase velocity of a wave depends on its frequency. For example, if visible white light refracts at a glass, the angle of the light components varies, due to their different wavelengths. In particular, the refraction of light close to ultraviolet waves with λ_{UV} is higher than the light close to infrared waves with λ_{IR} , as illustrated on the right-hand side. Besides, the homogeneous property implies, that the material is not a function of the position.



Furthermore, a dielectric material is an electrical insulator, i.e., electric charges do not flow through it, and isotropy media is uniform in all orientations, i.e., the material properties do not depend on a particular direction.

It depends on the amplitude \hat{U}_s , the circular frequency $\omega = 2\pi c_M/\lambda$, the wave traveling vector \mathbf{k} , the wavenumber

$$k = |\mathbf{k}| = \frac{2\pi}{\lambda}, \quad (3.57)$$

the position \mathbf{r} , and the time. The complex representation is quite common in the wave theory, but it is sometimes also described only by the imaginary part $\text{Im}\{U_s\}$ or with the sine representation [PedrottiPedrotti93]. If the attention is restricted to regions of space, that are very close to the optical axis and far away from the wave origin, the approximation for paraxial rays and far-propagations can be used, see also Section 3.3.1. With the distance $r = \sqrt{\Delta z^2 + (x_2 - x_1)^2 + (y_2 - y_1)^2}$ from the source, the spherical wave approximation results in

$$U_s(x_2, y_2, \Delta z) \approx \hat{U}_s \frac{e^{ik\Delta z}}{\Delta z} e^{i\frac{k}{2\Delta z}((x_2-x_1)^2+(y_2-y_1)^2)} \approx \hat{U}_s \frac{e^{ik\Delta z} e^{i\frac{k}{2\Delta z}(x_2^2+y_2^2)}}{\Delta z} e^{-i\frac{k}{\Delta z}(x_2x_1+y_2y_1)} \quad (3.58)$$

in the phasor domain, as discussed in [Enders11] and [Schmidt10]. Furthermore, the \mathbf{E} - and \mathbf{B} -field are proportional to each other. In vacuum, their amplitudes have the relation

$$\hat{E} = c_0 \hat{B} = \frac{1}{\sqrt{\varepsilon_0 \mu_0}} \hat{B}, \quad (3.59)$$

where c_0 again is the wave velocity, ε_0 is the permittivity and μ_0 is the permeability.

In the scope of wave optics, the *scalar diffraction theory* is often used to approximately describe the propagation of monochromatic, linear polarized light by spherical waves, including the effects of the surroundings and boundaries. It can be derived from the

Helmholtz equation, and it can be used, e.g., to estimate the spatial diffraction behavior and irradiance distribution at a slit according to Figure 3.21.

Thereby, the given source-plane optical field $U(x_1, y_1)$ at the slit position z_1 is propagating until to the observation-plane field $U(x_2, y_2)$, which is located at the distance Δz . In particular, the distribution of the wave amplitudes near to the slit can be computed by solving the *Kirchhof integral theorem*, which is based on the Huygens-Fresnel principle. Moreover, the Rayleigh-Sommerfeld theory eliminates the necessity of imposing boundary values, which represents the first simplification under certain assumptions [Goodman05]. The amplitude distribution and the related irradiance in an intermediate region can be described by the *Fresnel diffraction integral*, which uses the paraxial approximation. With the further assumption of far propagation distances, the description can be simplified similar to Equation (3.58). Hence, the *Fraunhofer diffraction integral*

$$U(x_2, y_2) = A(x_2, y_2) \iint_{-\infty}^{\infty} U(x_1, y_1) e^{-i\frac{k}{\Delta z}(x_1 x_2 + y_1 y_2)} dx_1 dy_1 \quad (3.60)$$

can be derived with the complex phase factor

$$A(x_2, y_2) = \frac{1}{i\lambda\Delta z} e^{ik\Delta z} e^{i\frac{k}{2\Delta z}(x_2^2 + y_2^2)}, \quad (3.61)$$

where

$$|A(x_2, y_2)|^2 = \frac{1}{(\lambda\Delta z)^2} \quad (3.62)$$

clarifies, that the phase information for the squared absolute value is lost, see also [Mack07, Goodman05]. Furthermore, the numerical evaluation of this integral is equal to a Fourier transformation and the related theory is called Fourier optics, which is introduced in Section 3.4.3.

There is the rigorous theory behind the classical and the quantum approach for the light description, and there is experimental evidence supporting both, e.g., the Young

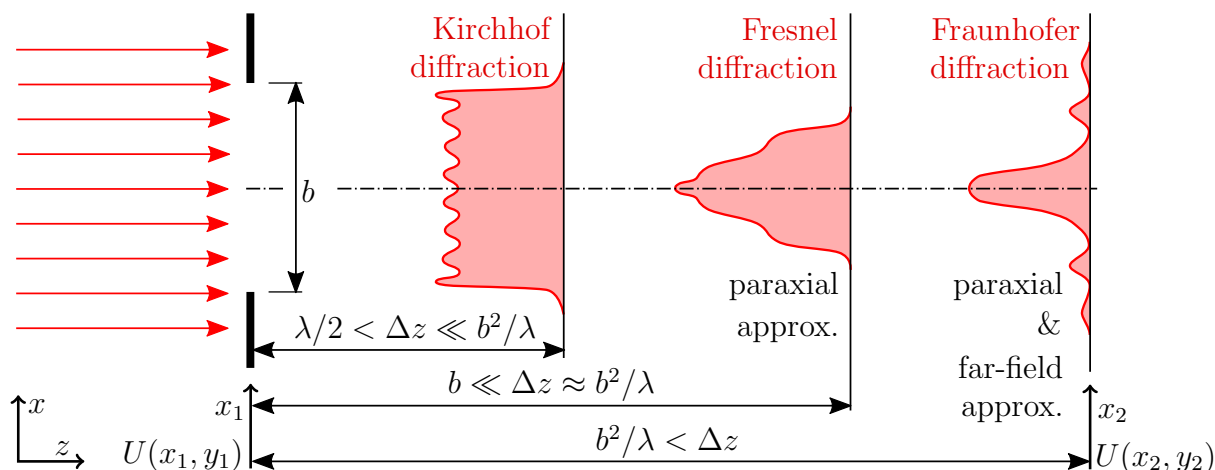


Figure 3.21: Regions of light irradiance due to the diffraction at a single slit.

experiment or the Taylor experiment. Neither approach can be dismissed, which leads to the wave-particle duality of light. In general, classical methods are used for macroscopic properties of light, while quantum methods can represent the submicroscopic properties of light [Schmidt10].

Next, the essential properties, oddities, and phenomena are introduced based on the wave-optical description of light.

3.4.2 Interference, Irradiance and Coherence

The Huygens-Fresnel principle provides a good basis for understanding and predicting wave propagation. Thereby, every point to which a luminous disturbance reaches becomes a source of a new spherical wavelet. Together with the principle of *interference*, one could explain both, the straight propagation of light and also diffraction effects. Figure 3.22(a) illustrates the wave field during the diffraction of monochromatic light at a single slit. The *irradiance* at the screen, which represents the power received by a surface per unit area, can be expressed according to Equation (3.59) with

$$I = \frac{1}{2}\varepsilon_0 c_0^2 \hat{E} \hat{B} = \frac{1}{2}\varepsilon_0 c_0 \hat{E}^2 = \frac{1c_0}{2\mu_0} \hat{B}^2, \quad (3.63)$$

as derived in [PedrottiPedrotti93]. In other words, the irradiance is proportional to the square of the superposed amplitudes of the connected \mathbf{E} - or \mathbf{B} -field. In the literature, the irradiance is sometimes also called *intensity*. Alternatively, the units of the coherent wave field $U(x, y, z)$ can be defined to be square-root Watts per meter ($1 \text{ W} = 1 \text{ J/s}$) so that the optical irradiance

$$I(x, y) = |U(x, t)|^2 \quad (3.64)$$

is in units of Watts per meter squared [Schmidt10]. For instance, Figure 3.22(b) shows the envelope of the amplitude and the envelope of the irradiance at the screen. Furthermore, the distributions are indicated for a time instant t .

Figure 3.23 illustrates the interference between two plane waves due to diffraction at a grating. The distance of the gratings is denoted by b . The screen is located at a distance Δz , and x_2 is the position of the interference maximum on the screen. Besides, the condition for the occurrence of interference maximum with the order of q at the angle α_q is derived.

However, for this principle of interference it is assumed, that there are perfect monochromatic light waves, which is not the case in reality. Thus, the so-called *coherence* describes the properties of the correlation between physical quantities of a single wave, or between several waves or wave packets. According to [PedrottiPedrotti93] one can distinguish between temporal, spectral and spatial coherence, which are sketched in Figure 3.24.

For the explanation of the temporal coherence, one can consider a partially coherent light source, which emitters monochromatic waves for varying coherence times $\tau_{c,i}$ in

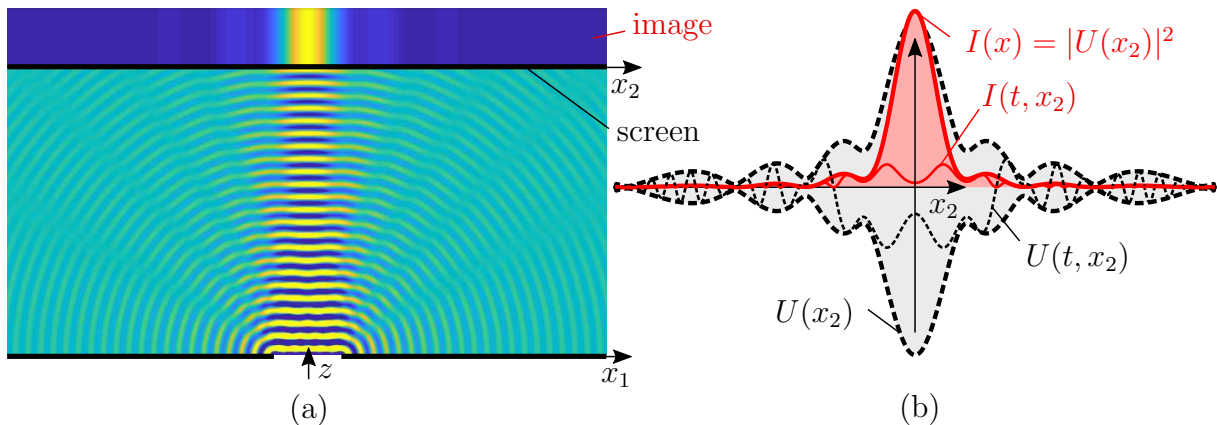


Figure 3.22: Explanation of the interference and the irradiance, at a single slit.

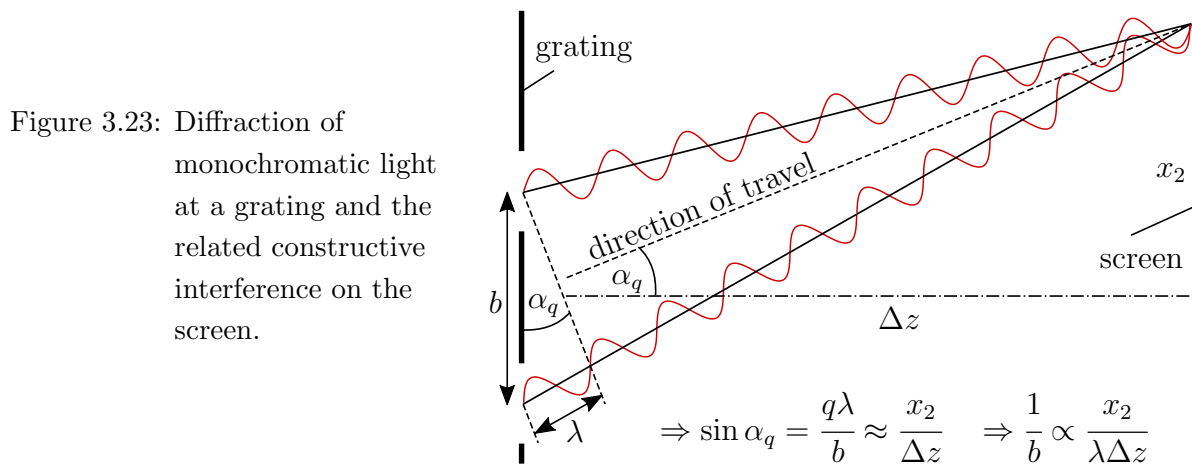


Figure 3.23: Diffraction of monochromatic light at a grating and the related constructive interference on the screen.

the longitudinal direction. The coherence length is the distance the wave travels in the coherence time. Usually, the related average values are used to represent the ability of interference. For laser light sources the coherence lengths are relatively long. Hence, the principle of interference can be applied to these sources. The spectral coherence results from the superposition of waves with different frequencies. If they have a fixed relative phase-relationship, they can interfere to form wave pulses, also known as wave packets. For example, the different wavelengths of white light can form wave packets with a coherence time τ_c , as shown in the center of Figure 3.24. Finally, the spatial coherence describes the correlation in phase between spatially distinct points of a radiation field concerning the lateral direction. According to the lower part of Figure 3.24, a spacious light source can be considered, which initially produces white and incoherent light and illuminates a small pinhole. Due to the diffraction, spatially coherent elementary waves with a spherical shape are generated approximately. A filter, which allows passing through only a specific wavelength, can moreover realize a spectral coherence.

The single amplitudes have to be summed up for the particular case of a coherent wave field. In contrast, the irradiation if the single wave sources have to be summed up for the incoherent case [PedrottiPedrotti93].

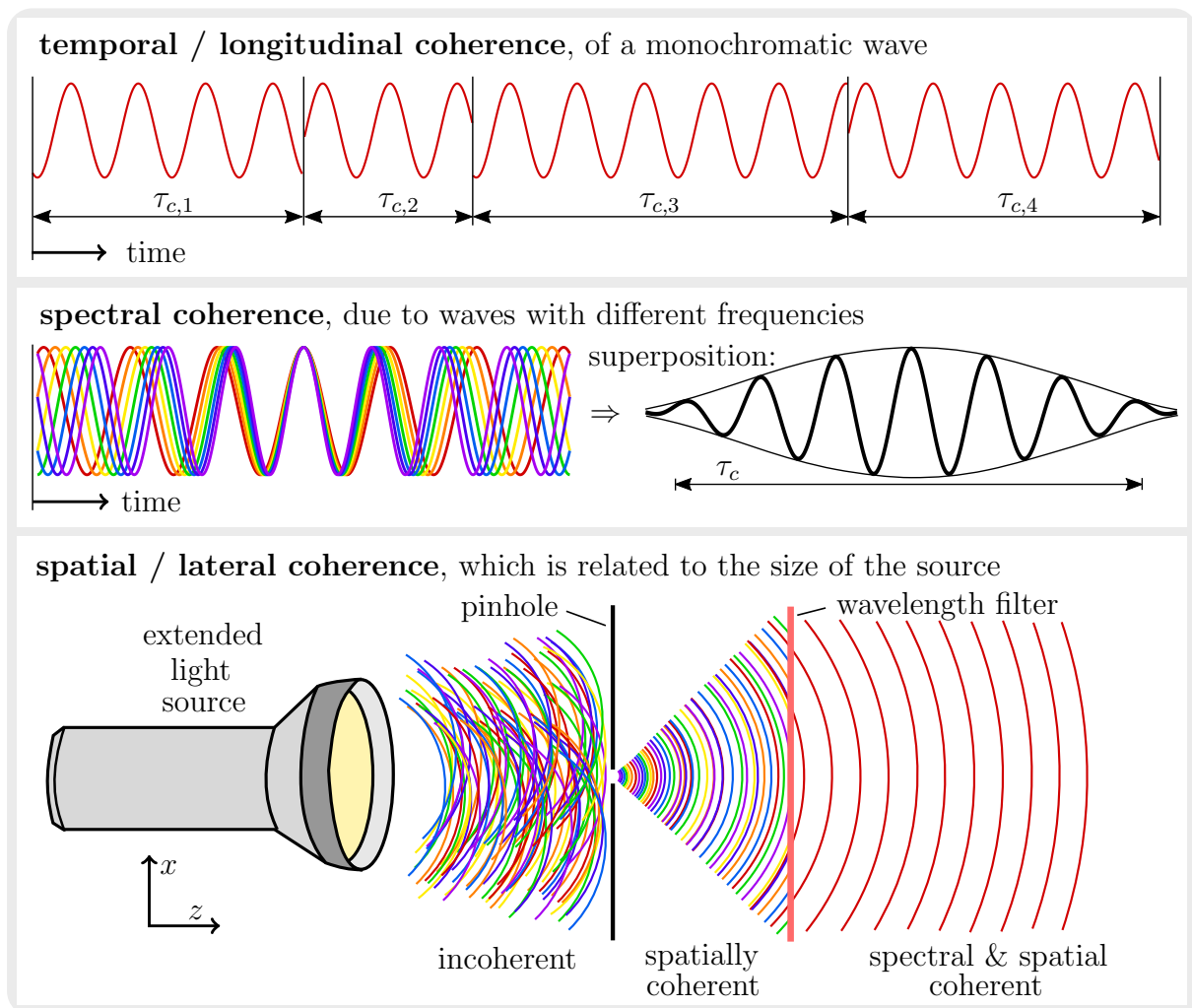


Figure 3.24: Explanation of coherence types.

After the most basic wave properties are introduced, it will be focused on the Fourier optical theory, which can conveniently approximate the diffraction behavior of light.

3.4.3 Fourier Optics

On closer consideration of the rear integral part at the Fraunhofer diffraction according to Equation (3.60), one can see that it is equal to a 2D-Fourier transformation of $U(x_1, y_1)$. First, the so-called spatial frequencies

$$f_x = \frac{x_2}{\lambda \Delta z} \quad \text{and} \quad f_y = \frac{y_2}{\lambda \Delta z} \quad (3.65)$$

can be introduced, which are related to the reciprocal grating distance $1/b$ of Figure 3.23. If the grating structure is small-sized, the spatial frequencies are high and vice versa. Hence, the imaging of a coherent source field $U_o(x_1, y_1)$ from the object plane until to an observation plane in the far-field can be recognized simply as a Fourier transform [Voelz11],

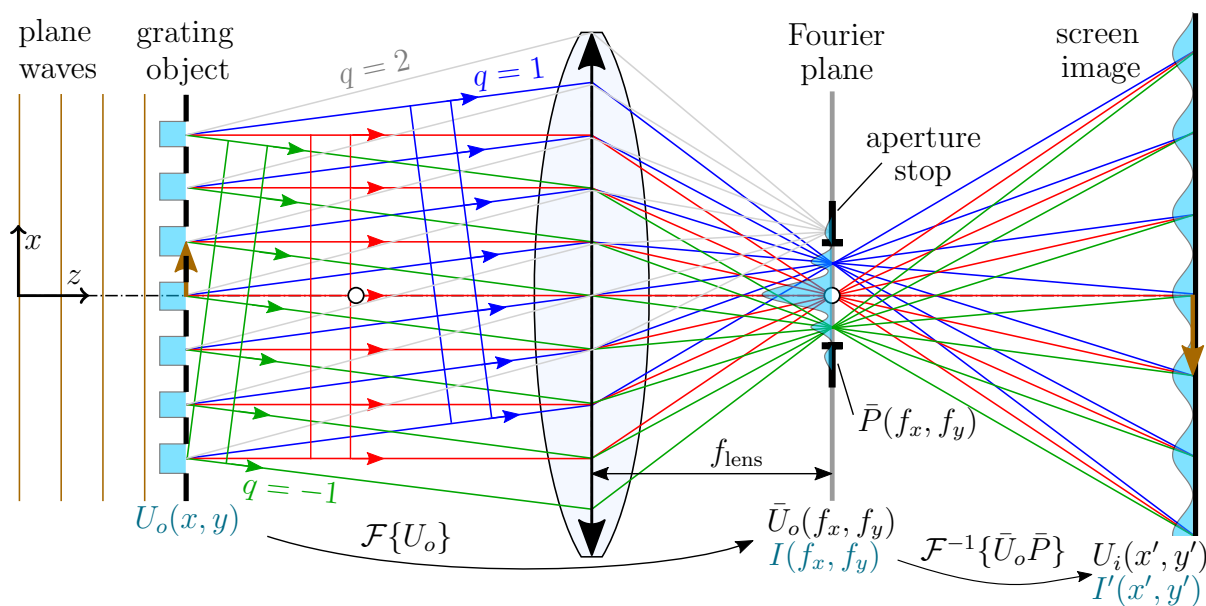


Figure 3.25: The Abbe theory of image formation, which is based on Fourier optics.

along with multiplicative factors out front,

$$\bar{U}_o(f_x, f_y, \Delta z) = A(f_x \lambda \Delta z, f_y \lambda \Delta z, \Delta z) \underbrace{\iint_{-\infty}^{\infty} U_o(x_1, y_1) e^{-i2\pi(f_x x_1 + f_y y_1)} dx_1 dy_1}_{\mathcal{F}\{U_o(x_1, y_1)\}}. \quad (3.66)$$

The corresponding irradiance distribution results under the consideration of the Equations (3.62) and (3.64) with

$$I(f_x, f_y, \Delta z) = |\bar{U}_o(f_x, f_y, \Delta z)|^2 = \frac{1}{\lambda^2 \Delta z^2} |\mathcal{F}\{U_o(x_1, y_1)\}|^2. \quad (3.67)$$

In most cases, this is the quantity of real interest, since it is measurable on the screen. Again it should be clarified, that these equations are only valid for coherent monochromatic light traveling freely from an object to an image plane at a far distance. For example, if a 1 mm slit is illuminated with visible light, this distance must be in the range of multiple meters, see also the formulated conditions in Figure 3.21. However, it is known by the *Abbe Theory of Imaging*, that a converging lens produces the Fraunhofer diffraction pattern at its focal plane [Gross05]. With the help of the lens, the far-field is already found close behind the lens, or to be more precisely, at the focal distance. As a consequence, the focal plane of an imaging system is also called *Fourier plane* or pupil plane.

The concept of image formation at a grating and an ideal lens is shown in Figure 3.25. Due to the diffraction, the plane waves on the right hand-side are split in specific directions at the grating. These directions point to the interference maxima in a far-field, with the order q . Furthermore, the lens focuses the resulting waves in the Fourier plane. There, the related pattern $\bar{U}_o(f_x, f_y)$ characterizes the magnitude of diffraction, i.e., it represents the spectrum of the spatial frequencies of the initial object field $U_o(x, y)$. If there is an aperture

stop placed, it acts as a low-pass filter to the spatial frequencies of the object, since the high order frequencies are removed [Gross05]. So the corresponding pupil function, which is defined as

$$\bar{P}(f_x, f_y) = \begin{cases} 1 & [f_x, f_y] \text{ within the AS,} \\ \frac{1}{2} & [f_x, f_y] \text{ at the boundary,} \\ 0 & \text{otherwise,} \end{cases} \quad (3.68)$$

can be multiplied with the spatial frequency spectrum of the object \bar{U}_o . If the imaging system is not ideal, but has a WFA ΔW according to Equation 3.37, the *coherent transfer function*

$$\bar{P}_w(f_x, f_y) = \bar{P}(f_x, f_y) e^{i2\pi \Delta W(f_x, f_y)} \quad (3.69)$$

results, which is also known as amplitude transfer function. Finally, the amplitude distribution on the screen with the coordinates x' and y' is proportional to the result of the inverse Fourier transformation

$$U_i(x', y') \propto \mathcal{F}^{-1}\{\bar{P}_w \bar{U}_o\} = \iint_{-\infty}^{\infty} \bar{P}_w(f_x, f_y) \bar{U}_o(f_x, f_y) e^{i2\pi(f_x x' + f_y y')} df_x df_y \quad (3.70)$$

as explained in [Wengert16, Voelz11].

4-*f*-Fourier Model

The resulting image amplitude can also be calculated by the convolution integral of the object wave field U_o and the *point-spread function* (PSF) denoted with P_w , if the PSF is shift-invariant. Therefore, a 4-*f*-Fourier model, which demonstrates the filtering property of an optical system [Gross05], is considered in the following. It is shown in Figure 3.26 and represents telecentric imaging with a magnification of -1 using two ideal and identical lenses. The object plane is located at the front-focal distance f of the first lens, and the circular AS is centered at the back-focal distance. The second lens and the image plane is arranged in the same way. In the case of coherent image formation, the related image amplitude yields

$$U_i(x', y') = \iint_{-\infty}^{\infty} P_w(x' - x, y' - y) U_o(x, y) dx dy = (P_w * U_o)(x', y'). \quad (3.71)$$

The influence of magnification at an imaging system is remarked in Excursion 3. According to the convolution theorem, it further results

$$U_i = P_w * U_o = \mathcal{F}^{-1}\{\mathcal{F}\{P_w\}\mathcal{F}\{U_o\}\} = \mathcal{F}^{-1}\{\bar{P}_w \mathcal{F}\{U_o\}\}. \quad (3.72)$$

As a consequence, the PSF, which is also called amplitude response or amplitude distribution function, can be obtained with an Dirac delta function in the object field $U_{o,\delta} = \delta$. Since $\mathcal{F}\{U_{o,\delta}\} = \mathcal{F}\{\delta\} = 1$, the PSF at the image plane can be computed with

$$P_w(x', y') = \mathcal{F}^{-1}\{\bar{P}_w(f_x, f_y)\}. \quad (3.73)$$

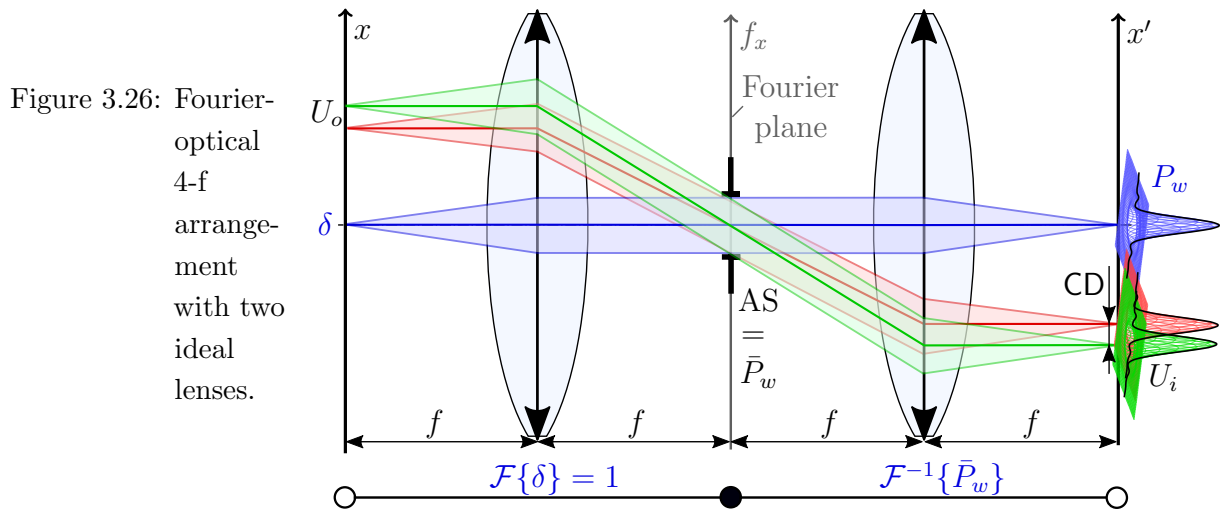


Figure 3.26: Fourier-optical 4-f arrangement with two ideal lenses.

Excursion 3: Generalization for Systems with Magnification.

As stated in [Goodman05, Voelz11], the Equation (3.71) can be generalized for diffraction-limited systems with a magnification M . For that, one can regard the screen irradiance as being a convolution of an ideal image with the impulse response that is the Fraunhofer diffraction pattern of the ExP, i.e., the PSF. Thereby, the geometrical optics can predict the ideal image $U_g(x, y) = \frac{1}{|M|}U_o(\frac{x}{M}, \frac{y}{M})$.

Afterward, it can be convoluted with the object field $U_o(x, y)$ according to Equation (3.72), to compute the amplitude distribution on the image plane. Figure 3.27 illustrates this two-step approach and the simulated irradiance at a lithographic objective.

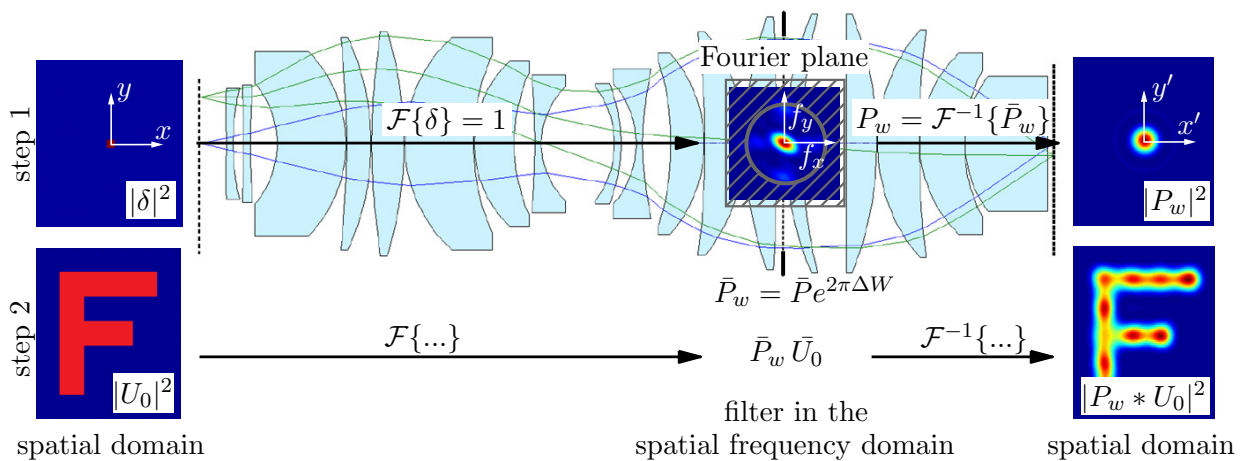


Figure 3.27: Image simulation using Fourier optics, similar to [Wengert16].

If no optical aberrations are present, the irradiance on the screen due to the PSF is identical to the so-called *Airy disk* $I_{\text{Airy}}(x', y') = |P(x', y')|^2$. With the angle of observation θ , the maximal irradiance I_{max} and the diameter D_{AS} of the AS, it can be expressed for a planar

cut as

$$I_{\text{Airy}}(\theta) = I_{\text{max}} \left(\frac{2J_1\left(\frac{\pi}{\lambda} D_{\text{AS}} \sin \theta\right)}{\frac{\pi}{\lambda} D_{\text{AS}} \sin \theta} \right)^2. \quad (3.74)$$

Thereby, the Bessel function J_1 of first kind is used [Gross05]. The inner ring in the diffraction pattern of the Airy disk has the diameter

$$D_{\text{Airy}} = 1.22 \frac{\lambda}{\text{NA}}. \quad (3.75)$$

This diameter is also used to estimate the resolution limit of an optical system, i.e. the critical distance of two overlapping Airy disks, see also the sketch on the right-hand side of Figure 3.26. On this base, the Rayleigh resolution criterion

$$\text{CD}_{\text{Rayl}} = \frac{D_{\text{Airy}}}{2} = 0.61 \frac{\lambda}{\text{NA}} \quad (3.76)$$

results, which is related to the Abbe criterion according to Equation (1.1).

Finally, the irradiance on the image plane depends on the case of spatial coherence. If the phase of the point light source is identical in all direction, Equation (3.64) can be used. Otherwise, the image irradiance is the convolution of the object intensity with the irradiance due to the PSF [Schmidt10]. Thus, it yields

$$I'(x', y') = \begin{cases} |P_w * U_o|^2, & \text{for spatial coherence} \\ |P_w|^2 * |U_o|^2, & \text{for spatial incoherence.} \end{cases} \quad (3.77)$$

In conclusion, the relations for a spatial coherent and spatial incoherent image formation are illustrated in Figure 3.28 as a flowchart. The best strategy in practice is to obtain the aperture dimensions and the WFA, in order to calculate the PSF by an inverse Fourier transformation. Afterwards, it can be convoluted with the known object amplitude field and the image amplitude on the screen results. For the case of spatial coherence, the irradiance can be calculated by the squared absolute value. In contrast, the object intensity must be convoluted with the intensity response for the spatial incoherence case.

3.4.4 Exposure Simulation

Sometimes, the image is moving or changing during an exposure or observation time, as explained in Chapter 1. Hence, the related and time-dependent irradiance field on the screen has to be superposed for that period. As already stated in Figure 3.16, LOS can describe the motion of the irradiance center. The related LOS trajectory can be determined with

$$L(x', y', t) = \begin{cases} 1 & \text{it } x' = x_{\text{los}}(t), y' = y_{\text{los}}(t), \\ 0 & \text{otherwise.} \end{cases} \quad (3.78)$$

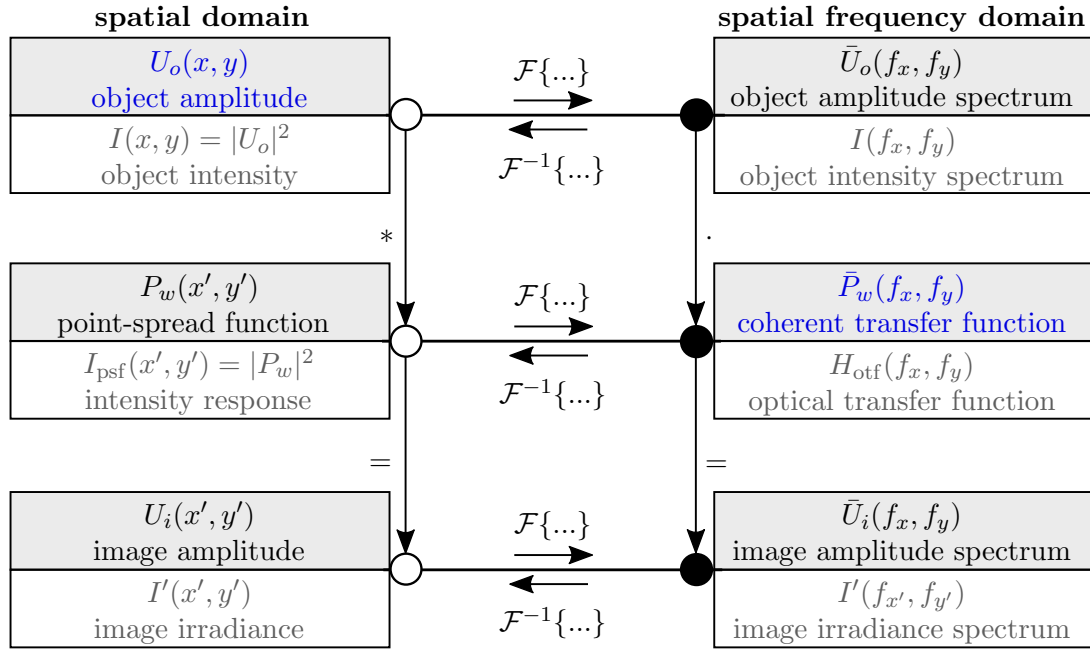


Figure 3.28: Schematic relations of spatial coherent image formation in the upper boxes and the incoherent image formation in grey, in the lower boxes, see also [Gross05].

Furthermore, the local irradiance field of the image I'_{local} can be expressed in relative coordinates x_{rel} and y_{rel} , as introduced in Equation (3.42). Thus, the concept of convolution can also be used for the simulation of the absolute radiant exposure

$$E_{\text{exp}}(x', y') = \int_{t_0}^{t_{\text{end}}} I'(x', y', t) dt = \int_{t_0}^{t_{\text{end}}} L(x', y', t) * I'_{\text{local}}(x_{\text{rel}}, y_{\text{rel}}, t) dt, \quad (3.79)$$

as proposed in [Wengert16]. This means, that the local irradiance at each time instant is placed and superposed at the related LOS position. If the local image is hardly changing, i.e. almost constant, the LOS mainly influences the behavior. Then it results

$$E_{\text{exp}}(x', y') = \underbrace{\int_{t_0}^{t_{\text{end}}} L(x', y', t) dt}_{E_{\text{los}}(x', y')} * I'_{\text{local}}(x_{\text{rel}}, y_{\text{rel}}, t_0). \quad (3.80)$$

The exposed image of the LOS trajectory is denoted with E_{los} and the procedure is also illustrated in Figure 3.29.

This chapter described several approaches to simulate optical phenomena. However, polarization effects or birefringence are not considered here, although they can significantly influence the ray tracing and consequently the image appearance on the screen. There are some suggestions to take these effects into account, e.g., by Jones vectors, index ellipsoids, and single-path approximations [Wengert16, PedrottiPedrotti93, GrossSingerTotzeck05].

Next, the concept of dynamical-optical simulations is explained, which combines the mechanical and optical representation of a system.

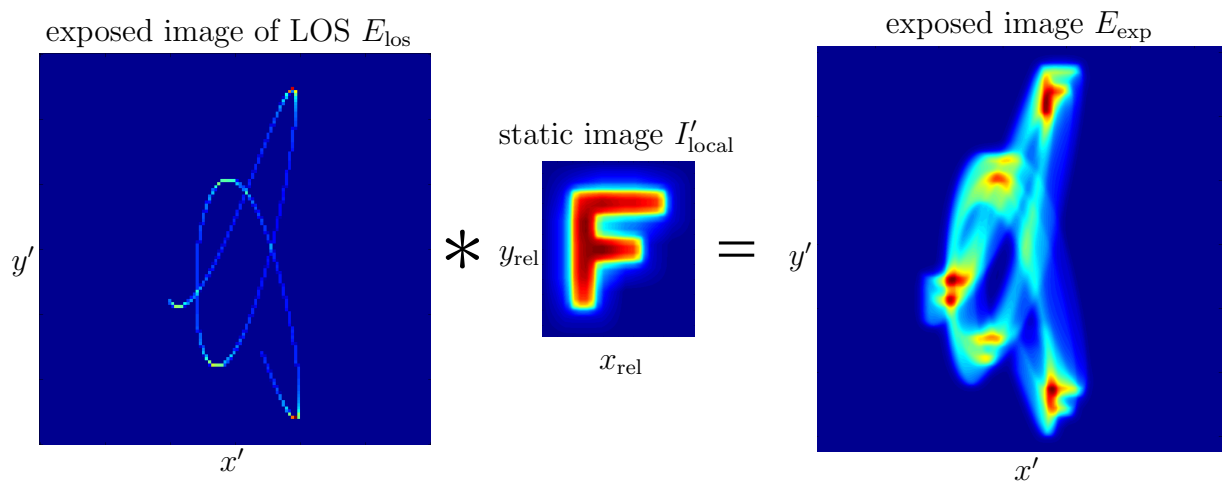


Figure 3.29: Exposure simulation for a static image convolution with the LOS, similar to [Wengert16].

Chapter 4

Dynamical-optical Simulations

This section includes the most important procedures and approaches, in order to realize a mechanical-optical simulation. In particular, the dynamical-optical behavior and performance is thereby identified and analyzed for different example models. First, an overview of a typical simulation workflow is given. Second, some particular implementations for the mechanical-optical coupling are introduced. Afterward, a mechanical simulation process of an elastic mirror is demonstrated which is followed by a linear dynamical-optical analysis. In order to clarify the benefit of a multidisciplinary simulation model, further investigations concerning the influence of the chosen MOR method and the simulation strategy are presented. Finally, the model-based design of an AO controller is developed for a segmented telescope.

4.1 Simulation Strategies

The mechanical behavior of optical systems regarded in this work can be simulated with EMBS in combination with optical models, as also proposed in [Wengert16]. First, existing FE programs like Ansys [ANSYS16] can be employed and second, a MOR toolbox called MatMorembs and an EMBS toolbox named Neweul-M² for general use was developed. Within this research project, the optical simulation toolbox OM-Sim with an interface to elastic multibody simulations is developed, see also [StörkleEberhard16]. Figure 4.1 shows the general procedure for dynamical-optical simulations using cooperating software packages and some parts are discussed in the following.

In order to investigate the system behavior in the time domain during a mechanical excitation, two methods are proposed. On the one hand, the *standard method* directly performs the time integration to obtain the generalized coordinates. Unfortunately, for the optical-dynamical simulation the deformation at each time instant has to be polynomially approximated, ray traced and optically investigated, as illustrated in the left lower part in

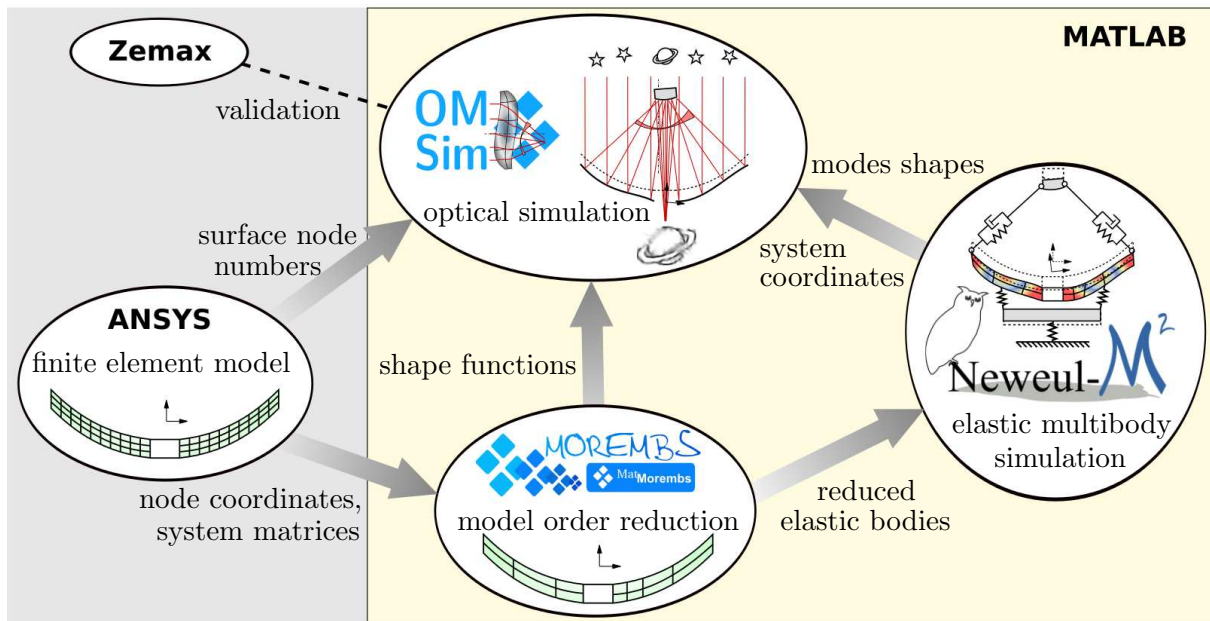


Figure 4.1: Schematic process of the polynomial approximation and preparation of a meshed surface section.

Figure 4.2. For long simulation times, the arising computational cost can be enormous.

On the other hand, a *modal method* is suggested including modal analysis and transformation of the EMBS, shown on the right side in Figure 4.2. This transformation leads to a decoupled system with simplified equations of motions which allows extensive time integrations at the minimal computational effort. As a result, the modal coordinates describe the system behavior as the amplitudes of the eigenmodes. Furthermore, the resulting eigenmodes can be optically analyzed in a first step. Therefore, the shape functions of an elastic body obtained during the MOR can be approximated with polynomials for the later ray tracing. Additionally, the kinematics of all surfaces, which are relevant for the optical simulation, have to be transferred from the mechanical to the optical model.

In contrast to the former method, the great benefit is, to investigate only the optical behavior of each mode in terms of their optical sensitivity and not to consider the full system for each time instant. Finally, the time integration results of the modal coordinates can be multiplied with the modal-optical sensitivities to obtain the time-related WFA and LOS results. As explained in Section 3.4.4, an exposure simulation can be also performed using Fourier optical methods and consider each time instant.

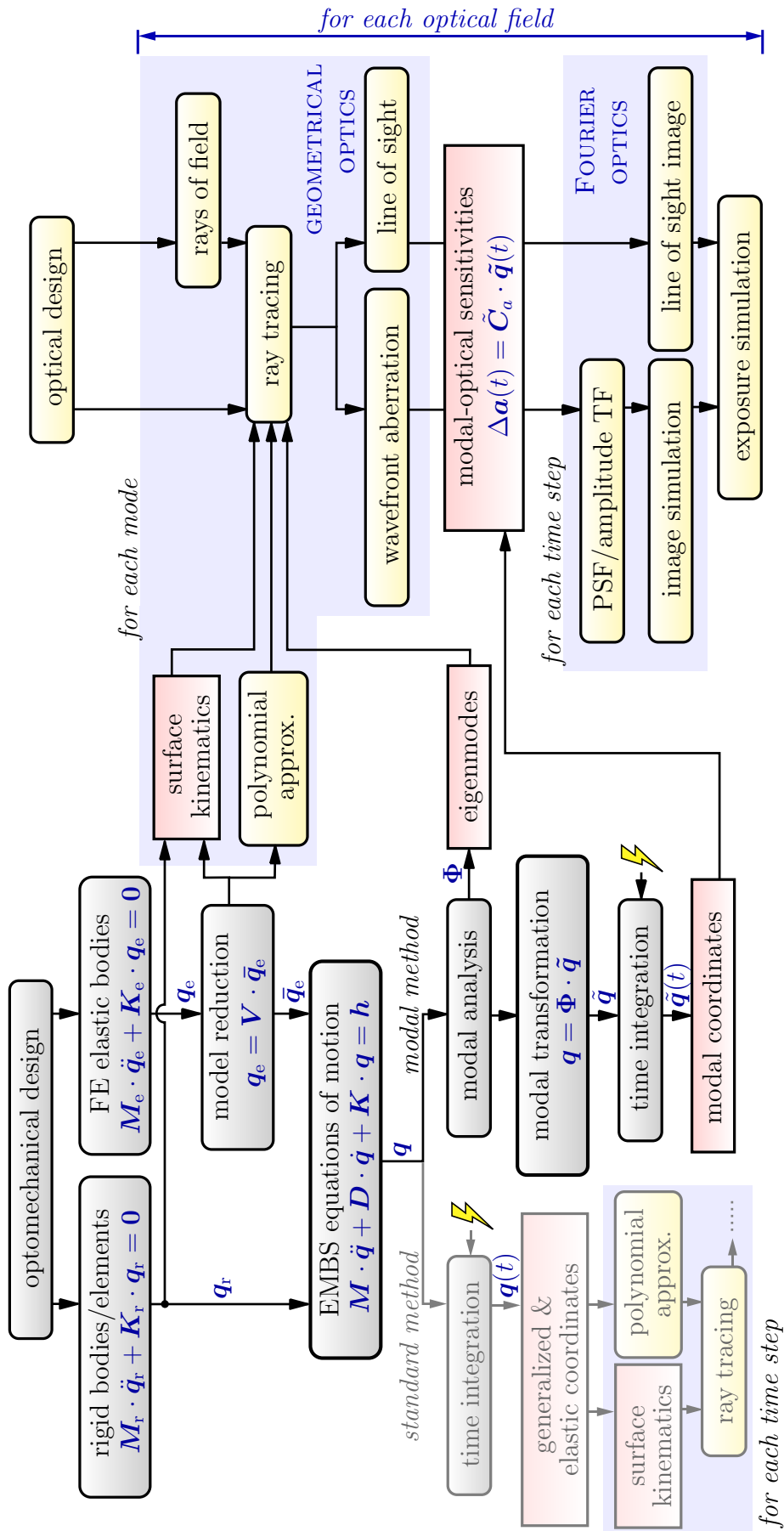


Figure 4.2: Workflow of the mechanical and optical modeling and simulation process.

4.2 Implementations for the Integrated Modeling

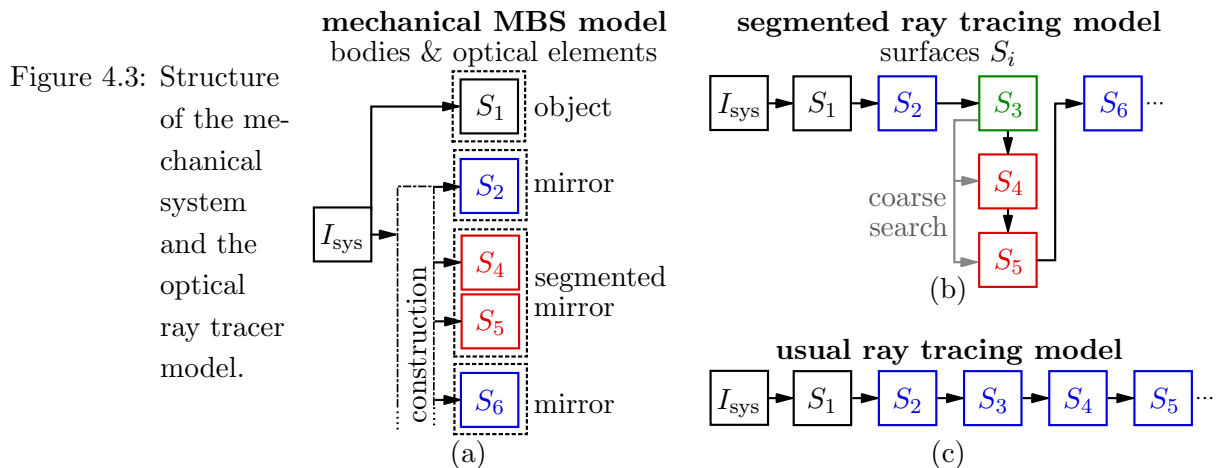
One of the most important challenges during a dynamical-optical simulation is the handling and preprocessing of the interface data which has to be transformed from the mechanical to the optical model. Thereby, the surface kinematics and the polynomial approximation are substantial tasks which are explained in the following. Furthermore, a non-sequential ray tracing is introduced for the simulation of systems with segmented mirrors. Finally, two different implementations for the wavefront analysis are proposed.

4.2.1 Kinematics of Optical Surfaces

The rigid body motion of the bodies within the mechanical model is represented by the rigid body generalized coordinates $\mathbf{q}_r(t)$, as explained in Figure 2.1(b). Due to visualization purposes, the related absolute kinematics with respect to the inertial frame of reference I_{sys} are usually computed during the mechanical simulation. However, the sequential ray tracing algorithm needs a relative position \mathbf{s}_i and orientation \mathbf{R}_i of the considered optical surface S_i with respect to the previous one S_{i-1} , see also Section 3.2.1. Thus, the kinematics of the bodies have to be translated for each time instant to the relative kinematics of the optical surfaces, i.e.

$$\mathbf{q}_r(t) \Rightarrow \mathbf{s}_i(t), \mathbf{R}_i(t). \quad (4.1)$$

The absolute body-wise description is very advantageous for the mechanical analysis of coupled systems, whereas the relative surface-wise description is necessary for an efficient ray tracing. For instance, both are shown for a segmented mirror system in the Figures 4.3(a) and (b). The first surface is always the object plane and the last one is the image plane. While a lens is characterized by two surfaces, a usual mirror is defined by only one. Furthermore, a segmented mirror element is described by multiple surfaces: One reference surface, for the coarse search during the ray tracing, and one surface for each



segment. Figure 4.3(c) indicates the usual ray tracing of a system with sequential optical surfaces.

In Figure 4.4, a typical system is visualized. It is described by the related optical surfaces and the absolute positions and orientations of the surfaces are expressed with $\hat{\mathbf{s}}_i$ and $\hat{\mathbf{R}}_i$. Thus, for the absolute kinematics it yields

$$\hat{\mathbf{s}}_i = \hat{\mathbf{s}}_{i-1} + \hat{\mathbf{R}}_{i-1} \cdot \mathbf{s}_i \quad \text{and} \quad \hat{\mathbf{R}}_i = \hat{\mathbf{R}}_{i-1} \cdot \mathbf{R}_i. \quad (4.2)$$

During the motion of the surfaces, one can further distinguish between the initial *reference configuration*, the imaginary configuration due to the change of the previous surface, and the *current configuration*. This is clarified in Figure 4.5. The relative position and orientation in the *reference configuration* are denoted with $\mathbf{s}_{0,i}$ and $\mathbf{R}_{0,i}$. Furthermore, the relative displacement $\Delta\mathbf{s}_i$ and the relative rotation $\Delta\mathbf{R}_i$ can be introduced with the relation

$$\mathbf{s}_i = \mathbf{s}_{0,i} + \Delta\mathbf{s}_i \quad \text{and} \quad \mathbf{R}_i = \mathbf{R}_{0,i} \cdot \Delta\mathbf{R}_i. \quad (4.3)$$

From the combination of the Equations (4.3) and (4.2) it follows

$$\Delta\mathbf{s}_i = \hat{\mathbf{R}}_{i-1}^\top \cdot (\hat{\mathbf{s}}_i - \hat{\mathbf{s}}_{i-1}) - \mathbf{s}_{0,i} \quad \text{and} \quad \Delta\mathbf{R}_i = \mathbf{R}_{0,i}^\top \cdot \hat{\mathbf{R}}_{i-1}^\top \cdot \hat{\mathbf{R}}_i. \quad (4.4)$$

After this computation, the relative displacement \mathbf{s}_i and relative rotation \mathbf{R}_i are known according to the Equations (4.3). Both quantities are required for the ray tracing algorithm, e.g., during the transformation of a ray into another reference frame, see also Equation (3.11).

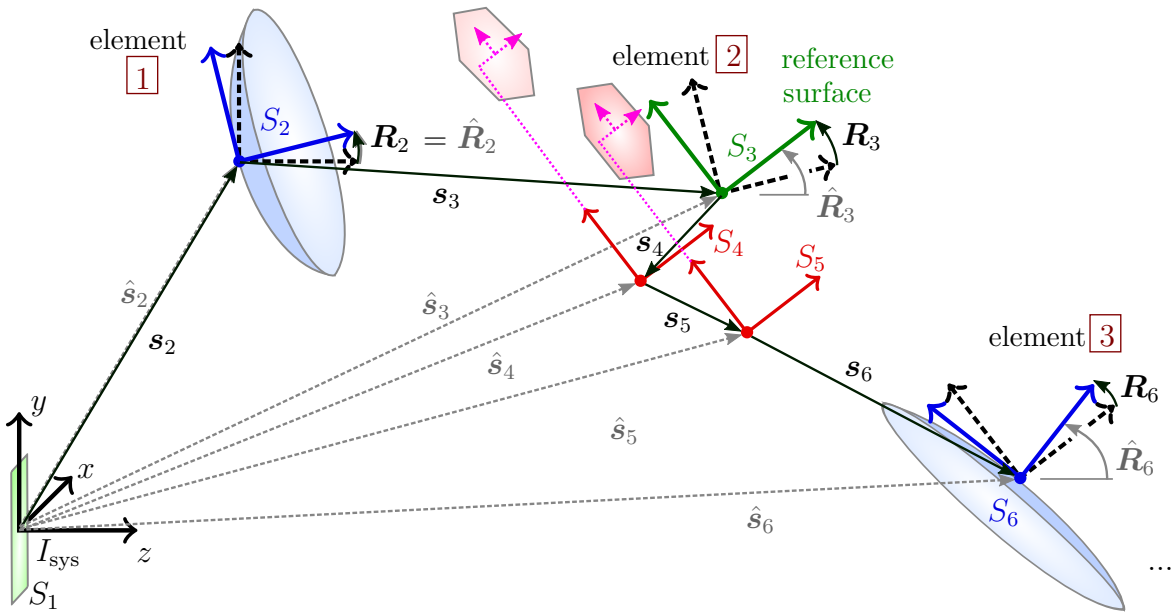
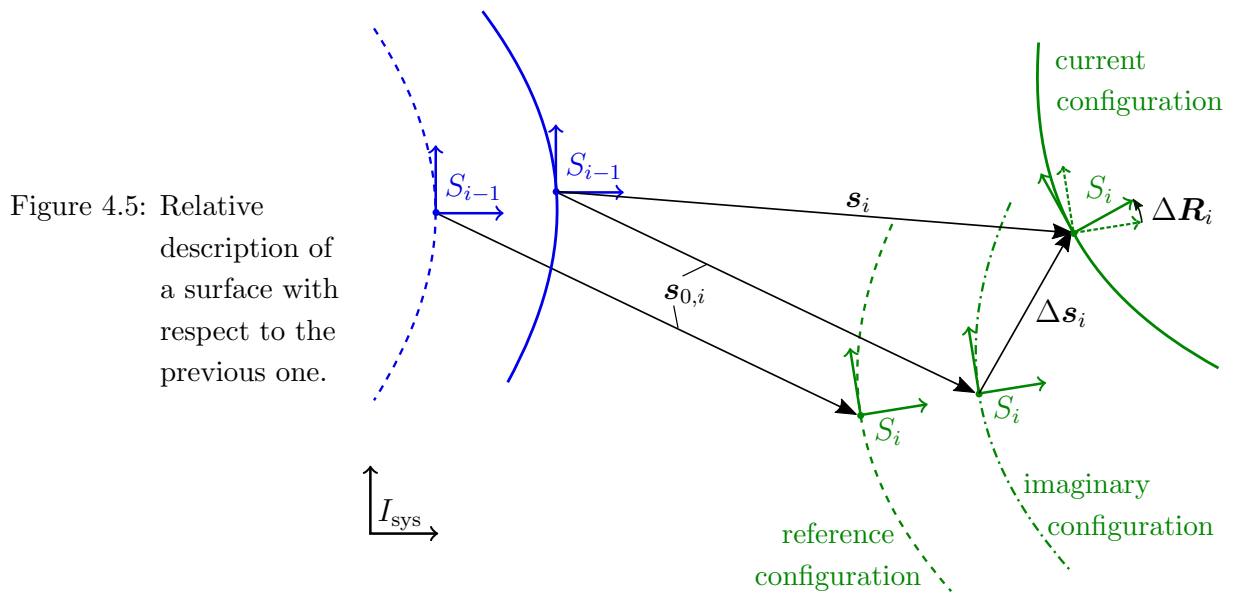
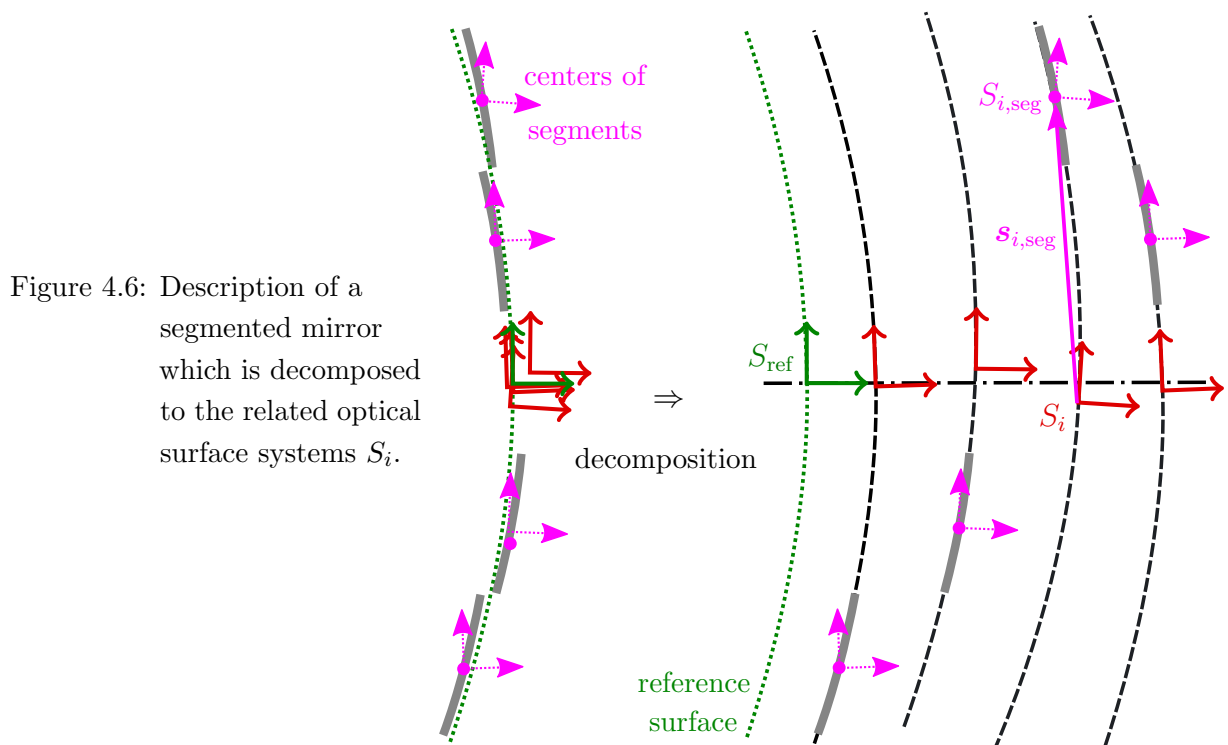


Figure 4.4: Relative and absolute quantities of the surface description.



In Figure 4.6, a mirror system consisting of rigid segments is sketched. Usually, the ideal shape of a segmented mirror can be continuously described with one reference surface S_{ref} . However, in order to take also individual misalignments of the segments into account, each segment is separately represented by an optical surface S_i . This surface is just a copy of S_{ref} but can have a different position or orientation in a considered *current configuration*. Thus, the segmented mirror can be decomposed into single surface systems, and their relative kinematics are equally calculated as for usual optical surfaces.



First, the kinematic behavior of the elastic body has to be considered in greater detail, as illustrated in Figure 4.8. According to Section 2.4, a deformable optical element can be described with a reduced elastic body. In the *reference configuration*, the related Buckens floating frame of reference K_{cog} is thereby located in the center of gravity of the body. Furthermore, the reference frame of the optical surface S_i is fixed to K_{cog} at the position $\mathbf{p}_{\text{mech2opt}}$. In the ideal case, the locations of the FE-nodes on the optical surface satisfy the continuous description $z_{\text{ref}}(x, y)$ which can consist of spherical or aspherical parts, see also Section 3.2.2.

If any mechanical excitation is assumed in the *current configuration*, the change of the elastic body is presented by the rigid body motion $\mathbf{q}_r(t)$ and the reduced elastic coordinates $\bar{\mathbf{q}}_e(t)$. In combination with the projection matrix \mathbf{V} , the latter approximately describe the node displacements $\mathbf{q}_e(t)$ in the x , y and z -direction which is caused by the body deformation. Next, the node positions are transformed to S_i by means of $\mathbf{p}_{\text{mech2opt}}$, and the node displacements $\mathbf{q}_e(t)$ are added. The resulting deformed shape can afterward be approximated with polynomials, as explained in the following.

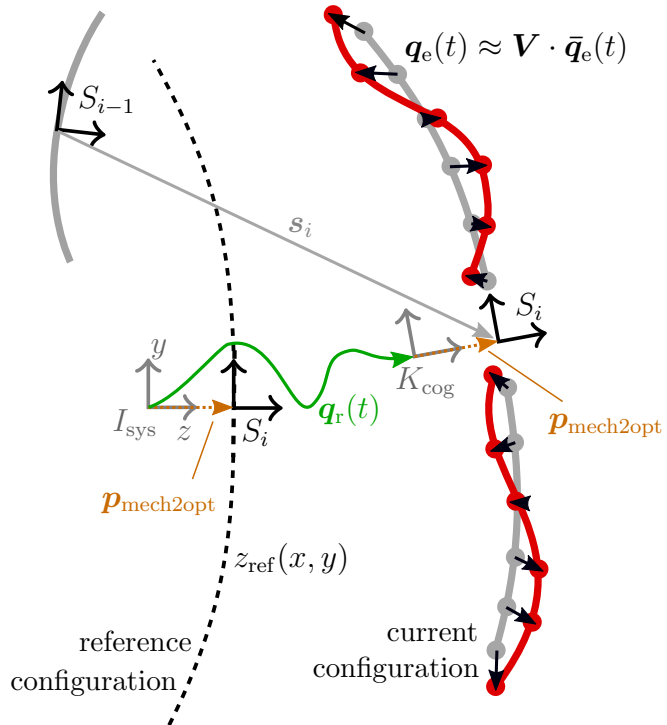


Figure 4.8: Kinematics of a deformed optical surface which is part of an elastic body.

The process of an annular surface approximation, from the FE nodes to the ray tracing, is schematically sketched in Figure 4.9. In particular, the deformation with respect to the z -direction can be identified with $z_{\text{deform},i} = z_i - z_{\text{ref}}(x_i, y_i)$, whereby the displaced positions of the nodes are named $\{x_i, y_i, z_i\}$. Next, the x_i and y_i coordinates are scaled to the unit circle by means of the outer radius R_z of the deformed mesh, which has to be stored for further evaluations. In case of an annular shape, there is also an inner

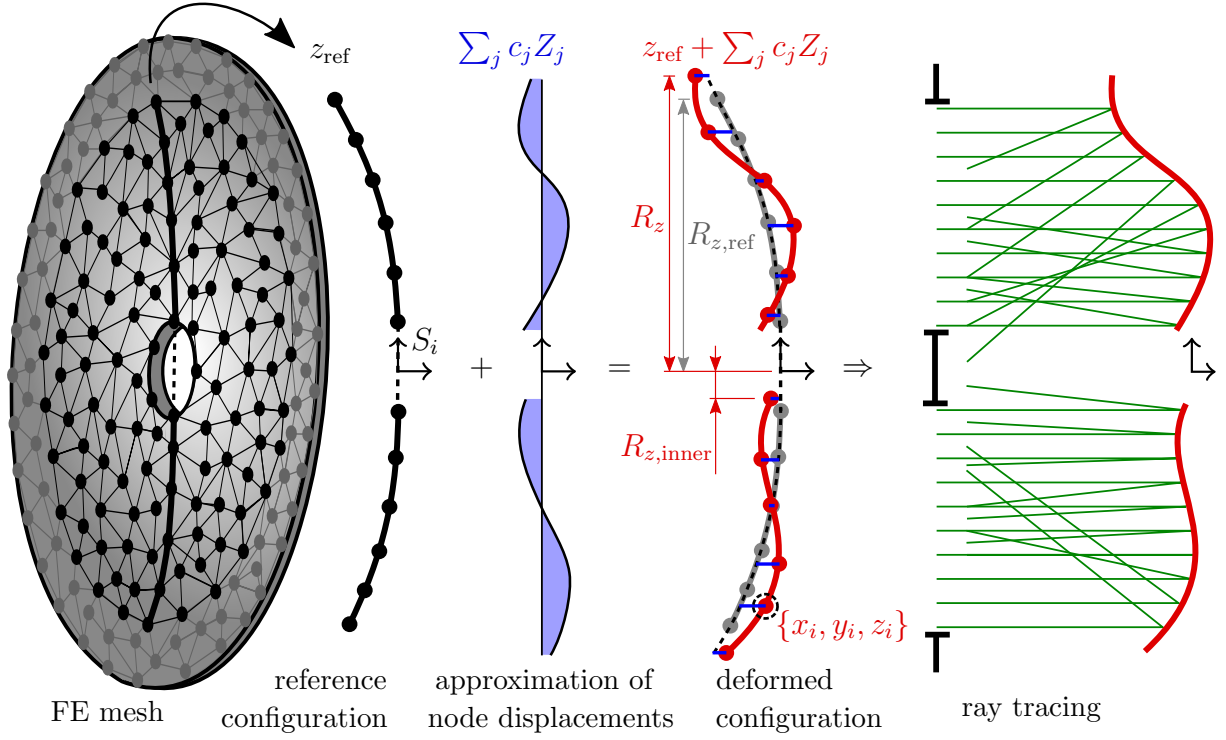


Figure 4.9: Schematic process of the polynomial approximation and preparation of a meshed surface section.

radius $R_{z,\text{inner}}$. Then, the approximation using superposed Zernike polynomials in the form

$$z_{\text{deform}}(x, y) = \sum_j c_j Z_j(x, y) \quad (4.8)$$

is required. The method of least squares can calculate the unknown coefficients of the polynomials c_j which can be read as

$$\underbrace{\begin{bmatrix} z_{\text{deform},1} \\ z_{\text{deform},2} \\ \vdots \\ z_{\text{deform},n_i} \end{bmatrix}}_{\mathbf{z}_{\text{deform}}} \approx \underbrace{\begin{bmatrix} Z_1(x_1, y_1) & Z_2(x_1, y_1) & \cdots & Z_{n_j}(x_1, y_1) \\ Z_1(x_2, y_2) & Z_2(x_2, y_2) & \cdots & Z_{n_j}(x_2, y_2) \\ \vdots & \vdots & Z_j(x_i, y_i) & \vdots \\ Z_1(x_{n_i}, y_{n_i}) & Z_2(x_{n_i}, y_{n_i}) & \cdots & Z_{n_j}(x_{n_i}, y_{n_i}) \end{bmatrix}}_{\mathbf{Z}} \cdot \underbrace{\begin{bmatrix} c_1 \\ c_2 \\ \vdots \\ c_{n_j} \end{bmatrix}}_{\mathbf{c}_z}. \quad (4.9)$$

As a result, the minimization problem with the Euclidean norm $\min_c \|\mathbf{Z} \cdot \mathbf{c}_z - \mathbf{z}_{\text{deform}}\|_2^2$ has to be solved. If the nodes are not isometrically distributed on the regarded surface mesh, they have to be weighted with respect to their surroundings by the matrix \mathbf{W} during the least square fit [FahrmeierKneipLang09]. For that, the problem can be transformed to the weighted Gaussian normal form

$$\mathbf{c}_z \approx (\mathbf{Z}^\top \cdot \mathbf{W} \cdot \mathbf{Z})^{-1} \cdot \mathbf{Z}^\top \cdot \mathbf{W} \cdot \mathbf{z}_{\text{deform}}, \quad (4.10)$$

which leads to a linear matrix multiplication. The resulting coefficients of the polynomials c_j qualify the amount of deviation in the z -direction with respect to the initial node positions.

As a consequence, the computational effort only depends on the number and order of used Zernike polynomials, which also determine the approximation error. Usually, it is suitable, to use the first few Zernike polynomials. For circular areas it is practical until to a single index number of about 231 and for annular areas, 105 is an advisable number. However, in some cases, this limit has to be adjusted in order to avoid a so-called overfitting [Wengert16]. An alternative solution could be to describe the deformation as compact as possible with the choice of an optimal set of Zernike polynomials [Schäfer15]. For that, the relative accuracy of an approximated surface given by the node coordinates $\{\mathbf{x}_k, \mathbf{y}_k, \mathbf{z}_k\}$ can be assessed with

$$\varepsilon_{\text{apprx}} = \frac{\text{rms}(\sum_j c_j Z_j(\mathbf{x}_k, \mathbf{y}_k) - \mathbf{z}_k)}{\text{rms}(\mathbf{z}_k)}. \quad (4.11)$$

The global reference surface of a segmented mirror is illustrated in Figure 4.10(a) which determines the number and positions of the segments during the modeling with the global inner radius $R_{z,\text{inner}}$ and the global outer radius R_z . In Figure 4.10(b) the approximation of an individual segment is shown in the *reference configuration* with the side length $R_{z,\text{ref}}$ and in the deformed configuration with the outer radius R_z . Thereby, the segment deformation is also approximated by circular Zernike polynomials with respect to the segment center reference frame $S_{i,\text{seg}}$.

The presented transformation method within this section is called *DeformOnlyTrafo*, since elastic coordinates are merely converted to the deformation described by Zernike polynomials. In contrast to this method, the deformed optical surface can also be

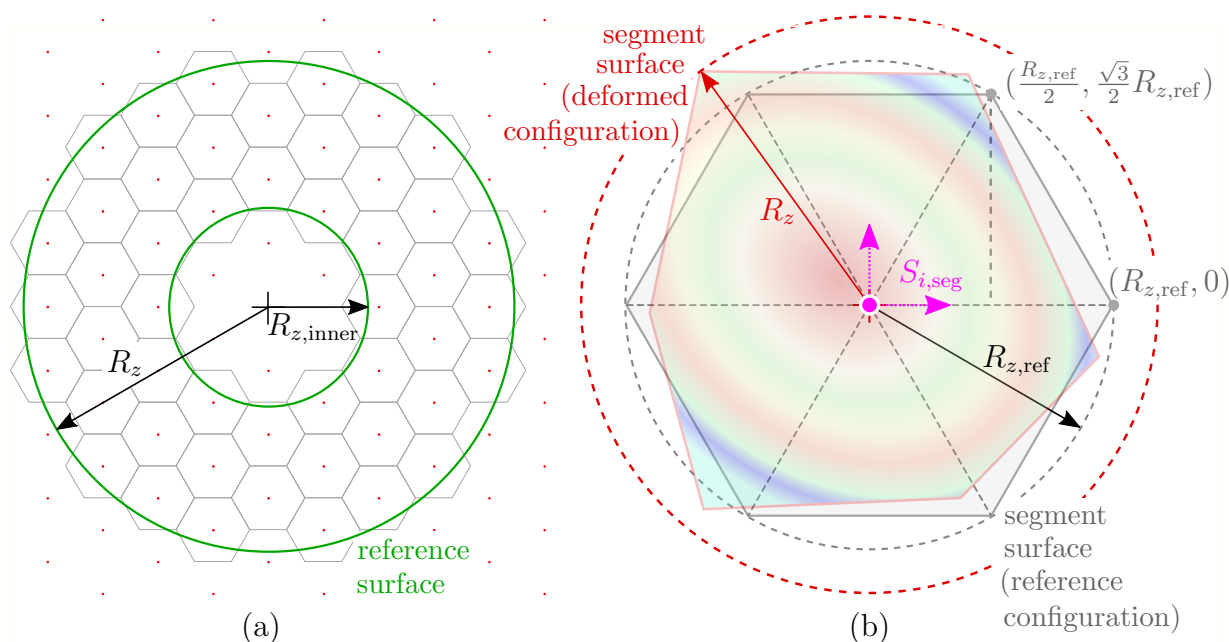


Figure 4.10: Surface definition and approximation at a segmented mirror and an individual segment.

approximated in a different and more sophisticated way, as stated in [Wengert16]. In a first step, it is thereby proposed to search for a numerical-optimal position for S_i and the orientation is determined with the help of an auxiliary plane. The further approximation by means of Zernike polynomials is quite similar to the approach above. However, the additional step of using the auxiliary plane does not significantly improve the numerical accuracy. Besides, a center node is thereby required which does not exist in the case of an annular mirror. Thus, the simplified *DeformOnlyTrafo* method is used for the following dynamical-optical simulations.

4.2.3 Non-sequential Ray Tracing for Segmented Mirrors

In order to simulate the ray optical behavior of a segmented mirror, the sequential ray tracing according to Section 3.2 has to be adjusted. On the one hand, the rays have to be assigned to the different segments which are usually next to each other. On the other hand, the computation should be as efficient as possible. Therefore, the algorithm contains a coarse search based on the reference surface in the undisturbed *reference configuration* and a subsequent fine search. The latter is used for the computation of the real reflection at the disturbed segments in the *current configuration*. This procedure is illustrated in Figure 4.11, where a specific segment is considered.

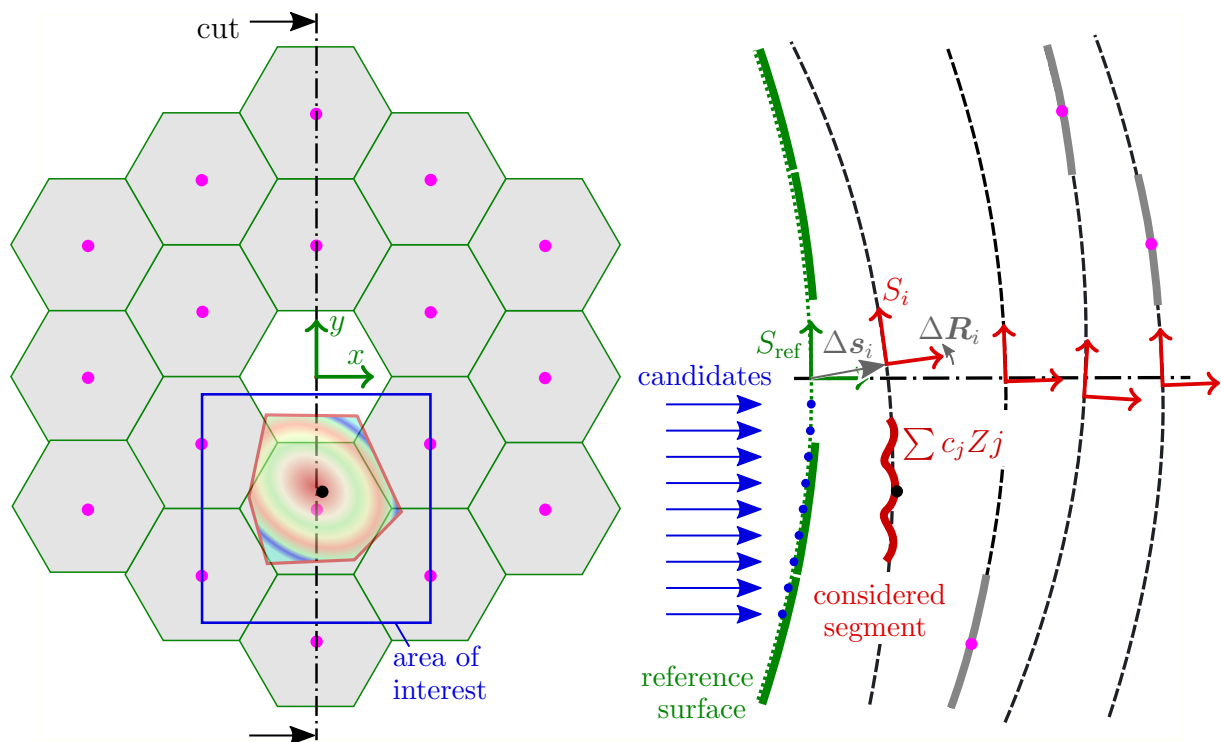


Figure 4.11: Ray tracing at a disturbed segmented mirror. In particular, the considered segment with the surface S_i is not only deformed, but also has a rigid body motion.

The detailed ray tracing steps for a segmented mirror can be formulated as follows:

1. Compute intersection points of all rays with the reference surface S_{ref} .
2. Loop through all segments with the following substeps:
 - (a) Select the ray candidates of the related intersection points within a quadratic area of interest in the neighborhood of the considered segment (coarse search).
 - (b) Transform *all* rays into the surface system S_i of the considered segment, whereby the rigid body translation $\Delta \mathbf{s}_i$ and rotation $\Delta \mathbf{R}_i$ is also taken into account.
 - (c) Compute the actual intersection points of the ray candidates with the moved and deformed surface which belongs to the considered segment (fine search).
 - (d) Obtain the corner points of the considered segment in the *current configuration* which could be distorted due to surface deformation.
 - (e) Select the actual intersection points within the distorted hexagon shape.
 - (f) Store the indices, coordinates, directions and normal vectors of the resulting rays which can be assigned to the considered segment.
3. Remove all rays which are not assigned to a segment.
4. Calculate the new directions of all remaining rays according to the reflection law using the incident ray directions and the normal vectors.

Since the final intersection points and new direction vectors of all outgoing rays are presented with respect to the last segmented surface, the usual sequential ray tracing can be continued.

4.2.4 Wavefront Analysis

This section explains the computation of the WFA through the results of the ray tracing with two different approaches, the *Optical-Path-Difference* method and the *Derivative* method. The first approach is simple, but it is necessary, to simulate the CR and to compute the OPLs of all rays. The second approach is only based on the ray directions and the related intersection points at the image plane so that the CR and the OPLs are not required.

Optical-Path-Difference Method

For this approach, the optical path difference (OPD) is calculated at the ExP, which means that the OPLs of all rays are compared with the OPL of the CR [Zemax11]. For example,

this is illustrated in Figure 4.12 and explained in the following steps. In order to simplify the notation, a single aberrated ray is considered only.

1. The related ray direction \mathbf{d}_{Im} , the intersection point \mathbf{r}_{Im} with the image plane, and the total OPL denoted with $s_{\text{opl,ObIm}}$ are obtained by ray tracing.
2. The CR of the regarded optical field is also traced to the image plane and the related position and direction determines the coordinate system C_{cr} . There, a Gaussian reference sphere is constructed, such that it intersects with the optical axis at the ExP position.
3. The intersection point \mathbf{r}_{Ref} of the aberrated ray with the reference sphere is computed and the distance from the image plane to the reference sphere results with $s_{\text{ImRef}} = |\mathbf{r}_{\text{Ref}} - \mathbf{r}_{\text{Im}}|$.
4. Next, the OPL of the aberrated ray from the object plane to the reference sphere follows with $s_{\text{opl,ObRef}} = s_{\text{opl,ObIm}} - s_{\text{ImRef}}$. In analogy, it can be also calculated for the CR with $s_{\text{opl,ObRef,cr}} = s_{\text{opl,ObIm,cr}} - s_{\text{ImRef,cr}}$.
5. The OPD results with $\Delta s_{\text{opl}} = s_{\text{opl,ObRef,cr}} - s_{\text{opl,ObRef}}$.

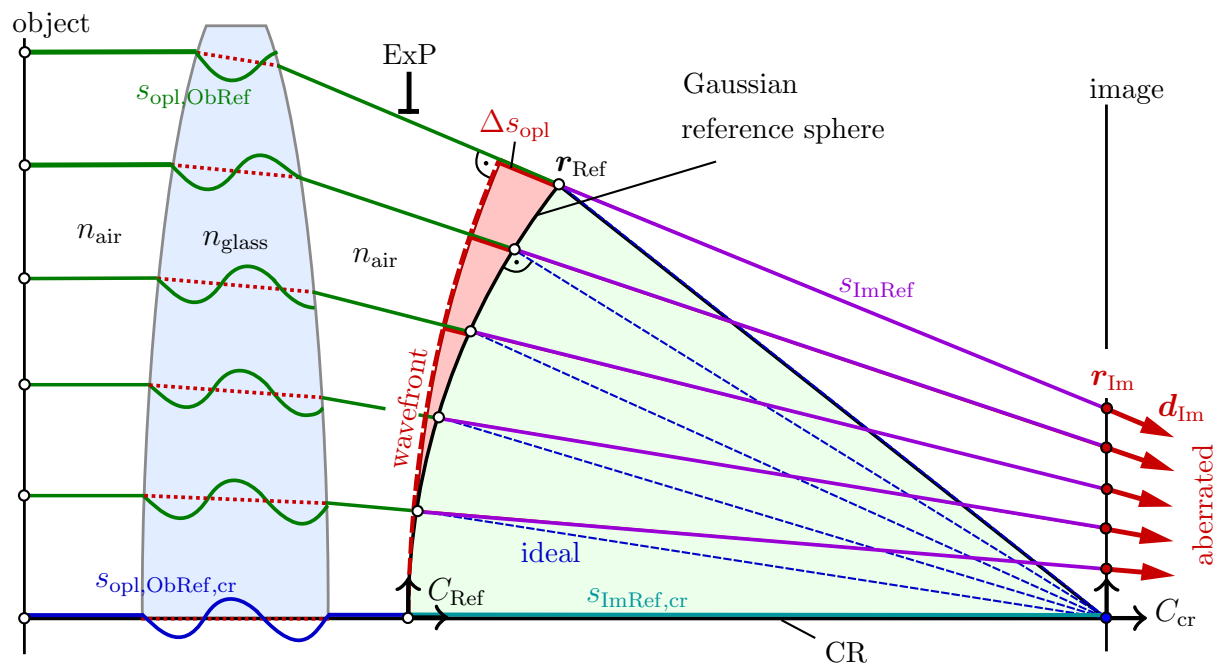


Figure 4.12: Computation of the OPD for a centered field which is not correctly focused on the image plane. Since the OPL within the glass lens is longer than the geometrical path, the optical paths are indicated by sinus-shaped lines.

Often the OPD will furthermore be referred to the corresponding wavelength in order to normalize it to the multiple of a wave. As a result, the specific OPD is defined as

$$\Delta s_{\text{opl,spec}} = \frac{\Delta s_{\text{opl}}}{\lambda}. \quad (4.12)$$

The computation of the OPD is usually repeated for at least 500 rays in the usual case and for 2000 rays in the segmented case. These rays should be uniformly distributed over the pupil. Finally, the simulated points of the WFA result with $\{r_{x,\text{Ref}}, r_{y,\text{Ref}}, \Delta s_{\text{opl,spec}}\}$. They can be further approximated with Zernike polynomials according to Section 3.3.4. This can also be formulated as $\Delta W(r_{x,\text{Ref}}, r_{y,\text{Ref}}) \Rightarrow c_j, Z_j$.

Calculating the WFA from Ray-Slopes

In the previous section it was shown, how the WFA can be identified by means of the OPL in comparison to the ideal wavefront W_{ideal} at the ExP.

Within this section, an alternative calculation method for the WFA is proposed which is based on the slopes of the rays. A wavefront is always perpendicular to the related ray slopes. Hence, the idea is to approximate the reciprocal value of the ray slopes with the first derivative of the Zernike polynomials using the least square fit, to reproduce the real wavefront W_{real} .

Furthermore, the same can be done for W_{ideal} and the corresponding difference is defined as the WFA, see also Equation (3.37). However, this method can also be optimized by considering the differences of the ray slopes, whereby the WFA directly results.

In the following, this method will be explained at a planar example and in consideration of the outer ray on the left-hand side of Figure 4.13, which shows a similar and rotated version of Figure 4.12.

Based on the ray tracing, the ray position \mathbf{r}_{Im} and the direction $\mathbf{d}_{\text{Im}} = [d_{\text{Im},x} \ d_{\text{Im},y} \ d_{\text{Im},z}]^T$ are known at the image plane.

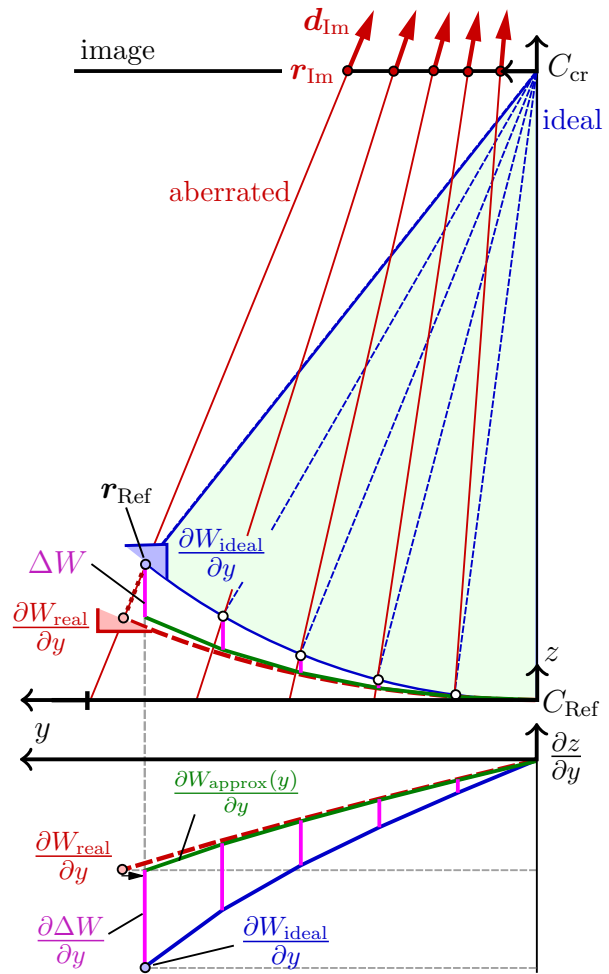


Figure 4.13: Computation of the WFA by means of the ray-slopes.

First, the intersection point \mathbf{r}_{Ref} of the aberrated ray with the reference sphere W_{ideal} is computed. Second, the slope of the ideal ray $\mathbf{d}_{\text{ideal}}$ can be obtained. Third, the real and ideal wavefront slope yields the relations

$$\frac{\partial W_{\text{real}}}{\partial y} = \frac{d_{\text{Im},y}}{d_{\text{Im},z}} \quad \text{and} \quad \frac{\partial W_{\text{ideal}}}{\partial y} = \frac{d_{\text{ideal},y}}{d_{\text{ideal},z}}. \quad (4.13)$$

Since the y -values of the real aberrated wavefront are unknown, it will be assumed, that both slopes have the similar related y -values. This is identical to a scaling of the distribution in the y -direction, i.e.

$$\frac{\partial W_{\text{real}}(y)}{\partial y} \approx \frac{\partial W_{\text{approx}}(y)}{\partial y}. \quad (4.14)$$

The difference of the known wavefront slopes can be read as

$$\Delta W_y = \frac{\partial \Delta W}{\partial y} = \frac{\partial W_{\text{real}}}{\partial y} - \frac{\partial W_{\text{ideal}}}{\partial y}, \quad (4.15)$$

which describes the WFA slope along the y -axis. The same formulation can be derived for the x -direction and it can be formulated with

$$\Delta W_x = \frac{\partial \Delta W}{\partial x} = \frac{\partial W_{\text{real}}}{\partial x} - \frac{\partial W_{\text{ideal}}}{\partial x}. \quad (4.16)$$

Afterwards, the derivative of the WFA can be represented in the polar coordinates

$$x = \rho \cos \theta \quad \text{and} \quad y = \rho \sin \theta, \quad (4.17)$$

whereby it results due to the chain rule

$$\Delta W_\rho = \frac{\partial \Delta W}{\partial \rho} = \Delta W_x \underbrace{\cos \theta}_{\frac{\partial x}{\partial \rho}} + \Delta W_y \underbrace{\sin \theta}_{\frac{\partial y}{\partial \rho}}, \quad (4.18)$$

$$\Delta W_\theta = \frac{\partial \Delta W}{\partial \theta} = \Delta W_x \underbrace{(-\rho \sin \theta)}_{\frac{\partial x}{\partial \theta}} + \Delta W_y \underbrace{\rho \cos \theta}_{\frac{\partial y}{\partial \theta}}. \quad (4.19)$$

Finally, the least square fit can be used again to approximate the derivative of the WFA with the polar derivatives of the Zernike polynomials $Z_\rho(\rho, \theta) = \frac{\partial Z(\rho, \theta)}{\partial \rho}$ and $Z_\theta(\rho, \theta) = \frac{\partial Z(\rho, \theta)}{\partial \theta}$. Thereby, the coefficient of the first constant Zernike polynomial is dropped. However, this piston aberration is not important for the characterization of the WFA, anyhow. If the number of simulated rays is determined with n_i and the maximal index of Zernike

polynomials is n_j , it follows

$$\begin{bmatrix} \Delta W_\rho(\rho_1, \theta_1) \\ \Delta W_\rho(\rho_2, \theta_2) \\ \vdots \\ \Delta W_\rho(\rho_{n_i}, \theta_{n_i}) \\ \Delta W_\theta(\rho_1, \theta_1) \\ \Delta W_\theta(\rho_2, \theta_2) \\ \vdots \\ \Delta W_\theta(\rho_{n_i}, \theta_{n_i}) \end{bmatrix} \approx \begin{bmatrix} Z_{\rho,2}(\rho_1, \theta_1) & Z_{\rho,3}(\rho_1, \theta_1) & \cdots & Z_{\rho,n_j}(\rho_1, \theta_1) \\ Z_{\rho,2}(\rho_2, \theta_2) & Z_{\rho,3}(\rho_2, \theta_2) & \cdots & Z_{\rho,n_j}(\rho_2, \theta_2) \\ \vdots & \vdots & & \vdots \\ Z_{\rho,2}(\rho_{n_i}, \theta_{n_i}) & Z_{\rho,3}(\rho_{n_i}, \theta_{n_i}) & \cdots & Z_{\rho,n_j}(\rho_{n_i}, \theta_{n_i}) \\ Z_{\theta,2}(\rho_1, \theta_1) & Z_{\theta,3}(\rho_1, \theta_1) & \cdots & Z_{\theta,n_j}(\rho_1, \theta_1) \\ Z_{\theta,2}(\rho_2, \theta_2) & Z_{\theta,3}(\rho_2, \theta_2) & \cdots & Z_{\theta,n_j}(\rho_2, \theta_2) \\ \vdots & \vdots & & \vdots \\ Z_{\theta,2}(\rho_{n_i}, \theta_{n_i}) & Z_{\theta,3}(\rho_{n_i}, \theta_{n_i}) & \cdots & Z_{\theta,n_j}(\rho_{n_i}, \theta_{n_i}) \end{bmatrix} \cdot \begin{bmatrix} c_2 \\ c_3 \\ \vdots \\ c_{n_j} \end{bmatrix}. \quad (4.20)$$

In analogy to Equation (4.10), the coefficients can be computed by the Gaussian normal form.

In the following, the procedure and analysis of a typical dynamical-optical simulation are presented by means of an elastic mirror example. First, the mechanical modeling is demonstrated and afterward, the system is investigated in the frequency domain and in the time domain.

4.3 Mechanical Simulations

The introduced methods are applied to a parabolic circular and annular mirror which should serve as academic examples demonstrating the general procedures and analyses. The regarded mirrors have a diameter of 1 m, a thickness of 20 mm and the material properties of aluminum. Besides, the annular mirror has an inner diameter of 0.4 m. In Figure 4.16(a), the FE bodies of the mechanical models are illustrated, which are described with respect to the reference frames in their center of mass. Furthermore, three interface nodes are selected on these bodies and serve as inputs and outputs, since it is assumed that struts mount this mirrors at that locations. This model is also used in [Schäfer15, Bechler17].

In order to assess the accuracy of the resulting models, the mechanical transfer functions at the interface nodes are observed, which can be regarded as the inputs and outputs of the dynamical system. For both FE models, the Frobenius norm of the transfer matrices for the interface nodes are plotted in Figure 4.14. The first 108 eigenfrequencies are listed in Figure 4.15. As expected, the annular mirror behaves not as stiff as the circular mirror, since the first few eigenfrequencies of the circular mirror are slightly higher than of the annular mirror. Nevertheless, the frequencies are very similar. The first and second eigenmode shapes (i.e., free interface normal modes) of the free-floating mirrors are also very similar and are depicted in Figures 4.16(b) and 4.16(c). They give an idea of the dominating shapes during a vibration.

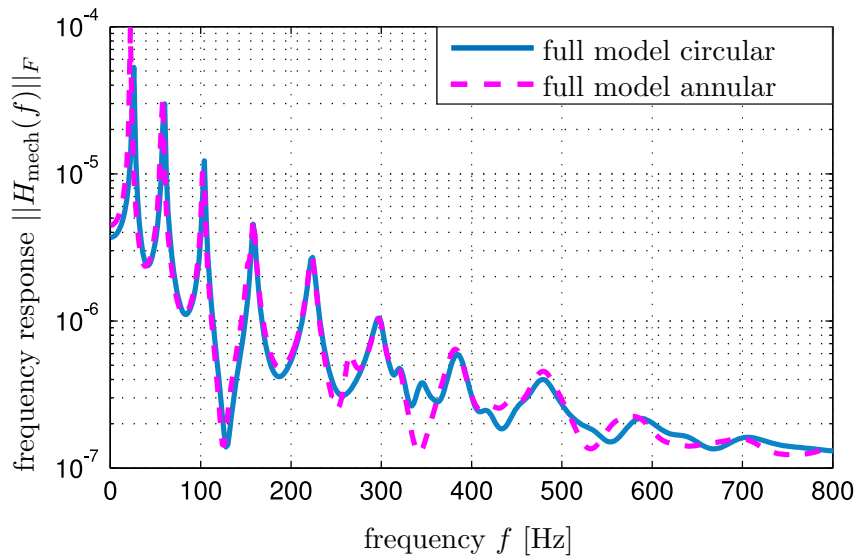


Figure 4.14: Comparison of the full FE model of the annular and circular mirrors, with respect to the interface nodes by means of the Frobenius norm of the transfer matrices.

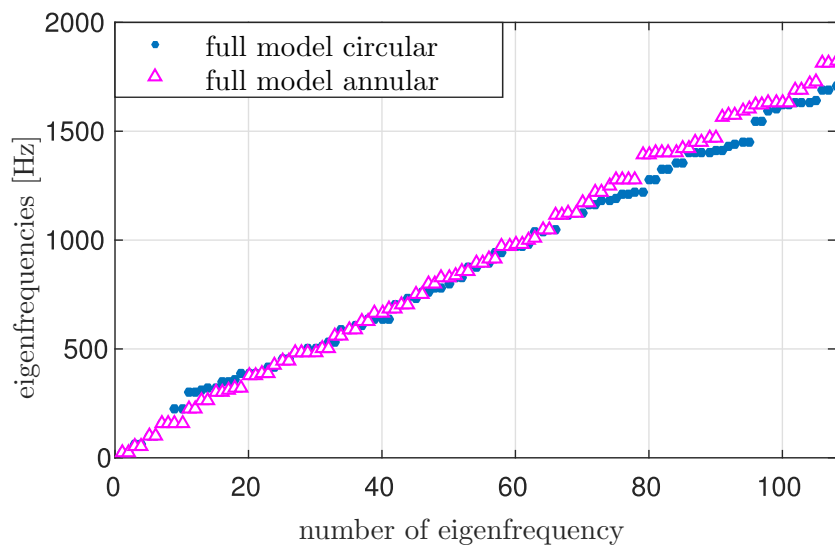


Figure 4.15: Eigenfrequencies of the full FE model of the annular and circular mirrors.

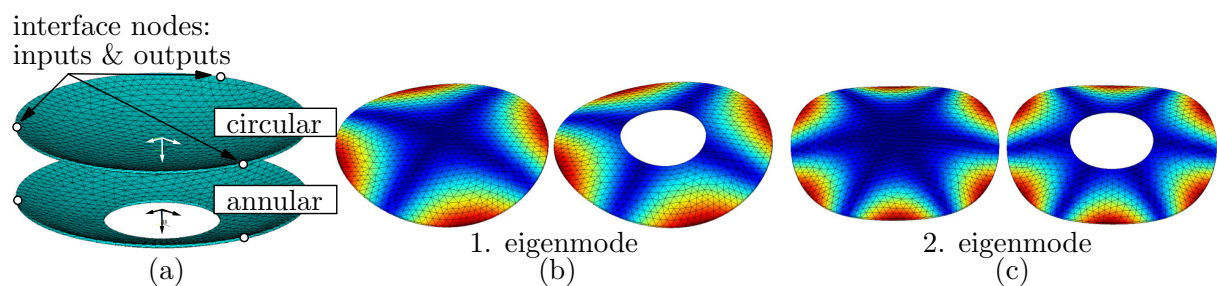


Figure 4.16: The first and second eigenmode shapes of the free-floating annular and circular mirror model.

Choice of the MOR Method

In particular, the accuracies of the MOR methods according to Section 2.3 are investigated in the following. For the MOR, mainly three different methods are compared using MatMorembs. At first, the *Craig-Bampton* MOR is applied with the orders of 36, 72 and 108 modes. Due to the three inputs in all three translational directions, this number contains nine static interface constraint modes, and all the rest are fixed interface normal modes. Next, the MOR method based on *Krylov* subspaces at one, two and three moment-matching points of second order is used, which also leads to 36, 72 and 108 DOF [Lehner07]. Finally, the *Balanced Truncation* MOR method is applied with a reduction order of 36 and for the frequency range of 0-400Hz.

4.3.1 Frequency Domain

At first, the circular mirror model is investigated in the frequency domain. The resulting Frobenius norm of the transfer matrices is depicted in Figure 4.17. For the Krylov method, the frequencies of the moment-matching points are given in the brackets of the legend labels. According to the frequency responses, all of the methods represent the system behavior satisfyingly within the range of 0-250Hz. In the plot of the relative error in Figure 4.18, the deviation of the Krylov method with a reduction order of 36 at the single second-order moment-matching point of 150Hz is remarkably small. As expected, this so-called *krylov36* model behaves in this region close to the system response of the full model. However, already at frequencies about 300Hz and higher, the error is significantly increased. With the usage of the matching points of second order at 200Hz, 450Hz and 700Hz, the number of DOF results in 108, and the relative reduction error is minimal in the whole range. In comparison, the Craig-Bampton method yields higher deviations, even if the order of reduction is increased to the number of 108.

However, the performance of the sparse reduced order models worsens sharply at higher frequencies. In particular, the models *krylov36* and *craigb36* are inaccurate for frequencies above around 400 Hz, which is clearly noticeable in the frequency response in Figure 4.17. In contrast, the models *craigb108* and *krylov108* are quite accurate until 1200Hz. Thus, the latter model serves as a reference during the following assessment of the EMBS simulation results, since the related error is negligibly small.

The resulting mode shapes of the different reduced models can be compared with the eigenmodes of the full model by means of the modal assurance criterion (MAC) [TrebuñaEtAl12]. The MAC is an indicator of correlation between vectors and can be visualized in a matrix. According to that, the big dark squares in Figure 4.19 represent a close similarity between a mode shape before and after the reduction. In contrast, a smaller and lighter square indicates mixed relations. The two different reduced models with 36 DOF are compared

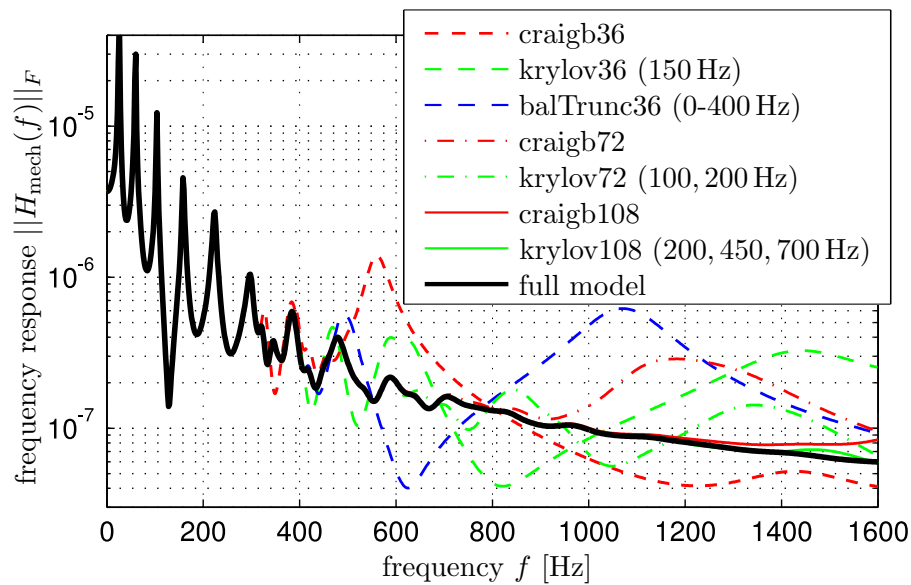


Figure 4.17: Comparison of the MOR methods with respect to the interface nodes by means of the Frobenius norm of the transfer matrices, in a wide frequency range, for the circular mirror.

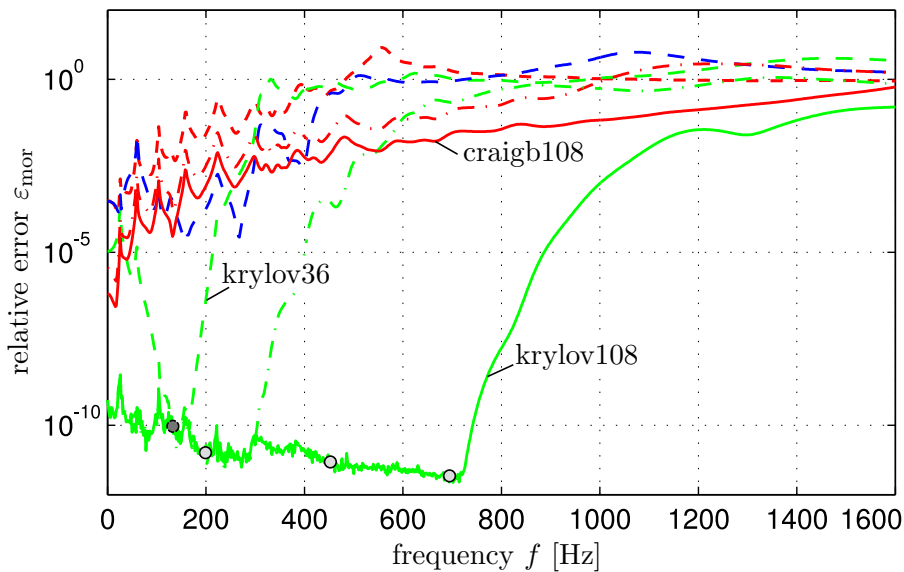


Figure 4.18: Comparison of the MOR methods with respect to the interface nodes by means of the Frobenius norm of the relative errors, in a wide frequency range, for the circular mirror.

to the full model. It is obvious, that on the one hand, the first 25 mode shapes of the model *craigb36* are mostly consistent with the full model since the squares are dominant on the diagonal region of the matrix. On the other hand, the mode shapes of the *krylov36* model in Figure 4.19(b) strongly differ from the initial eigenmodes for the numbers higher than 15. Therefore, it is expected, that the further optical mode shape analysis of the different reduced models delivers similar results for only the first few modes.

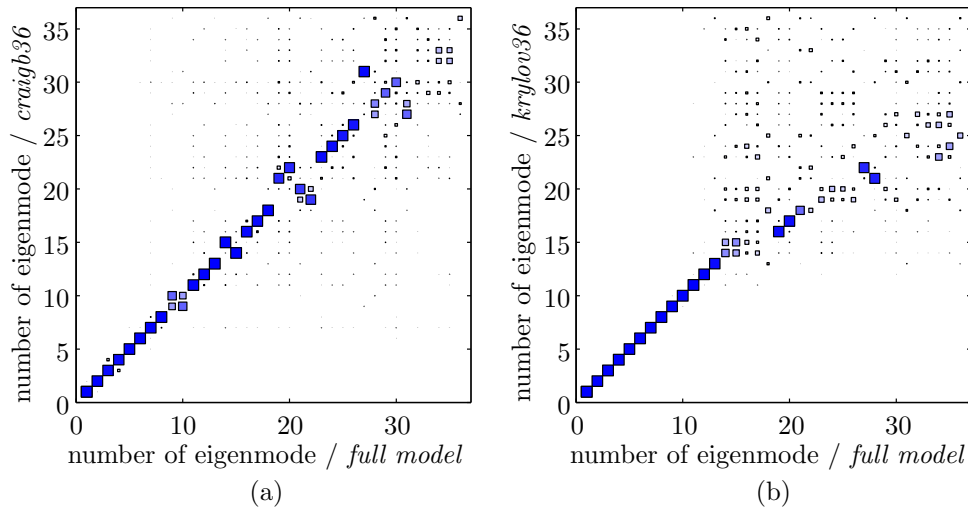


Figure 4.19: Visualization of the matrices with the MAC values of the different MOR methods.

The choice of the moment-matching frequencies during the Krylov reduction method strongly influences the accuracy of the model. This circumstance is shown in the error plot of Figure 4.20, where the three moment-matching points are varied. On the one hand, the error in the quasistatic range should be minimal, and on the other hand, the behavior for higher frequencies should also be approximated reasonably. In case of the current circular mirror example, the choice of 200 Hz, 450 Hz and 700 Hz represents a good compromise. At first sight, the choice of 100 Hz, 200 Hz and 400 Hz also seems to be adequate, just for the consideration of these results in the frequency domain.

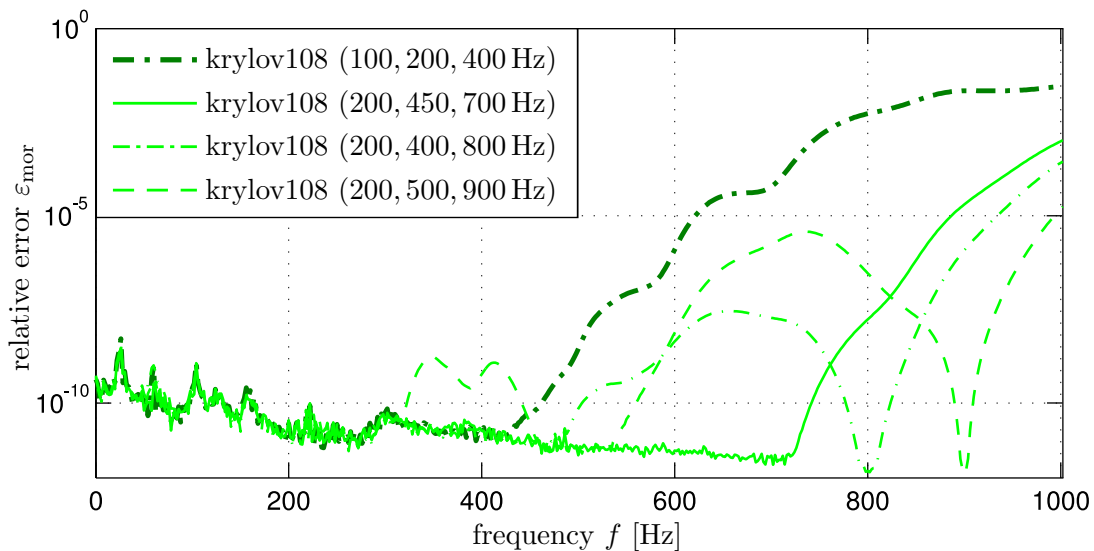


Figure 4.20: Comparison of the choice of matching frequencies for the Krylov reduction method by means of the relative errors of the frequency response.

According to Figure 4.14, the full FE models of the annular and circular mirror behave very similarly, and the reduced models also show similar results. As a consequence, instead

of presenting results of an analogous frequency domain response of the annular mirror, the accuracy of circular models in the time domain is investigated. With this, the quantitative impacts of the MOR methods during a time simulation is identified.

4.3.2 Time Domain

For the transient EMBS simulation, the Matlab program *Neweul-M²* is used which derives the equations of motion symbolically. The three interfaces are spatially fixed to each other and are excited abruptly in the z -direction with a sinusoidal constrained motion of $10\ \mu\text{m}$ amplitude and with a frequency of 100 Hz. For the fixation, nine constraint equations are formulated. Thus, one has to declare the same number of dependent coordinates in order to satisfy the constraints during the EMBS simulation [SchwertassekWallrapp99]. Here, the six rigid body coordinates are chosen in combination with three elastic coordinates of high-frequency modes.

Furthermore, the model accuracies at an excitation frequency of 300 Hz will be investigated. In order to perform the dynamical-optical simulation, the *modal method* according to the lower left part of the flowchart in Figure 4.2 is used.

Due to the projection of the mechanical system equations within the application of an MOR, the system properties are changed with respect to the eigenfrequencies. Figure 4.21(a) lists the pseudo-eigenfrequencies for the investigated models *craigb36*, *krylov36*, *craigb72*, *krylov72*, *craigb108* and *krylov108*, calculated by solving the eigenvalue problem after the reduction again. It is conspicuous, that depending on the MOR method, the system has increased pseudo-eigenfrequencies, especially for the models based on the Krylov method. The model *krylov108* with the choice of the frequency-matching points at 100 Hz, 200 Hz and 400 Hz stands out with its highest frequency of around 60 kHz. This frequency is non-physical, and the related model cannot be used for time integrations since the high frequency significantly decreases the sampling time and hence increases the computation time. Therefore, the moment-matching points have to be well chosen by assessing both, the reduction error according to Figure 4.20 and the highest resulting pseudo-eigenfrequency of the reduced model given in Figure 4.21(a).

In the following, the results of the EMBS simulation in the time domain are assessed. Therefore, the resulting z -motion of a representative test-node is illustrated in Figure 4.21(b). The related discrepancies $z_{\text{motion}} - z_{\text{ref}}$ of the MOR methods are shown in Figure 4.22(a) and the relative errors $|z_{\text{motion}} - z_{\text{ref}}| / \max|z_{\text{ref}}|$ are illustrated in Figure 4.22(b), whereby in both cases the results of the model *krylov108* are used as a reference. Despite the fact, that the model *krylov36* has a promising performance in the low-frequency domain, the *craigb36* results with smaller discrepancies. So it is obvious, that also the model deviations occurring above 300 Hz influences the accuracy for an excitation of 100 Hz. Especially for the later optical simulation, even small discrepancies can result in remarkable aberrations. In

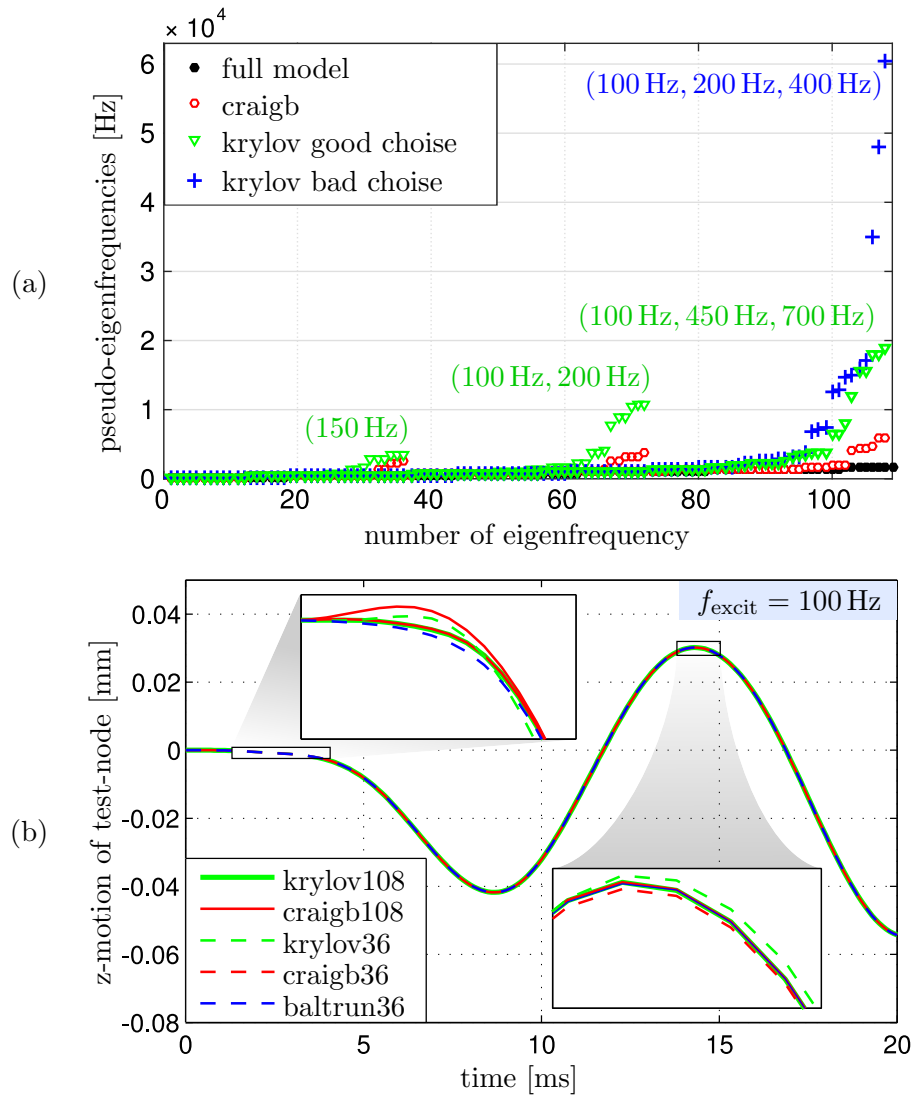


Figure 4.21: Pseudo-eigenfrequencies (a) and motion of a test-node in (b) for the different reduced models.

Figure 4.22(b), a line is drawn at a relative error of 1‰. It clarifies that all of the models represent the behaviors very accurately for the applied sinusoidal excitation at 100 Hz.

In order to investigate the limits of the MOR methods, the excitation frequency of 300 Hz is chosen and simulated. Thereby it is expected, that the deviations for the strongly reduced models are significantly increased since this behavior is already indicated in the frequency response according to Figure 4.17. The results of the test-node motion are illustrated in Figure 4.23. It is noticeable that in particular, the *krylov36* model leads to high deviations up to 14%. As a consequence, the expectation is confirmed, that even small deviations in the frequency domain result in remarkable differences in the time domain.

The location of the analyzed test-node is shown in Figure 4.24. Moreover, it visualizes the snapshot result at the time instant $t = 15$ ms in an exaggerated manner with the

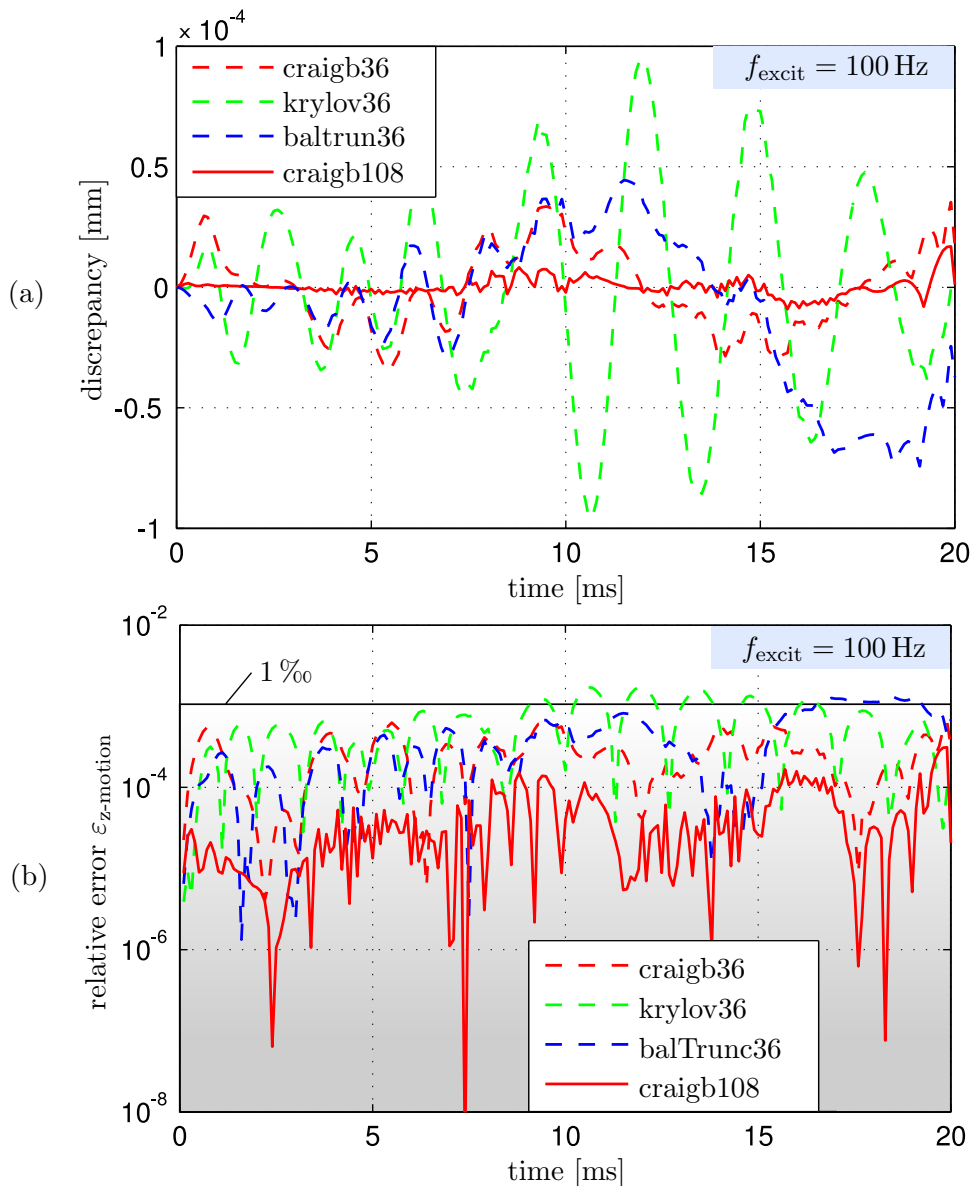


Figure 4.22: Discrepancy in (a) and relative error in (b) of the motion of a test-node, for the different reduced models.

scale factor of 1000. On the left side, the whole mirror body with colored deformations is depicted. For the optical simulation, the optical surface is extracted and approximated with polynomials according to Section 4.2.2 in order to allow the ray tracing optical analysis illustrated on the right side.

Figure 4.25 refers to videos which visualize further results of a dynamical-optical simulation. For that, the *krylov108* model is excited in the directions x , y and z , whereby the corresponding results are scaled.

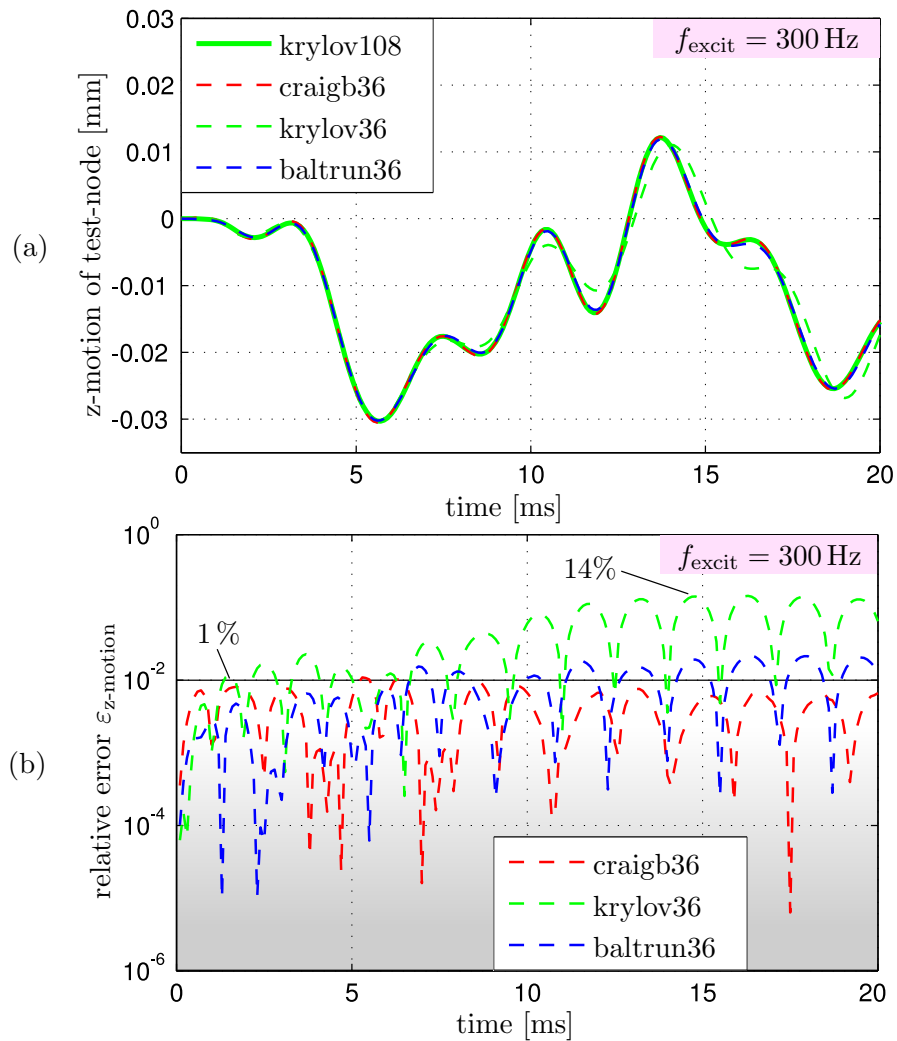


Figure 4.23: Motion and the related relative error of a test-node, for the different reduced models.

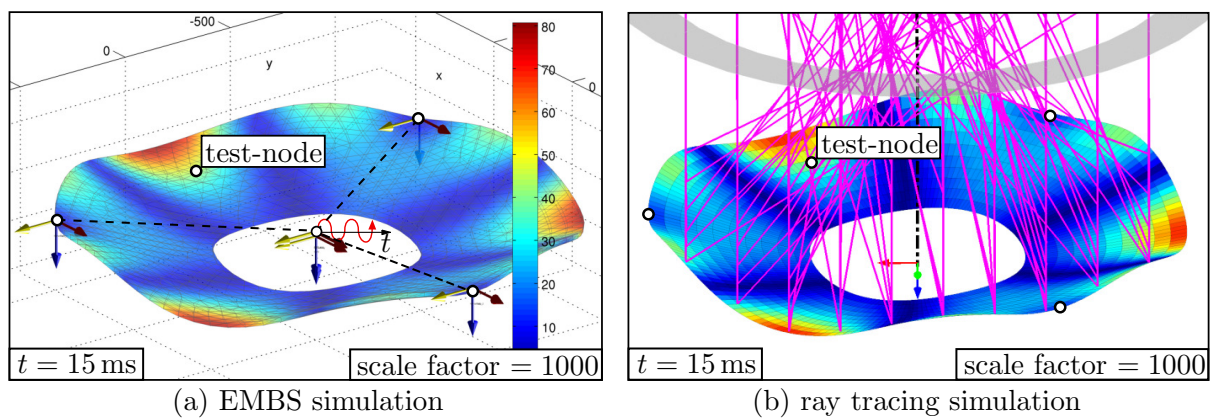


Figure 4.24: Visualization of the deformed mirror during the mechanical and the optical simulation.

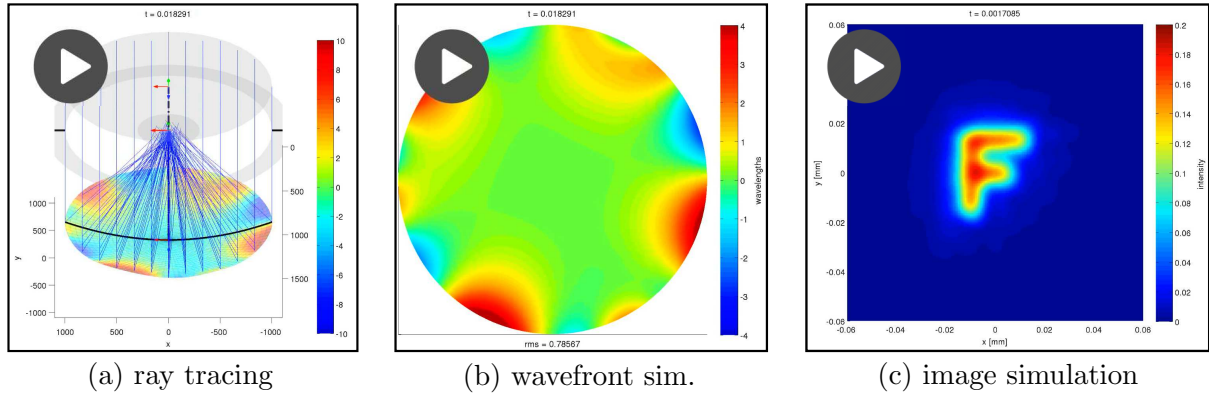


Figure 4.25: Videos of a dynamical-optical simulation:

http://www.itm.uni-stuttgart.de/research/optics_dynamics

4.4 Linear Dynamical-optical Analysis

Since the motions due to disturbances in dynamical-optical systems are usually very small, the system of equations can be linearized at an regarded operation state. This not only reduces computational cost during the simulation, but also simplifies the related analysis. In particular, the kinematic-optical sensitivities can be computed, which are needed, e.g., for the mechanical-optical transfer functions. In the following, the corresponding fundamentals and analyses are demonstrated for the elastic mirror example.

4.4.1 Kinematic-optical Sensitivities

According to Section 3.3.3, an optical system can be quantitatively assessed with the LOS and WFA. If the LOS position on the image plane is denoted with $[\Delta x_{\text{los}} \Delta y_{\text{los}}]^\top$ and the WFA is expanded in Zernike polynomials with the coefficients c_j , a vector of optical aberrations \mathbf{a} containing these entries can be introduced. Usually, the static optical system has even in the *reference configuration* an optical aberration called \mathbf{a}_0 . In the case of small disturbances, the relative optical aberration can be evaluated with $\Delta \mathbf{a} = \mathbf{a} - \mathbf{a}_0$. For a single elastic body, the relationship between the kinematic DOF given by the generalized coordinates \mathbf{q} and the related relative aberration $\Delta \mathbf{a}$ can be expressed by the kinematic-optical sensitivities. They can be collected in the matrix \mathbf{C}_a which corresponds to the relation

$$\Delta \mathbf{a} = \underbrace{[\Delta x_{\text{los}} \quad \Delta y_{\text{los}}]}_{\Delta \mathbf{a}_{\text{los}}} \quad \underbrace{[c_4 \quad c_5 \quad \dots \quad c_j \quad \dots \quad c_k]}_{\Delta \mathbf{a}_{\text{wfa}}}^\top = \mathbf{C}_a \cdot \mathbf{q}. \quad (4.21)$$

In the case of a pure elastic deformation it results

$$\Delta \mathbf{a} = \mathbf{C}_{a,e} \cdot \mathbf{q}_e \approx \underbrace{\mathbf{C}_{a,e} \cdot \mathbf{V}}_{\bar{\mathbf{C}}_{a,e}} \cdot \bar{\mathbf{q}}_e. \quad (4.22)$$

The so-called matrix of modal-optical sensitivities $\bar{\mathbf{C}}_{a,e}$ is derived in combination with Equation (2.7). The columns of $\bar{\mathbf{C}}_{a,e}$ can be obtained through ray tracing analyses during a single mode shape deformation. However, for elastic bodies it is recommended to scale the mode shapes at first by means of their values $\text{rms}(\mathbf{v}_{\text{sum}})$, as explained in Figure 2.1(c). In the following, the strategy of obtaining the matrix of kinematic-optical sensitivities is exemplified for a rigid optical element described by $\mathbf{q}_r = [q_x \ q_y \ q_z \ q_\alpha \ q_\beta \ q_\gamma]^\top$, whereby the sensitivity in z -direction is considered:

1. Determine a small motion $h \ll 1$ (e.g. $h \approx 10^{-6}$, see also [Trautwein16]) for a single DOF. For the z -direction, the generalized coordinates result in $\mathbf{q}_{r,z} = [0 \ 0 \ h \ 0 \ 0 \ 0]^\top$.
2. Compute the motion-caused optical aberration $\Delta \mathbf{a}_z$ by means of ray tracing.
3. Collect the reverse-scaled values in the column which corresponds to the regarded DOF. This yields $\mathbf{C}_{a,r} = \frac{1}{h} [\dots \ \Delta \mathbf{a}_z \ \dots]$.
4. Repeat the procedure for the remaining columns.

The idea of using kinematic-optical sensitivities is also visualized in Figure 4.26, where the WFA according to some example eigenmodes are sketched. In comparison to Example 1, the superposition of this optical mode shapes can represent the current aberration state.

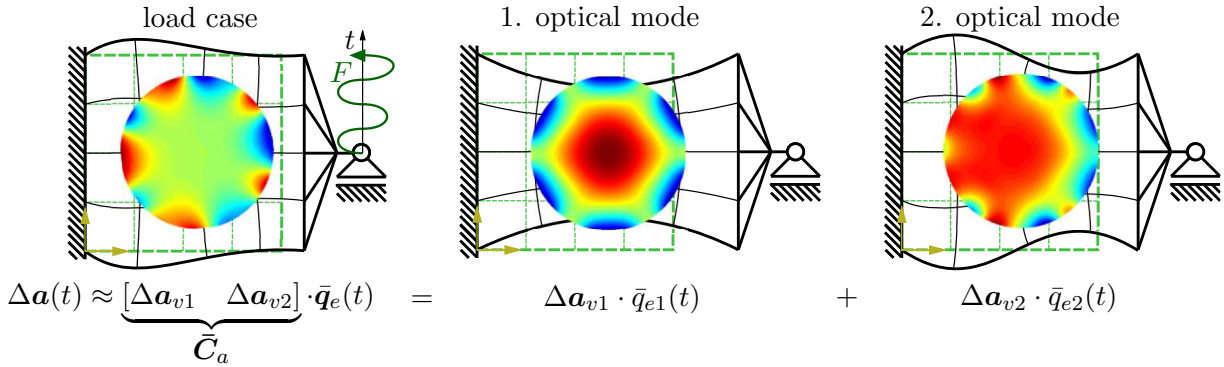


Figure 4.26: Sketch of the superposition of optical modes according to mechanical eigenmode shapes for an example planar plate.

Since the Equations (4.21) can be treated as output equations to the linear system of equations (2.8) for a single elastic body, the mechanical-optical transfer functions can also be derived [StörkleWengertEberhard14]. Therefore, the equations in time domain have to be reformulated in the frequency domain using the Laplace transformation. With the complex frequency parameter s , the transfer functions from each mechanical input to each optical aberration serving as outputs result to

$$\mathbf{H}_{\text{mech,opt}}(s) = \bar{\mathbf{C}}_{a,e} \cdot (\bar{\mathbf{M}}_e s^2 + \bar{\mathbf{D}}_e s + \bar{\mathbf{K}}_e)^{-1} \cdot \bar{\mathbf{B}}_e. \quad (4.23)$$

It should be noted, that if a mode normalization according to Equation (2.12) is applied, the individual factors $\text{rms}(\mathbf{v}_{\text{sum}})$ have to be multiplied with the optical mode shapes contained in the columns of matrix $\bar{\mathbf{C}}_{a,e}$. If the rigid body motions of all elastic bodies in the EMBS according to Equations (2.11) are translational, the transfer function of the global system can also be obtained.

Until now, the models were analyzed during determined excitations. However, to further understand the dynamical-optical system results, it could be advantageous, investigating the overall mechanical-optical behavior in the frequency domain.

4.4.2 Mechanical-optical Transfer Function

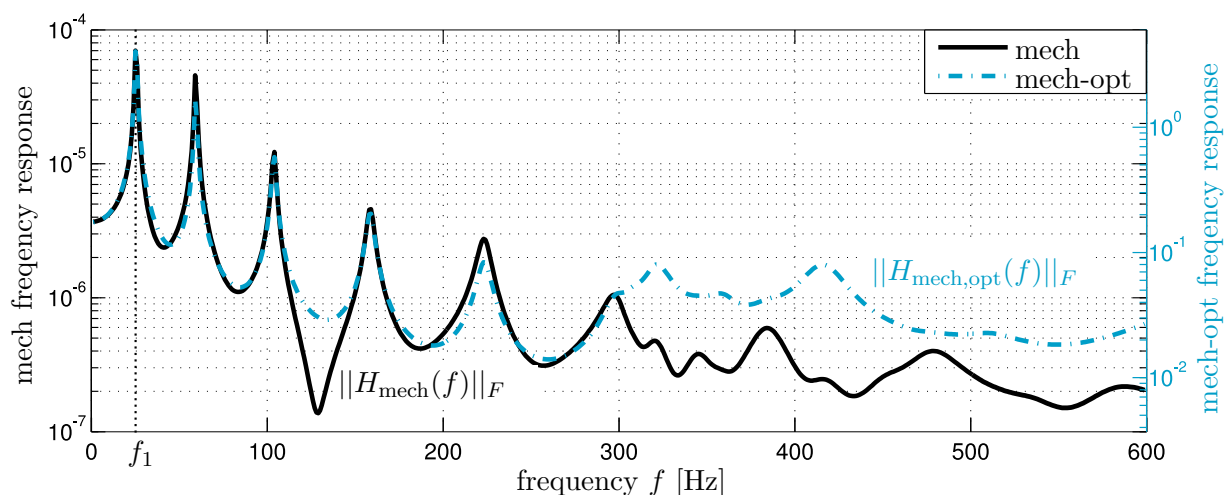


Figure 4.27: Pure mechanical and combined mechanical-optical frequency response, where two different ordinate scales are introduced.

Eventually, the mechanical-optical frequency responses for the free elastic mirror according to Equations (4.23) are analyzed using the model *krylov108*. Therefore, Figure 4.27 shows the mechanical frequency response $\|\mathbf{H}_{\text{mech}}(f)\|_F$ qualitatively compared with the mechanical-optical frequency response $\|\mathbf{H}_{\text{mech,opt}}(f)\|_F$ which results from the Frobenius norm of the frequency responses of the Zernike coefficients $\{c_2, \dots, c_j, \dots, c_{231}\}$. Therefore, the two different linear ordinate scales are adapted just that the frequency responses are similar at the first eigenfrequency f_1 . Analysing the differences at the higher frequencies it shows, that the mechanical-optical transfer function can also behave very sensitive in high-frequency ranges, although the pure mechanical frequency response decreases.

For a more detailed optical analysis, the WFA of the mode shapes can be investigated. In Figure 4.28, the deformed shapes colored concerning the z -deformation are illustrated. Furthermore, the related WFAs of a few modes colored with respect to the phases are presented. With the colors, it is clearly shown that the shape of the deformation is mostly similar to the shape of the WFA. For instance, if a location next to the boundary is

deformed in the direction towards the image plane, the values of the WFA are positive and have the same color as the deformation. Furthermore one can estimate in consideration to the results of f_{14} and f_{23} , that the deformation of the central region does not affect the WFA as much as the deformation of a decentral area next to an edge. This circumstance results from the fact, that paraxial rays of an optical system usually behave almost linear, while the other rays far from the optical axis propagate in a nonlinear manner through the system. The dominated optical aberration is given in Figure 4.28.

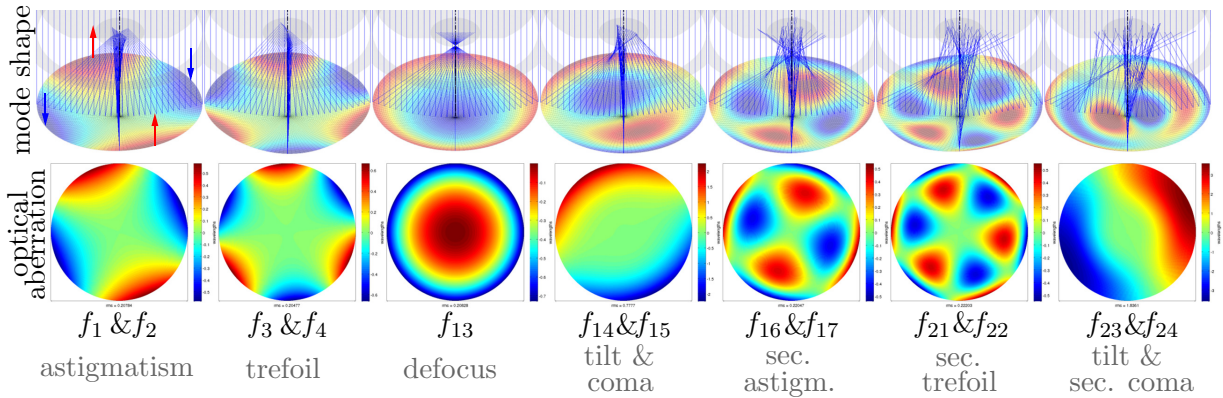


Figure 4.28: Deformation and optical aberration of a few mode shapes at the frequencies f_i of the *krylov108* model.

In Figure 4.29(a), the influences of the mechanical inputs on the optical WFA are represented using the Zernike coefficients c_j according to Noll's notation [Noll76]. Since the Frobenius norm considers all three input nodes simultaneously, the behavior of the same kinds of aberrations concerning the x - and y -axis are identical. For instance, the coefficients c_2 and c_3 characterize tilts of the image with respect to the x - and y -axis. Both responses lead to the same results, as well as c_5/c_6 representing astigmatism, c_7/c_8 describing primary coma and c_9/c_{10} indicating trefoil. Regarding just the tilt aberration it is conspicuous, that they are not very sensitive to the first few eigenfrequencies, but the amplitude increases for higher frequencies. In contrast, the coefficient c_4 represents the defocus, and it is sensitive to the frequency range around 300Hz. The defocus shape, and also some of the other mode shapes, are marked by their associated frequencies and their related kinds of WFA are illustrated in Figure 4.28.

Finally, the influence of the different MOR methods on the optical aberrations for various frequencies of excitation can be addressed. The deviations are clarified for different Zernike coefficients in Figure 4.29(b). Thereby it is obvious, that the results for low frequencies are quite similar, while for the high frequencies the behavior is entirely different. This fact is also distinctly clarified in Figure 4.30, where the Frobenius norms and the corresponding relative errors are regarded. In the last plot it is recognizable, that the *krylov36* model yields the best results until 250Hz, whereby it fails for the frequencies above, as also seen in the mechanical results. However, the *baltrun36* model and especially the *craigb36* model perform acceptably, even until to a frequency of 450Hz. In comparison to the mechanical

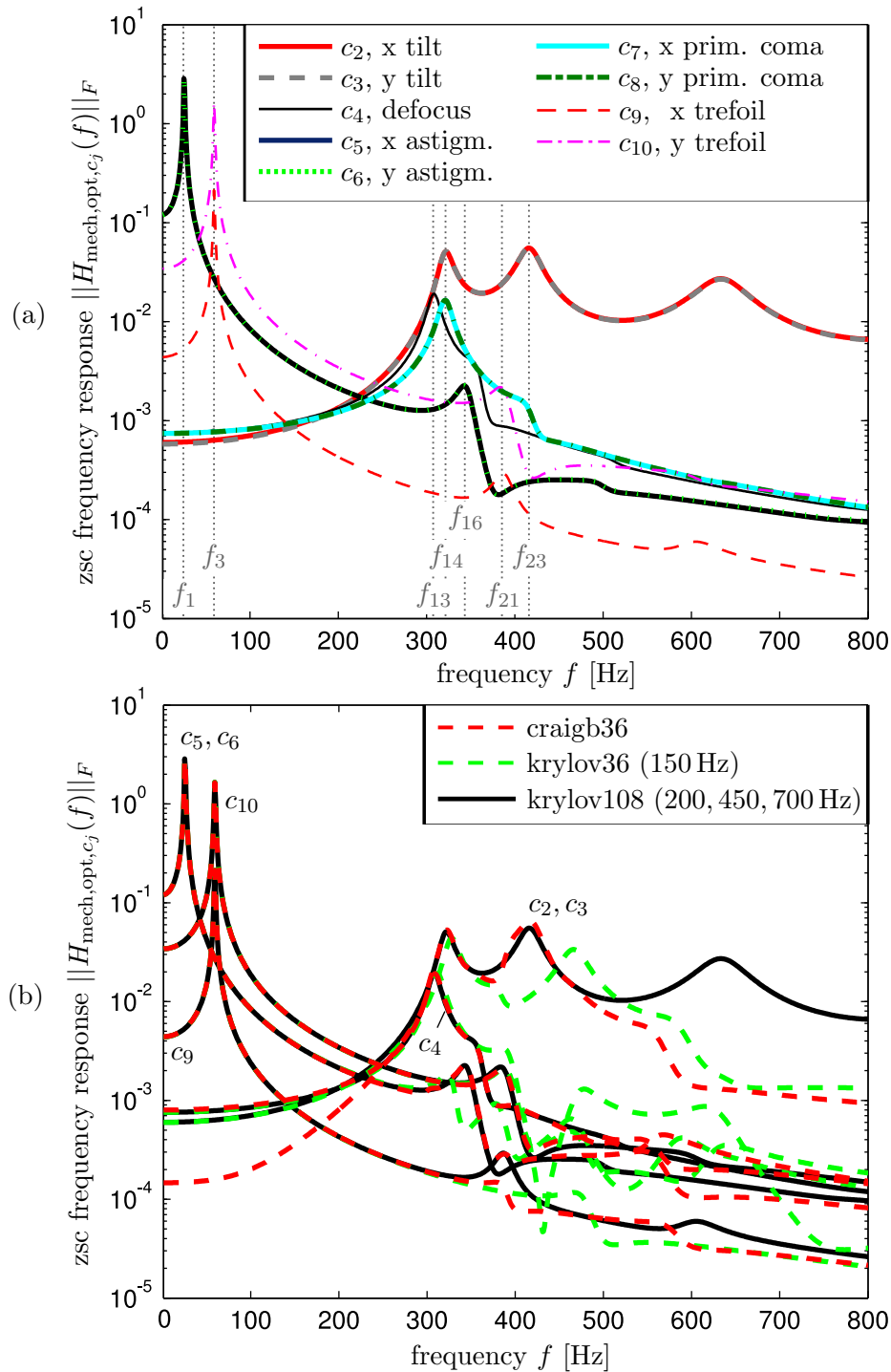


Figure 4.29: In (a), the sensitivity of specific optical aberrations in the frequency domain is characterized by their related Zernike coefficients. In (b), the deviations of the different MOR methods are clarified.

frequency response according to Figure 4.17, the relative errors at higher frequencies are slightly smaller. This observation leads to the conclusive presumption that the combined mechanical-optical system better excuses high-frequent deviations due to a MOR. One

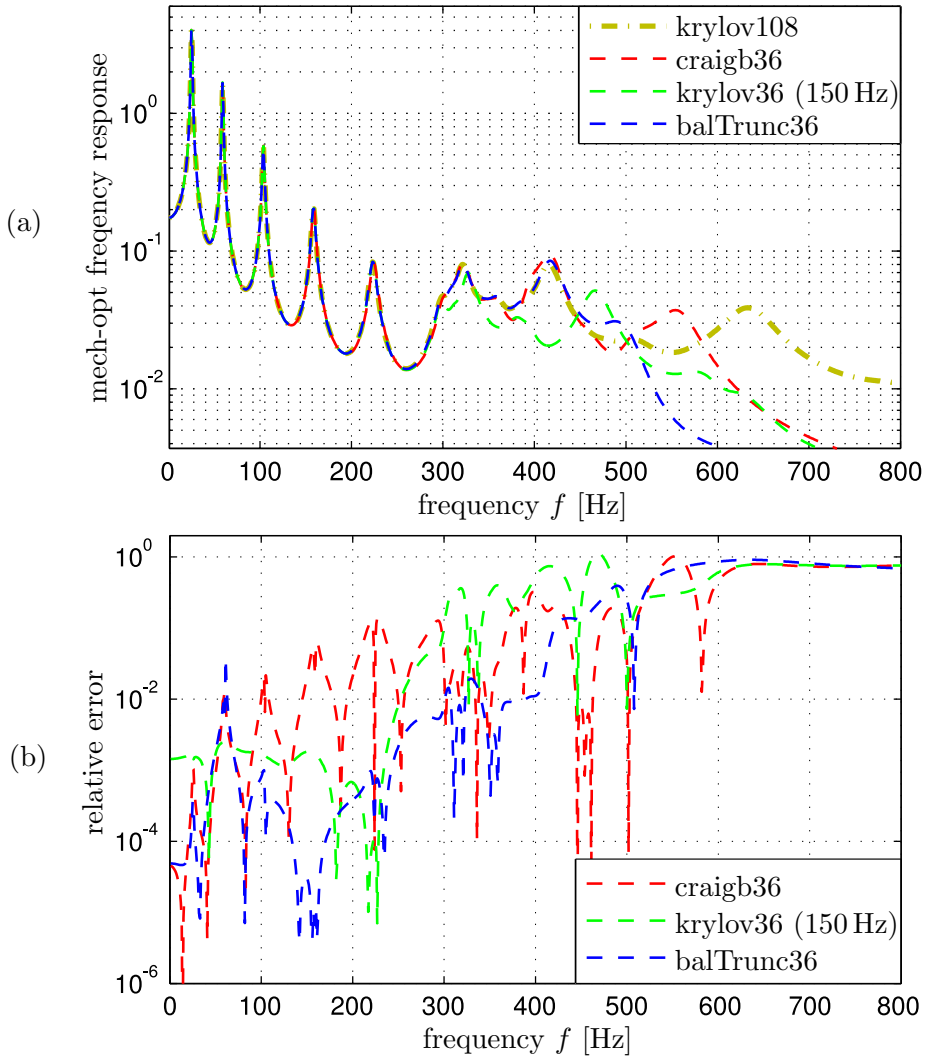


Figure 4.30: Comparison of different MOR methods by the Frobenius norms of the mechanical-optical frequency responses and their relative errors which are calculated with respect to the *krylov108* model.

can summarize that on the one hand, the relative error of the Craig-Bampton method for the static case is low and grows continuously with higher frequencies, and on the other hand, the sophisticated MOR methods accurately represent the system behavior only in specific and sometimes limited frequency ranges.

4.5 Further Investigations

The dynamical-optical model of the elastic mirror example can furthermore be used in order to investigate the influence of the MOR methods on the optical simulation results. In addition, the difference between the *standard method* and the *modal method*, which are described in Section 4.1, can be evaluated and assessed.

4.5.1 Influence of the MOR on optical Simulation

For a central field of parallel rays from an infinite object, the RMS of the WFA over the time of the mechanical simulation is shown in Figure 4.31. Again, the dynamical-optical behavior is investigated for a sinusoidal z-excitation of 100 Hz and an amplitude of $10 \mu\text{m}$. The x- and y-motions of the interface nodes are constrained. In the left part, the results of the various reduced models are clarified. The differences between the various reduced models with respect to the *krylov108* system are shown in the right part. Regarding the result of the *craigb108* model, the difference is vanishingly low. For the other previously investigated models *krylov36* and *craigb36*, the differences are only in a range of 1.5% of the maximal RMS value, which is quite small. For the *craigb36* model one can see, that the difference at the beginning of the simulation is maximal and decreasing with the time and progressing excitation and for the *krylov36* model, the opposite phenomena can be observed.

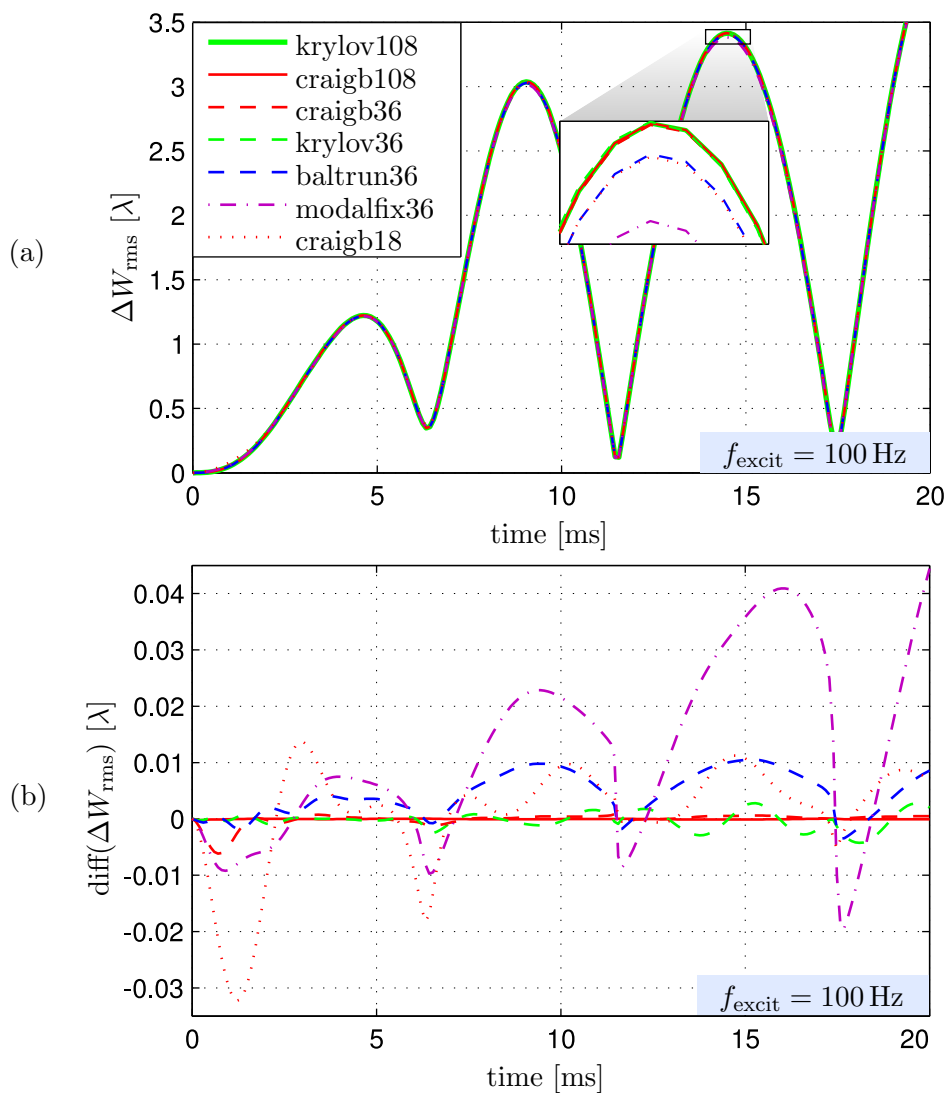


Figure 4.31: Optical results given by the RMS of the WFA for different MOR methods.

In addition to the previously analyzed models, the results of a model called *craigb18* with nine static interface constraint modes and nine fixed interface normal modes are presented. Here, the deviation at the beginning of the simulation is maximal and is also decreasing with the progressing excitation, like for the *craigb36* model discussed before. Of course, the model is not as accurate as the others. However, the deviations are for the most cases acceptable, and the model size is quite small, so its computational cost is quite cheap.

Furthermore, the results of a model named *modalfix36* are depicted in Figure 4.31. It is based on *Guyan's Static Condensation* according to Section 2.3, where the first 36 fixed interface normal modes of the mirror are used for the projection basis. In comparison with the sophisticated methods of Krylov and Craig-Bampton, the deviation is significantly higher. It is proportional to the magnitude of the RMS, but maybe in some cases also acceptable. Nevertheless, the Guyan reduced model only behaves appropriately, if the interface nodes in the EMBS are suitably fixed to each other during the excitation. In contrast, the other methods are valid for more general excitations at the interfaces.

Figure 4.32(a) depicts the transient results of the RMS of the WFA at an excitation of 300 Hz for various MOR methods. In particular, the *krylov36* model shows for some time instants large deviations which results in a relative error of up to 18%. The related exposed images are illustrated in Figure 4.32(b), which are the results of an exposure simulation by considering the irradiance over the time, see also Section 3.4.4. On the upper side, the perfect static case for the parabolic mirror is shown and on the lower side, the case of the dynamical excitation with 300 Hz is shown for a scale factor of 1000. Thereby, the models *krylov108* and *krylov36* are represented. The LOS is visualized with the line in the center of the image. The discrepancy between the two images is apparent, although the WFA differs only in short time ranges.

In the next section, the different introduced simulation methods are validated by means of representing the optical aberrations, and they are compared for the computational cost.

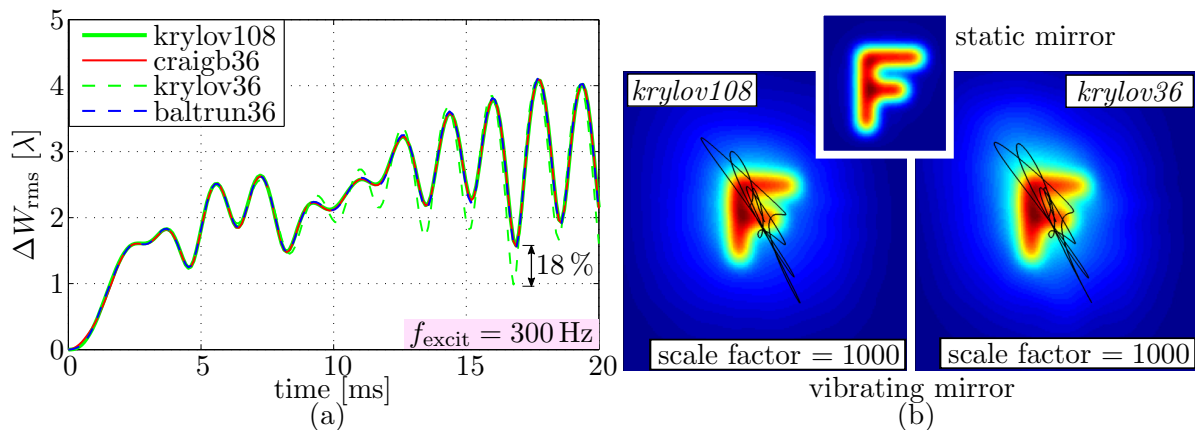


Figure 4.32: Optical results for an excitation frequency of 300Hz and the corresponding simulated images after 20ms of exposure for the static and the dynamic case.

4.5.2 Influence of the Dynamical-optical Simulation Method

Within this section, the RMS results of the different dynamical-optical simulation methods are investigated. On the one hand, the optical results can be computed with the *modal method* using kinematic-optical sensitivities and on the other hand with the *standard method*, see also Section 4.1. In Figure 4.33, the behavior of the *krylov108* and *craigb36* models excited with the load case at an excitation frequency of 100 Hz is compared.

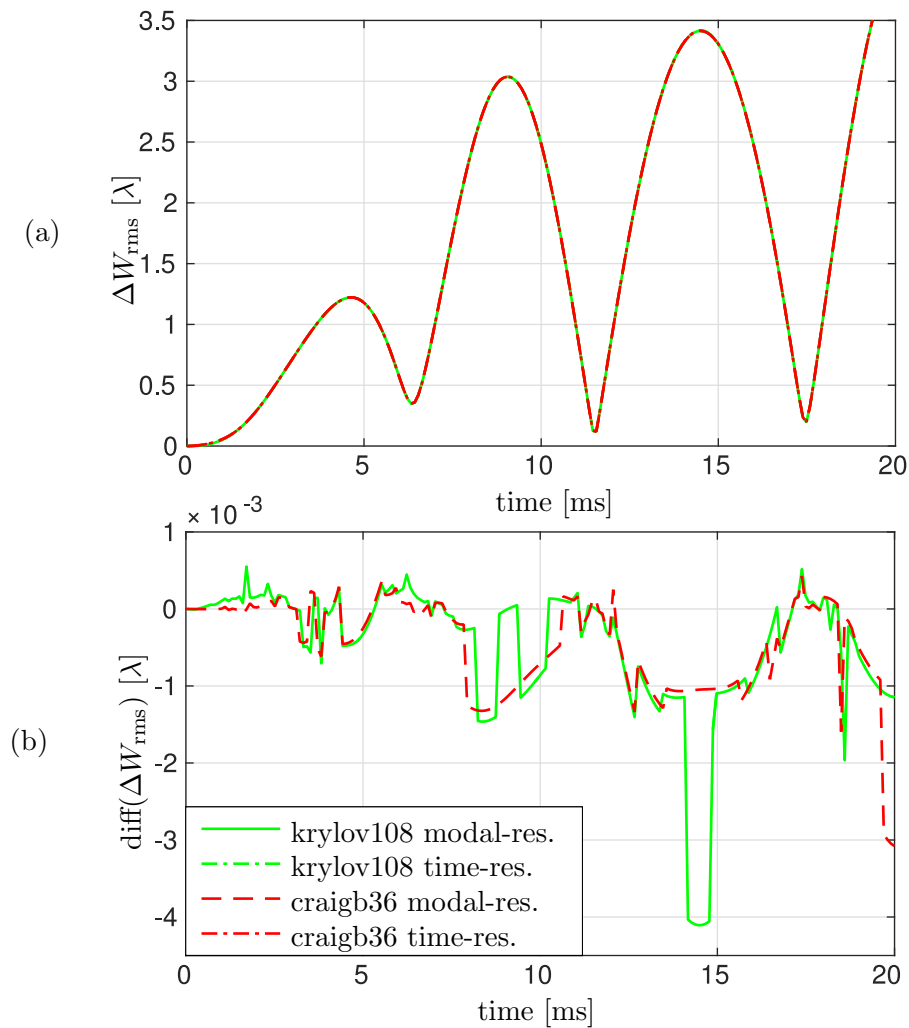


Figure 4.33: Optical results of the different dynamical-optical simulation methods.

The results are very similar, and the small deviations are almost proportional with about 1‰ of the corresponding RMS values. Since one can assume that the systems behave entirely linear for these small excitations, motions and deformations, the source of inaccuracy is probably the surface approximation described in Section 4.2.2. An explanation could be, that for the *standard method*, the deformation at one time instant is approximated, whereby a small deviation occurs. In contrast, for the *modal method* a small deviation may appear for every mode. With the superposition of all approximated modes, also the deviation could be finally increased.

Table 4.1: Computational costs in seconds for different MOR and optical simulation methods.

Name of model simulated time:	craigb18	craigb36	kryl36	craigb18	craigb36	kryl36
	$t_{\text{sim}} = 20 \text{ ms}$			$t_{\text{sim}} = 200 \text{ ms}$		
init. optical model, OM-Sim	0.040	0.046	0.047	*	*	*
FE modeling, Ansys	5.034	5.240	5.009	*	*	*
FE data import to Matlab	10.881	11.418	12.333	*	*	*
MOR, MatMorembs	4.936	5.604	3.424	*	*	*
derive the EMBS, Neweul-M ²	84.201	150.245	158.294	*	*	*
num. integration, Neweul-M ²	4.133	9.721	10.173	9.014	20.848	29.957
optical sim. <i>standard method</i>	22.876	22.023	31.147	187.285	187.235	195.226
optical sim. <i>modal method</i>	8.137	15.018	20.198	9.041	14.996	21.141

In order to assess not only the accuracy but also the computational performance of the proposed strategies, simulations are done, and the needed durations are compared in Table 4.1. In the center column, the computational time of the Craig-Bampton MOR method is confronted with the Krylov MOR method. Since the latter method leads to a higher maximal pseudo-eigenfrequency, the numerical integration of the EMBS consumes a little bit more time than for the EMBS with the Craig-Bampton reduced mirror. The durations of modeling, the import and the MOR of the elastic body are very similar for all models. For the optical simulation, 200 time instants are extracted from the mechanical results to get snapshots in sampling rates of 0.1 ms. In case of applying the *standard method*, all the snapshots are individually approximated for the optical simulation as shown for the *craigb18* model in Figure 4.34. Of course, this leads to higher computational time than using the *modal method* which just optically analyses the mode shapes. In Figure 4.35, all the mode shapes of the *craigb18* model are visualized, whereby the first few are almost identical to the first few normal modes of the full model, see also Figure 4.19.

This behavior can be clarified extending the simulated time to 200ms, which leads to 2000 time instants and is listed in the right-hand part of the table. The computational cost of the *modal method* hardly changes, which is marked with a "*", whereas for the current examples, the tenfold simulated time for the *standard method* results in a computational duration increased by a factor around seven. In other words, the longer the simulation time, the more it makes sense to use the *modal method*.

Nevertheless it should be noted, that the quality of the Zernike approximation for the last few modes during the *modal method* usually is not as good as for the others, since these last modes describe local deformations at the interface nodes. According to Equation (4.11), the relative accuracies of the approximation of the mode shapes are listed in Figure 4.36 for the different MOR methods with 36 DOF. It is noticeable that mostly the last few modes are difficult to approximate. Especially for the *krylov36* model, the approximation error of the last 9 modes is high compared to the other modes. Usually, these modes are the correction modes which mostly characterize the static or dynamic behavior of the interface nodes locally. So one reason for the challenging approximation could be the

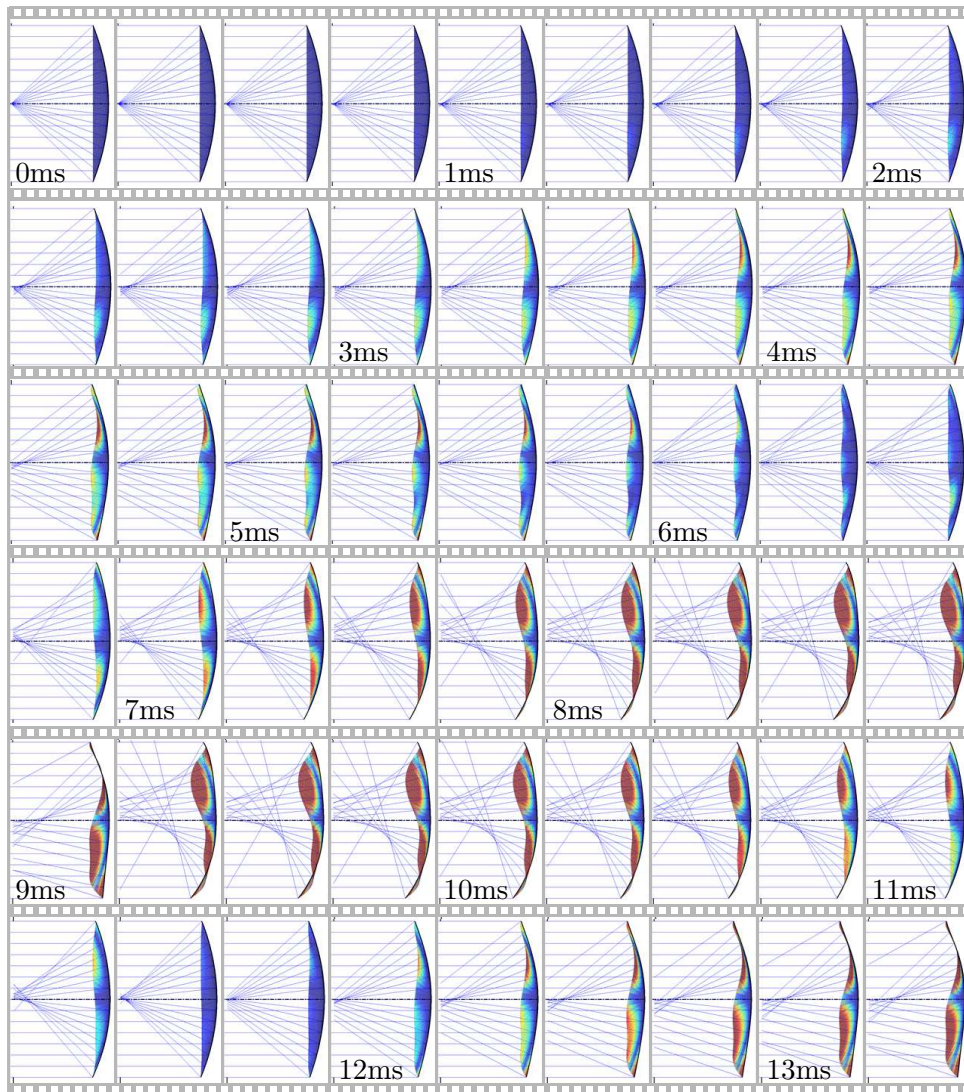


Figure 4.34: Snapshots of the time results for the dynamical-optical simulation with the *standard method*.

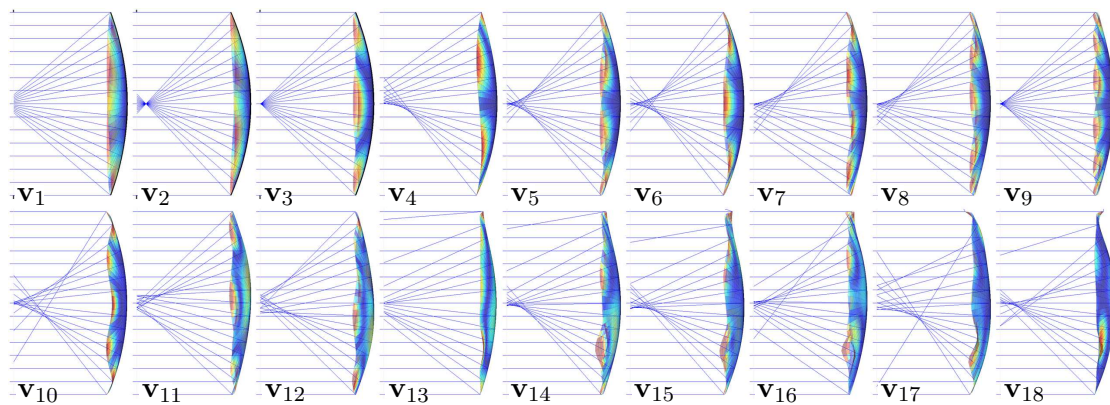


Figure 4.35: Optical analysis of Craig-Bampton modes, for the dynamical-optical simulation with the *modal method*.

complicated and somehow strange shape of these modes.

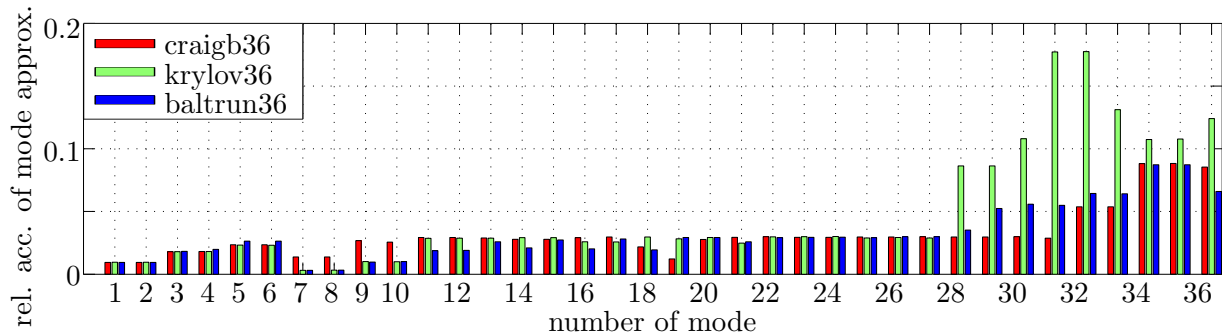


Figure 4.36: Relative accuracy of the approximation of the mode shapes with Zernike polynomials.

In the following, a practical and complex astronomical telescope is considered during the simulation-based design of a related AO control.

4.6 Adaptive Optics for a Segmented Telescope

The last dynamical-optical simulation model within this work represents the AO control of a mechanical-disturbed telescope. Thereby, the model parameters of the TMT construction proposal according to [AbrahamEtAl07] are used which describes a typical astronomical ground-based telescope. For the following investigation, visible light with a wavelength of $\lambda = 550$ nm is taken into account. First, the kinematic-optical model is explained. Second, the design of the controller for the optical compensation is derived, and finally, the simulation results clarify the functionality.

4.6.1 Kinematic-optical Model Under Disturbance

The TMT consists of a segmented primary mirror (M1) with a global diameter of 30 m, a deformable secondary mirror (M2) and a planar tertiary mirror (M3). A sketch of the optical model and a visualization of the optical surfaces are introduced in Figure 4.37. Since the M2 stops the incident rays at the center region of the field, the optical system is obscured, such that M1 has an annular shape. In Table 4.2, the related optical data of the surfaces are listed. In particular, the M3 is rotated with an angle of 45° with respect to the y -axis. For the construction, it is proposed to realize the M1 with 492 mirror segments. However, to demonstrate the simulation-based control of the M2 at low computational cost, the system is simplified to 18 segments. This resulting model is similar to the JWST.

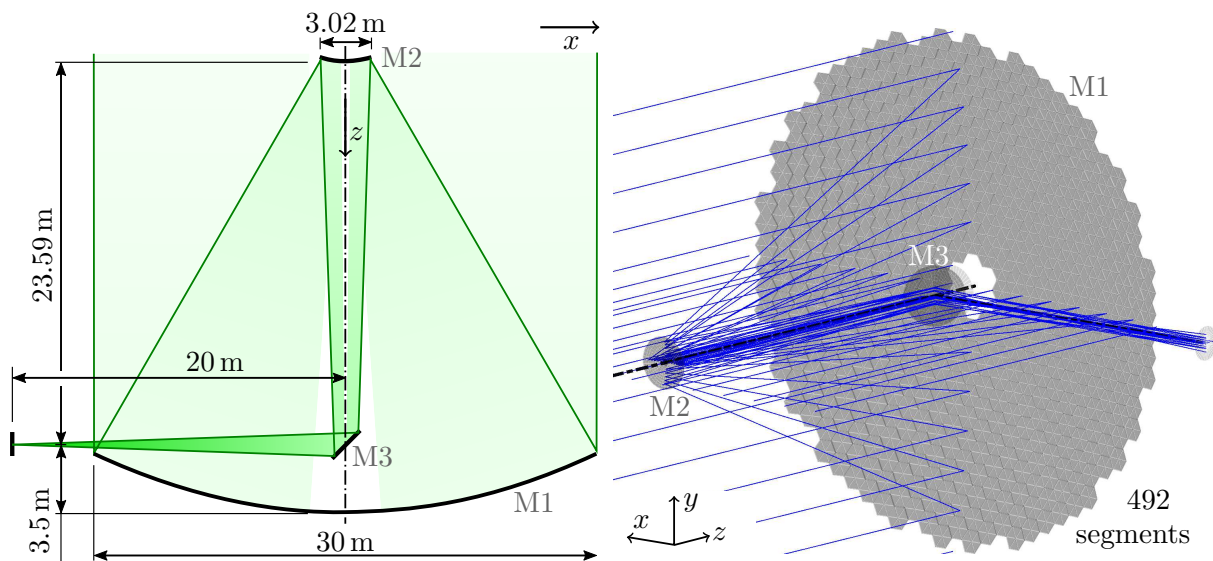


Figure 4.37: Sketch and visualization of the optical model of the TMT.

Table 4.2: Data of the relatively described optical surfaces of the TMT [AbrahamEtAl07].

surface	radius	conic	semidia	z -distance	x -distance
object	∞	0	15e3	30e3	0
AS	∞	0	[15e3, 1.5122e3]	1.8749721e3	0
M1	-60e3	-1.0009535	[1.5122e+03, 15e3]	-27.093750e3	0
M2	-6.22768e3	1.31822813	1.5122e+03	23.59375e3	0
<i>rotation of 45° around the y-axis</i>					
M3	∞	0	1.75395e3	-14.142136e3	-14.142136e3
<i>rotation of 45° around the y-axis</i>					
image	∞	0	1e3	0	0

The considered telescope system is illustrated in Figure 4.39(a), where the 6th-segment is marked. It is further assumed, that only the segments of the M1 are mechanically disturbed in the z -direction, which results in a maximal segment translation of $\pm\Delta s_z \approx 70$ nm. Thereby, the optical system remains diffraction-limited according to Equation (3.55). The corresponding motions of the individual segments indicated by their numbers are illustrated in Figure 4.38 for a considered simulation duration of 100 ms. With a second model, the influence of the deformation of the 6th-segment is simulated, whereby the related values are in the same range.

Anyway, the actual optical system and the related WFA at the simulated time $t = 95$ ms are shown in Figure 4.39(a) and (b). Thereby, it is assumed that the inner and outer incident rays are stopped according to the cornered shape of the segmented mirror. As a result, the AS, the EnP, and the ExP are also edgy. On the right-hand side, the colors represent the accuracy of the optical system with respect to the z -translations of the segments. However, since Zernike polynomials used for the WFA approximation are annular, there are

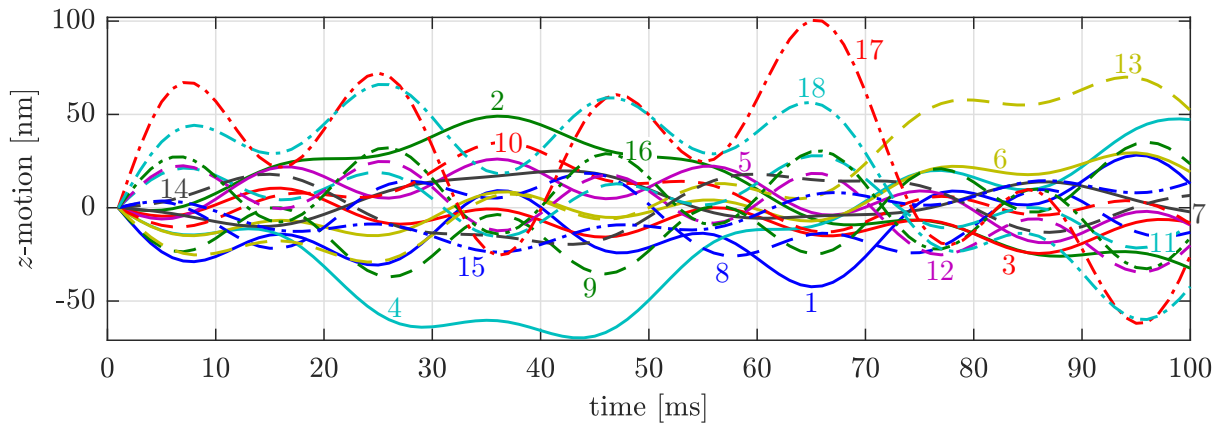


Figure 4.38: Rigid body motion of the M1 segments due to the mechanical disturbances.

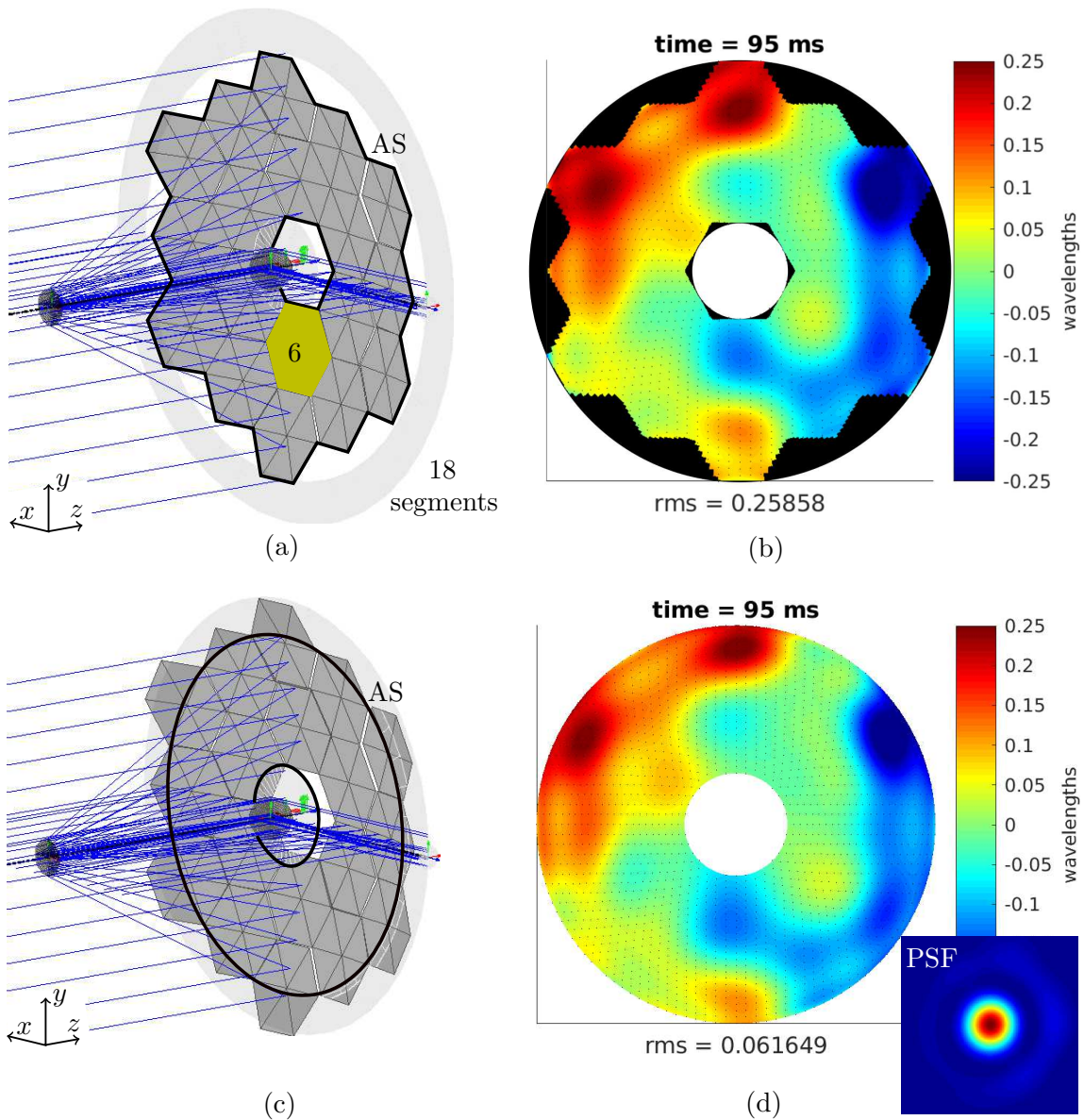


Figure 4.39: Visualization of the two different kinematic-optical models with 18 segments.

some undefined regions next to the outer and inner segment bounds. Thus, the resulting polynomial coefficients c_j and the related RMS value are not representative for the actual aberration. At least, the influence of the segment translations on the WFA is correctly visualized within the segments.

In contrast to that, Figures 4.39(c) and (d) depict the system with an annular AS. The remaining rays are uniformly distributed on the whole annular pupil within the segmented area. Hence, the approximated Zernike polynomials perfectly describe the WFA through their coefficients, and this annular model is considered in the following during the controller design. In the PSF plot on the lower right-hand side one can also see the distinct outer ring due to the annular pupil shape.

4.6.2 Control Strategy for M2

As introduced in Section 1.1, the strategy during AO is to compensate for optical aberrations actively using a controllable mirror. For the regarded telescope, two different approaches are investigated for the control of M2, as illustrated in Figure 4.40.

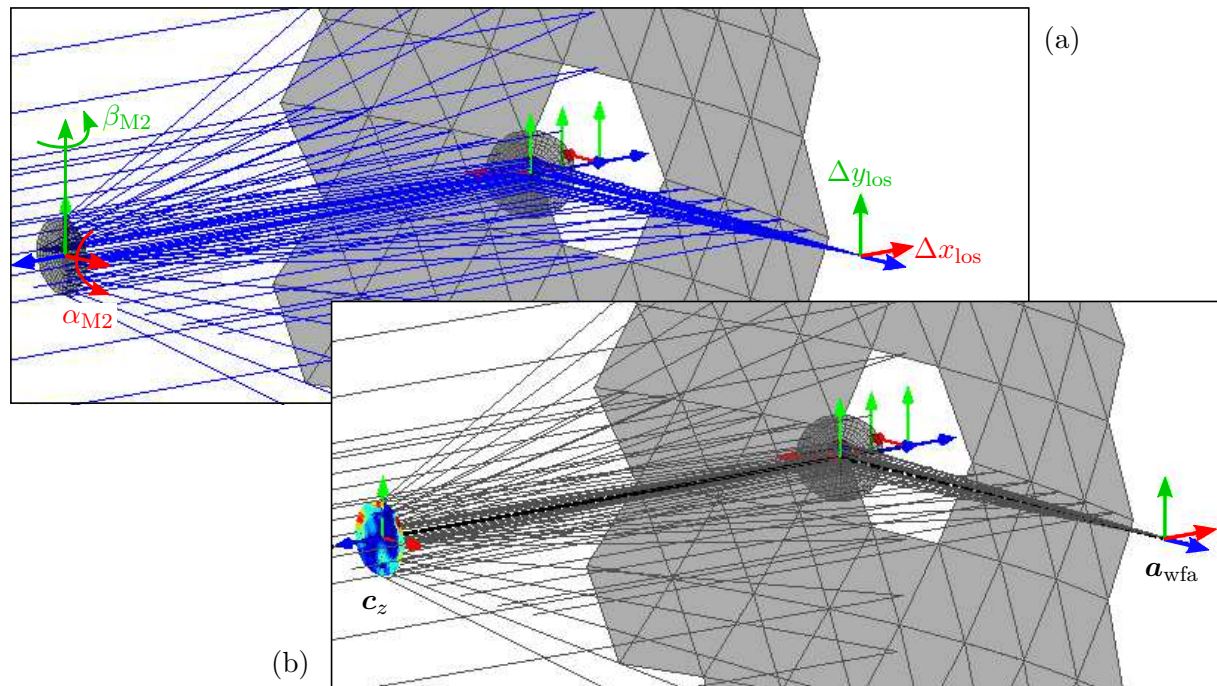


Figure 4.40: Strategy for the optical compensation by means of either a rigid (a), or deformable (b) M2.

On the one hand, the LOS aberration due to the disturbed M1 can be corrected by means of a target rigid body motion of the M2. Thus, a rotation around the x - and y -axis can be applied with the angles α_{M2} and β_{M2} , as indicated in Figure 4.40(a). This change results in the LOS displacements Δx_{los} and Δy_{los} on the image plane and the sensitivity

analysis can be performed. According to Section 4.4.1, the corresponding matrix of the kinematic-optical sensitivities can be computed, e.g., with $h = 1\text{e-}6$ rad ≈ 0.2 arcsec. This leads to

$$\underbrace{\begin{bmatrix} \Delta x_{\text{los}} \\ \Delta y_{\text{los}} \end{bmatrix}}_{\Delta \mathbf{a}_{\text{los}}} = \underbrace{\begin{bmatrix} -2.4945\text{e-}5 & -85460 \\ 85460 & 1.7364\text{e-}5 \end{bmatrix}}_{\mathbf{C}_{a,r,\text{los}}} \cdot \underbrace{\begin{bmatrix} \alpha_{\text{M2}} \\ \beta_{\text{M2}} \end{bmatrix}}_{\mathbf{q}_{r,\text{M2}}}, \quad (4.24)$$

where the rigid body motions are collected in the vector $\mathbf{q}_{r,\text{M2}}$. In order to compensate the occurring LOS motion $\mathbf{a}_{\text{los}}(t)$ during a disturbance, the target motion of the M2 can be calculated by means of the rearrangement

$$\mathbf{q}_{r,\text{M2,target}}(t) = -\mathbf{C}_{a,r,\text{los}}^{-1} \cdot \mathbf{a}_{\text{los}}(t). \quad (4.25)$$

On the other hand, the general WFA described by 105 Zernike coefficients can be corrected by means of an appropriate target deformation of the M2. As indicated in Figure 4.40(b), one can investigate the influence of an M2-deformation $\mathbf{c}_{z,\text{M2}}$, which is also described by 105 Zernike coefficients, on the WFA. The latter is denoted with $\Delta \mathbf{a}_{\text{wfa}}$. In analogy to the upper case, the matrix of kinematic-optical sensitivities $\mathbf{C}_{a,e,\text{wfa}}$ for the individual coefficients describing a Zernike deformation can be computed, e.g., with $h = 1\text{e-}5$ mm. This can be formulated with

$$\underbrace{\begin{bmatrix} \vdots \\ c_j \\ \vdots \end{bmatrix}}_{\Delta \mathbf{a}_{\text{wfa}}} = \mathbf{C}_{a,e,\text{wfa}} \cdot \underbrace{\begin{bmatrix} \vdots \\ c_{j,z,\text{M2}} \\ \vdots \end{bmatrix}}_{\mathbf{c}_{z,\text{M2}}}. \quad (4.26)$$

The resulting matrix is visualized in Figure 4.41. Obviously, the fully occupied diagonal entries clarify a strong relation between a Zernike deformation-coefficient with a Zernike aberration-coefficient of the same type. In addition, for most of the Zernike deformations there are small dependencies at lower orders of optical aberrations, probably due to the nonlinear projection of the optical rays.

In order to compensate the occurring WFA denoted with $\mathbf{a}_{\text{wfa}}(t)$ during a disturbance, the target deformation of the M2 can be calculated through the rearrangement

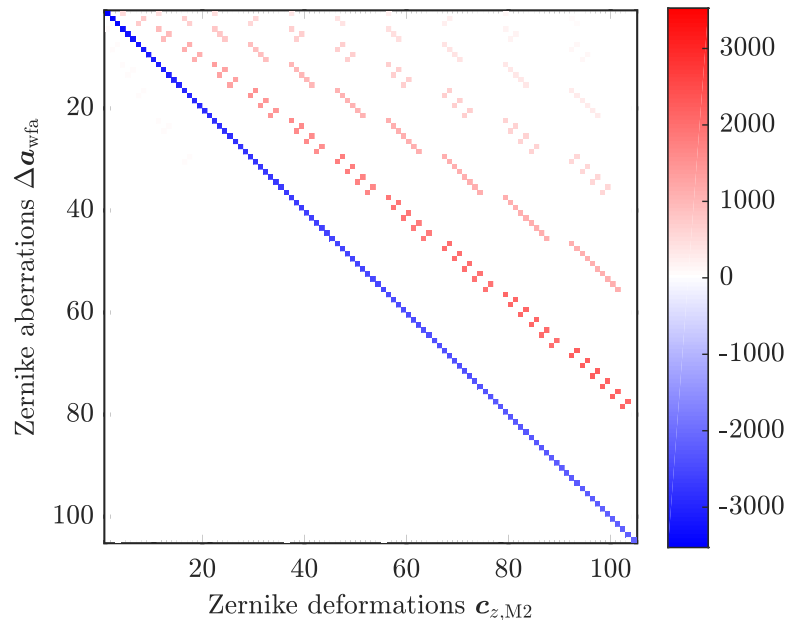
$$\mathbf{c}_{z,\text{M2,target}}(t) = -\mathbf{C}_{a,e,\text{wfa}}^{-1} \cdot \mathbf{a}_{\text{wfa}}(t). \quad (4.27)$$

Next, the control strategies are tested within the simulation model.

4.6.3 Simulation of the AO-Control

The derived compensation approaches are finally investigated utilizing the considered kinematic-optical simulation model. Thereby, the aberrations of the uncontrolled system

Figure 4.41: Matrix of kinematic-optical sensitivities $\mathbf{C}_{a,e,wfa}$, for a deformable M2.



can be simulated in a preprocessing step, and the target M2-motion and deformation are executed during the actual AO simulation.

Figure 4.42 shows the AO simulation results at $t = 95$ ms. At this time instant, the segments are displaced with about ± 70 nm, which is indicated by the corresponding colors. For the optical compensation, it is required to deform the M2 according to the color distribution of the lower left-hand side, whereby the values are also in the same order of magnitude. One can also see according to the colors, that the shape of the deformation is to the contrary of the segment displacements. In the box on the lower right-hand side, the resulting WFA is visualized which is computed by means of 2000 rays and it is quite small in the whole region. This is also represented by the vanishingly small RMS value. Thus, the design AO-control works perfectly within the simulation. However, for practical applications there are usually some inaccuracies and latencies, due to the internal dynamics of the sensing and actuating systems, which also have to be taken into account.

In order to assess the AO performance during the complete simulation duration, the varying LOS of the different models are considered according to Figure 4.43. Obviously, the initial disturbed motions $x_{\text{disturbed}}$ and $y_{\text{disturbed}}$ are perfectly corrected for both AO approaches, the first with the tilts of a rigid M2 according to Equation (4.25) and the second with a deformation of an elastic M2 of Equation (4.27).

However, the corresponding RMS values of the WFA with respect to the simulation time are drawn in Figure 4.44. As expected, the values of the rigid AO are not decreased in comparison to the uncontrolled and fully disturbed results, since the corrected tilts are not considered within the RMS, see also Equation (3.40). Anyway, the elastic AO method optimally compensates the remaining RMS.

Next, one can also perform an exposure simulation with the different models. The resulting

images of the static and the disturbed system are presented in Figure 4.45(a) and (b). The disturbance is scaled by a factor of 5, such that the shape of the LOS and the other

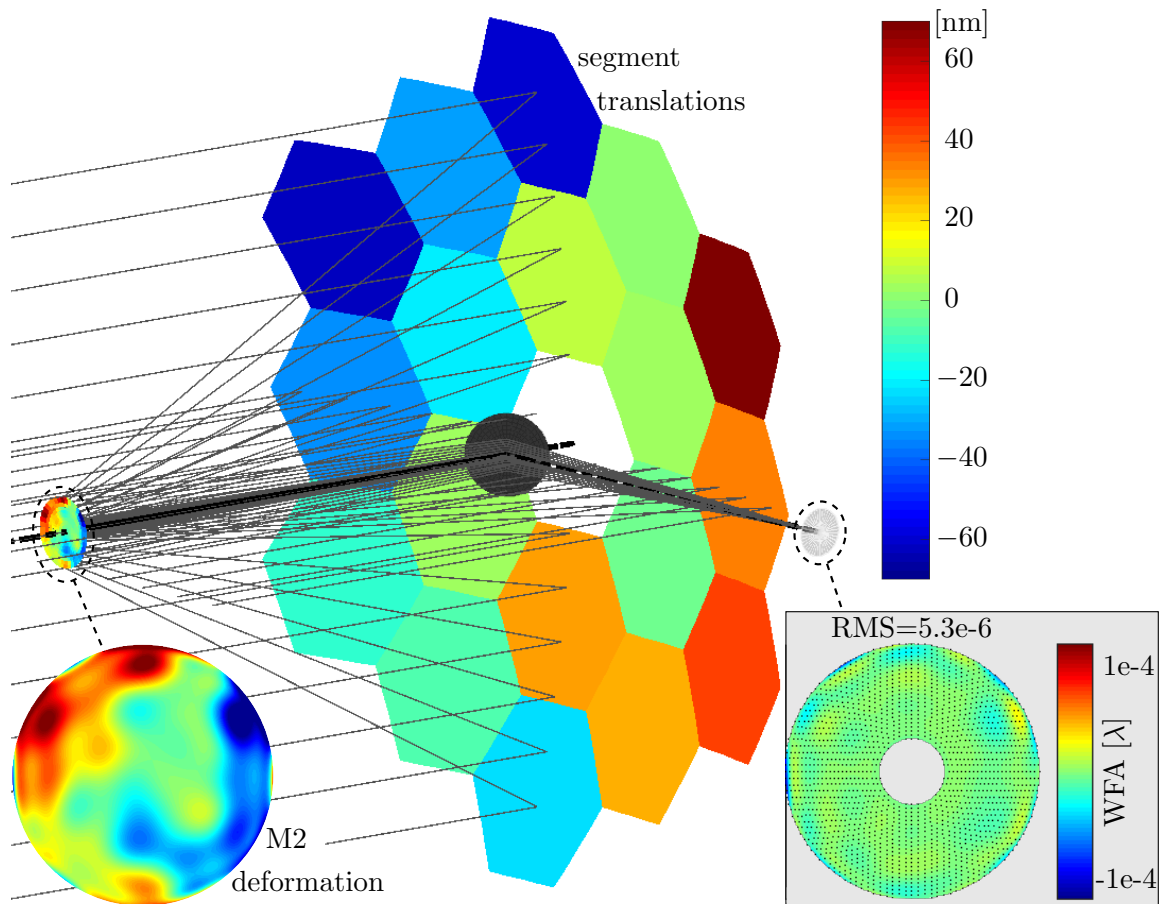


Figure 4.42: Visualization of the displacements of the M1 segments, the correcting M2 deformation and the vanishing optical aberrations, at $t = 95$ ms.

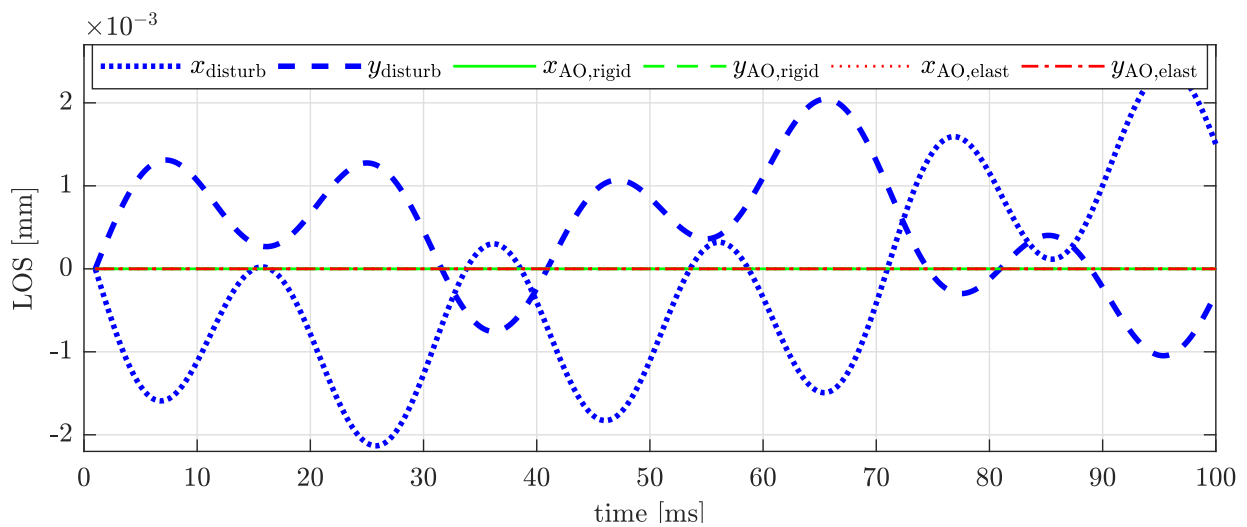


Figure 4.43: Simulated LOS for the different models.

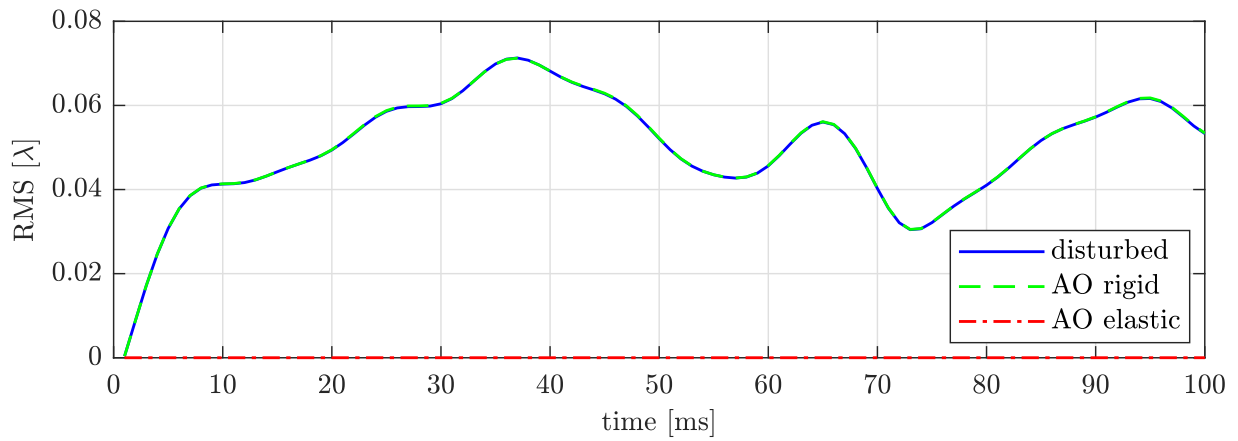


Figure 4.44: Simulated RMS for the different models.

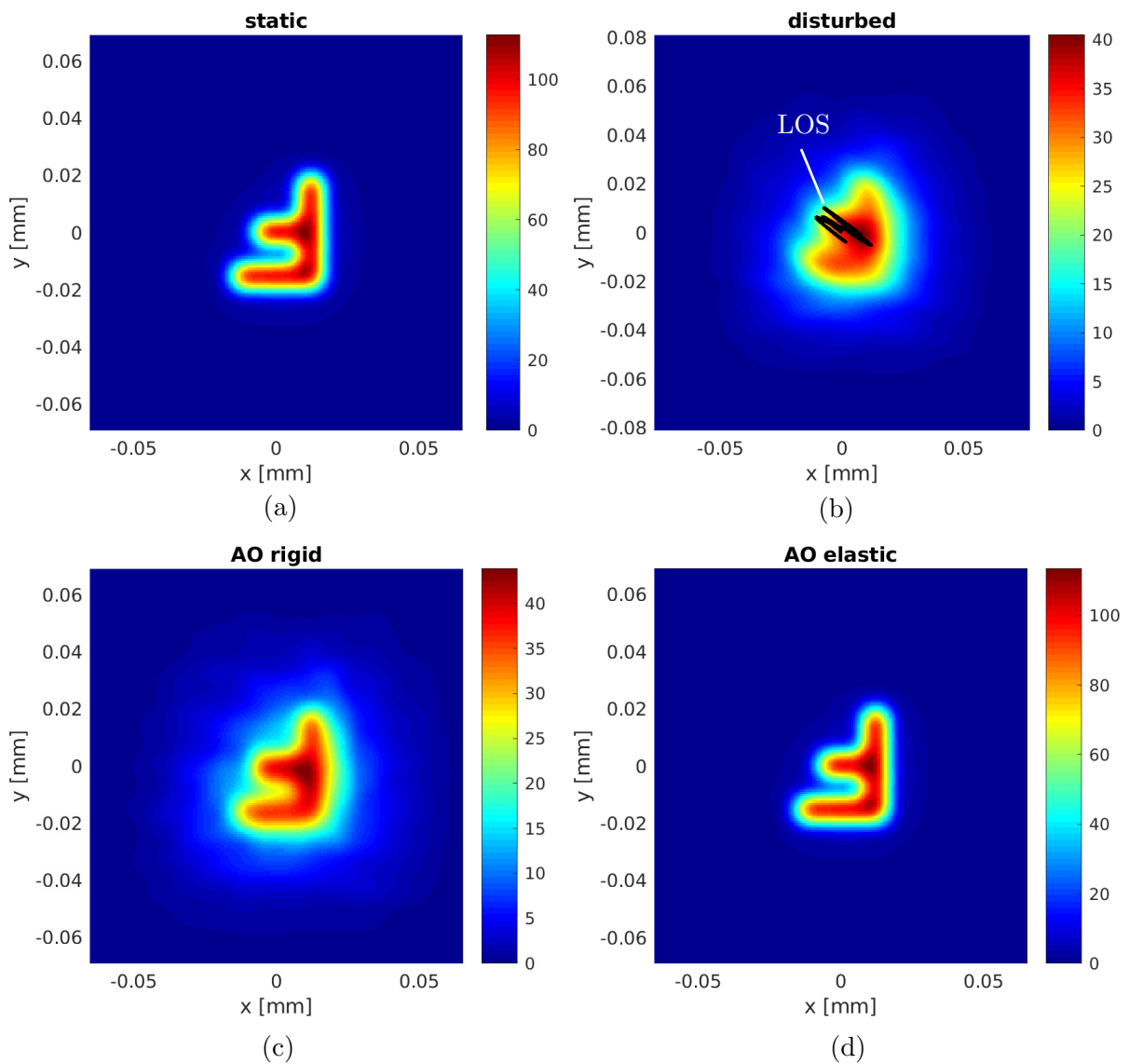


Figure 4.45: Resulting images of the different models after an exposure duration of 100 ms.

optical aberrations are clarified. The models with the rigid- and the elastic-controlled M2 are shown in Figure 4.45(c) and (c). On the one hand, the rigid AO model yields an improved image, and on the other hand, the elastic AO model leads to a perfect result, which is almost identical to the static case.

Finally, the investigation can be extended to the consideration of possible elastic segment deformations which could occur due to mechanical disturbances [NijenhuisHamelinckBraam12]. Figure 4.46 briefly illustrates, that the proposed AO compensation concepts are also applicable. The local aberration due to the disturbed segment is corrected by means of a local deformation of M2 and the resulting WFA is perfectly eliminated.

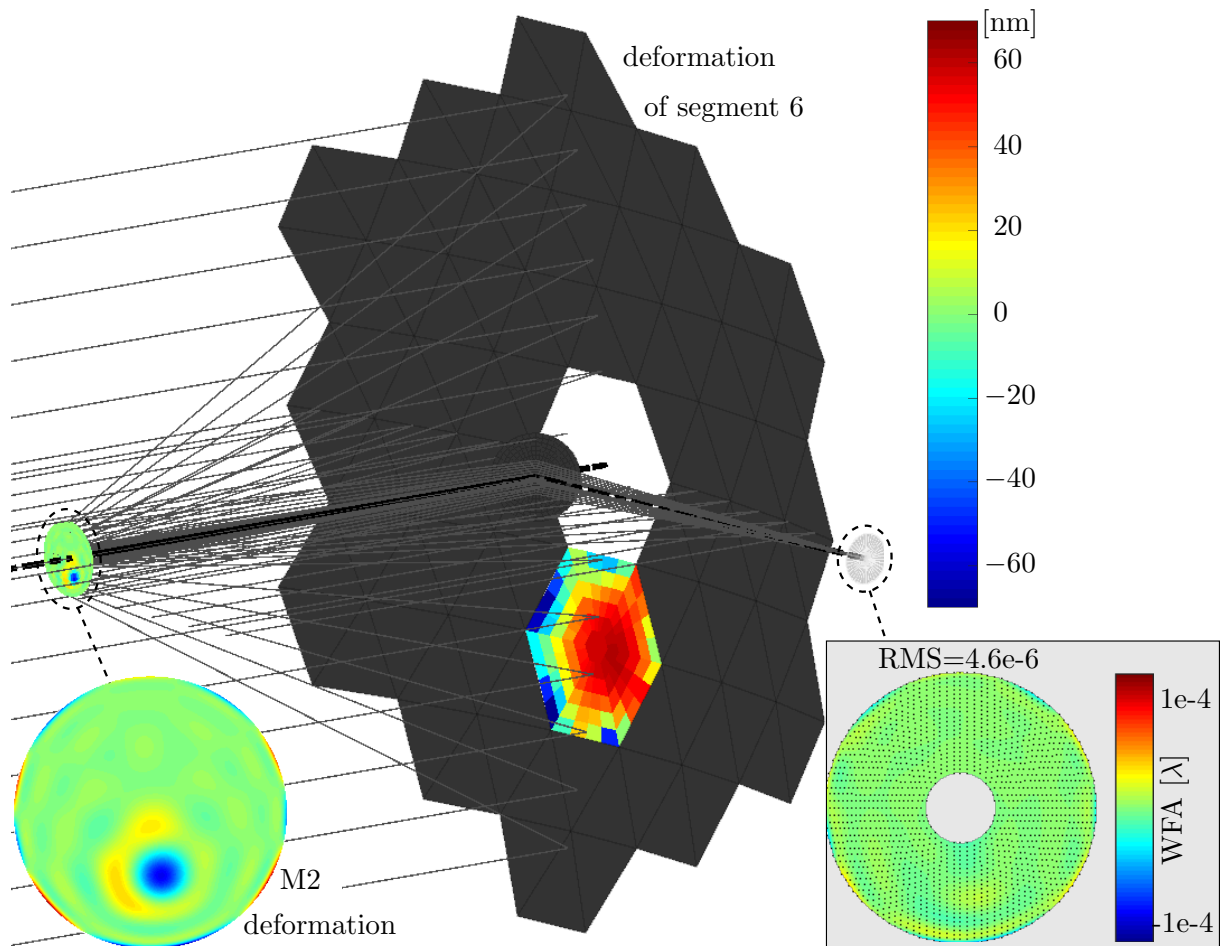


Figure 4.46: Visualization of the deformation of the 6th-segment of M1, the correcting M2 deformation and the vanishing optical aberrations, at $t = 95$ ms.

This chapter has presented the theoretical methods, strategies and several examples for different kinds of dynamical-optical simulations. In the following, an experimental setup is designed and realized, whereby some of the introduced concepts are tested in practice.

Chapter 5

Experimental Realization of a Dynamical-optical Control

This part presents a contribution to the active image stabilization of optical systems, involving model development, control design, and the hardware setup. A laboratory experiment is built, which demonstrates the vibration sensitivity of a mechanical-optical system. In order to stabilize the undesired image motion actively, a model-based compensation of the image vibration is developed, realized and tested. Beside a linear actuator motion system, a force sensor system and a position sensor system are introduced, validated and analyzed. In particular, various low-cost hardware components of the Arduino platform are used, which support the deployment of the controller software based on Matlab-Simulink. A high-speed vision sensor system measures the remaining image motion, and the performance of the overall system is assessed for different model parameters.

5.1 Conception and Modeling

In order to design an active image stabilization for an exemplary mechanical-optical system, methods and procedures are investigated and applied, see also [StörkleEberhard17b]. Furthermore, a laboratory experiment is designed, which should demonstrate the real behavior and validate the developed models and control strategies. Another purpose of this project is to provide a test setup for student training and laboratory education based on low-cost hardware, similar to [BarberHorraCrespo13] or [RegueraEtAl15]. Therefore, the capability and suitability of components from the *Arduino platform* [Arduino18] has to be investigated additionally. As a consequence, the final demonstrator can be used to transfer knowledge in the scope of mechanics, optics, electronics, and control.

First, the previous and initial setup of the experiment is introduced, which is followed by the description of the new active control extension. Second, the different hardware

subsystems are arranged, tested and explained. Third, the overarching control strategy of the dynamical-optical compensation is designed, simulated, and implemented. Finally, the experimental results are presented and assessed.

5.1.1 Previous Test Setup

In a previous work according to [WengertEberhard13] and [Wengert16], an experimental setup has been planned and built. It demonstrates a passive suppressing of optical aberrations, i.e., an image stabilization, by means of a structural optimization changing masses and stiffnesses. The setup is roughly derived from a lithographic objective with six projection lenses, whereby the dynamical behavior of the mounting and housing is represented by a rigid multibody system according to [SchiehlenEberhard14] using the generalized coordinates $\mathbf{q}(t)$. Thus, the out-of-plane displacement of lenses within an objective due to dynamical disturbances are regarded.

Figure 5.1 illustrates the main structure of the realized setup. On the left-hand side, the object is represented by a transparent circle with a radius of 5mm and with a light source behind, so that this light point is propagating through the glass lenses onto the image plane on the right-hand side. There, a paper screen is used to make the image of the light point visible, with a radius of approximately 2.5 mm. The oscillations of the lenses cause the image motion $a(t)$, i.e. the LOS motion. The excitation results from a hammer impulse, which imitates a disturbance. In the case of small motion, the equations of motion

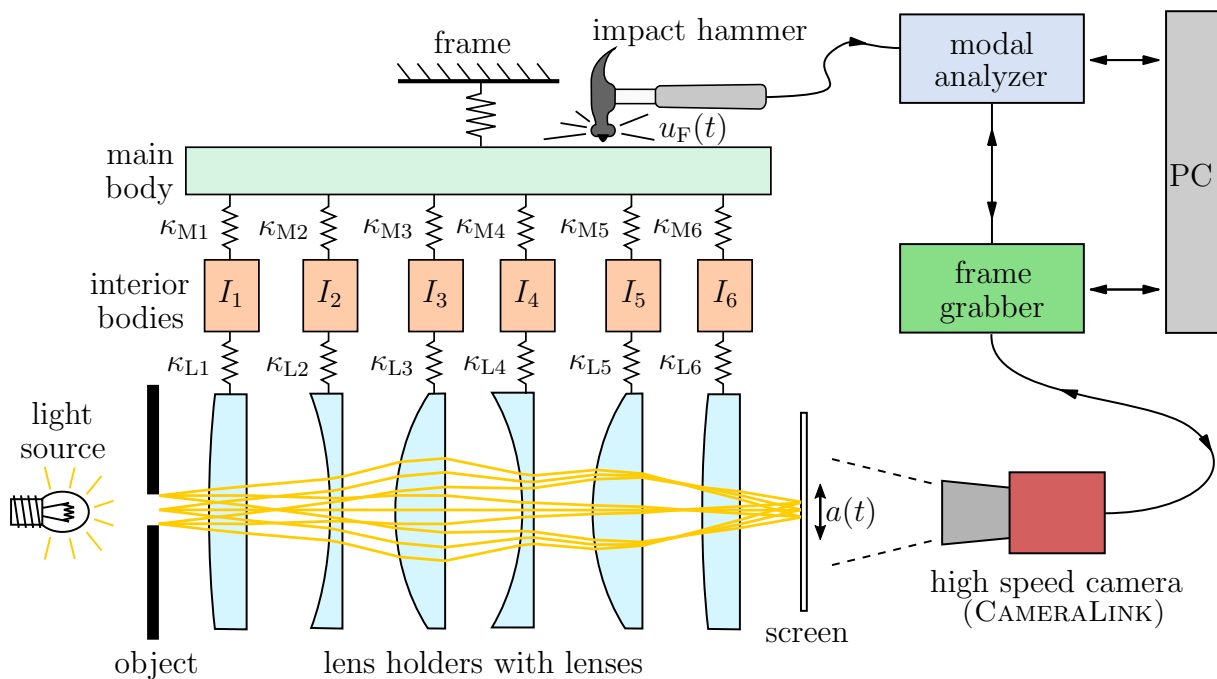


Figure 5.1: Principle of the measurement setup: the coupled lenses with peripheral measurement devices, according to [WengertEberhard13].

are linear. Thus, the kinematic-optical sensitivities can express the relationship between the displacement of the lenses and the resulting optical aberrations. The matrix \mathbf{C}_a collects these sensitivities. The image displacement is the only regarded optical aberration. Hence, \mathbf{C}_a is a vector, and the equation for the system output can be read as

$$a(t) = \mathbf{C}_a \cdot \mathbf{q}(t). \quad (5.1)$$

The six lenses are supported with pendulums, which are coupled via springs to intermediate masses and the housing. Hence, the mechanical system has 13 DOF. Since the springs with the different stiffnesses κ_k are exchangeable and the moments of inertia I_k are modifiable, it is possible to create different test systems, e.g., with low frequencies and high amplitudes. Anyway, the simplified equations of motion result with the structure

$$\mathbf{M}(I_k) \cdot \ddot{\mathbf{q}}(t) + \mathbf{D} \cdot \dot{\mathbf{q}}(t) + \mathbf{K}(\kappa_k) \cdot \mathbf{q}(t) = \bar{\mathbf{B}} u_F(t) \quad (5.2)$$

with the inertia-depending mass matrix \mathbf{M} , the damping matrix \mathbf{D} , the spring-depending stiffness matrix \mathbf{K} and the mechanical input matrix $\bar{\mathbf{B}}$. The related force of the impact hammer, which acts as the system input $u_F(t)$, is measured as during a typical experimental modal analysis. In order to identify the image motion resulting as a system output, a high-speed camera with a Camera Link interface is used in combination with a frame grabber card. The latter is connected to a computer and triggered via the modal analyzer. After the recording of the frames, the image processing for the motion identification of the light point is done. With the knowledge of the force input and image motion output of the mechanical-optical system, the dynamical-optical transfer function can be experimentally identified. By neglecting the damping properties of the real springs and hinges, the system of equations (5.2) and (5.1) can be simplified, rewritten in modal coordinates and transformed to the frequency domain, see also [StörkleWengertEberhard14]. As a consequence, the related transfer function with the individual eigenfrequencies ω_j results as

$$H(i\omega) := \frac{a(i\omega)}{u_F(i\omega)} = \sum_{j=1} \frac{\tilde{C}_{a,j} \tilde{B}_j}{\omega_j^2 - \omega^2} \quad (5.3)$$

with the components of the modal kinematic-optical sensitivities $\tilde{C}_{a,j}$ and the components of the modal-transformed input matrix \tilde{B}_j . These eigenfrequencies and the related amplitudes can be validated with the measurement of the image motion and the experimental modal analysis [Wengert16].

Since the dynamical behavior of the mechanical system can be adjusted via the exchangeable springs and modifiable moments of inertia, an optimization can be performed with the design parameters κ_k and I_k . For that, a criterion could be to minimize the dynamical-optical sensitivity, i.e. a force excitation should result in a minimal image motion. This

leads to the reformulated optimization problem

$$\min_{\kappa_k, I_k} f(\kappa_k, I_k) \quad \text{with} \quad f(\kappa_k, I_k) = \sum_{j=1} \frac{\tilde{C}_{a,j}(\kappa_k, I_k) \tilde{B}_j(\kappa_k, I_k)}{2\omega_j} u_F(\omega_j), \quad (5.4)$$

whereby further details and the optimization results, which show that the dynamical-optical robustness can be significantly improved, are described in [Wengert16, Zheng15, StörkleWengertEberhard14].

Figure 5.2 shows the actual realization of the setup with horizontal lens motions. Despite the pendulum design and the use of translational springs according to Figure 5.2(a), the mechanical system can be considered to behave linear for small excitations and displacements, as investigated in [Teske16]. Most of the construction parts shown in Figure 5.2(b) are designed using CAD, realized with acrylic glass and manufactured with a laser cutting machine.

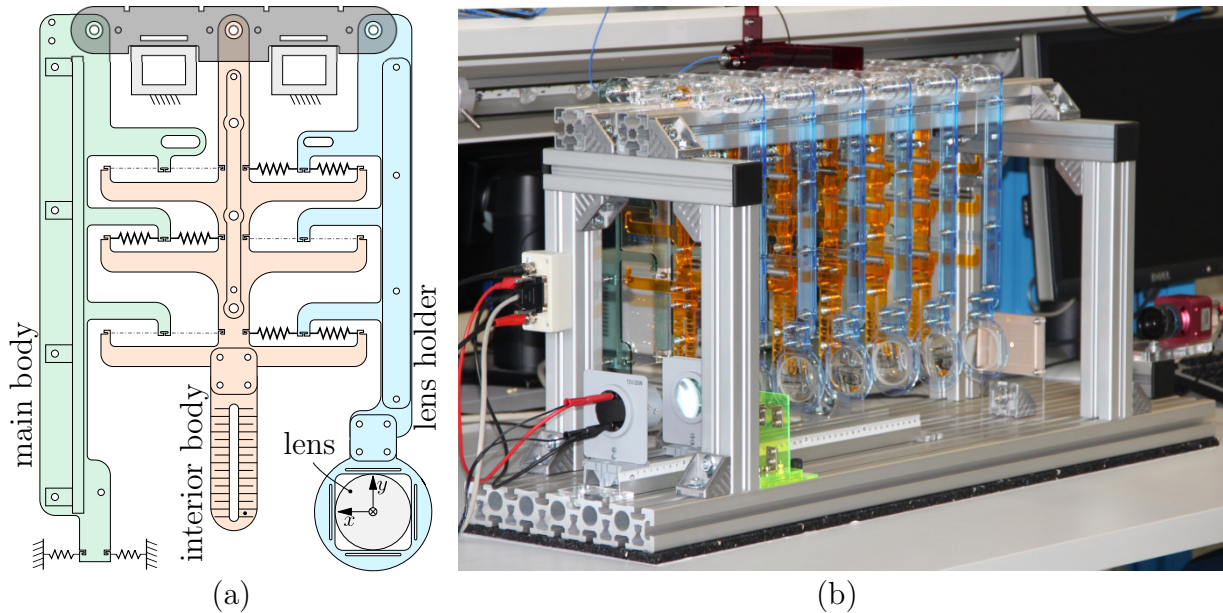


Figure 5.2: The realization of a single mass-spring component of the experimental setup in (a), and a photograph of the initial setup for the passive suppression of the optical aberrations in (b).

In conclusion, this introduced test setup demonstrates the influence of a structural optimization based on a dynamical-optical simulation model. However, in order to add technical features and further analyzing possibilities, the experiment is extended as described in the following.

5.1.2 Active Control Extension

The purpose of the extended setup is, to realize and demonstrate an actively controlled image stabilization experiment based on a dynamical-optical simulation model, an actuator,

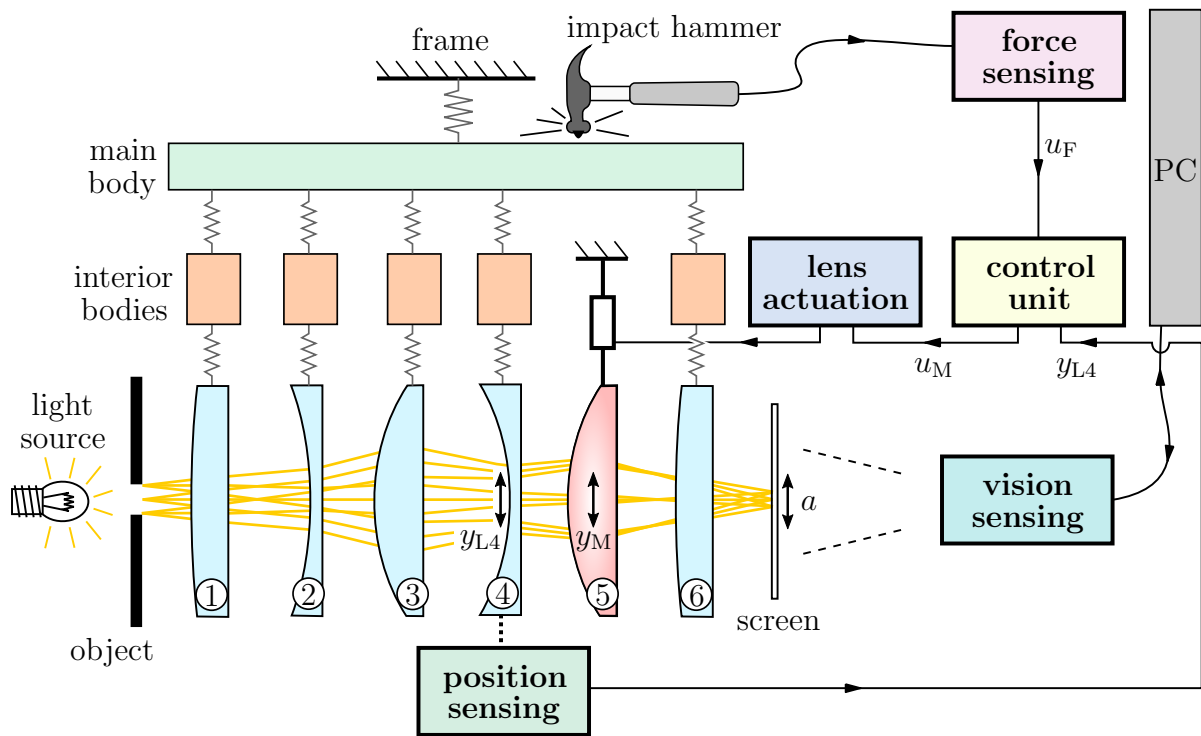


Figure 5.3: Principle of the extended setup.

and different sensors. Therefore, in particular, the 5th lens according to Figure 5.3 is mounted on a linear actuator stage to compensate for the optical aberrations actively. Furthermore, the position of the 4th lens is measured to allow a model-based estimation of the light point motion.

At first, the changed mechanical multibody system without the 5th lens and its intermediate mass is derived and identified in the form of the equations of motion (5.2) with 11 DOF. For the stiffnesses and moments of inertia the initial design parameters according to [Wengert16] are chosen. Figure 5.4 illustrates the related pole-zero map and Figure 5.5 compares the image motion calculated by the simulation model with the results of the vision sensor system. For this, the Rayleigh damping parameters $\alpha_R = 0.03 \text{ s}^{-1}$ and $\beta_R = 3 \cdot 10^{-4} \text{ s}$ are estimated, the controller is deactivated and a hammer shock is applied. The results in Figure 5.5 indicate that the simulation model meets the real system behavior quite well, shortly after the impact. However, the model-based result diverges after the first few seconds, since the linear model of the free-running pendulums is only a simplified approximation of the real behavior, e.g., since the bearing friction is neglected.

According to Figure 5.3 and in contrast to the previous setup, the control setup looks quite complicated, although the image stabilization task seems very simple. Actually, the pure purely force-induced image error, denoted as displacement a_F , has to be negatively superposed with the image error a_M caused by the shift of the compensation lens. In order

Figure 5.4: Pole-zero map of the modeled multibody system. Since the imaginary parts of the eigenvalues are between approximately 20 rad/s and 80 rad/s, the eigenfrequencies are in the range of 3 Hz to 13 Hz.

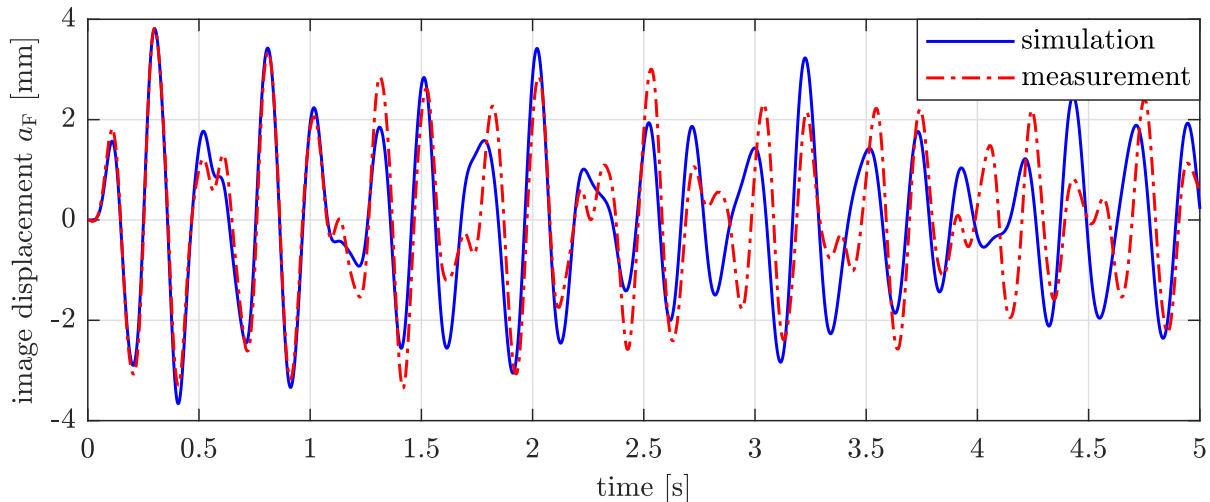
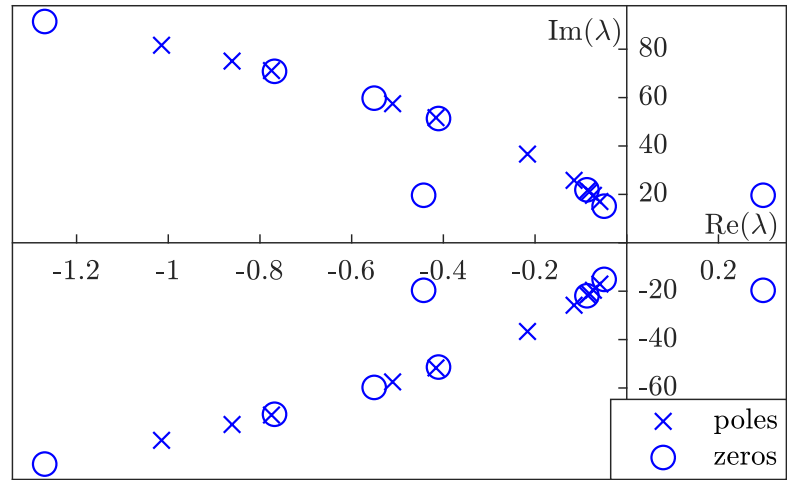


Figure 5.5: Comparison of the simulated and measured image motion due to a hammer shock, for the model with 11 DOF.

to extinguish the total imaging error a according to Equation (5.1), it yields

$$a(t) = a_F(t) + a_M(t) \stackrel{!}{=} 0. \quad (5.5)$$

With the kinematic-optical sensitivity s_{L5} of this compensation lens, as listed in Table 5.1 and obtained by experiments [Wengert16] and simulations [Teske16], the required position of the related actuator results in

$$y_{M,\text{target}}(t) = -\frac{a_F(t)}{s_{L5}}. \quad (5.6)$$

This finding can be used to estimate the requirements for the actuator system, as investigated in [Teske16]. The required travel range is approximately 6 mm and the velocity should be at least 100 mm/s.

Table 5.1: Kinematic-optical sensitivities of the 6 lenses, identified in [Teske16].

denotation	s_{L1}	s_{L2}	s_{L3}	s_{L4}	s_{L5}	s_{L6}
value $\left[\frac{\text{aberration in mm}}{\text{displacement in mm}} \right]$	0.071	-0.366	1.303	-0.913	1.394	0.145

However, an actuator and vision sensor behave time-delayed due to the subordinate motor control, the inherent latency of the camera, the image acquisition, and the expensive image processing. According to further investigations of the overall system, the vision sensor system requires a maximum sample time of 5 ms and real-time capability to provide stabilizing feedback. Therefore, an appropriate industrial machine vision system with a high-performance processor should be used, as explained in [West01]. Due to the low-cost vision system *Basler ace-acA800-200gm* used in this work for an educational purpose, it is therefore not possible to fulfill the real-time and sample time requirements. As a result, the vision sensing system is only used for the offline assessment of the image stabilization task. Nevertheless, to realize the dynamical-optical control based on feedback, the following approach is chosen.

A real-time capable control unit system *Arduino Due* with a sample time of 2-8 ms is used in combination with a position sensor at the 4th lens. This model-based controller handles the signal u_F of the force subsystem and the signal y_{L4} of the position sensor subsystem, estimates the expected image aberration through a state observer, and commands the actuator subsystem with the signal u_M accordingly. Figure 5.3 indicates the corresponding subsystems with labeled boxes.

In the following section, these subsystems are described and arranged. The functional principles, the hardware designs, the specified settings and the related signal processing are thereby explained.

5.2 Arrangement of the Hardware Systems

The hardware setup of the final system is shown in Figure 5.6 and discussed in this section. The main devices and the signal flows for the communications are shown. In addition, the most important analog signals u_F , y_{L4} , u_M and y_M are highlighted, which can be monitored with an oscilloscope.

At the lower left, the linear actuator stage is illustrated, which mounts the compensation lens. This motor is driven and positioned by the related motor controller. It steers the stage according to a given analog input, which represents the commanded trajectory given from the main control unit system. The latter is realized by means of the *Arduino Due*. In order to provide a lens position feedback for the dynamical-optical control, a Hall-effect

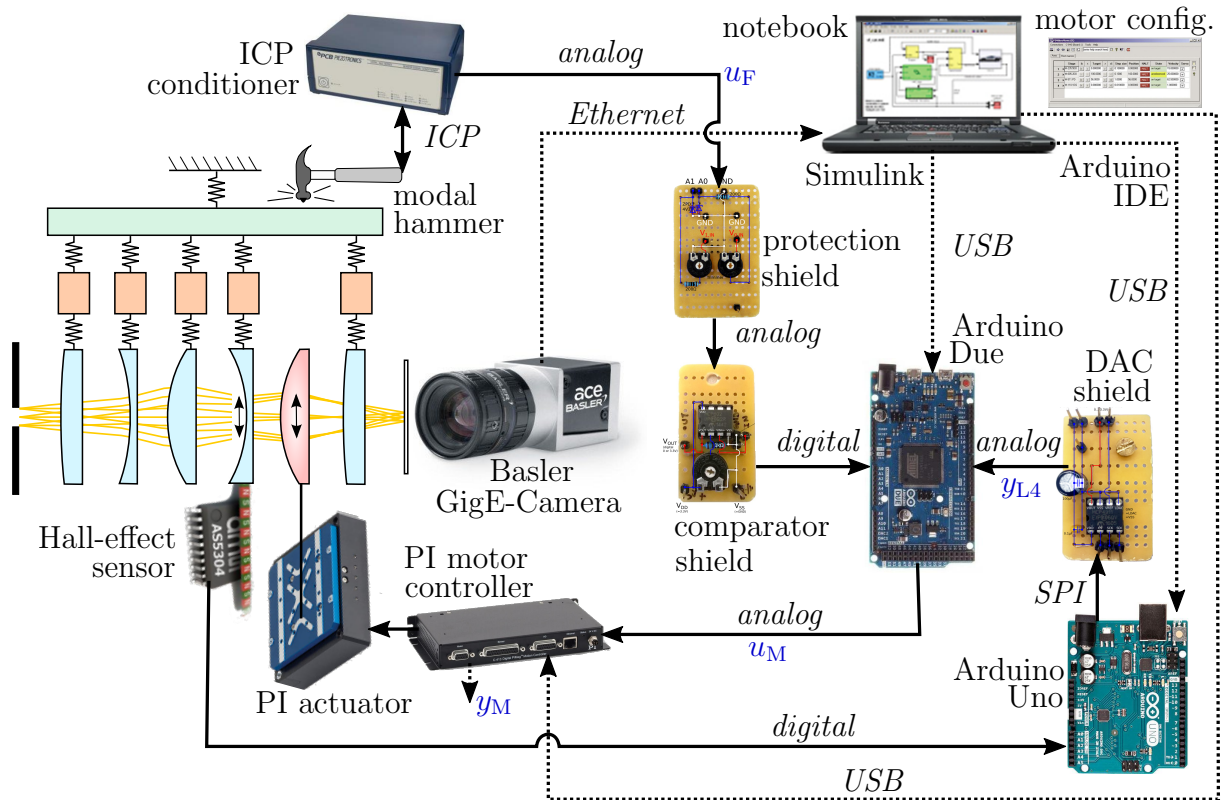


Figure 5.6: Overview of the hardware realization for the dynamical-optical control.

sensor is utilized, which is monitored by an *Arduino Uno*. For the transmission of the position data to the *Arduino Due*, a digital-analog converter is used, which provides the information by means of an analog signal.

At the upper left, the devices for sensing the force are depicted. Since the modal hammer has a force sensor included, which is based on the integrated circuit piezoelectric (ICP) technology, it needs to be supplied by an ICP conditioner. This device supplies the sensor and further amplifies the slight force signal to a recognizable analog signal. In order to prevent the occurrence of high voltages, a protection shield is interposed, and besides, a comparator shield is used to trigger the feed-forward control within the *Arduino Due*. During the deployment of the software on the microcontrollers, they have to be connected to the notebook. Also for the configuration of the motor controller, it must be plugged into the notebook. Finally, for offline verification purposes, the *Basler GigE camera* can be connected to the notebook, which further can perform an image processing.

Figure 5.7 depicts the final setup in the laboratory during the experiments. The oscilloscope and the notebook are only required for the monitoring, analysis, and assessment of the controller performance.

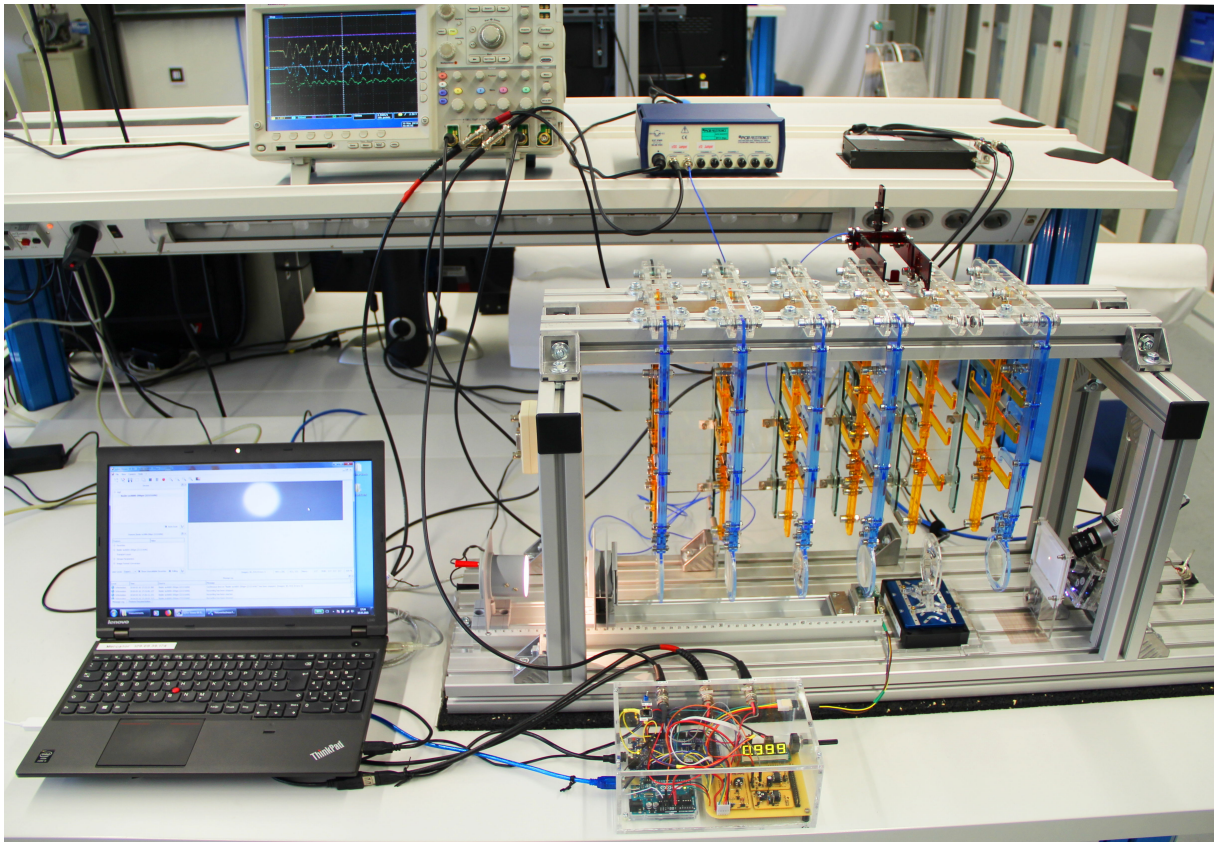


Figure 5.7: Final setup with the active control extension, captured in the laboratory.

5.2.1 Lens Actuator System

The actuator system is realized with the *V-528.1 PIMag Linear Stage* [PI16] and the related *C-413.20A PIMag Motion Controller* [PI15], which are illustrated in Figure 5.8. This motor meets the requirements formulated in Section 5.1.2 since it has a travel range of 20 mm and maximal velocity of 250 mm/s. The compensation lens is mounted onto the motor stage through stiff and lightweight construction, as shown in Figure 5.8(a). It consists of acrylic glass and aligns the 5th lens with the other lenses on the optical axis for the initial position $y_M = 0$ mm. In order to power, to position and to move the stage, an appropriate motor controller has to be used, depicted in Figure 5.8(b). In particular, the chosen type of device can also handle analog inputs and can report information by means of analog outputs. Thus, it can control the stage position according to a commanded position u_M and the actual value y_M of the position encoder can be monitored.

For the configuration of the related parameters as well as for necessary tests, the motion controller can be connected to a computer via USB. The supplemented *PIMikroMove* software allows not only to adjust the trajectory tracking control based on a PID cascade but also to change the filter settings. On the one hand, this can reduce the noise of the incoming signal, and on the other hand, it can introduce an undesirable phase shift causing

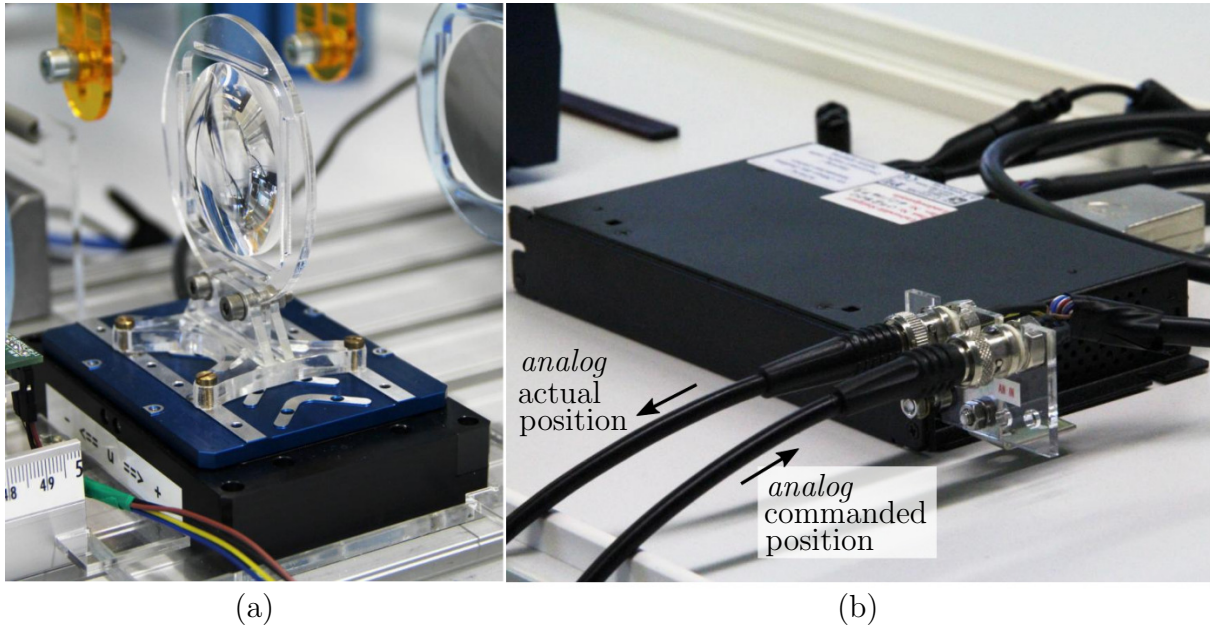


Figure 5.8: The V-528.1 PIMag Linear Stage (a) and the C-413.20A PIMag Motion Controller (b).

a time lag. Thanks to a dynamic link library, which is also provided by the manufacturer, the configuration, and the quasi-static actuator position can be adjusted using Matlab or LabView.

Additionally, the incoming and outgoing analog signals can be scaled. In the so-called *analog input control source mode*, an input voltage given by a normalized value V_n is translated to a position scaled value V_s with

$$V_s = \Delta V + K V_n. \quad (5.7)$$

For example, if the input voltage range is $[0.55, 2.75]$ V, this results in $V_n = [5.5, 27.5]$. The ΔV is the adjustable offset and K is the adoptable gain. In case of an individual position range, the related parameters have to be calculated by

$$K = \frac{V_{s,\max} - V_{s,\min}}{V_{n,\max} - V_{n,\min}} \quad \text{and} \quad \Delta V = V_{s,\max} - K V_{n,\max}. \quad (5.8)$$

As an example, if a travel range of $[-5, 5]$ mm should be reached with the input voltage range mentioned above, the parameters are $K = \frac{5 - (-5)}{27.5 - 5.5} = 0.44$ mm and $\Delta V = -7.22$ mm.

Furthermore, the integrated *Profile Generator* is enabled by default, which plans a smooth trajectory according to the given input signal. However, for a fast response behavior, this should be deactivated, since it results in a significant delay between the analog input signal of commanded position and the actual position of the stage. As a result, the trajectory tracking control is mainly determined by the servo PID-control parameters and low-pass filter settings, which are tuned empirically.

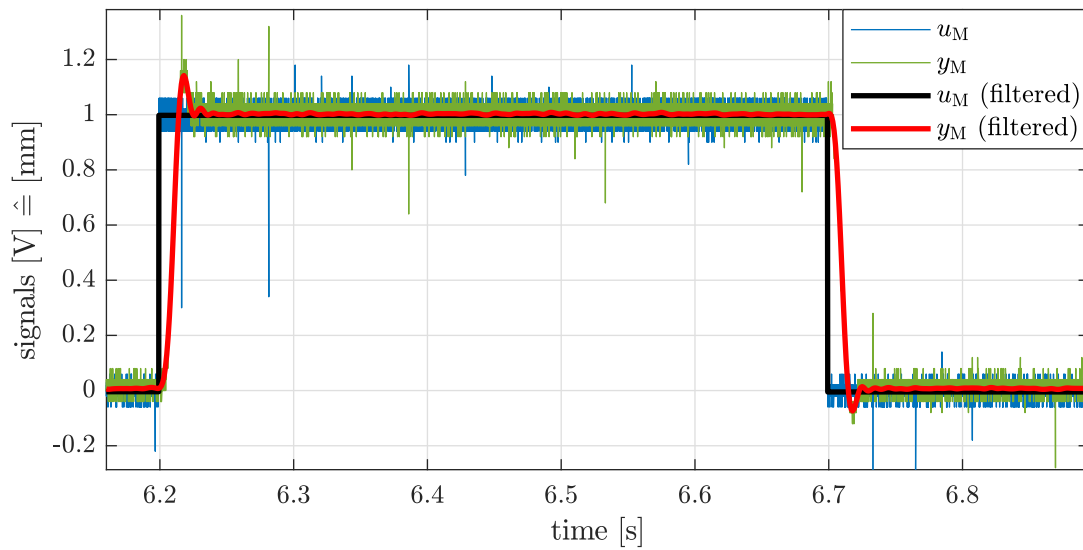


Figure 5.9: Measured step response of the closed-loop lens actuator system.

Next, the behavior of the closed-loop lens actuator system is identified for further simulations. Figure 5.9 shows the measured step response, where the analog signal of the commanded position u_M and the actual position y_M of the motor encoder are recorded with an oscilloscope. Thereby, these input and output signals of the *Motion Controller* are scaled so that 1 V corresponds to 1 mm. In order to analyze the noisy signals further, a 5th-order Butterworth filter with a cutoff frequency of 100 Hz is applied. The resulting data is used to estimate a simplified closed-loop transfer function of the actuator system through the instrumental variable (IV) method [YoungJakeman80]. This IV method is implemented in the `tfest` function of the System Identification Toolbox in Matlab.

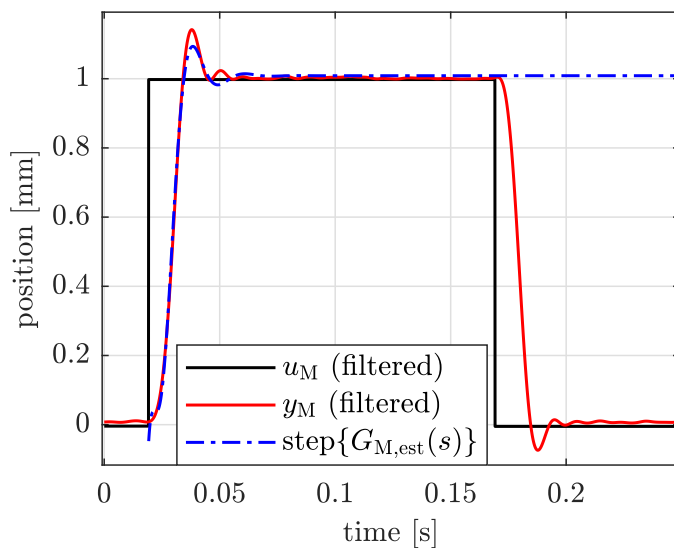


Figure 5.10: Step responses of the measured and the identified system.

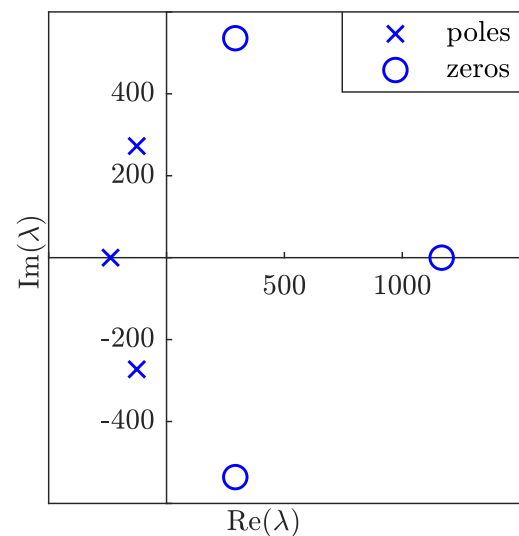


Figure 5.11: Pole-zero map of the identified system.

The step response of the estimated transfer function $G_{M,\text{est}}(s)$ in comparison to the measurement y_M is illustrated in Figure 5.10. It is obvious that the main behavior is well approximated, despite the rough estimation with only three poles and three zeros, as represented in Figure 5.11. The initial direction of the simulated step response followed by a direction reversal is due to the positive zeros of the transfer function [HoaggBernstein07]. Since the real lens actuator system in the closed-loop mode behaves nonlinear, the estimated step response is representative for only steps of around 1 mm, as regarded. Besides, higher steps are investigated during the system identification process. However, it turns out during the later dynamical-optical control, that the motor behavior is quite well represented through the considered transfer function scaled by a factor of 0.97, as plotted in Figure 5.12. Roughly speaking, the time difference between the signals $u_M(t)$ and $y_M(t)$ for the target travel profile is about 8 ms.

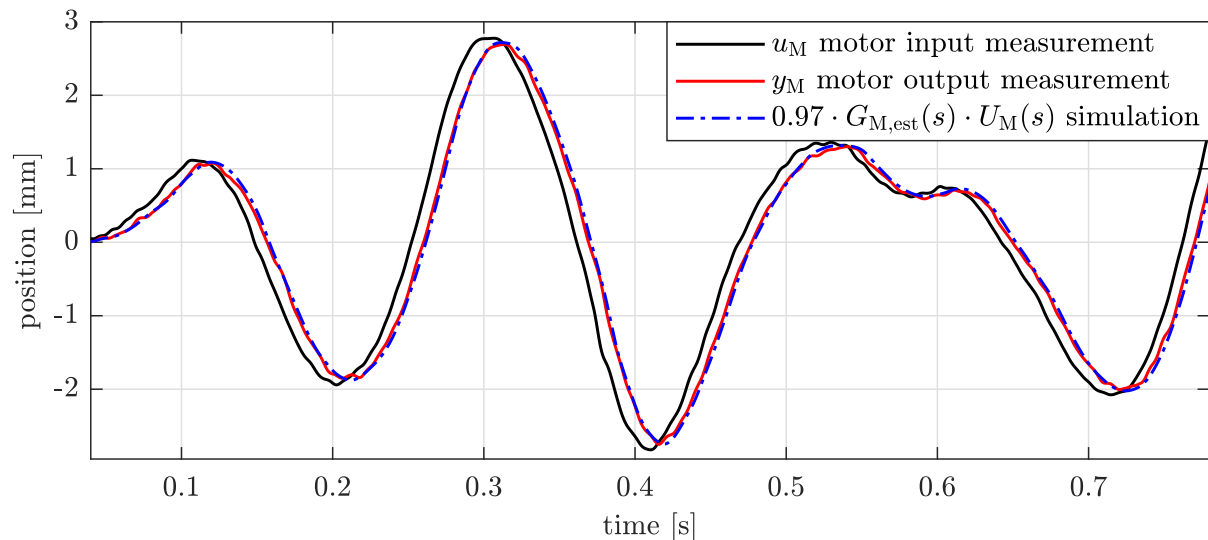


Figure 5.12: Measured response during the hammer impulse of the closed-loop lens actuator system in comparison to the response simulated with the identified transfer function.

5.2.2 Force Sensor System

In order to excite the mechanical system with a detectable force, a modal hammer is utilized. It is installed in a pendulum mechanism according to Figure 5.13(a) for the generation of a reproducible impulse. The related *ICP conditioner* according to [PCB16] is illustrated in Figure 5.13(b). It not only powers the corresponding force sensor at the hammer tip, but it also provides a signal proportional to the force, and a further amplification can be applied, e.g., by a factor of 100. However, if the hammer shock is accidentally strong, too strong voltages can damage at the sensitive microcontroller input. In order to limit the voltage signal, a protection shield is realized according to Figure 5.14.

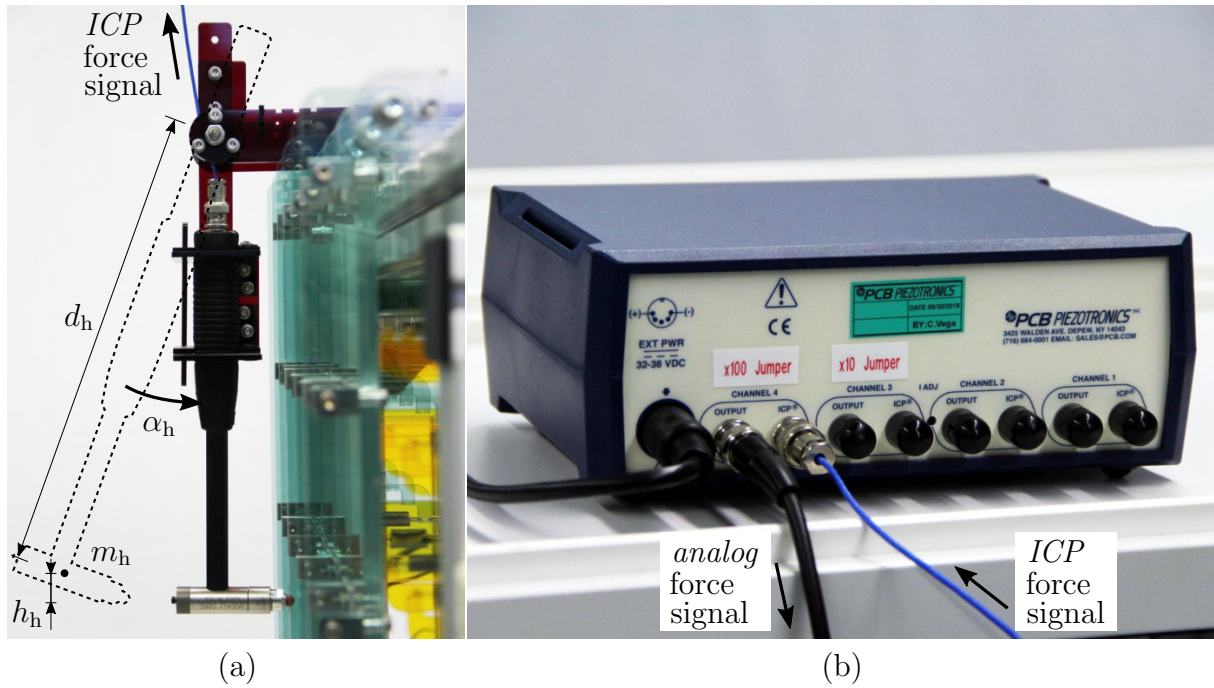


Figure 5.13: Mounted modal hammer with integrated piezoelectric force sensor (a) and the related ICP conditioner (b).

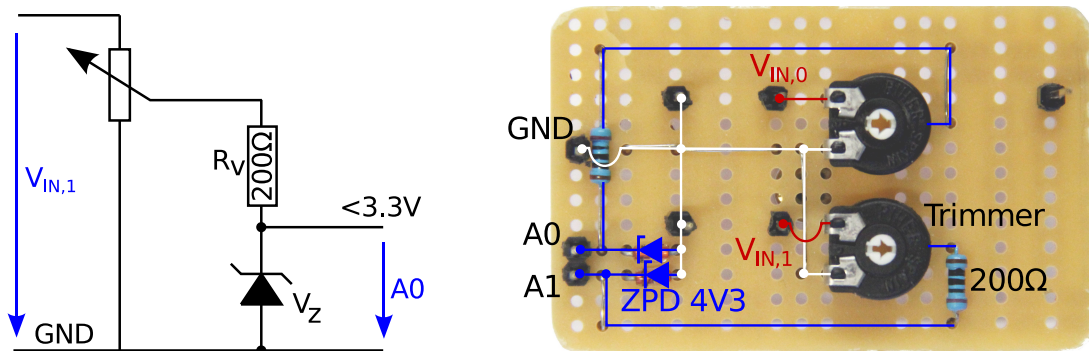


Figure 5.14: Electric circuit and photograph of the protection shield for two channels based on Zener diodes and resistors.

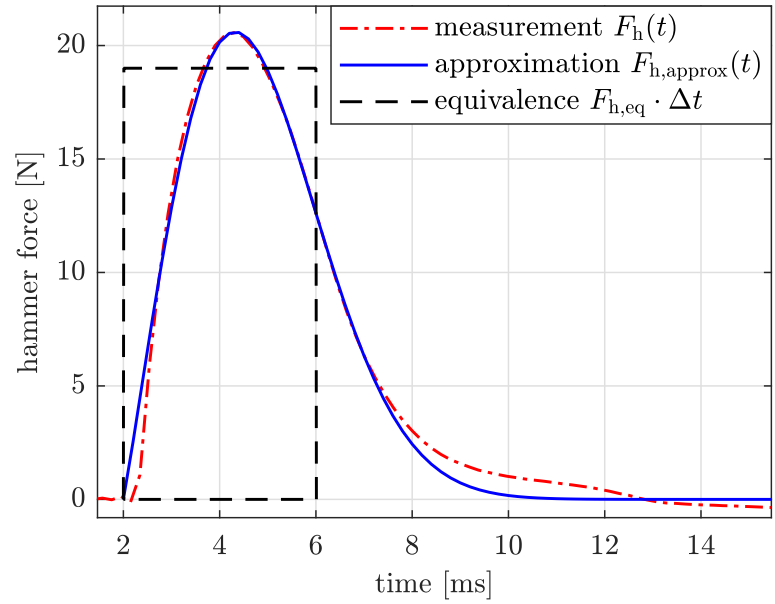
Since the manufacturer specifies the sensor sensitivity in mV/N, one can translate the measured voltage to the actual force distribution $F_h(t)$, as shown in Figure 5.15. In addition, the force distribution can be approximated by

$$F_{h,\text{approx}}(t) = p_3 \left(\frac{t}{p_1} \right)^{(p_2-1)} e^{-\left(\frac{t}{p_1}\right)^{p_2}} \quad (5.9)$$

with the parameters $p_1 = 0.0032$ s, $p_2 = 2.065$ and $p_3 = 48.55$ N. This simplifies the numerical simulation and prevents the use of a lookup-table. For the validation of the measured force, the change in momentum can be estimated with

$$\Delta p_h = \int_{t_1}^{t_2} F_h(t) dt = m_h \Delta v_h, \quad (5.10)$$

Figure 5.15: The measured hammer force F_h during an impulse excitation. In addition, the approximated function $F_{h,\text{approx}}$ is shown and $F_{h,\text{eq}}\Delta t$ indicates the area of an equivalent force impact.



where t_1 and t_2 denote the regarded time period, m_h is the hammer mass and Δv_h describes the change of the velocity. Within the period $[2, 10]$ ms, the area under the measured curve amounts to $\Delta p_h = 0.0764$ Ns. The unknown velocity can be estimated by means of the energy conservation, so the equivalence of the kinetic and potential energy can be written as

$$\frac{1}{2}m_h v_h^2 = m_h g h_h \quad (5.11)$$

with the gravitational constant g . Furthermore, the mechanism allows according to Figure 5.13(a) a maximal twist of $\alpha_h = 20^\circ$. The distance between the bearing and hammer hat is known as $d_h = 0.220$ m. Thus, the velocity of the hammer tip immediately before the shock can be estimated to

$$v_h = \sqrt{2 g L_h (1 - \cos(\alpha_h))} \approx 0.51 \frac{\text{m}}{\text{s}}. \quad (5.12)$$

If one assumes, that the kinetic energy of the hammer is completely transferred to the shock, it yields $\Delta v_h = v_h$. Finally the mass can be validated by means of Equation (5.10) with

$$m_h = \frac{\Delta p_h}{v_h} \approx 150 \text{ g}, \quad (5.13)$$

which is close to the actual mass of the hammer hat.

The magnitude of excitation does not change due to the determined mechanism. Therefore, the computational effort for the overarching control unit can be reduced, since the change of momentum can also be replaced by a constant equivalent force acting for a sample time of, e.g., $\Delta t = 4$ ms. This procedure leads to

$$F_{h,\text{eq}} = \frac{\Delta p_h}{\Delta t} \approx 19 \text{ N}, \quad (5.14)$$

which is also indicated in Figure 5.15. Consequently, the control unit only needs to get a trigger signal immediately when the hammer is hitting the main body. Therefore, one can use a comparator circuit consisting of an operational amplifier. Moreover, a trimmer can be added to activate the switch only for inputs above an adjustable threshold value. The load resistor further stabilizes the output signal. Figure 5.16 shows the realized comparator shield based on the *Microchip Technology MCP602* [MT07] and the related electric circuit.

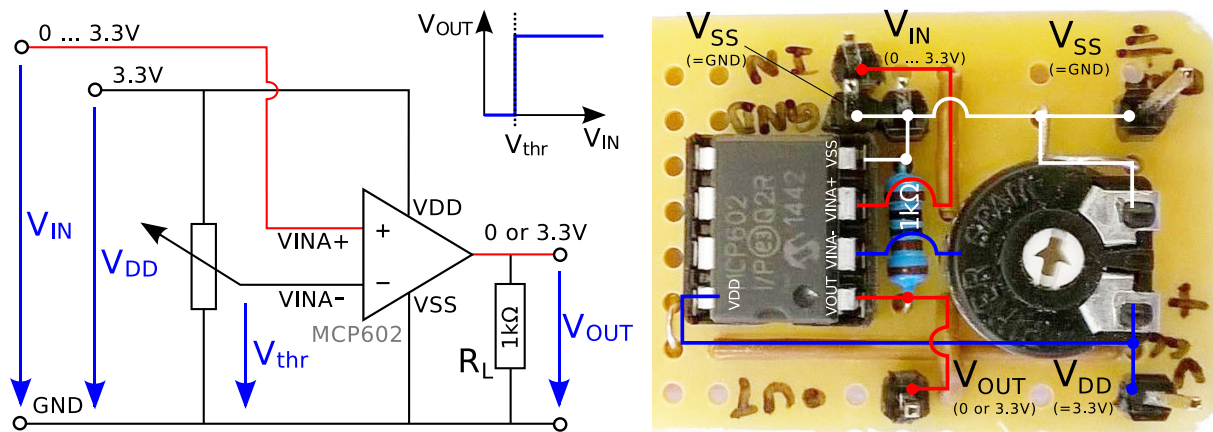


Figure 5.16: Electric circuit and photograph of the comparator shield based on the operational amplifier chip MCP602 and several resistors.

5.2.3 Position Sensor System

As mentioned in Section 5.1.2, a position sensor is utilized to observe the behavior of the mechanical system and to estimate the image displacement through a KF. Therefore, the low cost *AS5306 magnetic incremental linear position sensor* according to [AMS17], which is based on the Hall-effect, is installed at the 4th pendulum. For the detailed fundamentals and the principles of operation see [Ramsden11]. In combination with the *Magnetic Multipole Strip MS12-15*, described in [AMS14] and shown in Figure 5.17(a) and 5.17(b), a wide range of displacements can be detected. Each pole of the corresponding magnet strip has a length of 1.2 mm and since they are next to each other, the vertical component of the magnetic field B_{pk} is changing with respect to the axial location. The considered Hall-effect sensor transforms this change to a digital signal with four connectors, two for the power supply and the other two provide a quadrature incremental output. This output consists of the quadrature signal A and the 90°-shifted signal B , which further allows to identify the travel direction. Figure 5.17(c) indicates an exemplary measurement nearby a pole pair.

Thanks to an included interpolation circuit, the length of a pole pair is divided into 160 positions, and it is further decoded into 40 quadrature pulses, see also [AMS17]. As a

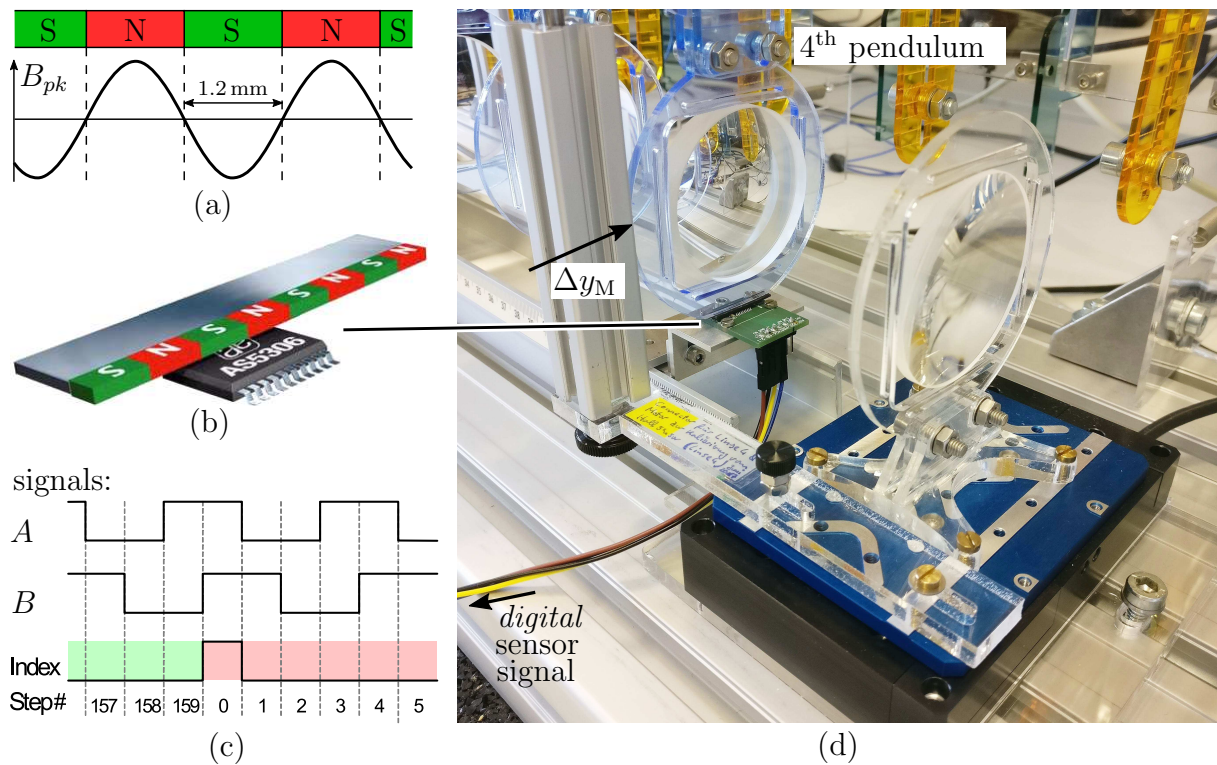


Figure 5.17: Illustrations of the operating principles of the Hall-effect sensor in (a), (b) and (c). In (d) the setup is shown during the validation of the sensor by means of the firmly connected actuator.

result, the sensor resolution yields approximately $15\ \mu\text{m}$. The magnetic strip is slightly bent and glued to the bottom of the 4th pendulum. Furthermore, the Hall-effect sensor is fixed to the ground, as shown in Figure 5.17(d). Hence, the constant gap between the magnet and the chip of about $0.5\ \text{mm}$ can be ensured.

In order to obtain the actual measured position, an *Arduino Uno* microcontroller is used, which runs an interrupt-based quadrature decoding algorithm represented in Listing 5.1. Due to a production-related deviation of the pole length and the slight bending of the magnetic strip, the step width of the sensor is empirically adjusted to $13.6\ \mu\text{m}$.

Listing 5.1: Code example for the Arduino sketch, which represents an interrupt-based quadrature decoding algorithm similar to [MyDiyElectronics14].

```

volatile float distance = 0; // in mm
const byte pinA = 3;
const byte pinB = 2;
void setup(){
  Serial.begin(9600); //start serial connection
  pinMode(pinA, INPUT); //signal A
  pinMode(pinB, INPUT); //signal B
  attachInterrupt(digitalPinToInterrupt(pinA), APulse, CHANGE);
  attachInterrupt(digitalPinToInterrupt(pinB), BPulse, CHANGE);
}

```

```

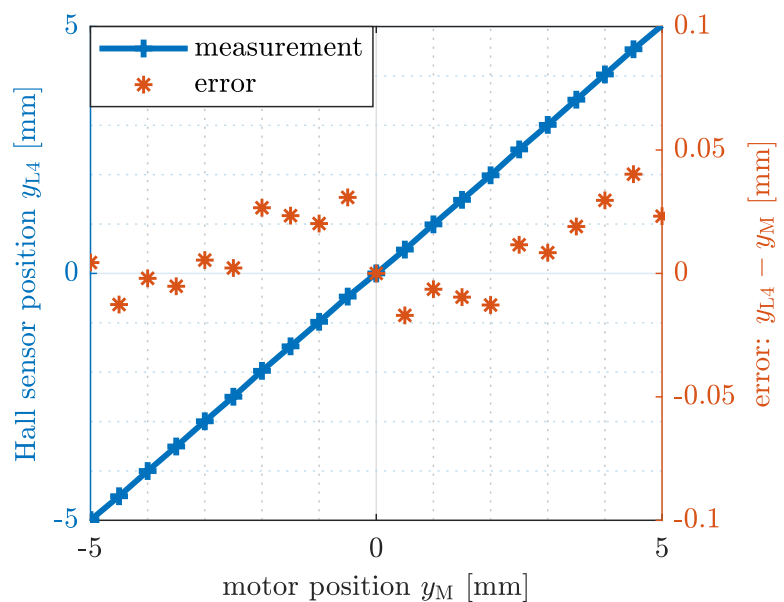
void APulse(){
  if (digitalRead(2) == digitalRead(3))
    distance += 0.0136;
  else
    distance -= 0.0136;
}
void BPulse(){
  if (digitalRead(2) == digitalRead(3))
    distance -= 0.0136;
  else
    distance += 0.0136;
}
void loop(){
  Serial.println(distance); // Print to serial monitor
}

```

For the validation of the position sensor subsystem, the 4th lens is connected to the high precision linear actuator, see Figure 5.17(d). Then, the lens is quasi-statically displaced employing the motor with 0.5 mm steps. As a result, the measured position y_{L4} of the Hall-effect sensor according to Figure 5.18 is analyzed. The measurement shows that y_M and y_{L4} are almost identical, with a slight error of the absolute position of maximum $\pm 40 \mu\text{m}$, as indicated with respect to the axis on the right-hand side.

In order to transfer the lens position in a range of $[-8, 8]$ mm to the control unit, an external 10 bit digital-analog converter (DAC) is utilized. It is connected via a serial peripheral interface (SPI) to the Arduino Uno and is realized with a *Microchip Technology MCP4911* according to [MT10]. The analog output is determined in the range of $[0, 3.3]$ V, which is suitable for the analog input of the Arduino Due. Figure 5.19 presents the measured lens position y_{L4} for a typical hammer impulse within the first two seconds.

Figure 5.18: Validation of the position y_{L4} measured by the Hall-effect sensor. The difference of the measured and the actual position is represented as the error, with respect to the axis on the right-hand side.



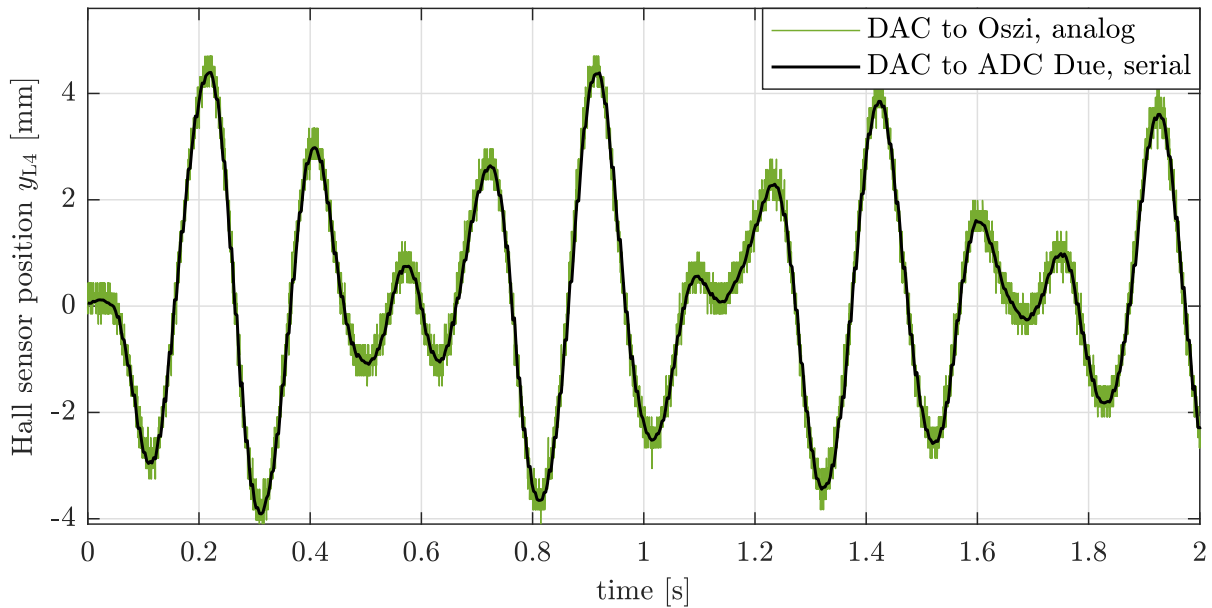
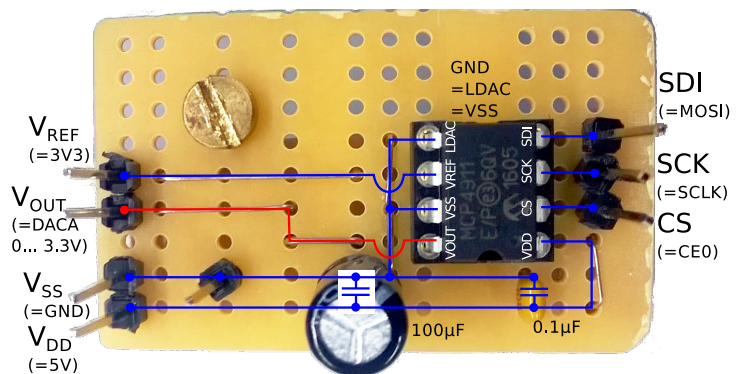


Figure 5.19: The lens position based on the Hall-effect sensor is monitored by the Arduino Uno and communicated to the external DAC.

Thereby, the analog signal of the DAC is compared to the signal detected by the control unit, which uses a 12 bit analog-digital converter (ADC) and can write the values via the serial interface to a text file on a computer.

The *MCP4911* is soldered on a separate board since it further needs some capacitors. As a result, Figure 5.20 depicts the realized DAC shield and the related electric circuit.

Figure 5.20: The realized DAC shield, which is based on the *MCP4911* microchip. It is recommended to use it in combination with capacitors.



5.2.4 Control Unit System

The *Arduino Due* board performs the main control task. It provides not only multiple analog inputs but also two analog outputs, all of them with 12 bits resolution. With the clock speed of 84 MHz and flash memory of 512 KB, it is currently the most capable Arduino board that is compatible with the *Simulink Support Package for Arduino Hardware*, see

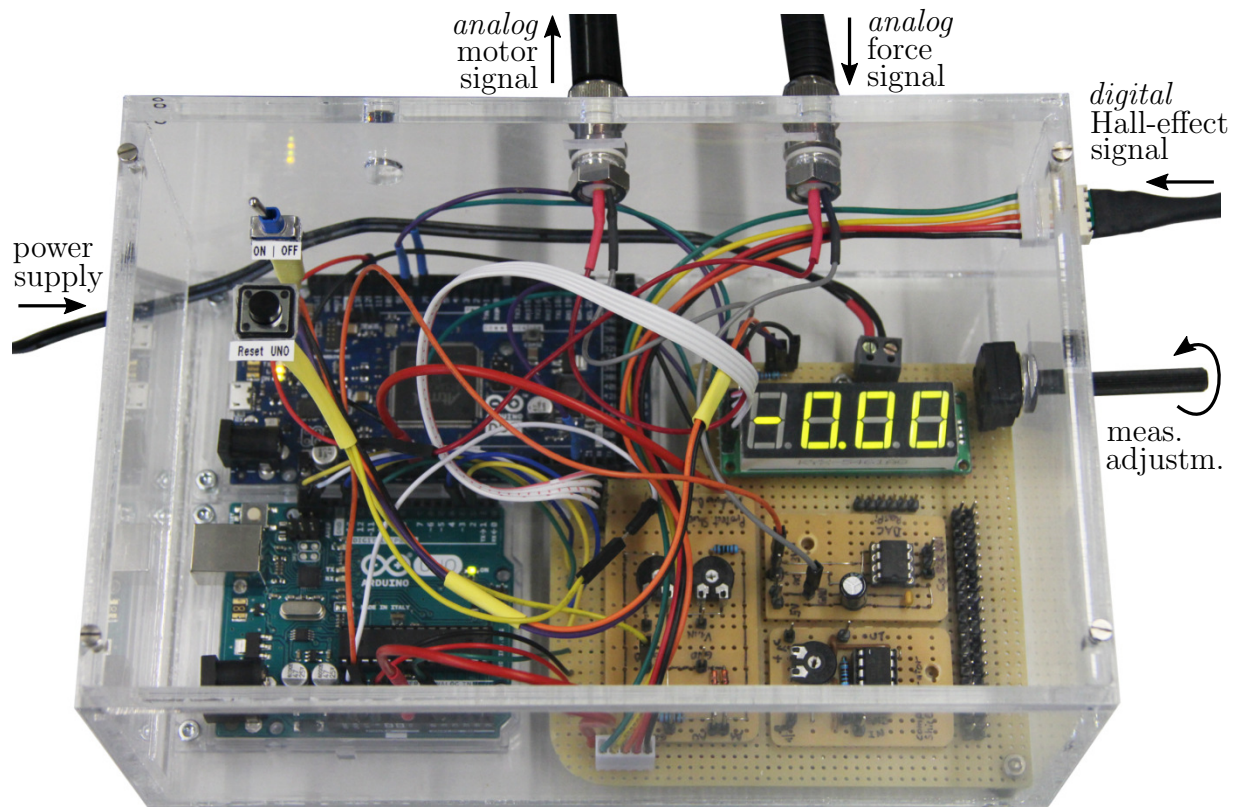


Figure 5.21: The final hardware box containing the Arduino microcontrollers and the additional boards for the signal processing.

also [Mathworks18]. Thus, a control algorithm can be graphically developed using Simulink, which is commonly taught to students during their university education. As a result, it is well suited to visualize the structure of a control strategy and to demonstrate the change of parameters, for instance, during a student training in the laboratory. Based on the designed model, the Simulink Support Package is generating C-code, performs a compilation appropriately to the processor, and deploys the result to the USB-connected board. It is even possible to integrate custom Arduino libraries in Simulink via the *S-Function Block Builder*, as explained in [Medium17]. The minimal value of the constant sample time depends on the expenses of the algorithm, and the performance of the microcontroller limits it. For instance, if the model size is huge and the numerical integration cannot be performed within the determined sample time, it is automatically increased by the microcontroller. Hence, one should check the actual sample time, e.g., by means of writing out a periodic step signal at a digital output.

Figure 5.21 pictures the final hardware box, which contains not only the control unit board but also the introduced shields and devices of the other subsystems. Furthermore, a switch, a button, a rotary potentiometer and a display are installed for the activation of the controller, the adjustment of the measurement magnitude, performing a reset of the systems, and to information about the current control algorithm.

5.2.5 Vision Sensor System

In this last hardware section, the vision sensor system is described. It utilizes a *Basler ace-acA800-200gm* high-speed camera according to [Basler17] in combination with a *FL-CC1614A-2M* lens with a focal length of 16 mm. The camera is based on a complementary metal-oxide-semiconductor (CMOS) sensor, and it is connected to a standard notebook via Ethernet. On the one hand, it can be powered over Ethernet (PoE), whereby a particular Ethernet port has to be available. On the other hand, a separate power supply can be used. At the full resolution of 800×600 pixel, the maximum rate of monochrome images is 200 frames/s. This image acquisition is tested using the supplemented *Pylon Viewer* software and in combination with the *Pylon GigE Vision Driver*, see also [Basler15].

As an alternative, the camera can be used via the Image Acquisition Toolbox of Matlab/Simulink [Corke17], since it supports the GigE Vision standard. Figure 5.22 illustrates the block diagram of an example, where the current frame is grabbed from the device, the pixels are filtered by means of a threshold and the center of intensity is calculated with

$$x_I = \frac{\sum_i i \cdot I_{\text{col},i}}{\sum_i I_{\text{col},i}}. \quad (5.15)$$

The sums of the intensities with respect to each pixel column i are indicated with $I_{\text{col},i}$. Finally, the image and the resulting position can be displayed instantly.

However, this image acquisition and image processing require an enormous processor performance, and the used notebook does not run a real-time capable operating system. Therefore, the maximum frame rate is limited to approximately 66 frames/s and this value is further affected by the varying processor load.

As explained in Section 5.1.2, this low-cost vision sensor system is only intended for the offline assessment of the dynamical-optical control. Only if it were possible to acquire and

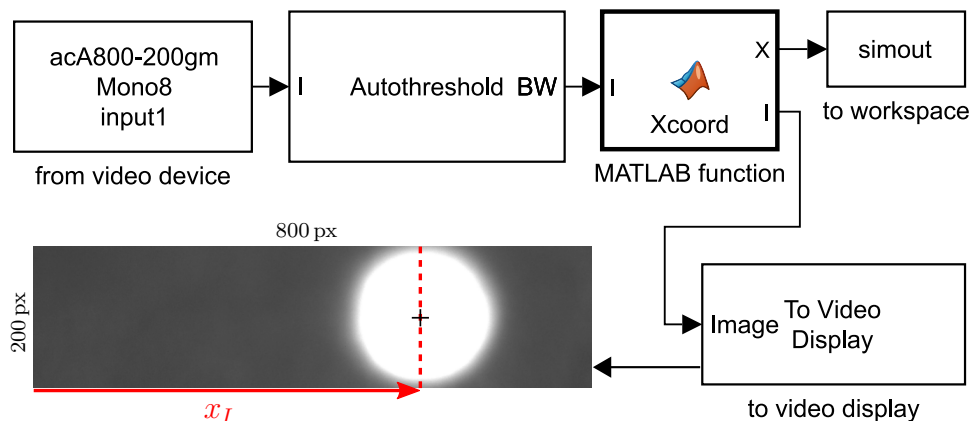


Figure 5.22: Example of a Simulink model for the image acquisition and image processing, in order to obtain the position of the light point. The model is based on the Image Acquisition Toolbox.



Figure 5.23: Back view of the installed camera.

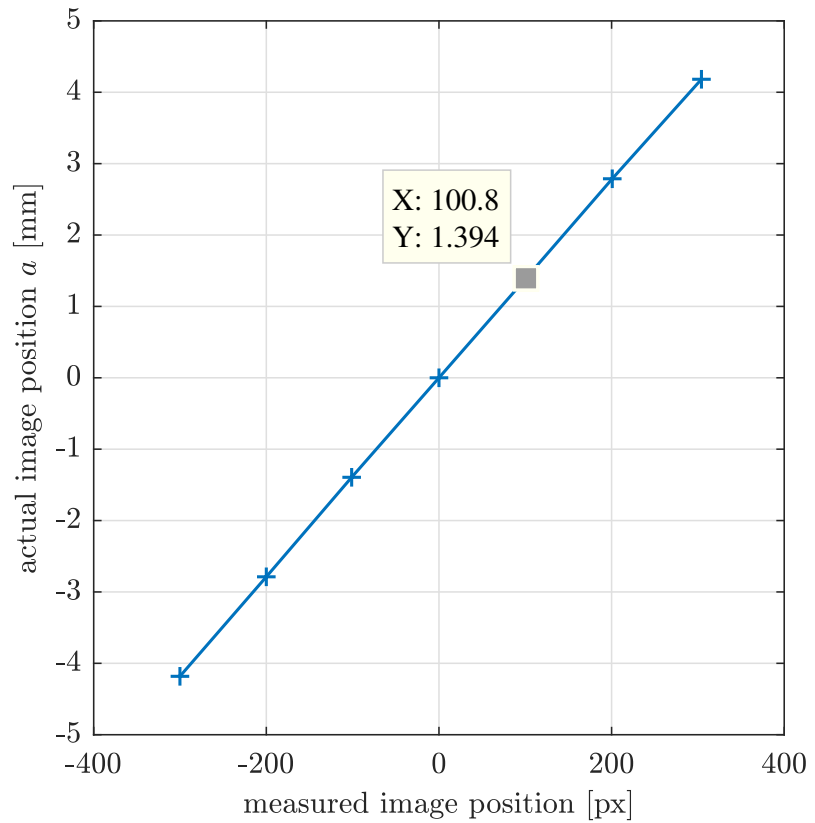


Figure 5.24: Calibration curve of the camera.

process one image within 5 ms, it would be feasible to use the visual feedback directly for the control. Another issue is to communicate the detected position feedback within this time step to the control unit system which commands the actuator. In order to meet such a requirement, the regarded camera should be operated in combination with a high-performance embedded system, which has to be real-time capable [West01] or a Field Programmable Gate Array (FPGA) based system, as recommended in [Imaginghub17].

Figure 5.23 shows the high-speed camera, which is mounted in front of the screen. Since the small displacement of the light point should be detected as accurate as possible, the thread of the lens is extended. This extension allows placing the camera close to the screen due to the decreased focal length. As a result, the horizontal light point motion of about ± 4 mm can be captured with the full width of the sensor. The image area of interest (AOI) is further adjusted to 800×200 pixel, equal to the example in Figure 5.22. For the vision measurement, the single frames are recorded and stored in the video container format AVI. Afterward, an image processing can be performed according to Equation (5.15) in order to obtain the motion of the light point.

Next, one can perform a calibration of the vision sensor system to get the relation between the measured position in pixel and the actual position in mm. Fortunately, the kinematic-optical sensitivities are accurately known according to Table 5.1. Thus, the 5th lens can

Figure 5.25: Installed Pixy camera.

The detected position of the light point can be passed to an oscilloscope. Via USB it can not only be powered but also configured, e.g., with the help of the supplemented PixyMon software.

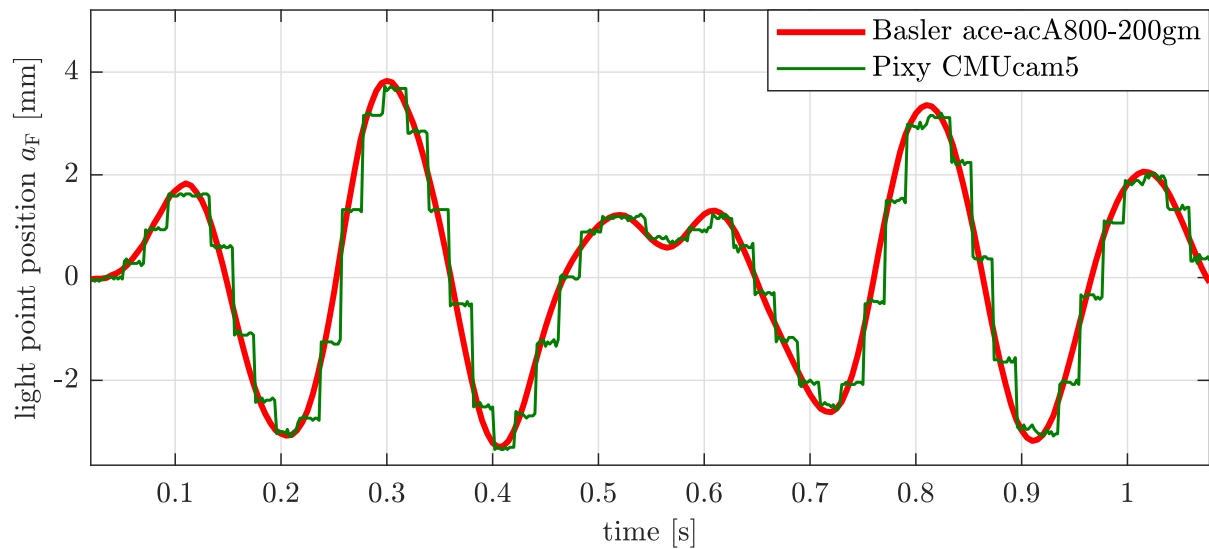
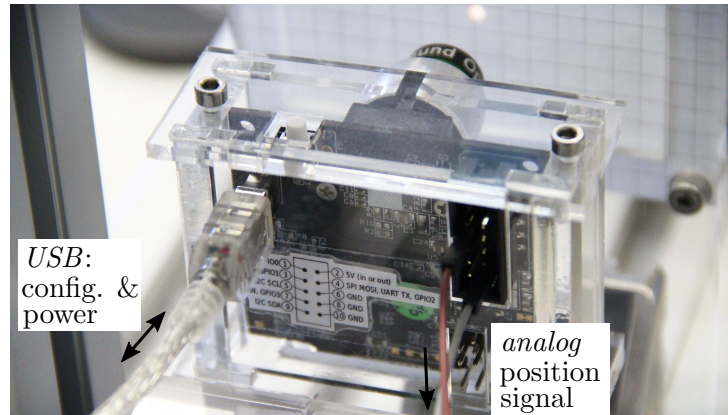


Figure 5.26: Comparison of the force-induced light point motion, which is captured by the Basler ace-acA800-200gm and instantly detected by the Pixy CMUcam5.

be displaced employing the actuator, and the actual image position can be estimated with $a \approx s_{L4} \cdot y_M$. Figure 5.24 depicts the resulting relation, whereby the motor was moved by steps of 1 mm and within the range of ± 3 mm. Consequently, in order to convert the captured motion of a light point from pixel to mm, this lookup table can be used for the interpolation.

Finally, a second low-cost vision sensor named *Pixy CMUcam5* is installed at the experiment, as shown in Figure 5.25. It is based on an open source project for embedded vision and it can detect the position of defined objects using the on-board image processing feature [CMUcam18]. On the one hand, it can transfer the results of the defined objects to an Arduino microcontroller via SPI, and on the other hand, it can directly provide an analog signal. This signal is nearly proportional to the detected x- or y-position and can be monitored, e.g., with an oscilloscope. Figure 5.26 compares the Pixy cam with the Basler camera, whereby the latter provides better results.

After this description of the hardware arrangement, as well as the introduction and validation of the subsystems, the development of the actual control strategy is presented in the following.

5.3 Development of the Control Strategy

Besides the controller design, the prepared simulation model and the tuning of the controller are described in this section. Finally, the deployment to the hardware is discussed.

5.3.1 Controller Design

As indicated in Section 5.1.2, it is the primary computational task of the control unit to reconstruct the motion of the light point with the help of a state observer. For this purpose, a KF according to [Kalman60] is used, which is introduced and explained in Section 2.5.

The actual design of the control strategy is shown in Figure 5.27. The main structure is not only based on the KF block, but also on a *future-integration* (FI) block and a *feed-forward* (FF) control. First, the system equations of the coupled lenses in analogy to the Equations (5.2) and (5.1) can be formulated in the state-space representation

$$\underbrace{\begin{bmatrix} \dot{q} \\ \dot{q} \end{bmatrix}}_{\dot{\mathbf{x}}} = \underbrace{\begin{bmatrix} \mathbf{0} & \mathbf{I} \\ -M^{-1} \cdot \mathbf{K} & -M^{-1} \cdot \mathbf{D} \end{bmatrix}}_{\mathbf{A}} \cdot \underbrace{\begin{bmatrix} q \\ \dot{q} \end{bmatrix}}_{\mathbf{x}} + \underbrace{\begin{bmatrix} \mathbf{0} \\ M^{-1} \cdot \bar{\mathbf{B}} \end{bmatrix}}_{\mathbf{b}} u_{\text{F}}. \quad (5.16)$$

Since the complete lens system is mechanically coupled, the observability condition is satisfied for the measurement of a single and arbitrary state. The motion y_{L4} of the 4th lens due to the excitation u_{F} has a significant influence on the image aberration, so it is chosen for the position measurement, as explained in Section 5.2.3. Hence, the KF according to Equation (2.19) results in the state space representation with

$$\dot{\hat{\mathbf{x}}} = \underbrace{(\mathbf{A} - \mathbf{L}_{\text{opt}} \cdot \mathbf{C})}_{\mathbf{A}_{\text{KF}}} \cdot \hat{\mathbf{x}} + \underbrace{\begin{bmatrix} \mathbf{B} & \mathbf{L}_{\text{opt}} \end{bmatrix}}_{\mathbf{B}_{\text{KF}}} \cdot \underbrace{\begin{bmatrix} u_{\text{F}} \\ y_{\text{L4}} \end{bmatrix}}_{\mathbf{u}}. \quad (5.17)$$

This differential equation can be solved by means of a numerical integration. Furthermore, the image aberration due to the force excitation can be approximately ascertained with

$$\hat{a}_{\text{F}}(t) = \mathbf{C}_{\text{optic}} \cdot \hat{\mathbf{x}}(t), \quad (5.18)$$

whereby $\mathbf{C}_{\text{optic}}$ contains the kinematical-optical sensitivities of Table 5.1 with respect to the mechanical DOF of the related state space. Second, the design is extended by the FI

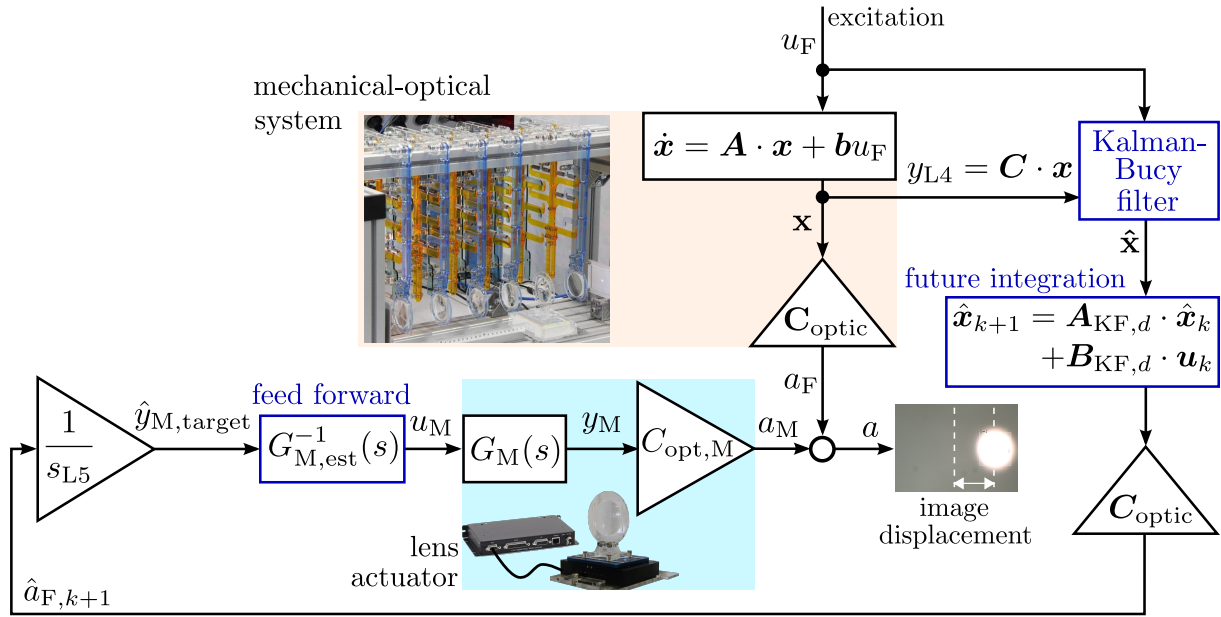


Figure 5.27: Block diagram of the control strategy, which is mainly based on the KF, the FI and the FF block. The blocks representing the real mechanical-optical system and the real lens actuator are indicated by means of the adjacent pictures.

block, as indicated in Figure 5.27. It should estimate the system behavior of the future time step $\hat{\mathbf{x}}_{k+1}$ by means of the discrete model equations

$$\hat{\mathbf{x}}_{k+1} = \underbrace{e^{\mathbf{A}_{\text{KF}} T_d}}_{\mathbf{A}_{\text{KF},d}} \cdot \hat{\mathbf{x}}_k + \underbrace{\mathbf{A}_{\text{KF}}^{-1} \cdot (e^{\mathbf{A}_{\text{KF}} T_d} - \mathbf{I}) \cdot \mathbf{B}_{\text{KF}}}_{\mathbf{B}_{\text{KF},d}} \cdot \mathbf{u}_k \quad (5.19)$$

as derived in [Lunze10]. As a result, the signal latency due to the position measurement and lens actuator system can be reduced by the use of the future aberration $\hat{a}_{F,k+1}$, which is expected after the next sampling period T_d . In order to estimate even another step further, one could neglect the change of the input with the assumption $\mathbf{u}_{k+1} \approx \mathbf{u}_k$. Hence it would yield

$$\hat{\mathbf{x}}_{k+2} \approx \mathbf{A}_{\text{KF},d}^2 \cdot \hat{\mathbf{x}}_k + (\mathbf{A}_{\text{KF},d} + \mathbf{I}) \cdot \mathbf{B}_{\text{KF},d} \cdot \mathbf{u}_k. \quad (5.20)$$

Third, the design of the FF control is discussed. Fortunately, the transfer function $G_{M,\text{est}}(s)$ of the lens actuator system is identified according to Figure 5.10. Hence, the performance of the trajectory tracking control can be improved by adding a system, which contains the inverse behavior. As a consequence, the original zeros become the new poles and vice versa. However, they are interchanged to the right-hand side of the pole-zero map and, therefore, an unstable filter would result. In order to solve this issue, an approximated filter based on an all-pass [DeliyannisSunFidler98] can be designed with

$$G_{M,\text{est}}^{-1}(s) \approx (-1)^{n_{\text{poles}}} \text{gain}\{G_{M,\text{est}}(s)\} \frac{\text{poles}\{G_{M,\text{est}}(s)\}}{-\text{zeros}\{G_{M,\text{est}}(s)\}}. \quad (5.21)$$

The number of poles is denoted by n_{poles} and the gain of the original transfer function has also to be taken into account.

Next, the introduced design is tested and tuned through a simulation model, before it can be deployed on the hardware.

5.3.2 Simulation and Tuning

In order to apply and investigate the control strategy of Figure 5.27, it is implemented in Simulink. The mathematical models represent the actuator and pendulum systems. Furthermore, the observer gain matrix \mathbf{L}_{opt} within the KF according to Equation (5.17) has to be computed through the Equations (2.22) and (2.23). Thereby, the noise input matrix is determined as an identity matrix $\mathbf{G} = \mathbf{I}$, i.e., all states are considered to have independent process noise $\mathbf{w}(t)$. Besides, the weighting matrices \mathbf{Q} and \mathbf{R} must be chosen, which characterize the model and measurement inaccuracies. The guess of the latter is based on the performance of the position sensor system according to Section 5.2.3. One can assume, that the position signal y_{L4} of the Hall-effect sensor in combination with the DAC is subjected to a noise, which complies with a normal distribution [BronshteinEtAl07] and has a maximal amplitude of 0.1 mm. If 99,7% of the measurement samples are within this range, the standard deviation is

$$\sigma_v = \frac{0.1 \cdot 10^{-3} \text{ m}}{3} \approx 3.3 \cdot 10^{-5} \text{ m}. \quad (5.22)$$

As a result, the regarded matrix yields

$$\mathbf{R} = \text{cov}\{y_{L4}(t_1), y_{L4}(t_2)\} = \sigma_v^2 \approx 1 \cdot 10^{-9} \text{ m}^2. \quad (5.23)$$

In the confidence that the measurement is accurate compared to the rough approximated model, the inaccuracy of the later should be higher penalized, which means $\|\mathbf{Q}\| \gg \|\mathbf{R}\|$. This action gives more weight to the measurement and the estimation accuracy than to the model accuracy. The final matrix $\mathbf{Q} = \text{diag}\{5 \cdot 10^{-8}\}^{22 \times 22}$ is determined by means of a parameter tuning study in [Liang17].

The corresponding simulation results of the reconstructed light point position based on the $y_{L4}(t)$ -measurement are shown within the first three seconds in Figure 5.28. Thereby, the KF is simulated in combination with, and without the measured excitation $u_F(t)$. Besides, the measurement of the vision sensor and the response of the coupled lens system according to Equation (5.16) are presented. As expected, the KF without the input u_F initially differs from the measurement and the other curves, since the hammer excitation is thereby not considered. However, already after 0.5 s, the actual light point position is quite well estimated by the KF, no matter if with, or without the excitation knowledge. One can also recognize, that the estimation without the KF drifts away from the measurement after

a while. This is especially obvious in the plot of the later period according to Figure 5.29. In conclusion, the designed KF reconstructs the light point motion quite well by means of the measured lens motion, even if the excitation is not detected.

Furthermore, the target motor position $\hat{y}_{M,target}$, which is based on the estimated light point motion according to Equation (5.6) can be calculated, as illustrated in Figure 5.30.

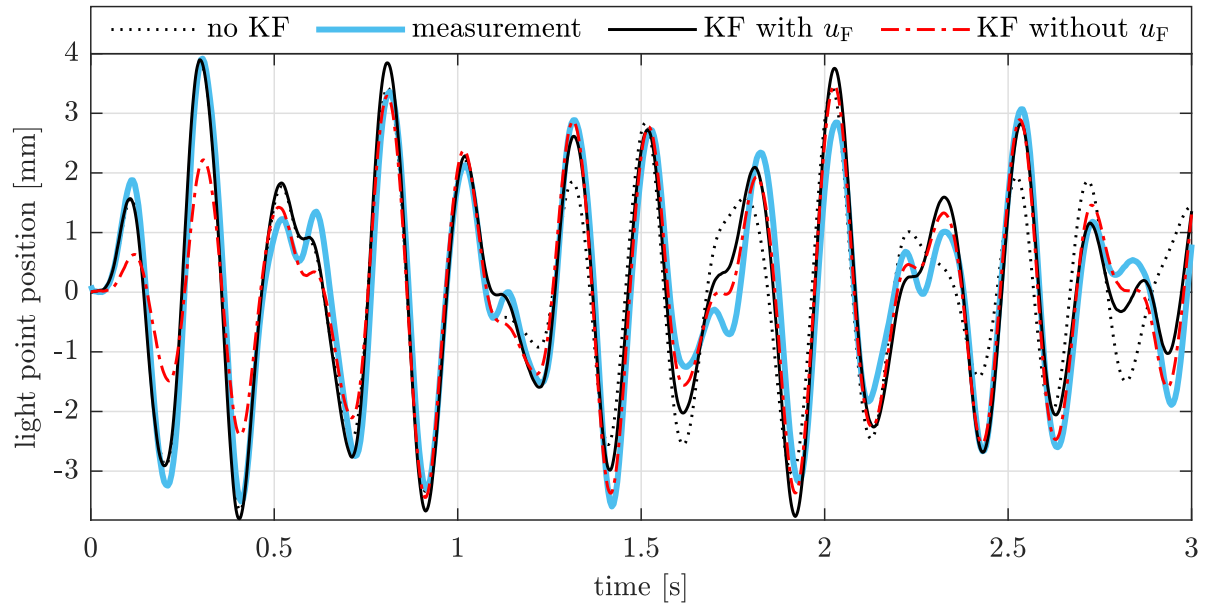


Figure 5.28: Simulation results $a_F(t)$ of the designed KF in comparison to the vision measurement.

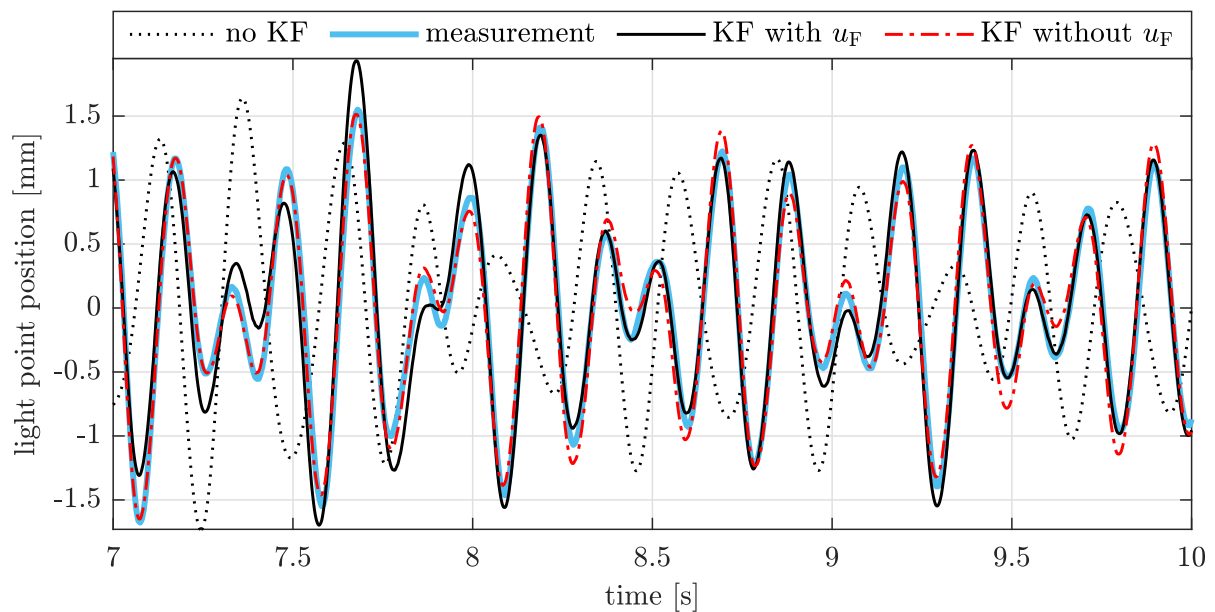


Figure 5.29: Simulation results $a_F(t)$ of the designed KF in the period 7s after the hammer shock. In addition, the vision measurement of the offline image-processing is presented.

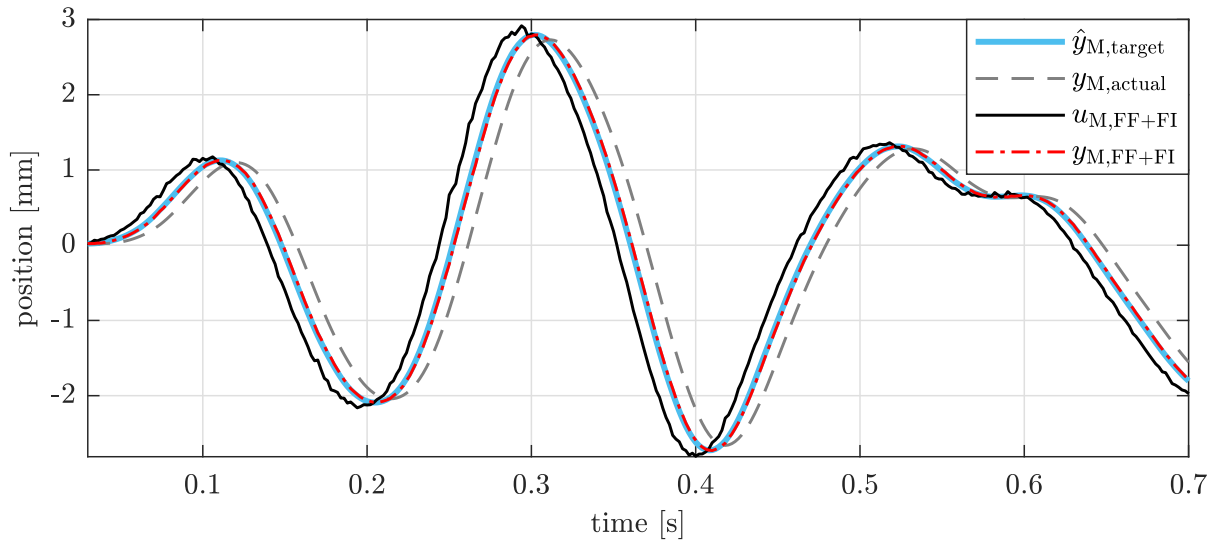


Figure 5.30: Simulation results of the commanded and expected motor motions, which are based on the KF with u_F , as well as the FI block and the FF control.

If this signal is directly commanded to the motor, the actual position $y_{M,actual}$ due to the delayed motor behavior occurs. However, according to the controller design in Section 5.3.1, the FI, and FF can provide a signal $u_{M,FF+FI}$ with a future guess and considered motor behavior. As a result, the simulated motor response $y_{M,FF+FI}$ perfectly meets the target position, so it is expected, that the light point motion can be compensated quite well. If one superposes this motor-generated light point motion with the aberration measured by the camera, the remaining error can be assessed. It is depicted in Figure 5.31 and is mainly caused by the estimation error of the KF. Even a time shift of +2 ms or -2 ms between the two signals cannot improve the resulting behavior. This circumstance indicates that it is not possible to compensate for the motion of light point entirely within this experiment. Anyhow, the mean value and standard deviation of the measured impulse response is at least reduced by a factor of almost 4, according to this prediction.

For this simulations, a constant sample time of $T_d = 2$ ms and the ode3-solver according to the Bogacki-Shampine method [ShampineReichert97] is used, in order to perform the FF+FI control in correspondence to Equation (5.21) and Equation (5.20).

In the following, the developed controller design is tested on the control unit in combination with the realized hardware subsystems.

5.4 Experimental Investigation

Now, the developed algorithm has to be implemented on the real-time capable control unit. As soon as this is solved, the improvement of the optical compensation due to the realized control can be assessed, and the influence of changed model parameter can be

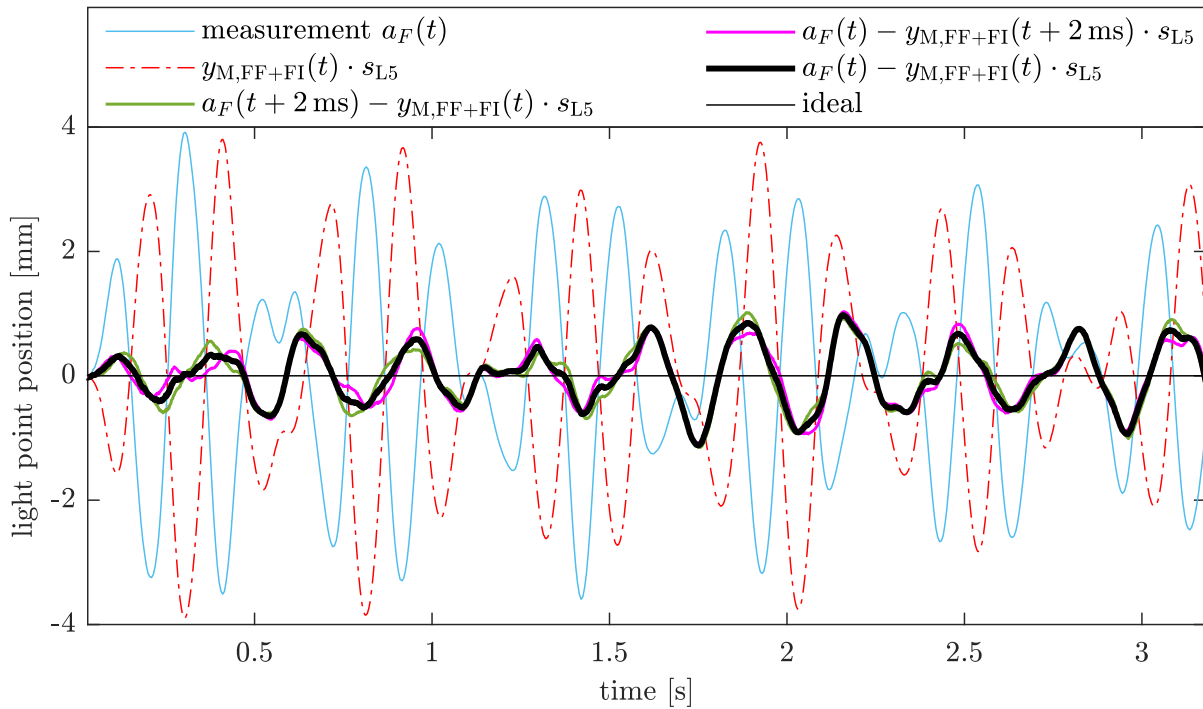


Figure 5.31: Remaining error based on simulation results, which is expected for the designed dynamical-optical compensation. During this investigation, the KF in combination with the known input u_F is used.

investigated additionally.

5.4.1 Deployment on Hardware

Since the control unit is based on the Arduino Due according to Section 5.2.4, it is only necessary to extend the developed Simulink model by means of the specific Arduino blocks. Then, one can automatically generate the code for the microcontroller and deploy it on the hardware.

However, due to the limited performance of the Arduino Due, it is not possible to run the complete FF+FI control at the sample time of $T_s = 2$ ms and with the chosen `ode3`-solver, as simulated in Section 5.3.2. Unfortunately, there is a conflict between the FF control and FI method. On the one hand, the two-step FI with 22 states is computationally expensive so that the sample time has to be increased and on the other hand, the numerical integration of the all-pass based FF control becomes unstable for an enlarged time step. Despite the usage of solvers like the `ode2` or the `ode1` with lower computational effort, this issue can not be resolved. As a result, the control strategies are separated, so that either the

- *FF model* with u_F and the `ode3`-solver at $T_s = 2$ ms, or the

- *FI model* without u_F and the `ode3`-solver at $T_s = 8$ ms

is running on the hardware. Further deployments with a varied sample time and different solver types are also tested but are not presented in this work. The Arduino Mega 2560, Arduino Uno and Arduino Leonardo [Arduino18] can also not stably realize the designed FF+FI control since they are not powerful enough.

Anyhow, the Simulink model of the pure FF model, without the FI part, is realized. A related analog input block can receive the sensor signals, and the signal for the motor navigation can be transferred with an analog output block. The digital inputs are used for the force detection and the realization of a switch. For the monitoring of the real-time capability, a pulse is reported via a digital output. Furthermore, the analog signals have to be scaled to their physical units, to match the model equations based on SI-units. The final FI model looks quite similar. It includes the discrete model equations instead of the FF, and in particular, it does not take the detected force u_F into account. The latter is neglected due to the fact, that the KF estimation with, and without the consideration of u_F is quite similar shortly after the force excitation, as already discussed in Figure 5.29. Besides, the force impact takes only 4 ms and the reliable detection through the controller with a fixed sample time of 8 ms is quite tough.

5.4.2 Measurement Results

The remaining optical aberration $a(t)$, which is represented by the light point displacement, is shown in Figure 5.32 for both, the FF model and the FI model. In order to clarify the effect of the control, the uncontrolled impulse response $a_F(t)$ is additionally plotted. The magnitudes of the motion are sufficiently reduced for both control concepts by a factor of approximately 4. The FF model demonstrates its advantage by the fast reaction directly after the initial force impact and keeps an excellent compensation behavior. Since the FI model does not consider the force impact, it has a worse performance at the beginning. However, after only one second, it performs at least as good as the other model.

The peak to peak values and the standard deviation of the light point motion in percentage are visualized in Figure 5.33. The latter is computed for the time range $t > 1$ s so that the initial behavior is neglected. It is obvious, that the FF model reduces both values to about 30 %, whereas the peak to peak value during the FI model results at 54 % because of the poor behavior at the beginning. The pleasant surprise is the decreasing of the standard deviation down to 17 % within the FI model for $t > 1$ s. Thus, the choice of the controller model depends on whether an improved behavior should be present directly after the excitation or for later times.

Moreover, the output signal of the control unit and the position of the linear actuator can be analyzed for both control models, FF and FI. Figure 5.34 and Figure 5.35 exemplify

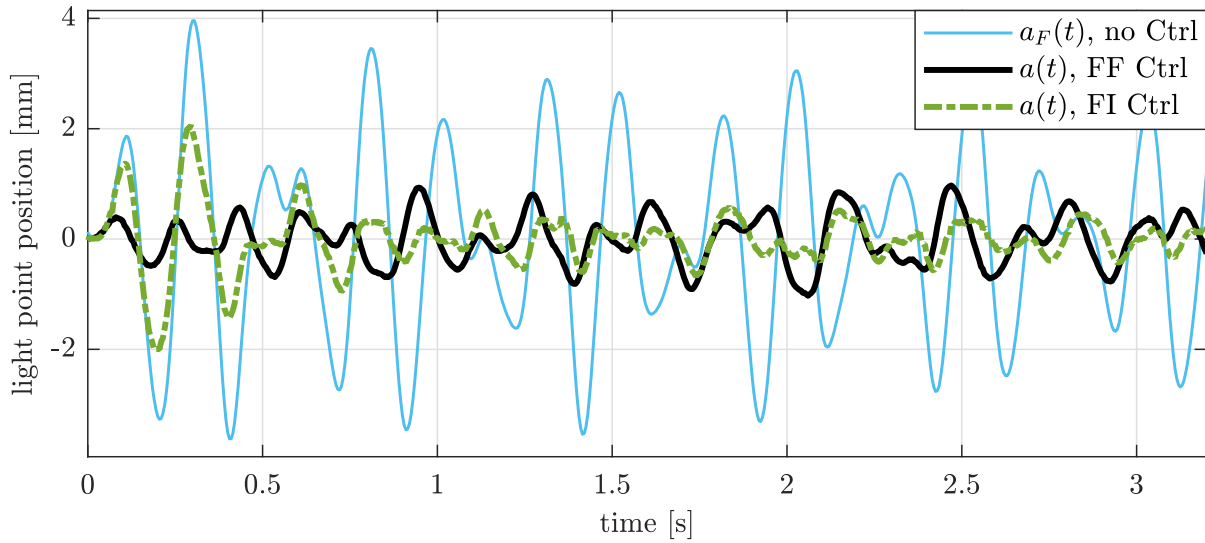


Figure 5.32: Plot of the remaining error due to controlled FF model and FI model, in comparison to the uncontrolled light point.

the experimental results within a small time range. Despite of the noise, the measurement of the generated motor input $u_{M,FF}$ meets the simulated signal $u_{M,FF+FF}$ quite well for the deployed FF model. The deviation of the measured and simulated actual motor position y_M is also very small. Both are close to the ideal target position $y_{M,target}$ estimated by the KF, as already discussed in Section 5.3.2. This measurement justifies the good performance of the dynamical-optical control using the FF model.

In analogy, the results of the deployed FI model within the same time range are regarded in Figure 5.35. Due to the relatively far future guess of 16 ms, the measurements are often in advance to the simulation, which is recognizable at around 3.25 s. The measurements also show some amplitude and phase deviations in comparison to the simulation results. One explanation for the differences could be, that the excitation force is not detected for

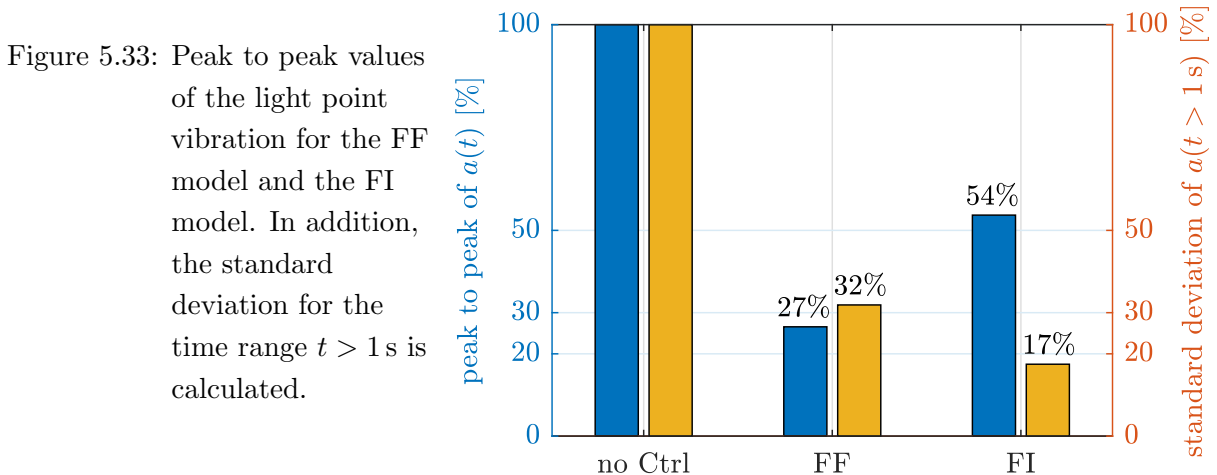


Figure 5.33: Peak to peak values of the light point vibration for the FF model and the FI model. In addition, the standard deviation for the time range $t > 1\text{ s}$ is calculated.

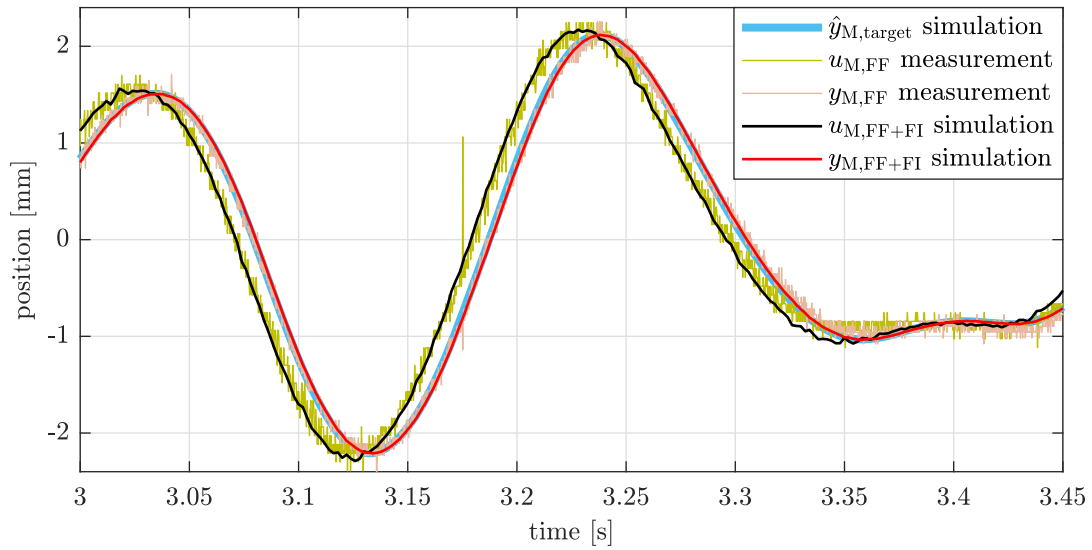


Figure 5.34: The measured motor input $u_{M,FF}$ and actual position $y_{M,FF}$, which are based on the running FF model, in comparison to the simulation results.

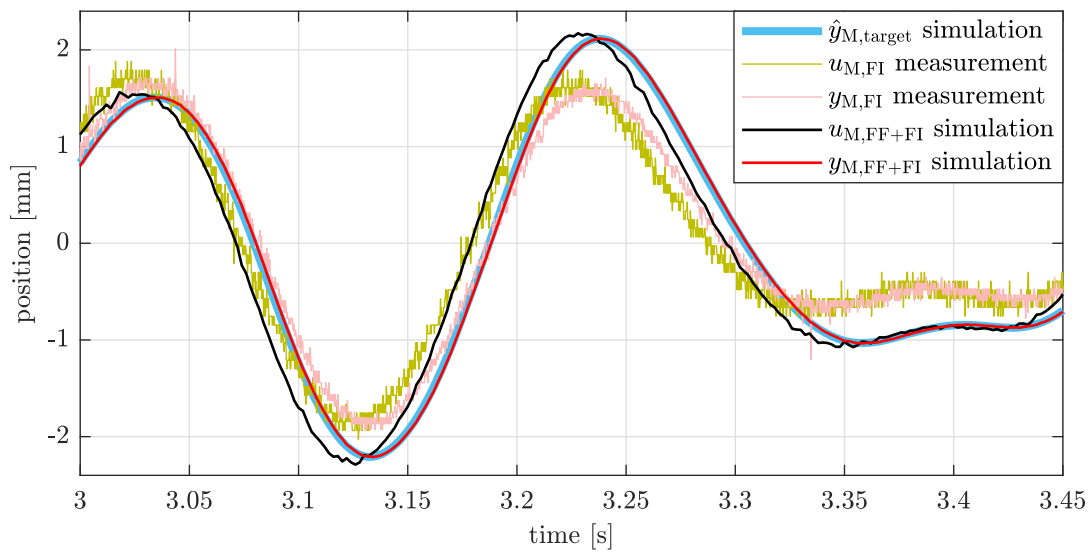


Figure 5.35: The measured motor input $u_{M,FI}$ and actual position $y_{M,FI}$, which are based on the running FI model, in comparison to the simulation results.

the deployed FI model and in contrast to the simulation. For other time periods, the differences are mostly smaller, which justifies the excellent compensation behavior of the dynamical-optical control using the FI model.

Finally, a screenshot of the oscilloscope is presented in Figure 5.36. The measurements illustrate the motion $y_{L4}(t)$ of the fourth lens due to the excitation $u_F(t)$. The FI control was activated after about one second since the commanded motor position varies and the related image motion $a(t)$ is nearly compensated. In comparison, the response of the image motion during an uncontrolled run is shown with the curve $a_F(t)$. It is proposed to

perform this measurement and analysis during the practical training with the students as prepared by [Dissanayaka18]. It clarifies the improvement due to the dynamical-optical control and imparts the handling of the oscilloscope.

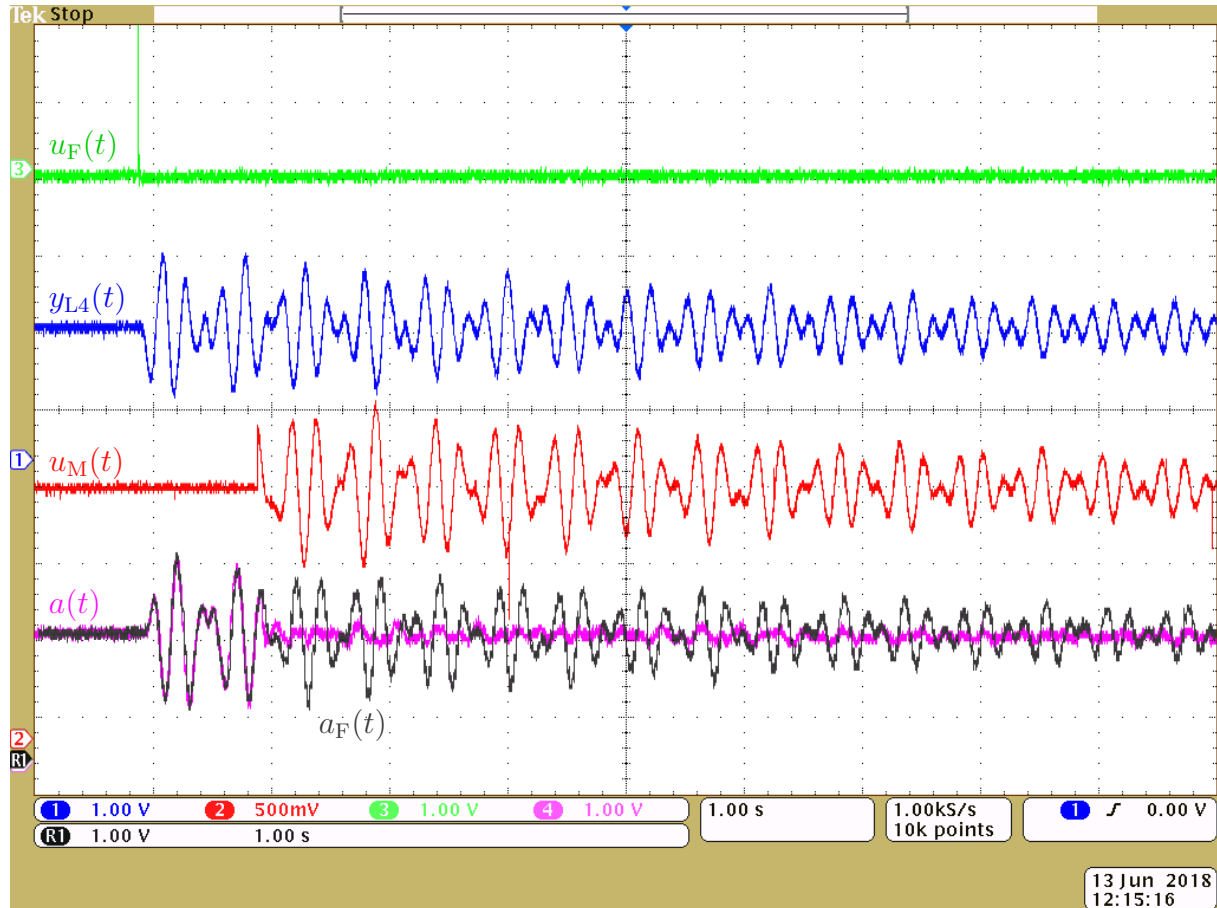


Figure 5.36: Screenshot of the oscilloscope, whereby the FI control is switched on after about 1 second after the hammer impact.

After it was shown, that the control approaches work for the considered mechanical model with a specific spring configuration quite well, it could be interesting to analyze the behavior for a model with a varied spring configuration in the following.

5.4.3 Variation of Model Parameters

For this final investigation, the stiffness distribution of the coupled lenses is changed in order to create another mechanical test setup. Since the developed control is model-based, it can be simply recalculated with the use of the changed model parameters and deployed to the hardware. The stiffness is realized by a combination of two different types of springs, which are vertically arranged according to Figure 5.2(a). Figure 5.37 sketches the initial and changed configurations of the springs schematically, whereby for the right one the

bottom spring is removed.

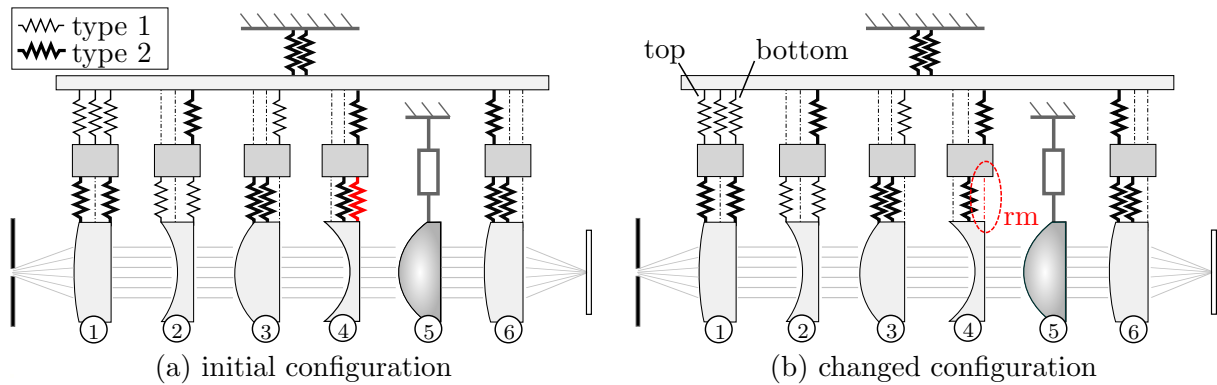


Figure 5.37: Schematic stiffness distribution of the coupled lenses, where in (a) the initial spring configuration and in (b) the changed configuration are sketched.

The experimental results of the remaining light point motion based on the changed spring configuration are shown in Figure 5.38. The controlled FF and FI models are measured and presented in comparison to the uncontrolled motion of the light point. Again, the reduction of the image vibration is obvious for both control models. In particular, the FF model leads to an improved behavior immediately after the hammer shock and the FI performs better afterwards. Fortunately, the residuals are in the same order of magnitude as during the initial configuration discussed in Figure 5.32.

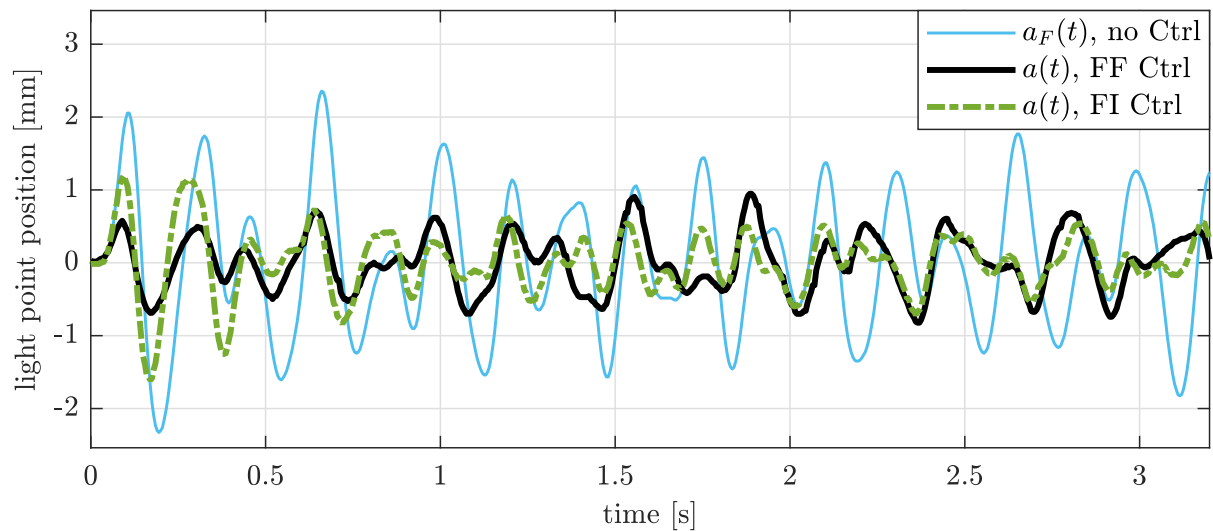
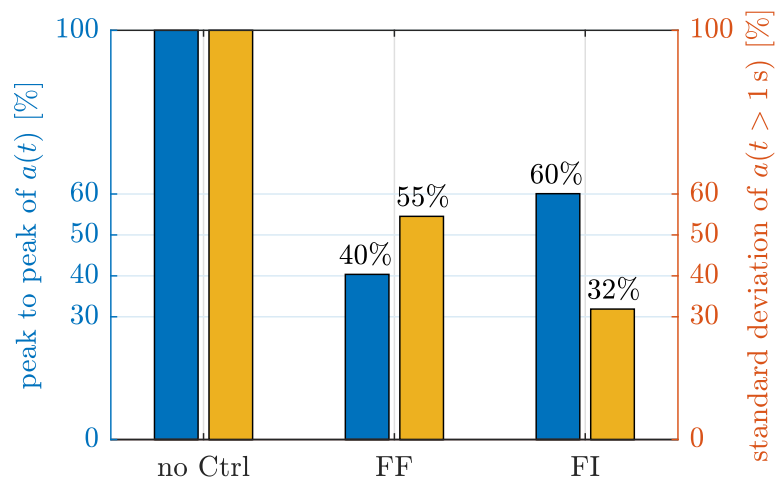


Figure 5.38: Remaining error of the controlled FF model and FI model, for the changed spring configuration.

This test demonstrates that the model-based image stabilization is also auspicious for varied parameters. However, it should be remarked, that the amplitudes of the uncontrolled response are smaller than for the previous configuration. Thus, the improvement expressed in percentage according to Figure 5.39 is lower.

Figure 5.39: Peak to peak values of the light point vibration for the changed configuration. In addition, the standard deviation for the time range $t > 1$ s is calculated.



Chapter 6

Conclusion and Outlook

Optical lithography systems and astronomical telescopes are two cutting-edge technologies, which are developed at the limits of physical feasibility. Due to raising requirements for accuracy and resolution, these optical systems are also sensitive to mechanical disturbances.

In the first part of the work, the fundamentals of the mechanical and optical modeling process were introduced. The mechanical models are based on the finite element method, model order reduction methods, and the elastic multibody system approach. Within the optical fundamentals, the basic equations for geometrical optics were derived and explained. Afterward, the typical descriptions of optical surfaces and the procedures during a usual ray tracing were presented. One discussed the image formation, optical aberration, Zernike polynomials and the definition of resolution in a followed step. These properties of optical systems were essential for the understanding of the subsequent simulation concepts. Besides, the ray-optical analyses and the possibilities of considering wave-optical phenomena were annotated. It was clarified that for an image simulation of diffraction-limited optics, not only ray optics have to be taken into account, but also wave-optical effects as refraction or interference have to be considered using Fourier optics. Thereby, it became clear, that an aperture stop acts like a low pass filter which limits the resolution. The related filter function additionally can contain wavefront aberrations, and the corresponding image is known as the point spread function. Finally, it was convoluted with the object function describing the desired object and the final image resulted.

In the principal part of this work, the workflow for the integrated modeling and several particular implementations for the preparation of the interface data were presented. These preparations were required due to the switch from the mechanical to the optical domain and to model and analyze segmented mirror systems efficiently. For instance, if a surface or segment is moving, the motion has to be passed to the ray tracing algorithm in a relative description. In addition, if there are deformable optical elements in the mechanical model, the related surfaces have to be translated to a continuous surface description, since a sequential ray tracing is used for the optical analyses. Furthermore, different MOR

methods for coupled dynamical-optical simulations were explained and demonstrated for an elastic, single mirror example. Concerning the simulation strategy, it was exemplified, that the *standard method* mainly depended on the number of regarded time instants, which were optically analyzed. In case of linear behavior of the mechanical-optical system, the *modal method* were proposed on the other hand. This method required the calculation of the optical mode shapes, which describe the kinematic-optical sensitivities. Their usage decreased the computational costs for extended time simulations. Finally, it was shown, that the dynamical-optical behavior can be analyzed using the mechanical-optical frequency responses of different kinds of optical aberrations, which can behave very sensitive at specific frequencies. As a consequence it was possible, to analyze the effects of model order reduction methods of Craig-Bampton, Krylov and the Balanced Truncation on the optical aberrations. In summary, it was recommended, to use the Krylov approach with multiple matching points for models, which should be very accurate for a large frequency range. For that, the mechanical frequency responses and maximal eigenfrequencies of the reduced model have to be assessed intensively for the choice of the moment-matching points, at first. Besides, the Craig-Bampton method should be used in all other cases, since it is simple to apply and it usually delivers reasonable results, even for fewer degrees of freedom. During the investigation of the dynamical-optical simulation method it was clarified that the modal method allows extensive simulations in the time domain, at low computational costs. In the last section of the dynamical-optical simulation chapter, the development of an adaptive-optical controller for an astronomical telescope was presented. The kinematic-optical model with a segmented primary mirror was simulated under disturbances. In addition, a control strategy for the deformable secondary mirror was designed, tested and simulated for different load cases.

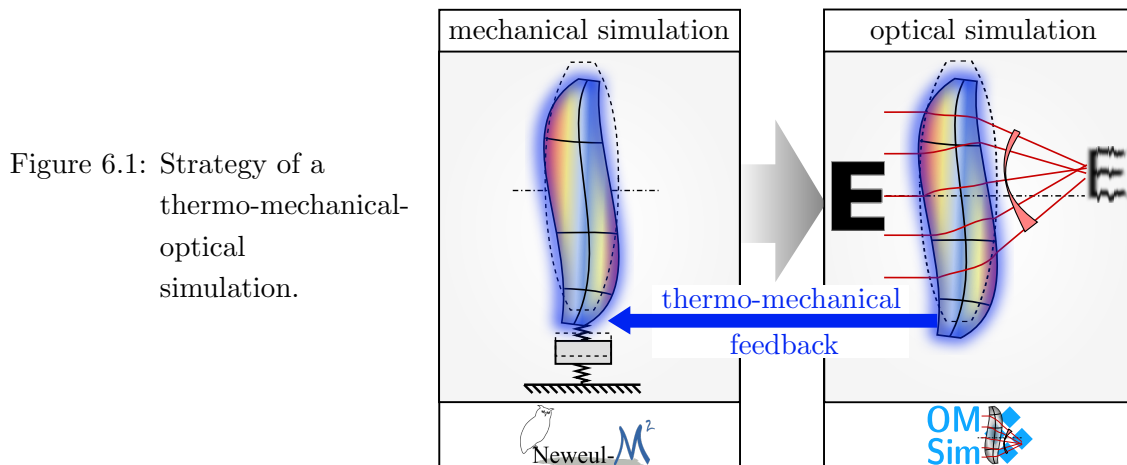
The realization of an active image stabilization experiment was demonstrated in the last part of this work. The constructed optical system consists of multiple lenses mounted by mechanically coupled pendulums. On the one hand, the built laboratory experiment demonstrates the vibration sensitivity of a mechanical-optical system, and on the other hand, the image vibration was reduced by means of the developed model-based compensation control. After the introduction and modeling of the test setup, the active control strategy was explained. Furthermore, the related hardware components and subsystems were arranged, investigated, and validated. The design and adjustment of the controller models were performed through simulations, and the control strategy is mainly based on the Kalman-Bucy filter, which serves as state observer. During the deployment of the models onto the real-time capable control unit based on components of the Arduino platform, some limitations regarding the sample time became clear. However, the use of this low-cost hardware also led to advantages for the favorable development and code-generation in Simulink. Finally, two different control models for the latency-included system were deployed and tested. The first is based on a feed-forward control and the second involves a discrete future-integration step. The remaining image motion was measured with a

high-speed vision sensor system, and a significant reduction of the image vibration was proven. In some cases, it was decreased down to 17% of the initial error. Besides, the variation of model parameters was investigated.

Outlook

In further studies, one can consider many applications, which require the investigation through dynamical-optical models. In the following, some fascinating topics are listed.

- The built simulation models can be extended with additional bodies representing struts or mounting elements and the elastic multibody systems can also be investigated at different load cases, to assess the whole simulation process and to identify further limits.
- It would be interesting, to apply the methods of model order reduction, the elastic multibody system approach, and the ray- and wave-optical simulation process to a complex telescope construction, to predict the mechanical-optical behavior for realistic dynamical excitations. In particular, for a ground-based telescope different operating points and mirror orientations can be considered, where also the gravity and the change of compliance play a significant role.
- One of the main purposes of doing integrated modeling for optical systems is to evaluate the effect of a designed controller on the image quality. However, the model order reduction methods also need to be selected and evaluated based on its effect of controller design. For instance, the adaptive-optical controller design based on reduced order systems and model-predictive control [Schnelle18] can be unstable for a full order system or a model order reduction method could introduce unstable poles and zeros in the system, which impair the controller performance. Hence, the imaging performance of the closed-loop system can be affected ultimately. As a result, it is necessary to investigate such effects further.
- The analysis of the thermo-mechanical-optical behavior would also be obvious since the heat generated at the optical elements causes thermo-mechanical stresses due to the absorption of light. These stresses disturb the optical behavior and lead to birefringence and polarization effects [Wengert16]. Hence, the transient heating process of an irradiated lens could be analyzed. Thereby, the irradiance from the optical simulation can be used as a feedback for the mechanical simulation, as sketched in Figure 6.1.
- Another exciting topic could be the dynamical-optical simulation of lithographic enhancement processes, as multi-patterning or optical proximity correction [Bisschop16],



in combination with mechanical disturbances. Thereby, the developed exposure simulation approach based on Fourier-optical methods could be beneficial.

- In the field of metrology, there are also a few optical systems with high-dynamical motions and loads. For instance, adaptive compensators are used to focus dynamically on different distances utilizing rigid lens motions. Further applications as diffractive structures on top of a deformable membrane lens require also an mechanical-optical modeling [Herkommer14].
- In order to shrink down and improve the optics of cameras within consumer products like smartphones, liquid lenses and deformable membranes are introduced [DingEtAl17, KongEtAl16, ZhangLiGuo13]. These optical zoom systems with deformable liquid lenses should be studied using hydro-dynamical-optical simulations.
- There are also some human eye diseases, e.g., the tremor or the nystagmus, which are involuntary muscle contraction and relaxation involving oscillations or twitching movements. For the investigation of such diseases, one could develop biomechanical models of the human eye, which are coupled to optical simulations, see also [Lyapunov18].
- Finally, the built dynamical-optical experiment with the oscillating lenses could be extended with additional sensors and actuators, to observe and control the system behavior more precisely. By the use of a more powerful microprocessor, e.g., one of the future Arduino versions, or the utilization of a single-board computer, like the Raspberry Pi, the control unit could be capable of running enhanced control strategies, which can further improve the compensation performance.

Appendix

A.1 Derivation of the GRIN Ray Equation

In this following, the theory of calculus according to [BornWolf99] and [Meschede08] will be used to derive the partial differential equation for the GRIN-refraction, as introduced in Section 3.1.

In Figure A.2 the GRIN-refraction of a ray is sketched in detail with the refraction index n at the regarding position \mathbf{r} . Since the differential geometrical path length ds is assumed to be infinitesimal small, the distance $\xi \rightarrow 0$ and the vectors \mathbf{d} and $d\mathbf{r}$ have the same direction. The differential geometrical path length can be obtained using the scalar product of the tangential unit vector and the displacement vector

$$ds = \mathbf{d} \cdot d\mathbf{r}. \quad (\text{A.1})$$

Furthermore, the differential OPL can be expressed by the gradient

$$ds_{\text{opl}} = \frac{\partial s_{\text{opl}}}{\partial \mathbf{r}} \cdot d\mathbf{r}. \quad (\text{A.2})$$

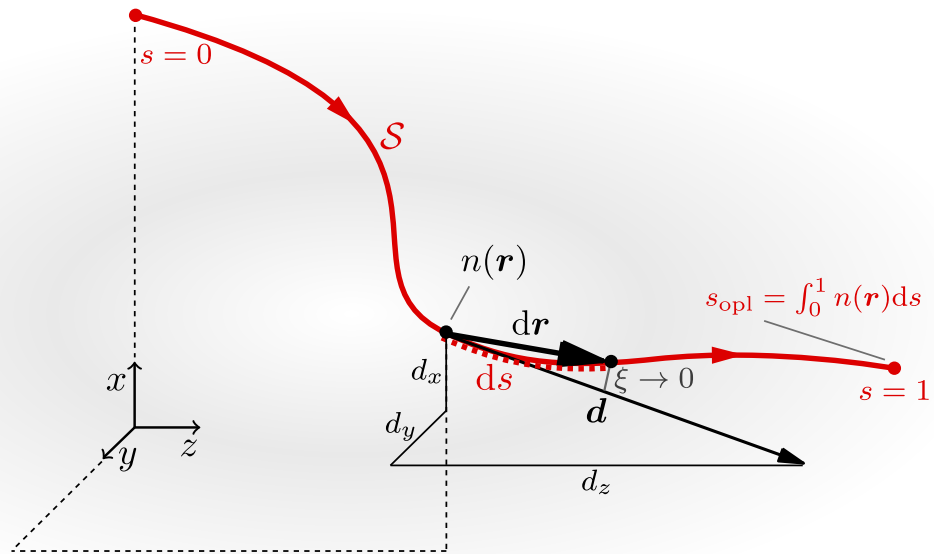


Figure A.2: Refraction of a ray in a graded index medium.

Next, the left-hand side of Equation (3.7) can be replaced by the Equation (A.2) and the right-hand side can be combined with Equation (A.1), so it follows

$$\frac{\partial s_{\text{opl}}}{\partial \mathbf{r}} \cdot d\mathbf{r} = n \mathbf{d} \cdot d\mathbf{r} \Leftrightarrow \frac{\partial s_{\text{opl}}}{\partial \mathbf{r}} = n \mathbf{d}. \quad (\text{A.3})$$

Since $|d\mathbf{r}| = ds$, and $d\mathbf{r}$ has the same direction as \mathbf{d} , one can formulate the tangential unit vector with

$$\mathbf{d} = \frac{d\mathbf{r}}{ds}. \quad (\text{A.4})$$

The following relation results from inserting Equation (A.4) into Equation (A.3),

$$\frac{\partial s_{\text{opl}}}{\partial \mathbf{r}} = n \frac{d\mathbf{r}}{ds} \Leftrightarrow \frac{d\mathbf{r}}{ds} = \frac{\partial s_{\text{opl}}}{\partial \mathbf{r}} \frac{1}{n}. \quad (\text{A.5})$$

Moreover, the so-called *Eikonal equation* follows by the squaring of Equation (A.3),

$$\left(\frac{ds_{\text{opl}}}{d\mathbf{r}} \right)^2 = (n \mathbf{d})^2 = n^2. \quad (\text{A.6})$$

After the differentiation of both sides of Equation (A.5) along the geometrical path, the chain rule yields

$$\frac{d}{ds} \left(n \frac{d\mathbf{r}}{ds} \right) = \frac{d}{ds} \left(\frac{\partial s_{\text{opl}}}{\partial \mathbf{r}} \right) \quad (\text{A.7})$$

$$= \frac{\partial}{\partial \mathbf{r}} \left(\frac{\partial s_{\text{opl}}}{\partial \mathbf{r}} \right)^\top \cdot \frac{d\mathbf{r}}{ds} \quad (\text{A.8})$$

$$= \frac{\partial}{\partial \mathbf{r}} \left(\frac{\partial s_{\text{opl}}}{\partial \mathbf{r}} \right)^\top \cdot \frac{\partial s_{\text{opl}}}{\partial \mathbf{r}} \frac{1}{n}, \quad (\text{A.9})$$

whereby again the Equation (A.5) is used for the latter rearrangement. The chain rule for a general vectorial function \mathbf{u} is defined as

$$\text{grad}(\mathbf{u} \cdot \mathbf{u}) = 2 \text{grad}(\mathbf{u})^\top \cdot \mathbf{u} \Leftrightarrow \text{grad}(\mathbf{u})^\top \cdot \mathbf{u} = \frac{1}{2} \text{grad}(\mathbf{u}^2) \quad (\text{A.10})$$

and thus, for $\mathbf{u} = \frac{\partial s_{\text{opl}}}{\partial \mathbf{r}}$ the right-hand side of Equation (A.9) results in

$$\text{grad} \left(\frac{\partial s_{\text{opl}}}{\partial \mathbf{r}} \right)^\top \cdot \frac{\partial s_{\text{opl}}}{\partial \mathbf{r}} \frac{1}{n} = \frac{1}{2} \text{grad} \left(\left(\frac{\partial s_{\text{opl}}}{\partial \mathbf{r}} \right)^2 \right) \frac{1}{n} \quad (\text{A.11})$$

$$\stackrel{(\text{A.6})}{=} \frac{1}{2} \text{grad}(n^2) \frac{1}{n} = \frac{1}{2n} 2n \text{grad}(n) = \text{grad}(n) = \frac{\partial n}{\partial \mathbf{r}}. \quad (\text{A.12})$$

Finally, the *GRIN Ray Equation* can be formulated as

$$\frac{d}{ds} \left(n \frac{d\mathbf{r}}{ds} \right) = \frac{\partial n}{\partial \mathbf{r}}, \quad (\text{A.13})$$

where the right-hand side describes the gradient of the refraction index, which is often named as $\text{grad}(n)$ or ∇n .

A.2 OM-Sim

OM-Sim is a Matlab-based tool for simulating the optical behavior according to the dynamical behavior of mechanically disturbed optical systems. It simplifies and accelerates an integrated dynamical-optical modeling process. The primary purpose is to simulate the optical behavior of dynamic excited optical systems, which are mechanically modeled elastic multibody systems. The results of the mechanic simulation have to be calculated by external elastic multibody system programs or finite-element tools. In order to analyze the dynamic-optical behavior, OM-Sim provides several interfaces, e.g., to Ansys [ANSYS16], MatMoremb, and Neweul-M². Furthermore, the implemented ray tracing algorithm calculates the optical properties and the imaging performance can be directly analyzed in OM-Sim using several methods based on wave optics. Simple models can even be exported to Zemax [Zemax11].

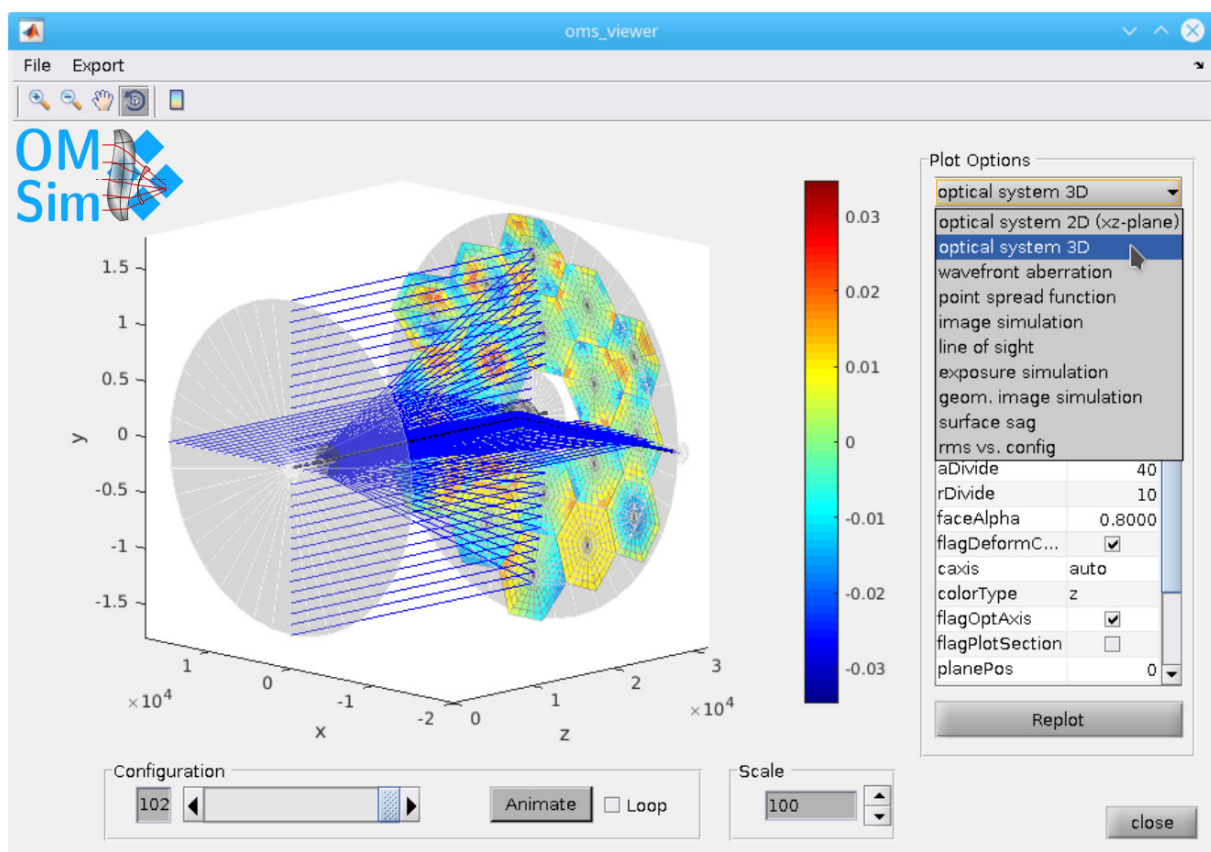


Figure A.3: Graphical user interface for dynamical-optical analyses, which is called `oms_viewer`.

Bibliography

- [AbrahamEtAl07] Abraham, B.; et al.: Thirty Meter Telescope - Construction Proposal. Tech. rep., TMT Observatory Corporation, 2007.
- [AMS14] AMS: Technical Note for the AS5306 Magnetic Multipole Strip, MS12-15 (Revision 2.0). AMS AG, 2014.
- [AMS17] AMS: Technical Note for the AS5304/AS5306 - Integrated Hall ICs for Linear and Off-Axis Rotary Motion Detection (Revision 2.0). AMS AG, 2017.
- [AndersenEnmark11] Andersen, T.; Enmark, A.: Integrated Modeling of Telescopes. Astrophysics and Space Science Library. New York: Springer, 2011.
- [AngeliEtAl14] Angeli, G.Z.; Xin, B.; Claver, C.; MacMartin, D.; Neill, D.; Britton, M.; Sebag, J.; Chandrasekharan, S.: Real time wavefront control system for the Large Synoptic Survey Telescope (LSST). In Proc. SPIE, Modeling, Systems Engineering, and Project Management for Astronomy V, Vol. 9150, pp. 9150–9150–16, 2014.
- [AngeliEtAl16] Angeli, G.Z.; Xin, B.; Claver, C.; Cho, M.; Dribusch, C.; Neill, D.; Peterson, J.; Sebag, J.; Thomas, S.: An integrated modeling framework for the Large Synoptic Survey Telescope (LSST). In Proc. SPIE, Modeling, Systems Engineering, and Project Management for Astronomy VI, Vol. 9911, pp. 9911–9911–20, 2016.
- [ANSYS16] ANSYS: Documentation for Ansys, Release 17.0. Canonsburg, 2016.
- [Arduino18] Arduino: Webpage - The open-source electronic prototyping platform. <https://www.arduino.cc/>, Accessed: February 15, 2018.
- [ASML18] ASML: Webpage of the ASML - Major milestone in the EUV revolution. <https://www.asml.com>, Accessed: June 25, 2018.
- [BarberHorraCrespo13] Barber, R.; Horra, M.; Crespo, J.: Control Practices using Simulink with Arduino as Low Cost Hardware. In IFAC Proceedings Volumes, Vol. 46, pp. 250–255, 2013.

- [BasdenEtAl14] Basden, A.; Morris, S.; Morris, T.; Myers, R.: AO modelling for wide-field E-ELT instrumentation using Monte-Carlo simulation. In Proc. SPIE, Adaptive Optical Systems Technology, Vol. 9148, pp. 9148–9148–9, 2014.
- [Basler15] Basler: Technical Note for Basler Cameras - Installation and Setup Guide for Cameras Used with Basler pylon for Windows (AW00061109). Basler AG, 2015.
- [Basler17] Basler: Technical Note for Basler ace - User's Manual for GigE Cameras (AW00089327). Basler AG, 2017.
- [Bathe96] Bathe, K.J.: Finite Element Procedures. Upper Saddle River: Prentice-Hall, 1996.
- [Bechler17] Bechler, F.: Flexible Mehrkörpersimulation von elastischen Spiegelsystemen mittels Simpack und Matlab (in German). Bachelor Thesis BSC-72, Institut für Technische und Numerische Mechanik der Universität Stuttgart, 2017.
- [Bisschop16] Bisschop, P.D.: Optical proximity correction: A cross road of data flows. The Japan Society of Applied Physics, Vol. 55, No. 6S1, pp. 06GA01–06GA01–11, 2016.
- [BöhmEtAl14] Böhm, M.; Pott, J.U.; Sawodny, O.; Herbst, T.; Kürster, M.: Real Time Vibration Compensation for Large Telescopes. MNRAS, Monthly Notices of the Royal Astronomical Society, Vol. 442, pp. 2446–2455, 2014.
- [BöhmEtAl16] Böhm, M.; Pott, J.U.; Sawodny, O.; Defrère, D.; Hinz, P.: Delay Compensation for Real Time Disturbance Estimation at Extremely Large Telescopes. IEEE Transactions on Control Systems Technology, Vol. 25, No. 4, pp. 1384–1393, 2016.
- [BornWolf99] Born, M.; Wolf, E.: Principles of Optics. Cambridge: Cambridge University Press, 1999.
- [BoyerEtAl14] Boyer, C.; Adkins, S.; Andersen, D.R.; Atwood, J.; Bo, Y.; Byrnes, P.; Caputa, K.; Cavaco, J.; Ellerbroek, B.; Gilles, L.; Gregory, J.; Herriot, G.; Hickson, P.; Ljusic, Z.; Manter, D.; Marois, C.; Otárola, A.; Pagès, H.; Schoeck, M.; Siquin, J.C.; Smith, M.; Spano, P.; Szeto, K.; Tang, J.; Travouillon, T.; Véran, J.P.; Wang, L.; Wei, K.: Adaptive optics program at TMT. In Proc. SPIE, Adaptive Optics Systems IV, Vol. 9148, pp. 91480X–91480X–15, 2014.
- [BronshteinEtAl07] Bronshtein, I.; Semendyayev, K.; Musiol, G.; Mühlig, H.: Handbook of Mathematics. Berlin: Springer, 2007.
- [BurdenFaires04] Burden, R.; Faires, J.: Numerical Analysis. Available Titles CengageNOW Series. Cengage Learning, 8. Edn., 2004.

- [Butler11] Butler, H.: Position Control in Lithographic Equipment, Applications of Control. IEEE Control Systems, Vol. 31, No. 5, pp. 28–47, 2011.
- [Clampin11] Clampin, M.: Overview of the James Webb Space Telescope observatory. In Proc. SPIE, UV/Optical/IR Space Telescopes and Instruments: Innovative Technologies and Concepts V, Vol. 8146, pp. 814605–814605–10, 2011.
- [CMUcam18] CMUcam: Webpage of the CMUcam Pixy - Open Source Programmable Embedded Color Vision Sensors. <http://cmucam.org/>, Accessed: February 21, 2018.
- [Corke17] Corke, P.: Robotics, Vision and Control - Fundamental Algorithms In MATLAB Second, Completely Revised, Extended And Updated Edition, Second Edition, Vol. 118 of Springer Tracts in Advanced Robotics. Springer, 2017.
- [Craig00] Craig, R.: Coupling of Substructures for Dynamic Analyses: An Overview. In Proceedings of the AIAA Dynamics Specialists Conference, Vol. 1, 2000.
- [DaiMahajan07] ming Dai, G.; Mahajan, V.N.: Zernike annular polynomials and atmospheric turbulence. J. Opt. Soc. Am. A, Vol. 24, No. 1, pp. 139–155, 2007.
- [DeliyannisSunFidler98] Deliyannis, T.; Sun, Y.; Fidler, J.: Continuous-Time Active Filter Design. Electronic Engineering Systems. CRC Press, 1998.
- [DickensStroeve00] Dickens, J.; Stroeve, A.: Modal Truncation Vectors for Reduced Dynamic Substructure Models. Paper 2000-1578, AIAA, 2000.
- [Dietz99] Dietz, S.: Vibration and Fatigue Analysis of Vehicle Systems Using Component Modes. VDI Fortschritt-Berichte, Reihe 12, Nr. 401. Düsseldorf: VDI-Verlag, 1999.
- [DingEtAl17] Ding, Z.; Wang, C.; Hu, Z.; Cao, Z.; Zhou, Z.; Chen, X.; Chen, H.; Qiao, W.: Surface profiling of an aspherical liquid lens with a varied thickness membrane. Opt. Express, Vol. 25, No. 4, pp. 3122–3132, 2017.
- [Dissanayaka18] Dissanayaka, A.: Extension of the Dynamical-optical Pendulae Experiment with an Active Control System. Master Thesis MSC-271, Institute of Engineering and Computational Mechanics, University of Stuttgart, 2018.
- [DoyleGenbergMichels12] Doyle, K.; Genberg, V.; Michels, G.: Integrated Optomechanical Analysis. SPIE Press monograph. SPIE Press, 2012.
- [Ebel14] Ebel, H.: Modellierung eines Shack-Hartmann-Wellenfrontsensors für dynamisch-optische Simulationen. Simtech-Projektarbeit SA-6, Institut für Technische und Numerische Mechanik, Universität Stuttgart, 2014.

- [EberhardStörkleMack18] Eberhard, P.; Störkle, J.; Mack, A.: Dynamical-optical Simulation of a Segmented Mirror Telescope for Performance Identification. In Chen, G. (Ed.): Extended Abstract of the 9th Asian Conference on Multibody Dynamics, pp. 1–2, 2018.
- [ElectroOptics18] ElectroOptics: Webpage of the Electro Optics - The future of EUV lithography, Issue of February 2016. <https://www.electrooptics.com>, Accessed: February 21, 2018.
- [Enders11] Enders, B.: Fourier-Transformations-Holographie - Bildrekonstruktion aus kohärenten Streudaten. Skript und Versuch im Fortgeschrittenenpraktikum, E17 Lehrstuhl für Biomedizinische Physik, Technische Universität München, 2011.
- [ESO18] ESO: Webpage of the ESO - The Extremely Large Telescope, the world's biggest eye on the sky. <https://www.eso.org/public/usa/teles-instr/elt/>, Accessed: June 26, 2018.
- [FahrmeierKneipLang09] Fahrmeier, L.; Kneip, T.; Lang, S.: Regression. Berlin: Springer, 2009.
- [Fehr11] Fehr, J.: Automated and Error-Controlled Model Reduction in Elastic Multibody Systems. Dissertation, Schriften aus dem Institut für Technische und Numerische Mechanik der Universität Stuttgart, Vol. 21. Aachen: Shaker, 2011.
- [Föllinger92] Föllinger, O.: Regelungstechnik. Heidelberg: Hüthig Buch Verlag, 1992.
- [Fransen12] Fransen, S.: Methodologies for launcher-payload coupled dynamic analysis. CEAS Space Journal, Vol. 3, pp. 13–25, 2012.
- [GenbergMichels17] Genberg, V.L.; Michels, G.J.: Using integrated models to minimize environmentally induced wavefront error in optomechanical design and analysis. In Proc. SPIE, Optomechanical Engineering 2017, Vol. 10371, pp. 103710I–103710I–9, 2017.
- [Gilbergs18] Gilbergs, H.: Identifikation statischer und dynamischer Veränderungen in optischen Systemen aus Wellenfrontmessungen (in German). No. 90 in Berichte aus dem Institut für Technische Optik. Stuttgart: Institut für Technische Optik, Universität Stuttgart, 2018.
- [Goodman05] Goodman, J.: Introduction to Fourier Optics. Englewood: Roberts & Company, 2005.
- [Gramlich13] Gramlich, G.: Lineare Algebra. Berlin: Pro BUSINESS, 2013.
- [GrewalAndrews11] Grewal, M.; Andrews, A.: Kalman filtering: theory and practice using MATLAB. Hoboken: John Wiley & Sons, 2011.

- [Gross05] Gross, H. (Ed.): Handbook of Optical Systems Vol. 1 - Fundamentals of Technical Optics. Weinheim: Wiley-VCH Verlag, 2005.
- [GrossSingerTotzeck05] Gross, H.; Singer, W.; Totzeck, M.: Handbook of Optical Systems Vol. 2 - Physical Image Formation. Weinheim: Wiley-VCH Verlag, 2005.
- [GrossSingerTotzeck07] Gross, H.; Singer, W.; Totzeck, M.: Handbook of Optical Systems Vol. 3 - Aberration Theory and Correction of Optical Systems. Weinheim: Wiley-VCH Verlag, 2007.
- [Guyan65] Guyan, R.J.: Reduction of Stiffness and Mass Matrices. AIAA Journal, Vol. 3, No. 2, p. 380, 1965.
- [Hamilton28] Hamilton, W.R.: Theory of Systems of Rays. In Graisberry, R. (Ed.): The Transactions of the Royal Irish Academy, 15, pp. 69–174. Academy, 1828.
- [Herkommer14] Herkommer, A.: Advances in the design of freeform systems for imaging and illumination applications. Journal of Optics, Vol. 43, No. 4, pp. 261–268, 2014.
- [Herschel18] Herschel: Webpage of the ESA - The Largest Infrared Space Telescope. <https://www.esa.int>, Accessed: June 25, 2018.
- [Hetzler08] Hetzler, H.: Zur Stabilität von Systemen bewegter Kontinua mit Reibkontakten am Beispiel des Bremsenquietschens. Ph.D. thesis, Karlsruhe Institute of Technology, 2008.
- [HoaggBernstein07] Hoagg, J.B.; Bernstein, D.S.: Nonminimum-phase zeros - much to do about nothing - classical control - revisited part II. IEEE Control Systems, Vol. 27, No. 3, pp. 45–57, 2007.
- [HolzwarthEberhard14] Holzwarth, P.; Eberhard, P.: Input-Output Based Model Reduction For Interconnected Systems. In Oñate, E.; Oliver, J.; Huerta, A. (Eds.): Proceedings of the 5th European Conference of Computational Mechanics, pp. 1–11, 2014.
- [HowardEtAl08] Howard, J.M.; Ha, K.Q.; Shiri, R.; Smith, J.S.; Mosier, G.; Muheim, D.: Optical modeling activities for NASA's James Webb Space Telescope (JWST): Part V. Operational alignment updates. In Proc. SPIE, Modeling, Systems Engineering, and Project Management for Astronomy III, Vol. 7017, pp. 70170X–70170X–10, 2008.
- [HowardFeinberg09] Howard, J.M.; Feinberg, L.D.: Optical modeling activities for NASA's James Webb Space Telescope (JWST): VI. secondary mirror figure compensation using primary mirror segment motions. In Proc. SPIE, UV/Optical/IR Space Telescopes: Innovative Technologies and Concepts IV, Vol. 7436, pp. 74360C–74360C–12, 2009.

- [IEEE18] IEEE: Webpage of the IEEE Spectrum - EUV Lithography Finally Ready for Chip Manufacturing. <https://spectrum.ieee.org>, Accessed: June 27, 2018.
- [Imaginghub17] Imaginghub: Webpage of Imaginghub - Community Portal, Article: Performance of Nvidia Jetson TK1 with Basler GigE, machine vision at 200 fps. <http://imaginghub.com>, Published: March 13, 2017. Accessed: February 20, 2018.
- [IYL15] IYL: Webpage of the International Year of Light and Light-based Technologies. <http://www.light2015.org>, Accessed: December 5, 2015.
- [JWST18] JWST: Webpage of the NASA - James Webb Space Telescope's Golden Mirror Unveiled. <https://www.nasa.gov>, Accessed: June 25, 2018.
- [Kalman60] Kalman, R.E.: A New Approach to Linear Filtering and Prediction Problems. *Transactions of the ASME - Journal of Basic Engineering*, Vol. 82, pp. 35–45, 1960.
- [KongEtAl16] Kong, M.; Zhu, L.; Chen, D.; Liang, Z.; Zhao, R.; Xu, E.: Effect of the Liquid Density Difference on Interface Shape of Double-Liquid Lens. *J. Opt. Soc. Korea*, Vol. 20, No. 3, pp. 427–430, 2016.
- [KunkemöllerEtAl15] Kunkemöller, G.; Maß, T.W.W.; Michel, A.K.U.; Kim, H.S.; Brose, S.; Danylyuk, S.; Taubner, T.; Juschkin, L.: Extreme ultraviolet proximity lithography for fast, flexible and parallel fabrication of infrared antennas. *Opt. Express*, Vol. 23, No. 20, pp. 25487–25495, 2015.
- [Laslandes12] Laslandes, M.: Space active mirrors - Active optics developments for future large observatories. *Theses, Aix-Marseille Université*, 2012.
- [LeEtAl14] Le, M.; Ellenbroek, M.; Seiler, R.; Put, van, P.; Cottaar, E.: Disturbances in reaction wheels : from measurement to modeling. In *9th International ESA Conference on Guidance, Navigation & Control Systems*, 2-6 Juny 2014, Porto, Portugal, 2014.
- [Lehner07] Lehner, M.: *Modellreduktion in elastischen Mehrkörpersystemen* (in German). Dissertation, *Schriften aus dem Institut für Technische und Numerische Mechanik der Universität Stuttgart*, Vol. 10. Aachen: Shaker Verlag, 2007.
- [Lemaitre09] Lemaitre, G.: *Astronomical Optics and Elasticity Theory*. Berlin: Springer, 2009.
- [LewisXiePopa08] Lewis, F.; Xie, L.; Popa, D.: *Optimal and robust estimation: with an introduction to stochastic control theory*. Automation and control engineering. CRC Press, 2008.

- [Liang17] Liang, S.: Dynamisch-optische Zustandsrekonstruktion am Beispiel des Experiments “Objektivschwingungen” (in German). Student Thesis STUD-475, Institut für Technische und Numerische Mechanik der Universität Stuttgart, 2017.
- [LiuMaghamiBlaurock08] Liu, K.; Maghami, P.; Blaurock, C.: Reaction Wheel Disturbance Modeling, Jitter Analysis, and Validation Tests for Solar Dynamics Observatory. In AIAA Guidance, Navigation and Control Conference and Exhibit, 2008.
- [Lunze08] Lunze, J.: Regelungstechnik 1, Systemtheoretische Grundlagen, Analyse und Entwurf einschleifiger Regelungen. Berlin: Springer, 2008.
- [Lunze10] Lunze, J.: Regelungstechnik 2, Mehrgrößensysteme, Digitale Regelung (in German). Berlin: Springer, 6. Edn., 2010.
- [Lyapunov18] Lyapunov, S.I.: Response of the visual system to sine waves under various external conditions. *J. Opt. Technol.*, Vol. 85, No. 2, pp. 100–105, 2018.
- [Mack07] Mack, C.: *Fundamental Principles of Optical Lithography*. Chichester: John Wiley & Sons, 2007.
- [MacMartinThompson15] MacMartin, D.G.; Thompson, H.A.: Vibration budget for observatory equipment. *Journal of Astronomical Telescopes, Instruments, and Systems*, Vol. 1, No. 3, pp. 034005–034005–9, 2015.
- [MacMynowskiEtAl10] MacMynowski, D.G.; Colavita, M.M.; Skidmore, W.; Vogiatzis, K.: Primary mirror dynamic disturbance models for TMT: vibration and wind. In *Proc. SPIE, Modeling, Systems Engineering, and Project Management for Astronomy IV*, Vol. 7738, pp. 77380E–77380E–10, 2010.
- [Mahajan81] Mahajan, V.: Zernike annular polynomials for imaging systems with annular pupils. *Journal of the optical Society of America*, Vol. 71, No. 1, pp. 75–85, 1981.
- [Mahajan13] Mahajan, V.N.: *Optical Imaging and Aberrations Wavefront Analysis*. SPIE Press, 2013.
- [Mathworks18] Mathworks: Webpage of the Simulink Support Package for Arduino Hardware. <https://www.mathworks.com/hardware-support/arduino-simulink.html>, Accessed: February 15, 2018.
- [Medium17] Medium: Webpage: Medium - Arduino Simulink S-function tutorial. <https://medium.com>, Published: March 13, 2017. Accessed: February 19, 2018.
- [Meschede08] Meschede, D.: *Optik, Licht und Laser*. Wiesbaden: Vieweg Teubner, 2008.

- [Moore65] Moore, G.E.: Cramming more components onto integrated circuits. *Electronics Magazine*, Vol. 38, No. 8, pp. 1–4, 1965.
- [MT07] MT: Technical Note for the Linear IC Operational Amplifier MCP602-I/P. Microchip Technology (MT) Inc., 2007.
- [MT10] MT: Technical Note for the MCP4911 - 10-Bit Voltage Output Digital-to-Analog Converter with SPI Interface. Microchip Technology (MT) Inc., 2010.
- [Müller05] Müller, M.: Modeling of the Structure-Optics-Interaction in Large Astronomical Telescopes. München: Dissertation, Lehrstuhl für Leichtbau, Technische Universität München, 2005.
- [MyDiyElectronics14] MyDiyElectronics: Webpage of the My DIY Electronics Projects - Linear Magnetic Encoder Test. <https://mydiyelectronics.wordpress.com>, Published: August 8, 2014. Accessed: February 19, 2018.
- [NijenhuisHamelinckBraam12] Nijenhuis, J.; Hamelinck, R.; Braam, B.: The optomechanical performance prediction of thin mirror segments for E-ELT. In *Proc. SPIE, Modern Technologies in Space- and Ground-based Telescopes and Instrumentation II*, Vol. 8450, pp. 84500A–84500A–9, 2012.
- [Noll76] Noll, R.: Zernike Polynomials and Atmospheric Turbulence. *Journal of the Optical Society in America*, Vol. 66, No. 3, pp. 207–211, 1976.
- [NowakowskiEtAl12] Nowakowski, C.; Fehr, J.; Fischer, M.; Eberhard, P.: Model Order Reduction in Elastic Multibody Systems using the Floating Frame of Reference Formulation. *Mathematical Modelling*, Vol. 7, pp. 40–48, 2012.
- [Panzer14] Panzer, H.K.F.: Model Order Reduction by Krylov Subspace Methods with Global Error Bounds and Automatic Choice of Parameters. Dissertation, Technische Universität München. München: Verlag Dr. Hut, 2014.
- [PCB16] PCB: Technical Note for the Four-Channel ICP Sensor Signal Conditioner (Model 482C15). PCB Piezotronics, Inc., 2016.
- [PedrottiPedrotti93] Pedrotti, F.; Pedrotti, L.: *Introduction to Optics*. London: Prentice-Hall International, 1993.
- [PI15] PI: User Manual for the C-413PIMag[®] Controller (MS224E). Physik Instrumente (PI) GmbH & Co. KG, 2015.
- [PI16] PI: Technical Note for the V-522, V-524, V-528 PIMag[®] Voice Coil Linear Stages (V522T0002). Physik Instrumente (PI) GmbH & Co. KG, 2016.

- [Preumont06] Preumont, A.: *Vibration Control of Active Structures: An Introduction. Solid Mechanics and Its Applications*. Springer Netherlands, 2006.
- [PütschStollenwerkLoosen17] Pütsch, O.; Stollenwerk, J.; Loosen, P.: Integrated optical design for highly dynamic laser beam shaping with membrane deformable mirrors. In *Proc. SPIE, Laser Resonators, Microresonators, and Beam Control XIX*, Vol. 10090, pp. 10090–10090–8, 2017.
- [Ramsden11] Ramsden, E.: *Hall-Effect Sensors: Theory and Application*. Oxford: Elsevier Science, 2011.
- [RegueraEtAl15] Reguera, P.; Garcia, D.; Dominguez, M.; Prada, M.; Alonso, S.: A Low-cost Open Source Hardware in Control Education. Case Study: Arduino-Feedback MS-150. In *IFAC-PapersOnLine*, Vol. 48, pp. 117–122, 2015.
- [Roddier04] Roddier, F.: *Adaptive Optics in Astronomy*. Cambridge: Cambridge University Press, 2004.
- [RuppelEtAl13] Ruppel, T.; Dong, S.; Rooms, F.; Osten, W.; Sawodny, O.: Feedforward Control of Deformable Membrane Mirrors for Adaptive Optics. *IEEE Transactions on Control Systems Technology*, Vol. 21, No. 3, pp. 579–589, 2013.
- [SalehTeich91] Saleh, B.E.A.; Teich, M.C.: *Fundamentals of Photonics*. John Wiley & Sons, 1991.
- [Schäfer15] Schäfer, S.: *Dynamical-Optical Simulation of Elastic Mirror Systems using Annular Polynomials for Surface Approximation*. Master Thesis DIPL-MSC-219, Institute of Engineering and Computational Mechanics, University of Stuttgart, 2015.
- [SchiehlenEberhard14] Schiehlen, W.; Eberhard, P.: *Applied Dynamics*. Heidelberg: Springer, 2014.
- [Schmidt10] Schmidt, J.: *Numerical Simulation of Optical Wave Propagation*. Bellingham: SPIE, 2010.
- [Schnelle18] Schnelle, F.: *Modellprädiktive Ansätze zur Regelung von unteraktuierten Mehrkörpersystemen (in German)*. Dissertation, Schriften aus dem Institut für Technische und Numerische Mechanik der Universität Stuttgart, Vol. 54. Aachen: Shaker Verlag, 2018.
- [SchootEtAl17] van Schoot, J.; Troost, K.; Bornebroek, F.; van Ballegoij, R.; Lok, S.; Krabbendam, P.; Stoeldraijer, J.; Loopstra, E.; Benschop, J.P.; Finders, J.; Meiling, H.; van Setten, E.; Kneer, B.; Kuerz, P.; Kaiser, W.; Heil, T.; Migura, S.; Neumann, J.T.: High-NA EUV lithography enabling Moore’s law in the next

- decade. In Proc. SPIE, International Conference on Extreme Ultraviolet Lithography, Vol. 10450, pp. 10450–10450–20, 2017.
- [SchwertassekWallrapp99] Schwertassek, R.; Wallrapp, O.: Dynamik flexibler Mehrkörpersysteme (in German). Braunschweig: Vieweg, 1999.
- [ScolaEtAl14] Scola, S.J.; Osmundsen, J.F.; Murchison, L.S.; Davis, W.T.; Fody, J.M.; Boyer, C.M.; Cook, A.L.; Hostetler, C.A.; Seaman, S.T.; Miller, I.J.; Welch, W.C.; Kosmer, A.R.: Structural-Thermal-Optical-Performance (STOP) model development and analysis of a field-widened Michelson interferometer. In Proc. SPIE, Novel Optical Systems Design and Optimization XVII, Vol. 9193, pp. 9193–9193–15, 2014.
- [SedghiEtAl11] Sedghi, B.; Muller, M.; Bonnet, H.; Esselborn, M.; Louarn, M.L.; Clare, R.; Koch, F.: E-ELT modeling and simulation toolkits: philosophy and progress status. In Proc. SPIE, Integrated Modeling of Complex Optomechanical Systems, Vol. 8336, pp. 8336–8336–13, 2011.
- [SedghiEtAl16] Sedghi, B.; Dimmler, M.; Müller, M.; Kornweibel, N.: Improving E-ELT M1 prototype hard position actuators with active damping. In Proc. SPIE, Ground-based and Airborne Telescopes VI, Vol. 9906, pp. 99062W–99062W–12, 2016.
- [SedghiMüllerJakob16] Sedghi, B.; Müller, M.; Jakob, G.: E-ELT vibration modeling, simulation, and budgeting. In Proc. SPIE, Integrated Modeling of Complex Optomechanical Systems II, Vol. 10012, pp. 1001202–1001202–9, 2016.
- [Seifried14] Seifried, R.: Dynamics of Underactuated Multibody Systems - Modeling, Control and Optimal Design, Vol. 205. Berlin: Springer, 2014.
- [ShampineReichelt97] Shampine, L.F.; Reichelt, M.W.: The MATLAB ODE Suite. SIAM Journal on Scientific Computing, Vol. 18, No. 1, pp. 1–22, 1997.
- [Störkle11] Störkle, J.: Anwendung der dynamischen Spannungsanalyse auf die Bildfehlerkompensation bei optischen Systemen (in German). Student Thesis STUD-367, Institut für Technische und Numerische Mechanik der Universität Stuttgart, 2011.
- [StörkleEberhard16] Störkle, J.; Eberhard, P.: Strategies for the dynamical-optical simulation of high-performance optics. In Proc. SPIE, Integrated Modeling of Complex Optomechanical Systems II, Vol. 10012, pp. 100120C–100120C–5, 2016.
- [StörkleEberhard17a] Störkle, J.; Eberhard, P.: Influence of model order reduction methods on dynamical–optical simulations. Journal of Astronomical Telescopes, Instruments, and Systems (JATIS), Vol. Vol. 3, No. No. 2, pp. pp. 024001–1 – 024001–18, 2017.

- [StörkleEberhard17b] Störkle, J.; Eberhard, P.: Model-based Control of a Mechanical-optical System demonstrated at a Laboratory Experiment. In Zahariev, E. (Ed.): Extended Abstract of the IUTAM Symposium on Intelligent Multibody Systems - Dynamics, Control, Simulation, pp. 1–2, Bulgaria, 2017.
- [StörkleWengertEberhard14] Störkle, J.; Wengert, N.; Eberhard, P.: Optimization and Investigation of the Dynamical-Optical Behavior of Mirror Systems. In Rodrigues, H. (Ed.): Proceedings of the Engineering Optimization IV, pp. 231–236, London: Taylor & Francis Group, 2014.
- [Tatian74] Tatian, B.: Aberration balancing in rotationally symmetric lenses. *J. Opt. Soc. Am.*, Vol. 64, No. 8, pp. 1083–1091, 1974.
- [Teske16] Teske, D.: Erweiterung des Experiments “Objektivschwingungen” durch eine dynamisch-optische Regelung (in German). Student Thesis STUD-446, Institut für Technische und Numerische Mechanik der Universität Stuttgart, 2016.
- [Trautwein16] Trautwein, F.: Modellreduktion von elastischen Spiegelsystemen unter Berücksichtigung von optischen Sensitivitäten (in German). Student Thesis STUD-450, Institut für Technische und Numerische Mechanik der Universität Stuttgart, 2016.
- [TrebuñaEtAl12] Trebuña, F.; Pastor, M.; Binda, M.; Harčarik, T.: Modelling of Mechanical and Mechatronics Systems Modal Assurance Criterion. *Procedia Engineering*, Vol. 48, pp. 543 – 548, 2012.
- [Tyson15] Tyson, R.: Principles of Adaptive Optics. CRC Press, 4. Edn., 2015.
- [UsudaEtAl14] Usuda, T.; Ezaki, Y.; Kawaguchi, N.; Nagae, K.; Kato, A.; Takaki, J.; Hirano, M.; Hattori, T.; Tabata, M.; Horiuchi, Y.; Saruta, Y.; Sofuku, S.; Itoh, N.; Oshima, T.; Takanezawa, T.; Endo, M.; Inatani, J.; Iye, M.; Sadjadpour, A.; Sirota, M.; Roberts, S.; Stepp, L.: Preliminary design study of the TMT Telescope structure system: overview. In *Proc. SPIE, Ground-based and Airborne Telescopes V*, Vol. 9145, pp. 91452F–91452F–10, 2014.
- [Voelz11] Voelz, D.: Computational Fourier Optics. Bellingham, Washington: SPIE, 2011.
- [VogiatzisThompson16] Vogiatzis, K.; Thompson, H.: On the precision of aero-thermal simulations for TMT. In *Proc. SPIE, Modeling, Systems Engineering, and Project Management for Astronomy VI*, Vol. 9911, pp. 991112–991112–8, 2016.
- [VoormeerenValkRixen11] Voormeeren, S.; Valk, P.V.D.; Rixen, D.: Generalized Methodology for Assembly and Reduction of Component Models for Dynamic Substructuring. *AIAA Journal*, Vol. 49, No. 5, pp. 1010–1020, 2011.

- [Wengert16] Wengert, N.: Gekoppelte dynamisch-optische Simulation von Hochleistungsobjektiven (in German). No. 40 in Dissertation, Schriften aus dem Institut für Technische und Numerische Mechanik der Universität Stuttgart. Aachen: Shaker Verlag, 2016.
- [WengertEberhard13] Wengert, N.; Eberhard, P.: Vibration Modification in an Opto-Dynamical Test Setup for Suppressing Aberrations. In Proceedings of the 11th ICOVP, Lisbon, Portugal, 2013.
- [West01] West, P.: High Speed, Real-Time Machine Vision. Technical Report, Automated Vision Systems Inc. and CyberOptics - Imagenation, 2001.
- [WitvoetEtAl15] Witvoet, G.; den Breeje, R.; Nijenhuis, J.; Hazelebach, R.; Doelman, N.: Dynamic analysis and control of mirror segment actuators for the European Extremely Large Telescope. *Journal of Astronomical Telescopes, Instruments, and Systems*, Vol. 1, No. 1, pp. 019003–019003–13, 2015.
- [YoungJakeman80] Young, P.; Jakeman, A.: Refined instrumental variable methods of recursive time-series analysis Part III. Extensions. *International Journal of Control*, Vol. 31, No. 4, pp. 741–764, 1980.
- [YuRobertsSharf04] Yu, R.; Roberts, S.C.; Sharf, I.: Model order reduction of structural dynamics of a very large optical telescope. In *Proc. SPIE, Modeling and Systems Engineering for Astronomy*, Vol. 5497, pp. 611–621, 2004.
- [ZamkotsianDohlenFerrari00] Zamkotsian, F.; Dohlen, K.; Ferrari, M.: Microdeformable mirror for adaptive optics systems on extremely large telescopes. In *Proc. SPIE, Adaptive Optical Systems Technology*, Vol. 4007, pp. 4007–4007–8, 2000.
- [Zeiss18] Zeiss: Webpage of the EUV Litho, Inc. - Latest developments in EUV optics. <https://euvlitho.com/>, Accessed: June 27, 2018.
- [Zemax11] Zemax: Zemax Optical Design Program - User's Manual. Radiant ZEMAX LLC, 2011.
- [Zernike34] Zernike, F.: Beugungstheorie des Schneidverfahrens und seiner verbesserten Form, der Phasenkontrastmethode (in German). *Physica*, Vol. 1, No. 7–12, pp. 689 – 704, 1934.
- [ZhangLiGuo13] Zhang, W.; Li, D.; Guo, X.: Optical Design and Optimization of a Micro Zoom System with Liquid Lenses. *J. Opt. Soc. Korea*, Vol. 17, No. 5, pp. 447–453, 2013.
- [Zheng15] Zheng, X.: Simulation und Optimierung dynamisch-optischer Spiegel- und Linsensysteme (in German). Bachelor Thesis BSC-48, Institut für Technische und Numerische Mechanik der Universität Stuttgart, 2015.

Abbreviation, Symbols and Notations

The following is a list of all important symbols that appear in this thesis. Vector quantities and matrices are marked by bold font, scalar quantities are displayed in normal font.

Abbreviations

AO	adaptive optical	KF	Kalman-Bucy filter
ADC	analog-digital converter	LDV	Laser Doppler vibrometer
AO	adaptive optics	LOS	line of sight
AOI	area of interest	LQE	linear-quadratic estimator
AS	aperture stop	LQR	linear-quadratic regulator
CAD	computer-aided design	LSST	Large Synoptic Survey Telescop
CMS	component mode synthesis	M1	primary mirror
CR	chief ray	M2	secondary mirror
DAC	digital-analog converter	M3	tertiary mirror
DOF	degrees of freedom	MAC	modal assurance criterion
ELT	Extreme Large Telescope	MBS	multibody systems
EMBS	elastic multibody systems	MIMO	multiple inputs and multiple outputs
EnP	entrance pupil	MOR	model order reduction
EUV	extreme ultraviolet	OPD	optical path difference
EVP	eigenvalue problem	OPL	optical path length
ExP	exit pupil	PoE	powered over Ethernet
FE	finite element	PSF	point-spread function
FEM	finite-element method	RMS	root mean square
FF	feed-forward	SHWFS	Shack-Hartmann Wavefront Sensor
FI	future-integration	SPI	serial peripheral interface
FPGA	Field Programmable Gate Array	STOP	Structural-Thermal-Optical-Performance
GRIN	gradient-index	TMT	Thirty Meter Telescope
ICP	integrated circuit piezoelectric	WFA	wavefront aberration
JWST	James Webb Space Telescope		

Latin Lower Case Letters

a	displacement of the light point	$\mathbf{d}_{i,\text{refl}}$	ray direction after the reflection at a surface S_i
\mathbf{a}	vector containing optical aberrations, e.g., LOS and WFA	\mathbf{d}_i	ray direction after a surface S_i , which is represented in S_i
a_i	distance between the two intersection points	${}^i\mathbf{d}_{i-1}$	ray direction after a surface S_{i-1} , represented in S_i
a_F	force-induced displacement of the light point	$\Delta\mathbf{a}$	change of optical aberration in comparison to reference config.
a_M	displacement of the light point caused by the actuated lens	$\Delta\mathbf{a}_{\text{los}}$	change of LOS in comparison to reference config.
\mathbf{a}_0	initial optical aberration of the reference configuration	$\Delta\mathbf{a}_{\text{wfa}}$	change of WFA in comparison to reference config.
$\bar{\mathbf{a}}_j$	local accelerations of the j^{th} body	$\Delta\mathbf{s}_i$	relative surface displacement
\mathbf{a}_{los}	vector containing the LOS coordinates	Δs_{opl}	optical path difference
$\mathbf{a}_{0,\text{los}}$	the LOS \mathbf{a}_{los} in the initial reference configuration	Δs_z	surface or segment translation in the z -direction
\mathbf{a}_r	translational rigid body motion	Δz	distance between optical source- and observation-plane
\mathbf{a}_{wfa}	vector of Zernike coefficients describing the WFA	\mathbf{e}	errors of the state estimation
$\mathbf{a}_{0,\text{wfa}}$	the WFA \mathbf{a}_{wfa} in the initial reference configuration	f	focal length in the object-space
b	slit width or distance of the gratings	f'	focal length in the image-space
c_0	speed of light in vacuum	\mathbf{f}^a	generalized applied forces of an elastic body
c_1	Zernike coefficient describing the piston	\mathbf{f}_j^a	applied forces of the j^{th} rigid body
c_2, c_3	Zernike coefficients describing tilts	\mathbf{f}^r	generalized reaction forces of an elastic body
c_M	phase velocity of light in the medium	f_x, f_y	spatial frequencies of the optical field
c_j	Zernike coefficients	\mathbf{g}	generalized reaction forces and moments
\mathbf{c}_z	vector of Zernike coefficients describing the deformation	\mathbf{h}^ω	generalized centrifugal and Coriolis forces of an elastic body
d	distance to the object with respect to the lens	\mathbf{h}_e	acting forces on the elastic body
d'	distance to the image with respect to the lens	i	index of an optical surface
\mathbf{d}_{Im}	ray direction at the image plane	j	index of a Zernike coefficient
$\mathbf{d}_{\text{ideal}}$	ideal direction of a ray, which is normal to the reference sphere	k	wavenumber
		\mathbf{k}	wave traveling vector

\mathbf{k}^c	generalized gyroscopic forces	\mathbf{q}_r	rigid body coordinates
k_{CD}	process factor for the resolution	\mathbf{r}	position vector
\mathbf{l}_j^a	applied moments of the j^{th} body	\mathbf{r}_i	intersection point of ray and surface S_i , represented in S_i
m	azimuthal frequency of the Zernike polynomials	${}^i\mathbf{r}_{i-1}$	intersection point of ray and surface S_{i-1} , represented in S_i
m_j	mass of the j^{th} body	\mathbf{r}_{Im}	intersection point of the ray with the image plane
\mathbf{m}_i	unit vector tangential to the surface	\mathbf{r}_{Ref}	intersection point of the ray with the reference sphere
n	index of refraction	r_x, r_y, r_z	components of the position \mathbf{r}
n	radial degree of the Zernike polynomials	$r_{x,\text{Ref}}$	x -coordinate of \mathbf{r}_{Ref}
n_{dof}	number of degrees of freedom	$r_{y,\text{Ref}}$	y -coordinate of \mathbf{r}_{Ref}
n_{glass}	index of refraction in glass	s	complex frequency $s = i\omega$
n_i	index of refraction after the surface S_i	s	geometrical length of light
n_i	number of indices i	s_{ImRef}	geometrical path length from reference sphere to image plane
\mathbf{n}_i	unit vector normal to the surface	$\mathbf{s}_{0,i}$	same as \mathbf{s}_i , but in the reference configuration
$\tilde{\mathbf{n}}_i$	vector with the same direction as \mathbf{n}_i , but not normalized	\mathbf{s}_i	relative position of a surface S_i , represented in S_{i-1}
n_j	number of indices j	$\hat{\mathbf{s}}_i$	absolute position of the i^{th} optical surface
n_k	number of nodes	${}^{i-1}\mathbf{s}_i$	relative position of a surface S_i , represented in S_{i-1}
$\mathbf{p}_{\text{mech2opt}}$	position of S_i from K_{cog}	s_{L5}	kinematic-optical sensitivity of the 5 th lens
$\mathbf{p}_{k,\text{node}}$	position of a node k in the initial configuration	s_{opl}	optical path length
q	order of the interference maximum	t	time
\mathbf{q}	generalized coordinates of a linear system	t_{opt}	needed traveling time of light
$\tilde{\mathbf{q}}$	modal representation of \mathbf{q}	\mathbf{u}	input vector for a dynamical system
\mathbf{q}^a	generalized applied forces	u_{F}	force excitation which acts as the system input
$\bar{\mathbf{q}}^a$	applied forces and moments	\mathbf{v}	observation noise of the measurements
$\bar{\mathbf{q}}^c$	Coriolis and gyroscopic forces	\mathbf{v}^*	mode shape, which is normalized by its RMS
\mathbf{q}_e	elastic coordinates of a body	\mathbf{v}_i	i^{th} eigenvector
$\bar{\mathbf{q}}_e$	reduced elastic coordinates of a body		
\mathbf{q}_{nl}	generalized coordinates, which could behave nonlinear		

$v_{k,\text{sum}}$	absolute displacement of the k^{th} node	\mathbf{x}_{nl}	state vector for a system, which could behave nonlinear
\mathbf{v}_{sum}	absolute node displacements	\mathbf{y}	system outputs, measurable states
\mathbf{w}	process noise of the model	y	height of the object
x, y, z	coordinates	y'	height of the image
\mathbf{x}	state vector of a linear system	$\hat{\mathbf{y}}$	estimated system outputs
$\hat{\mathbf{x}}$	estimated system states	$y_{i,\text{seg}}$	y -position of segment center
x', y'	absolute image coordinates	\mathbf{y}_k	vector of node y -displacements
x_1, y_1	coordinate at the optical source-plane	y_{LOS}	y -coordinate of the LOS motion
x_2, y_2	coordinate at the optical observation-plane	y_{M}	position of the motor and the attached lens
$x_{i,\text{seg}}$	x -position of segment center	z_{deform}	surface deformation with respect to the z -direction
x_{LOS}	x -coordinate of the LOS motion	z_{EP}	z -value of a surface described by an Extended-Polynomial
$x_{\text{rel}}, y_{\text{rel}}$	relative image coordinates	z_{EA}	z -value of a surface described by an Even-Asphere
\mathbf{x}_k	vector of node x -displacements	\mathbf{z}_k	vector of node z -displacements
$\hat{\mathbf{x}}_k$	discrete system states, estimated through KF	z_{ref}	z -value of continuous surface description, in reference config.

Latin Upper Case Letters

A	complex amplitude phase factor	\mathbf{B}_{KF}	input matrix of the Kalman filter
\mathbf{A}	system matrix of a linear system	$\mathbf{B}_{\text{KF,d}}$	input matrix of the discrete Kalman filter
\mathbf{A}_{KF}	system matrix of the Kalman filter	\mathbf{C}	output matrix of a linear system
$\mathbf{A}_{\text{KF,d}}$	system matrix of the discrete Kalman filter	\mathbf{C}_a	global matrix of kinematic-optical sensitivities
\mathbf{B}	input matrix of a linear system	$\mathbf{C}_{a,e}$	matrix of kinematic-optical sensitivities for pure elastic deformations
\mathbf{B}	magnetic vector field	$\bar{\mathbf{C}}_{a,e}$	similar to $\mathbf{C}_{a,e}$, but with respect to the reduced mode shapes
$\hat{\mathbf{B}}$	amplitude of the magnetic vector field \mathbf{B}	$\mathbf{C}_{a,e,\text{wfa}}$	matrix of kinematic-optical sensitivities, which describe the LOS motion with respect to \mathbf{q}_e
$\bar{\mathbf{B}}$	global input matrix of the mechanical system	$\mathbf{C}_{a,r}$	matrix of kinematic-optical sensitivities for pure rigid body motions
$\bar{\mathbf{B}}_e$	reduced input matrix of an elastic body		
\mathbf{B}_e	input matrix of an elastic body		

$C_{a,r,los}$	matrix of kinematic-optical sensitivities, which describe the LOS motion with respect to \mathbf{q}_r	\mathbf{H}_{mech}	matrix of mechanical transfer functions from mechanical inputs to mechanical outputs
C_{cr}	reference frame at CR on image plane with orientation of CR	$\mathbf{H}_{mech,opt}$	matrix of transfer functions from mechanical inputs to optical aberrations
CD_{Abbe}	critical distance according to Abbe	H_{otf}	optical transfer function, similar to \bar{P}_w
CD_{Rayl}	critical distance according to Rayleigh	\mathbf{I}	identity matrix
C_m	aspherical parameters for surface description	I	object intensity distribution if it depends on (x', y') or object intensity spectrum if it depends on (f_x, f_y)
C_{optic}	kinematical-optical sensitivities according to the DOF of the experiment	I_{Airy}	Airy disk, which describes an ideal irradiance
C_r	rotational coupling matrices of an elastic body	I'	image irradiance distribution if it depends on (x', y') or image irradiance spectrum if it depends on (f_x, f_y)
C_t	translational coupling matrices of an elastic body	\mathbf{I}_e	inertia tensor of an elastic body
D	feedthrough matrix of a linear system	\mathbf{I}_j	inertia tensor of the j^{th} body
D	damping matrix of a linear MBS	I_k	moments of inertia of the coupled pendulums
D_{Airy}	diameter of the Airy disk	I'_{local}	local irradiance field of the image
D_{AS}	diameter of the AS	I_{psf}	intensity response, which results from the PSF
D_e	damping matrix of an elastic body	I_{sys}	inertial reference frame of the regarded system
\bar{D}_e	reduced damping matrix of an elastic body	$\bar{\mathbf{J}}$	global Jacobian matrix
\mathbf{E}	electric vector field	J_1	Bessel function of first kind
\hat{E}	amplitude of the electric vector field \mathbf{E}	\mathbf{J}_{Rj}	rotational Jacobian matrix of the j^{th} body
E_{exp}	absolute radiant exposure	\mathbf{J}_{Tj}	translational Jacobian matrix of the j^{th} body
E_{los}	exposed image of the LOS trajectory	\mathbf{K}	stiffness matrix of a linear MBS
\mathbf{F}_j^r	distribution matrix for the reaction forces of the j^{th} body	K_{cog}	reference frame in the center of gravity
\mathbf{G}	matrix of the gyroscopic forces	\mathbf{K}_e	stiffness matrix of an elastic body
\mathbf{G}	noise input matrix	$\bar{\mathbf{K}}_e$	reduced stiffness matrix of an elastic body
$G_{M,est}$	estimated transfer function of the closed-loop motor	L	LOS trajectory
\mathbf{H}	matrix of transfer functions		
$\bar{\mathbf{H}}_{mech}$	matrix of transfer functions, of the reduced mechanical system		

L_j^r	distribution matrix for the reaction moments	$R_{z,\text{inner}}$	inner semi-diameter of the regarded annular area
L_{opt}	observer gain matrix	$\Delta \mathbf{R}_i$	relative surface rotation
M	magnification of the imaging system	$\Delta \mathbf{R}_{i,\text{seg}}$	rotation of the i^{th} segment
\mathbf{M}	inertia matrix of a linear MBS, also known as mass matrix	S_i	reference frame of a surface with the index i
$\bar{\mathbf{M}}$	global mass distribution matrix	$S_{i,\text{seg}}$	reference frame at the center of the i^{th} segment
\mathbf{M}_e	mass matrix of an elastic body	S_{ref}	reference surface of a segmented mirror
$\bar{\mathbf{M}}_e$	reduced mass matrix of an elastic body	U	optical wave field
\mathbf{M}_{nl}	inertia matrix for a system, which could be nonlinear	U_i	optical field at the image plane
\mathbf{N}	matrix of the non-conservative forces	U_o	optical field at the object plane
NA	numerical aperture	\bar{U}_o	object amplitude spectrum
\mathbf{P}	solution matrix of the Riccati equation	U_s	spherical wave field
\mathbf{P}	matrix of velocity-dependent forces	\hat{U}_s	amplitude of the spherical wave field
P	amplitude distribution of ideal PSF without WFA	V	potential formulation of a surface description
P_w	point-spread function	\mathbf{V}	projection matrix
\bar{P}	pupil function based on AS without WFA	\mathbf{W}	weighting matrix during the least square fit
\bar{P}_w	coherent transfer function, i.e., $\bar{P} + \text{WFA}$	W_{approx}	real wavefront approximated within $[r_{x,\text{Ref}}, r_{y,\text{Ref}}]$
\mathbf{Q}	matrix of position-dependent forces	W_{ideal}	ideal wavefront at the Exp
\mathbf{Q}	constant power spectral density matrix of \mathbf{w}	W_{real}	real wavefront at the Exp, which is usually disturbed
$\bar{\mathbf{Q}}$	global distribution matrix of generalized reaction forces	ΔW	wave front aberration
\mathbf{R}	constant power spectral density matrix of \mathbf{v}	ΔW_{pv}	peak-to-peak value of the WFA
$\mathbf{R}_{0,i}$	same as \mathbf{R}_i , but in the reference configuration	ΔW_ρ	slope of the WFA in radial coordinate ρ
R_i	curvature radius of surface S_i	ΔW_{rms}	RMS of the WFA, without c_1 , c_2 and c_3
\mathbf{R}_i	relative orientation of the surface S_i , which is represented in S_{i-1}	ΔW_θ	slope of the WFA in angular coordinate θ
$\hat{\mathbf{R}}_i$	absolute orientation of the i^{th} optical surface	ΔW_x	slope of the WFA in x -direction
R_z	semi-diameter of the regarded area for the approximation	ΔW_y	slope of the WFA in y -direction
		Z_ρ, Z_θ	polar derivatives of the Zernike polynomials
		Z_j	j^{th} basis function of the Zernike polynomials

Greek Letters

α	aperture angle	ε_r	material's relative permittivity
α_C	Cardan angle for x -rotation	γ	angle of incidence, refraction or reflection
$\bar{\alpha}_j$	local angular acceleration of the j^{th} body	κ	conic constant of an ellipsoid
α_r	rotational rigid body motion	κ_k	stiffnesses of coupled pendulums
α_R	mass-weighted Rayleigh coefficient	λ	wavelength
β_C	Cardan angle for y -rotation	μ_0	permeability in vacuum
β_R	stiffness-weighted Rayleigh coefficient	μ_r	material's relative permittivity
ω_j	angular velocity of the j^{th} body	ω	angular frequency
δ	Dirac impulse	ω_i	i^{th} eigenfrequency
ε	aperture ratio for annular pupils	Φ	modal matrix containing all eigenmode shapes
ε_0	permittivity in vacuum	ρ	radial part of the polar coordinates
$\varepsilon_{\text{apprx}}$	relative accuracy of an approximated surface	τ_c	coherence time
ε_{mor}	relative error of reduced system, with respect to full system	θ	angular part of the polar coordinates

General Mathematical Expressions and Symbols

$\ \mathbf{A}\ $	Frobenius norm of matrix \mathbf{A}
$\mathbf{a} \cdot \mathbf{b}$	vektor produkt of two vectors \mathbf{a} and \mathbf{b}
$\text{ceil}(a)$	round up
$\text{cov}(\mathbf{a}, \mathbf{b})$	covariance matrix of the vectors a and b containing random numbers
$\text{diag}(\mathbf{a})$	Diagonalmatrix mit den Elementen des Vektors \mathbf{a}
$E\{a\}$	expectation value of random number a
$\mathcal{F}\{f\}$	2-D Fourier transformation of the function f
$\mathcal{F}^{-1}\{f\}$	inverse 2-D Fourier transformation of the function f
$\text{floor}(a)$	round down
$g * f$	convolution of the two functions g and f
$\text{gain}(H)$	gain of transfer function H
$\text{grad}(f)$	gradient $\frac{\partial}{\partial \mathbf{r}}$ of the function f
$\text{min}_a(f)$	find a , which minimizes function f
$\text{poles}(H)$	poles of transfer function H
$\text{rms}(\mathbf{a})$	root mean square of vector \mathbf{a}
$\text{zeros}(H)$	zeros of transfer function H